Experimental and Computational Investigations on the Adsorption Applications of Covalent Triazine Frameworks

Sina Pourebrahimi

A Thesis
In the Department of
Chemical and Materials Engineering

Presented in Partial Fulfillment of the Requirements
For the Degree of
Doctor of Philosophy (Chemical Engineering)

at Concordia University
Montréal, Québec, Canada

July 2023

CONCORDIA UNIVERSITY
SCHOOL OF GRADUATE STUDIES

This is to certify that the thesis prepared

By: Sina Pourebrahimi

Entitled: Experimental and Computational Investigations on the Adsorption Applications of Covalent Triazine Frameworks

and submitted in partial fulfillment of the requirements for the degree of

Doctor of Philosophy (Chemical Engineering)

complies with the regulations of the University and meets the accepted standards with respect to originality and quality.

Signed by the final examining committee:

Manar Amayri Chair
Dr.

Phillip Choi External Examiner
Dr.

Melanie J Hazlett Examiner
Dr.

Deniz Meneksedag Erol Examiner
Dr.

Rachael A Mansbach Examiner
Dr.

Alex De Visscher Thesis Supervisor
Dr.

Gilles H Peslherbe Thesis Co-Supervisor
Dr.

Approved by

Dr. Zhibin Ye, Graduate Program Director

Date 2023 Dean of Faculty

Dr. Mourad Debbabi

Abstract

Experimental and Computational Investigations on the Adsorption Applications of Covalent Triazine Frameworks

Sina Pourebrahimi, Ph.D.
Concordia University, 2023

As an emerging subclass of advanced nanoporous materials, covalent triazine frameworks (CTFs) possess distinct properties such as high specific surface area, large pore volume, exceptional thermal/chemical stability, and structural designability. Thus, they have many real-world applications, including, but not limited to, catalysis, energy storage and conversion, adsorption, chemical sensing, and separation. In this doctoral dissertation, three projects related to CTF materials have been performed. Firstly, two electron-rich π-conjugated CTFs with high specific surface area and pore volume were synthesized *via* the facile and convenient Friedel-Crafts alkylation reaction of cyanuric chloride and trans-stilbene (TS) as well as diphenylacetylene (DPA), containing conjugated C=C double bond and C≡C triple bond functionalities, respectively. The iodine-capturing performance of these two electron-rich CTFs was investigated in a combined experimental-computational approach. Secondly, to design novel functionalized CTFs suitable for heavy metal cations removal from aqueous solutions, a DFT-assisted computational screening approach was employed on various CTFs featuring different electron-rich functionalities with negatively charged atom(s) for efficient adsorption of Cd^{2+}, Pb^{2+}, and Hg^{2+} cations as three most biohazardous heavy metal species. The metal removal process was also investigated in a combined experimental-computational approach. Thirdly, the gas adsorption and sensing properties of the pristine CTF-1 covalent triazine framework and its platinum atom (Pt)-doped counterpart were investigated computationally for SF_6 decomposition products (*i.e.*, H_2S, SO_2, SOF_2, and SO_2F_2 gases) using the density-functional theory (DFT) method. In this framework, density of states (DOS) analysis examined the adsorption and sensing mechanisms. Computational and experimental results obtained in this dissertation confirmed the promising performance of the CTF materials in efficiently eliminating environmental micropollutants via adsorption.

Acknowledgments

This Ph.D. study was conducted at Concordia University, located on unceded Indigenous territories, and I would like to highlight that. The lands and the water on which we are gathered today, Tiohtià:ke/Montreal, are acknowledged to belong to the Kanien'kehá:ka Nation as the ancestral homeland.

This thesis results from a cheerful and special period in my academic career. I appreciate the opportunity to learn from my loving supervisors, Prof. Alex De Visscher and Prof. Gilles H Peslherbe. Their unwavering assistance, fatherly counsel, and strategic insight into the research were priceless resources and powerful motivators. I especially would like to thank Prof. Gilles H. Peslherbe for enabling me to work with his great research group at Concordia University's Department of Chemistry and Biochemistry. He inspired my future academic career because of his technical expertise, professionalism, and humbleness. Additionally, I would like to thank Dr. Denis Koch from the Center for Research in Molecular Modeling (CERMM) and Mr. Majid Pirooz from Isfahan University in Iran for their technical assistance and support throughout my Ph.D. journey. I value the Natural Sciences and Engineering Research Council of Canada (NCERC) 's financial assistance. In addition, I am grateful for the full-tuition recruitment award and doctoral fellowship I received from Concordia University's School of Graduate Studies, Gina Cody School of Engineering, and the Department of Chemical and Materials Engineering. I am grateful for the financial assistance from my kind, generous, and thoughtful supervisor, Prof. Alex De Visscher. I particularly value the excellent computational means Prof. Gilles H Peslherbe provided me, including CERMM and the Digital Research Alliance of Canada.

Particular thanks to Ms. Erica Howse, Ms. Harriet Laryea, and Mr. Antonios Daskalakis from the Department of Chemical and Materials Engineering for their helpful assistance. Ultimately, I would like to thank my family for their efforts. My charming and beautiful sister Sareh, my dear mother, Fatemeh, and my father, my role model, Hassan. They never ceased making sacrifices so that I could have the greatest education in the area. The kind wishes and prayers of my family have always been with me.

Contribution of Authors

Chapter 2:

Sina Pourebrahimi performed the literature review, gathered data, wrote the first draft, and edited the manuscript. Majid Pirooz gathered data and edited the manuscript. Chapter 2 is part of a comprehensive review paper entitled "Functionalized Covalent Triazine Frameworks as Promising Platforms for Environmental Remediation: A Review" authored by Sina Pourebrahimi and Majid Pirooz and published in the Cleaner Chemical Engineering Journal.

Chapter 5:

Sina Pourebrahimi conceptualized the idea, designed the experiments, conducted the experiments, performed the DFT calculations, analyzed data, and wrote the first draft of the manuscript. Majid Pirooz helped with some of the experiments and edited the first draft of the manuscript. Dr. Gilles H Peslherbe administrated the project, analyzed data and edited the manuscript. Dr. Alex De Visscher administrated the project, funded the project, and edited the manuscript. The results of this chapter are published in an article entitled "Highly Efficient and Reversible Iodine Adsorption Utilizing Amorphous Conjugated Covalent Triazine-Based Porous Polymers: Experimental and Computational Studies" in the Journal of Environmental Chemical Engineering.

Chapter 6:

Sina Pourebrahimi conceptualized the idea, designed the experiments, conducted the experiments, performed the DFT calculations, analyzed data, and wrote the first draft of the manuscript. Majid Pirooz helped with some of the experiments and edited the first draft of the manuscript. Dr. Gilles H Peslherbe administrated the project, analyzed data, and edited the manuscript. Dr. Alex De Visscher administrated the project, funded the project, and edited the manuscript.

Chapter 7:

Sina Pourebrahimi conceptualized the idea, performed the DFT calculations, analyzed data, and wrote the first manuscript draft. Dr. Gilles H Peslherbe administrated the project, analyzed data, and edited the manuscript. Dr. Alex De Visscher administrated the project, funded the project, and edited the manuscript.

All authors reviewed the final manuscripts and approved the contents.

Table of Contents

List of Figures

List of Tables

1 Chapter 1: Introduction

The excessive exploitation of natural resources such as fossil fuels (e.g., petroleum, crude oil, natural gas, and coal) for energy generation and material fabrication has triggered severe global environmental issues, imposing substantial threats to nature and human generations [1-3]. In the meantime, anthropogenic industrial activities such as mining, the uncontrolled release of industrial wastes to the environment, and the utilization of As-based pesticides, herbicides, and fertilizers have been posing undesirable and irretrievable impacts on the global ecosystem [4]. For instance, the excessive use of fossil fuels has led to the discharge of massive amounts of either direct greenhouse gases (e.g., CO_2, CH_4, and N_2O) or non-methane volatile organic compounds (NMVOCs) as indirect greenhouse gases (e.g., NO, NO_2, SO_2, and CO) into the atmosphere [5]. Besides, the rapid evolution of heavy industries, for example, nuclear energy, mining, and steelmaking, has led to the release of large quantities of heavy metal species (e.g., Hg, Cd, Pb, Ni, Cu, and Cr) and radionuclide pollutants (e.g., radioiodine) to the ecosystem [6, 7]. Therefore, the ever-increasing energy demand of today's human populations should be addressed in an environmental-friendly manner, such that the environmental consequences and their sustainable solutions must receive the highest priority. Several plausible resolutions for alleviating the abovementioned concerns have been proposed, including generating and utilizing renewable energies obtained through eco-friendly solar, water, wind, geothermal, and biomass resources [8]. Material science and technology play a significant role in implementing these alternative energies. In addition, implementing advanced treatment methods would be another viable solution for lessening the negative influences of human activities on the environment [9]. Nanoporous materials have been extensively investigated in this venue for their possible applications in addressing environment-related challenges and issues [10].

Nanoporous materials exhibit distinctive features and functions impossible to achieve in nonporous structures (e.g., nonporous adaptive crystals of pillararenes) [11]. Over the past century, significant advancements in chemistry and materials science have introduced diverse classes of porous materials, from inorganic to organic, from micro- to macroporous, from rigid networks to soft dynamic frameworks, and from two-to three-dimensional structures [12-14]. Nanoporous structures are mostly categorized as microporous (i.e., pore size below 2 nm), mesoporous (i.e., pore size between 2 and 50 nm), and macroporous (i.e., pore size above 50 nm) [15]. Several novel nanoporous materials have been rationally designed, synthesized, and used for the remediation and complete protection of the environment. In this regard, SiO_2 nanoparticles [16], activated carbons (ACs) [17-22], zeolites [23, 24], metal-organic frameworks (MOFs) [25-30], covalent organic frameworks (COFs) [31-35], and covalent triazine frameworks (CTFs) [36-39] are among the most broadly used nanoporous structures in the field of environmental remediation. However, zeolites and their hybrid composite materials have not shown a promising performance toward some environmental remediation processes (e.g., heavy metal removal from aqueous phase) due to the lack of diversity in task-specific functionalities (except ion-exchanged ones possessing certain types of task-specific functionalities) in their highly stable yet rigid structures with specific surface areas typically falling in the range of 300-800 $m^2\ g^{-1}$ [40] going up to partway through typical acceptable specific surface areas for iodine and heavy metals adsorption on industrial scales (i.e., the specific surface areas around 500-1500 $m^2\ g^{-1}$ is desirable for these ends). In the meantime, regarding small micropores within their structures (i.e., 2 to 8 Å) [41] and considering the adsorbate-adsorbate repulsion between charged species (e.g., heavy metal cations and (poly)iodides) within pores, zeolites may not be suitable to adsorb a considerable quantity of large

adsorbate species, particularly (poly)iodides (e.g., I_3^- and I_5^-). Despite the outstanding chemical/thermal stability of the carbon-based nanoporous materials and their capability of being equipped with desired functionalities, they suffer from some drawbacks, e.g., restriction in structural tunability [42]. In contrast, MOFs possess fascinating features in terms of functionality, structural versatility, composition tunability, and tailor-made porosity. Nevertheless, their chemical stability is low, particularly under harsh operational conditions, such as in a medium with low pH, since they consist of metallic clusters [43]. To overcome these limitations, COFs and CTFs can be used in real-world applications while possessing most MOFs' features along with exceptional thermal, chemical, and structural stability [44, 45].

CTFs are a novel subtype of porous organic polymers (POPs) in which organic building units precisely assemble to yield nanostructures with well-defined pores [36, 45]. CTFs constructed with triazine linkages (i.e., aromatic C=N) are receiving more and more attention since the first report on their synthesis via the ionothermal cyclotrimerization of carbonitrile-containing (i.e., cyano-functionalized) precursors by Kuhn et al. in 2008 [46]. 1,4-dicyanobenzene (DCB), 4,4'-dicyanobiphenyl (DCBP), 2,6-dicyanopyridine (DCP), 2,4-dicyanothiazole (DCT), and 1,3,5-Tris(4-cyanophenyl)-benzene (TCT) were the first nitrile monomers for fabrication of porous triazine-based polymers [46]. CTFs possess fascinating features, such as highly stable and robust aromatic C=N linkages (i.e., the triazine rings) and the lack of weak bonds in their structures, except for the C−H bonds appended to phenyl rings [45]. One of the properties that make CTFs distinctive is their designability. In principle, the organic building units' geometry, dimension, and functionalities control the resultant framework's textural, structural, and physicochemical properties. For instance, DCB-based CTF (CTF-1) shows a highly crystalline structure with long-range ordered channels in its microstructure attributed to the planar structure of DCB monomer and linearity of cyano functionalities appended to the phenyl rings [46, 47]. However, DCBP and TCT do not feature a planar but a slightly distorted structure [46]. In contrast, DCT and DCP do not own a linear arrangement of the cyano functionalities, rendering porous yet amorphous networks [46]. CTFs offer tailor-made supramolecular structures for efficient interaction with photons, electrons, ions, and various guest molecules (e.g., small gas species). In particular, CTFs show excellent thermal/chemical stability (as a result of the existence of highly stable triazine moieties in their structures), considerable nitrogen content, high specific surface area, and large pore volume, making them promising candidates for tackling growing energy-and environment-related challenges in areas including adsorption of small molecules [48], separation of gas mixtures [37], organic energy storage and conversion devices [49], and catalysis [50].

Previous studies and reports have investigated CTFs and their applications in adsorption, separations, heterogeneous catalysis, metal-free catalysis, electro-and photocatalysis, gas sensing, and bioengineering. Nonetheless, the design and synthesis of functionalized CTFs and their environmental remediation applications must be investigated more. That is, we need to attain a more profound understanding of the effects of incorporating organic functional groups on textural and structural properties, host-guest interactions, and applications of functionalized CTFs for environmental remediation through an in-depth analysis of the recently reported research. Due to the increasing popularity of CTF-based materials, several reviews have been published on their synthesis and applications in the last few years [37, 45, 48, 51]. However, they did not report the applications of functionalized CTF materials. Moreover, regarding the rapid growth of this field in the last few years, a new updated summary of their environmental remediation applications is

of prominent importance. This section exclusively concentrates on the state-of-the-art design and preparation techniques of functionalized CTFs, including bottom-up and post-synthetic modification strategies. Then, the environmental remediation applications of functionalized CTFs are discussed in detail. Ultimately, an outlook presenting prospects and challenges in this fascinating research area is further provided.

1.1 Preparation methods for CTFs

Several two-and three-dimensional CTFs have been successfully synthesized through a number of synthetic methods, including: (i) low-temperature zinc triflimide-promoted cyclotrimerization of tetrafluoroterephthalonitrile [52] (ii) high-temperature ionothermal cyclotrimerization of carbonitrile-containing aromatic building blocks in the presence of molten zinc chloride ($ZnCl_2$) as both solvent and Lewis-acid catalyst [46], (iii) room-temperature and (iv) microwave-assisted super acid-catalyzed polymerization of cyano-functionalized organic building units using trifluoromethanesulfonic acid as strong Brønsted-acid catalyst [53, 54], (v) elemental-sulfur (S_8) [55] and (vi) lithium-salt-mediated (LiTFSI) [56] preparation methods, (vii) strong base-assisted polycondensation reaction based on benzylamine-functionalized monomers [57], (viii) phosphorous pentoxide (P_2O_5)-catalyzed condensation of aromatic primary amides (i.e., $C(=O)-NH_2$ functional group) into s-triazine rings [58], (ix) catalyst-free Schiff-base condensation reaction between amidine-and aldehyde-functionalized aromatic monomers [59], and (x) acid-catalyzed Friedel-Crafts alkylation reaction between cyanuric chloride and phenyl species [60] are among the most widely used synthetic routes for CTFs. Figure 1.1 presents the typical synthetic routes for CTFs.

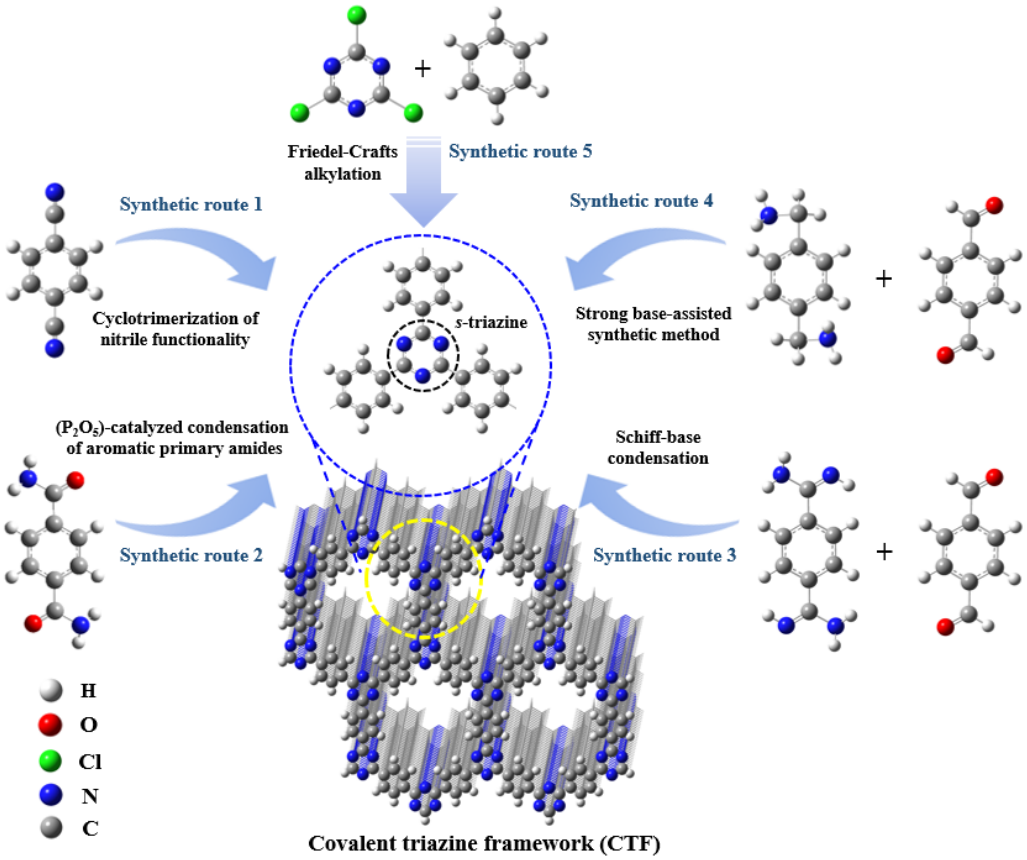

Figure 1.1. A summary of various synthetic methods for CTFs.

1.1.1 Ionothermal cyclotrimerization of nitrile functionalities

The conventional high-temperature (i.e., T≥400 °C) ionothermal cyclotrimerization of nitrile (i.e., cyano) functionalities appended to aromatic rings using molten $ZnCl_2$ as both the solvent and Lewis-acid catalyst involves a dynamic and reversible trimerization reaction during which self-optimization polymerization occurs (Figure 1.1, synthetic route 1). Ionothermal synthesis refers to using an ionic liquids (ILs) reaction medium, typically at high temperatures. The reversible dynamic ionothermal condition provides CTFs with error-checking and proofreading features usually marked in the synthetic pathway of MOF and COFs [61, 62]. The typical ionothermal synthesis temperature is 400 °C at which both monomer and catalyst melt and are thoroughly mixed, hampering the formation of oligomers and agglomerates and increasing the conversion of nitrile functionalities into the triazine moieties. Due to the acid-base interactions between molten $ZnCl_2$ (as a Lewis acid) and nitrile functionality (as a Lewis base) at high temperatures, carbonitrile-containing aromatic monomers display high solubility in the reaction medium (i.e., ionic melt). However, as $ZnCl_2$ is a mild Lewis acid, its Lewis base counter-anion (Cl^-) is a relatively strong Lewis base with high reactivity, resulting in side reactions in the ionic melt. For instance, Cl^- can react with the hydrogen atoms weakly appended to the phenyl rings, leading to rearrangements in the framework. Meanwhile, control of temperature and monomer/$ZnCl_2$ molar ratio are governing factors for preparing CTF materials with different physicochemical and textural characteristics [63]. Generally, the higher the synthesis temperature and $ZnCl_2$/monomer molar ratio, the higher the specific surface area and pore volume of the obtained CTF. This phenomenon might be because of graphitization and rearrangement of the atom positions, turning a crystalline framework into a highly porous yet amorphous structure [46].

In the low-temperature ionothermal approach, metal triflimide salts ($M(NTf_2)_n$), comprising a weak coordinating counter-anion (i.e., NTf_2^{-n}, a very weak Lewis base) with considerable electron delocalization throughout its structure, can act as Lewis superacids and be used as highly reactive catalysts for the cyclotrimerization of nitriles (Figure 1.1, synthetic route 1) [52]. Such high activity of these catalysts requires lower synthesis temperature and shorter reaction time than the conventional $ZnCl_2$-catalyzed ionothermal method described earlier (e.g., 250-300 °C and 24 h vs. 400-700 °C and 48 h, respectively). Besides, due to the higher catalytic activity of metal triflimide salts than the classical Lewis acids such as $ZnCl_2$ and $AlCl_3$, less amount of the catalyst is required (e.g., less than equimolar vs. 1-20 equivalents, respectively). In the meantime, the very weak Lewis base counter-anion with low reactivity exhibits a decreased tendency towards the cleavage of functional groups of the monomer, thus increasing the structural integrity of the resultant framework. With a similar approach, Zhou et al. developed a novel low-temperature ionothermal synthetic method using lithium bis(trifluoromethanesulfonyl)imide (LiTFSI) as both solvent and catalyst for cyclization of nitrile functionalities (Figure 1.1, synthetic route 1) [56]. Since LiTFSI has a lower melting point than $ZnCl_2$ (234 °C [64] vs. 290 °C, respectively), a lowered temperature of 300 °C was used to synthesize CTF materials. By using this catalyst, CTF materials were formed through the strong Lewis acid-base interactions in the melt-state.

1.1.2 Super acid-catalyzed cyclotrimerization of nitrile functionalities

As mentioned earlier, the main drawback of the ionothermal cyclotrimerization reaction is its harsh reaction conditions. Both the high temperature and high pressure essential for forming a molten-salt reaction medium restrict the application of this synthetic method to some extent. For instance, the ionothermal process is unsuitable for fabricating membrane materials as the materials obtained

through this method are always in powder. From the chemical/thermal stability, textural properties, and functionality points of view, CTFs are considered ideal candidates for separation, catalysis, and energy storage/conversion purposes. Nevertheless, the disadvantages discussed above hinder the practical application of CTFs as functional membrane materials.

To overcome this shortage, the low-temperature superacid-promoted cyclotrimerization of carbonitrile-containing monomers was proposed by Ren et al. in 2012 (Figure 1.1, synthetic route 1) [54]. In this regard, CF_3SO_3H was used as the catalyst to afford the CTF materials at room temperature and under microwave-assisted conditions. This synthetic approach involves several benefits compared with the ionothermal method, including (i) milder synthesis conditions, (ii) a lower degree of carbonization of the CTF materials, (iii) a trace amount of residual catalyst in the final product, (iv) and more straightforward purification step(s). Inspired by this innovative synthetic method, Zhu et al. synthesized a porous triazine-based freestanding membrane with permanent porosity (S_{BET} of 738 m^2 g^{-1}) and used it for CO_2 separation from flue gas [65]. Still, this method has drawbacks, such as the expensive catalyst and the safety-related challenges. Another disadvantage of the superacid-catalyzed synthetic method is that this method cannot accomplish the synthesis of the DCB-derived CTF (CTF-1), one of the most functional and applicable CTF materials. This drawback might be because of the structural rigidity of the DCB monomer elucidated earlier [47].

1.1.3 Elemental-sulfur-mediated synthesis of CTFs

As mentioned, due to the structural rigidity of DCB, the superacid-catalyzed polymerization is not capable of affording the CTF-1 material. The elemental-sulfur-mediated synthetic method was thus introduced to address this issue (Figure 1.1, synthetic route 1) [55, 66]. In this synthetic approach, the formation of CTF-1 proceeds by in-situ vulcanization with elemental sulfur (S_8), allowing the homogeneous distribution of sulfur within the internal channels of CTF-1. In other words, using elemental sulfur led to a sulfur-functionalized CTF-1 (S-CTF-1). The cyclotrimerization of nitrile functionalities in the presence of molten elemental sulfur is carried out firstly at 160 °C to dissolve sulfur thoroughly and then proceeds at 400 °C to enhance the elemental sulfur ring-opening, resulting in the polymerization of S_8 into a linear polysulfane.

Consequently, these highly reactive polysulfane species facilitate the cyclotrimerization of nitrile functionalities to triazine units. Using molten elemental sulfur allows the strong covalent bonding between sulfur species and the internal channels and its homogeneous distribution within the pores. S-CTF-1 showed a high sulfur content of up to 62 wt% and a well-shaped bipyramidal morphology acquired without external templates [55]. Hence, S-CTF-1 could be ideal for cathode materials in Li-S batteries. Constructing a conjugated framework comprising heteroatoms promotes electron transport and efficiently hinders Li-polysulfides' dissolution through increased binding affinity toward heteroatoms deliberately embedded within the pores [66].

1.1.4 (P_2O_5)-catalyzed condensation of amides into s-triazine rings

Most of the monomers employed for constructing CTFs are those with nitrile functionalities. To expand the diversity of the possible building blocks for CTFs, the P_2O_5-catalyzed direct condensation of aromatic amides (e.g., terephthalamide) has been recently offered by Yu et al. (Figure 1.1, synthetic route 2) [58]. P_2O_5 converts aromatic primary amide functionalities into s-triazine units in this synthetic strategy. P_2O_5 is a well-known catalyst for converting amides into

nitrile functional groups [67]. Subsequently, the newly formed nitrile functionalities can be condensed into s-triazine units. Accordingly, both aromatic amide and aromatic nitrile monomers can be utilized in the P_2O_5-catalyzed synthesis of CTFs [68]. Due to the nature of the catalyst used, this synthetic approach is more eco-friendly than the classical ionothermal or superacid-catalyzed synthetic methods. Nonetheless, as the melting point of the amide-functionalized monomers (e.g., terephthalamide) is often high (e.g., 350 °C), this method is classified as a high-temperature synthetic method.

1.1.5 Schiff-base condensation reaction

In search of finding new methods for the synthesis of highly crystalline CTF materials with increased structural integrity, Wang et al. developed a new strategy involving the polycondensation reaction of amidine-and aldehyde-containing building units to synthesize CTF materials (CTF-HUSTs) under mild conditions (e.g., T≤120 °C, no use of strong acid or base catalyst) (Figure 1.1, synthetic route 3) [59]. The optimum reaction conditions involved cesium carbonate (Cs_2CO_3) as a mild and available catalyst, DMSO as the solvent, and a reaction temperature of 120 °C, rendering CTF-HUST-1. Scalability is a critical factor for the practical applications of new materials. This process could readily be scaled up because it is a one-pot polymerization performed at a relatively low temperature and ambient pressure, without protection by an inert atmosphere, employing an inexpensive catalyst and a relatively non-toxic solvent. The polymerization of CTF-HUST-1 was successfully scaled up to 5 grams without any particular equipment. Moreover, the CTF materials obtained through this method showed layered structures with high crystallinity and enhanced photocatalytic activity. The latter results from avoiding undesired carbonization/graphitization occurring at high temperatures. Hence, colorful CTF materials and, thus, robust CTF-based photocatalysts could be obtained in the absence of carbonization.

1.1.6 Strong base-assisted synthesis of CTFs

CTFs derived from various monomers (e.g., aromatic nitriles, amides, amidines, and aldehydes) studied earlier possess variant properties due to the different crystallinity and peripheral residual functionalities originating from the composition of the starting materials. This, in turn, modulates the charge transport/separation and hydrophilicity of the resulting CTFs [69]. Hence, this would be of paramount importance to utilize novel monomers for synthesizing crystalline CTFs to expand the synthetic approaches and, thus, to introduce more possible pathways to control the structural properties of the resulting polymer. In this venue, Zhang et al. proposed a novel synthetic route for effectively synthesizing highly crystalline CTF materials through a strong base-assisted method using benzylamine-containing aromatic building units (Figure 1.1, synthetic route 4) [57]. By controlling the basicity of the catalyst (e.g., Cs_2CO_3, K_2CO_3, KOH, EtOK, and ^{t}BuOK) in the condensation reaction, a highly crystalline CTF (CTF-HUST-A1) with enhanced hydrophilicity was afforded. The base reagent was found to have a critical effect on the crystallinity and textural characteristics of the resultant CTF material.

1.1.7 Friedel-Crafts alkylation reaction

Friedel-Crafts alkylation of cyanuric chloride, which already owns the triazine linkages, is one of the most widely utilized methods for preparing CTF materials (Figure 1.1, synthetic route 5) [60, 70-72]. The most notable advantage of this synthetic method is that it significantly increases the variousness of suitable monomers since the typical carbonitrile functionality required in the

ionothermal and superacid-catalyzed synthesis is no longer needed. In the meantime, the Friedel-Crafts reaction often involves more facile reaction conditions, demanding considerably lower temperatures than with the ionothermal method (e.g., 70–140 °C vs. 400–700 °C), and thus avoiding the undesired carbonization/graphitization and loss of volatile elements (e.g., nitrogen, hydrogen, and halogens) that would compromise the structural integrity of the resulting CTFs. However, the CTF materials obtained through this method are exclusively amorphous, possibly due to the Friedel-Crafts reaction's fast, irreversible, and random nature, hindering their possible applications in research areas requiring materials with high crystallinity, such as photocatalysis.

1.2 Structural functionalization strategies for CTF materials

The designability of CTFs through a wide range of organic building units provides enormous opportunities to equip their structures with the desired functionalities. In the meantime, the tailor-made porous structure and adjustable chemical composition of CTFs make them promising platforms for incorporating various functional groups within their skeleton. The structural functionalization of CTFs could be realized via two approaches, including bottom-up and post-synthetic functionalization methods. Both methods render the desired functionalized CTFs while endowing them with different structural and physicochemical characteristics.

1.2.1 Bottom-up functionalization method

Using pre-functionalized (i.e., pre-designed) organic building units in one of the abovementioned synthetic procedures leads to constructing a functionalized CTF through the bottom-up approach. One representative piece of research on this method is performed by Dong et al., in which a carbonyl-functionalized CTF (BCK-CTF-400-5) is successfully synthesized [73]. To afford this functionalized CTF, bis(4-cyanophenyl) ketone (BCK) building block featuring carbonyl functionality is used as the monomer in the ionothermal cyclotrimerization synthetic method (Figure 1.2-A, step 1). Several functionalized CTFs have been synthesized using a similar approach [74-76]. In another study, Dong et al. obtained a hydroxyl-functionalized CTF (BCM-CTF) by the $ZnCl_2$-catalyzed ionothermal cyclotrimerization of bis(4-cyanophenyl) methanol (BCM) (Figure 1.2-B, step 1) [77]. However, it ought to be noted that specific protection followed by a deprotection protocol should possibly be taken into account to suppress the undesired side reactions of the functional groups during the CTF preparation step. Moreover, this approach suffers from other drawbacks, such as the challenging synthesis of functionalized monomers and difficulties in embedding large or bulky functionalities within the framework, which may disturb the regularity of the final structure and, therefore, hinder the formation of a fully extended network [78].

1.2.2 Post-synthetic functionalization method

The post-synthetic functionalization method offers a more robust framework than the bottom-up approach. Comparatively, it enables the introduction of various types of functional motifs into the structure of CTFs without deteriorating their structural integrity [79]. Besides, by employing this functionalization method, undesired side reactions would be hampered or minimized. This strategy comprises specific bond formation, host-guest interactions, and chemical reactions between the active centers within the pristine CTF (i.e., the pre-functionalized CTF) and the target functional moieties. For instance, Dong et al. synthesized an amino acid-functionalized CTF (BCK-CTF-Gly) through the post-synthetic modification of a carbonyl-containing CTF (BCK-CTF-400-5) by glycine (Figure 1.2-A, step 2) [73]. Moreover, they prepared an amine-functionalized CTF (BCM-

CTF-EDA) through the post-synthetic treatment of the as-synthesized BCM-CTF with ethylenediamine (EDA) (Figure 1.2-B, step 2).

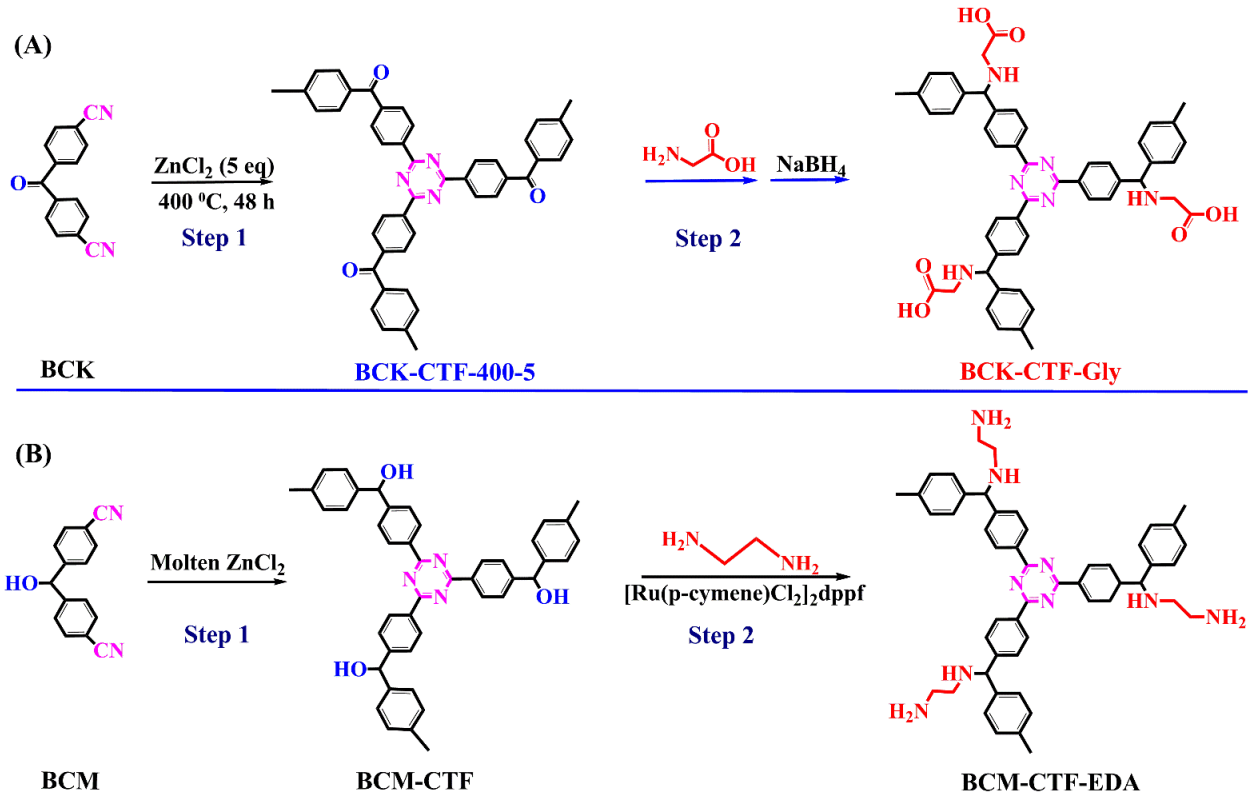

Figure 1.2. Examples of bottom-up and post-synthetic functionalization methods for CTFs.
Synthesis of the carbonyl-functionalized BCK-CTF-400-5 [73] and the hydroxyl-functionalized BCM-CTF [77] through the bottom-up strategy (A and B, respectively, step 1). Preparation of the amino acid-functionalized BCK-CTF-Gly [73] and the amine-functionalized BCM-CTF-EDA [77] through the post-synthetic strategy (A and B, respectively, step 2).

1.3 Feasibility for CTFs commercialization

The ideal adsorption capacity and surface area for commercializing CTFs depend on the specific application and target pollutants. The suitability of CTFs for commercial use is determined by their performance in adsorbing particular substances from a given environment. For reference, some typical adsorption capacities for various materials used in commercial applications include:

Activated Carbon: Commercial activated carbons often have surface areas of 500 to 1500 $m^2\ g^{-1}$. Some high-performance activated carbons can even exceed 2000 $m^2\ g^{-1}$. The surface area is a crucial factor in determining the adsorption capacity of activated carbon. The adsorption capacity of activated carbon varies depending on the adsorbate and the specific activated carbon grade. For common adsorbates such as organic contaminants, activated carbons typically have adsorption capacities ranging from 500 to 1200 mg g^{-1} or even higher in some cases. For gases like carbon dioxide or volatile organic compounds (VOCs), adsorption capacities can be lower, often 50 to 100 mg g^{-1}.

Zeolites: Zeolites are known for their well-defined and porous structures, contributing to their high surface areas. Commercial zeolites typically have surface areas of 300 to 800 $m^2\ g^{-1}$. Some specialized zeolites designed for specific applications may have even higher surface areas. The adsorption capacity of zeolites varies depending on the type of adsorbate and the specific zeolite structure. For water adsorption, typical adsorption capacities can range from 200 to 400 mg g^{-1}. For gases like carbon dioxide and ammonia, adsorption capacities can be 20 to 80 mg g^{-1}.

MOFs: MOFs are renowned for their extremely high surface areas, often surpassing other porous materials. Commercial MOFs typically have surface areas of 1,000 to 7,000 $m^2\ g^{-1}$. Some specialized MOFs can even exceed 10,000 $m^2\ g^{-1}$. The adsorption capacity of MOFs varies depending on the type of adsorbate (substance being adsorbed), the specific MOF structure, and the conditions of the adsorption process. For gases such as carbon dioxide, methane, and hydrogen, adsorption capacities can range from 20 to 100 mg g^{-1}. For the adsorption of organic molecules, the capacity can vary widely but is typically in the range of 100 to 600 mg g^{-1} of MOF.

As for CTFs, their feasibility for commercialization depends on several factors, including their adsorption capacity, surface area, stability, selectivity for specific adsorbates, and cost of production. Generally, higher adsorption capacities and surface areas are advantageous, but the specific requirements vary depending on the intended application. For example, CTFs with adsorption capacities of 100-500 mg g^{-1} for common water pollutants could be considered suitable in water treatment applications. Similarly, a 500-1500 $m^2\ g^{-1}$ surface area would be competitive with other commercial adsorbents.

1.4 Objective of the research and justification

CTFs have been studied much less than a related class of materials, metal-organic frameworks (MOFs). This is probably because of the much simpler synthesis of MOFs. However, CTFs have a number of advantages that merit more research. In particular, CTFs are more stable compounds and can be used more easily in real-world applications. The main objective of this thesis is to investigate interactions between CTFs and a range of compounds of environmental and health concern, and potential applications of these interactions.

The main objective of this thesis is to develop new CTF materials for adsorption and chemical sensing applications.

The following three sub-projects have been performed in this dissertation, along with a justification of their novelty and significance.

1.4.1 Conjugated CTF adsorbents for iodine adsorption

Two key factors directly affect the capability and capacity of an adsorbent in the iodine adsorption and storage process: (i) the (co)existence of high-affinity adsorption sites and suitable functionalities in the structure, facilitating iodination, and (ii) textural properties of the adsorbent (i.e., specific surface area, pore volume, and pore size distribution). Since the iodine molecule (I_2) is a Lewis acid, an adsorbent's basicity enhances its surface's affinity towards iodine molecules through acid-base interactions [80]. Hence, the capability and capacity of an adsorbent for iodine adsorption can be promoted by incorporating basic functional groups (e.g., O, S, P, $-NH_2$, $-NH-$, $-N=N-$, $-C=N-$, etc.) and/or electron-rich π-conjugated moieties (e.g., C=C double bond, C≡C triple bond, triazine ring, phenyl ring, porphyrin ring, etc.) within the structure [81].

Basic functional groups and electron-donating conjugated systems can share their lone-pair electrons and/or π electrons with iodine molecules, leading to stronger iodine-adsorbent interaction and thus enhancing the adsorption capability and capacity [82]. In the meantime, mutual polarization of the host (i.e., adsorbent) and guest (i.e., iodine species) electronic clouds leads to stronger dispersion (i.e., London) forces and thus stronger van der Waals interactions typical in physisorption [83]. The neutral iodine molecule (I_2) can be easily polarized and converted to (poly)iodide species, following $(n+1)I_2 \rightleftarrows I^-.nI_2 + I^+$ [84]. Charged (poly)iodide species such as I^-, I_3^-, and I_5^- evolved during adsorption can act as Lewis bases and form negatively charged complexes with molecular iodine (I_2). Hence, optimal adsorbents may also feature acidic functional groups and/or electron-withdrawing moieties to adsorb these iodine species adequately.

The optimal pore size of a CTF adsorbent for iodine adsorption, specifically targeting the I_3^- triiodide and I_5^- pentaiodide species, relies on the dimensions of these target ions. Both ions possess larger sizes than individual iodine atoms (I^-) and iodine molecules (I_2), necessitating a pore size that accommodates their size. Iodine atoms have a van der Waals radius of approximately 1.98 Å. However, when three iodine atoms or five iodine atoms combine to form I_3^- and I_5^- ions, respectively, the effective size of the ion increases due to the molecular arrangement. The precise dimensions can vary depending on the specific crystallographic configuration, but it generally exceeds the size of a single iodine atom. In a broader context, to effectively entrap I_3^- and I_5^- polyiodide species within a porous substrate like a CTF, it is crucial to ensure that the pore size substantially exceeds the effective dimensions of these adsorbate species. This accommodation allows the ions to access and be retained within the pores. Ideally, the pore size should be slightly larger than the effective size of the polyiodide ion, accounting for potential structural adaptability and interactions with the framework.

Solid adsorbent materials tend to adsorb iodine in its polyiodide form. The negatively charged polyiodide species (e.g., I^-, I_3^-, and I_5^-) may impose electrostatic repulsion when entering and/or forming within the pores. Hence, the pore size should be large enough to minimize such repulsive adsorbate-adsorbate interactions to avoid this steric effect between the polyiodide species. It is essential to acknowledge that selecting an appropriate pore size should also consider factors such as the kinetic accessibility of the pores, the kinetics of adsorption, and the overall stability of the CTF material. As such, there is a conjecture that CTF adsorbents featuring a hierarchical pore size distribution—where larger pores encompass smaller ones—and porous materials characterized by a broad pore size distribution, spanning from micropores to substantial mesopores, represent promising candidates in terms of pore size distribution for iodine adsorption. The hierarchical porous structures or those possessing a broad pore size distribution could adsorb various polyiodide species (e.g., I^-, I_3^-, and I_5^-, etc.).

Meanwhile, within the context of a given adsorption system, the development of polyiodide species is contingent upon the charge transferability characteristics of the adsorbent. In simpler terms, it hinges on the capability of the CTF structure to impart a significant charge to the iodine molecule, essentially causing the iodine molecule's electronic cloud to polarize and transform into polyiodide species. Consequently, when a CTF adsorbent incorporates task-specific functional groups to facilitate substantial charge transfer to the iodine molecule, the possibility of forming polyiodide species increases. In such adsorption scenarios, CTFs that feature spacious pores, or mesopores, are considered prime candidates. However, as elucidated in Chapter 5, it is noteworthy

that CTF materials can adsorb iodine in its molecular form (i.e., I_2) without converting it to charged polyiodide species of larger dimensions. This implies that CTF adsorbents lacking suitable functional groups for efficient charge transfer to iodine molecules may have marginally larger pores than that of the iodine molecule (2.67 Å), termed microporous CTFs.

While the nature of the interactions between iodine species and CTFs can be inferred with some confidence from their chemistry, it is not yet clear if these interactions are sufficient to warrant the use of CTFs as adsorbents for the adsorption of iodine. The purpose of the first sub-project is to address this gap.

In this sub-project, I have rationally designed and synthesized a robust conjugated CTF (CTF-DPA) through the convenient one-pot $AlCl_3$-catalyzed Friedel-Crafts alkylation reaction of cyanuric chloride with diphenylacetylene (DPA), which bears an electron-rich C≡C (ethyne) bridging unit between two phenyl rings. To demonstrate the effect of structural design on the properties and, thus, the iodine-capturing performance of the material, an analog CTF (CTF-TS) will be synthesized with trans-stilbene (TS), in which the bridging unit between the two phenyl rings is HC=CH (ethene). The resulting conjugated porous CTFs will be systematically characterized for their physicochemical, textural, and structural properties and evaluated for their performance towards iodine adsorption. XPS, Raman spectroscopy, and DFT calculations will further investigate the mechanism of iodine uptake by the synthesized CTFs.

1.4.2 Functionalized CTFs for heavy metals removal from water

Although some functionalized CTF adsorbents have been synthesized and previous studies have demonstrated their great potential in adsorption, systematic investigations are still needed to assess their performance in removing heavy metal ions from aqueous solutions. Such systematic studies are crucial for establishing structure-performance relationships for designing novel CTFs featuring suitable functionalities. Motivated by this gap in our knowledge, a systematic DFT-assisted computational study has been performed on some functionalized CTF materials as potential candidates for heavy metal ions removal from water. In this sense, the adsorption of the three most biohazardous heavy metal species, including Cd^{2+}, Pb^{2+}, and Hg^{2+} heavy metal cations upon various CTF adsorbents possessing different electron-rich functionalities (e.g., hydroxyl, carboxylic acid, thiol, and aldehyde) has been computationally investigated. Then, based on the obtained results, the functionalized CTF showing the highest adsorption affinity (i.e., adsorption energy) towards the heavy metal species has been prepared by the ionothermal cyclotrimerization of the carbonitrile-containing functionalized aromatic monomer (i.e., 2,5-dicyanobenzoic acid) for experimental performance evaluation/validation. It is worth mentioning that despite some MOFs being unstable in water under highly acidic conditions, CTF materials are highly stable chemically, thus appropriate candidates for practical applications such as removing heavy metal cations from industrial waters with low pH values.

In adsorbing heavy metal cations, notably Cd^{2+}, Hg^{2+}, and Pb^{2+}, CTFs can be engineered with negatively charged functional groups and/or electron-donating moieties. These modifications establish robust electrostatic and coordination interactions, enhancing the adsorption process's stability. Notably, heavy metal cations, comparatively smaller than the polyiodide species mentioned above and largely resistant to forming larger metallic clusters in highly acidic environments, require CTFs with a narrow pore size distribution, primarily consisting of micropores, particularly effective as adsorbents. However, as revealed by the heavy metal adsorption capacity findings, more than microporosity is needed to guarantee efficient adsorption.

Consequently, an ideal CTF-based adsorbent for heavy metal uptake should possess both the appropriate functional groups and a microporous structure to efficiently capture heavy metal cations.

Additionally, it is crucial to consider the size of functional groups incorporated within the internal pores of a given CTF adsorbent as a determinant in defining the optimal pore size. For instance, elongated functional groups like ethoxy may not be suitable for integration into the framework of a microporous CTF with small pores. These elongated functionalities can occupy substantial pore space in such cases, potentially leading to steric hindrance effects that impede efficient interactions between the functional groups and the adsorbate species.

1.4.3 CTF-1 and Pt-doped CTF-1 for gas adsorption and sensing

As an inexpensive insulating and arc-extinguishing agent, sulfur hexafluoride (SF_6) gas is typically loaded in gas-insulated switchgear (GIS) at high pressures (0.1−0.6 MPa) [85]. Nevertheless, the long-term operation of a GIS ultimately results in insulation deficiencies, leading to partial discharge. Consequently, the resultant partial discharge promotes the breakdown of SF_6 to different reduced sulfur fluoride species (SF_x, $1 \leq x \leq 5$) [86]. Trace impurities such as H_2O and O_2, often present in GIS, will react with SF_x rapidly and produce different decomposition species (*e.g.,* H_2S, SO_2, SOF_2, and SO_2F_2). On the one hand, most of these decomposition products are corrosive gases that, when interacting with H_2O and O_2, can promote the corrosion of the solid insulating chambers [87]. On the other hand, these gas species are highly toxic to the environment and human health [88]. Hence, it is crucial to monitor and manage the evolution of the SF_6 breakdown species from the viewpoints of process control, environment preservation, and human health. This objective can be accomplished by devising high-tech, chemiresistive, sensitive, and effective gas sensors.

The existence of electron-rich π-conjugated moieties, *e.g.*, phenyl and triazine rings, in the structure of CTFs, their high specific surface area, and considerable thermal/chemical stability make them promising candidates for gas adsorption and sensing applications [89]. In this sense, the triazine ring can serve as an electron-accepting moiety and the phenyl ring as an electron-donating one [90]. Among various CTF materials, CTF-1, a crystalline 2D nanoporous type of CTFs that exclusively comprises phenyl and triazine rings, is a promising material in several practical applications [36]. More interestingly, it has also been reported that CTF-1 can be delaminated/exfoliated through ultrasonication-assisted mild oxidation, rendering single-layered nanosheets with high surface-to-volume ratios [91], potentially suitable for gas sensing applications.

These findings inspired us to investigate the wider applications of CTF-based electrochemical sensors for detecting SF_6 decomposition products. The single-layered CTF-1 surface is selected due to its high thermal stability, electron-rich structure, and high nitrogen content, with the latter enabling efficient metal doping and, thus, superior gas sensing. Metal doping significantly affects a given material's gas adsorption and sensing properties, especially materials with poor electrical conductivity. Platinum (Pt) metal stands out among other metal atoms for its exceptional carrier mobility and gas interaction ability. Pt is therefore regarded as the appropriate doping metal in this sub-project to enhance the adsorption and sensing capabilities of CTF-1 nanomaterial. This subproject has highlighted the adsorption characteristics and sensing mechanism of the pristine

CTF-1 and Pt-doped CTF-1 single-layered nanosheet gas sensors upon interaction with H_2S, SO_2, SOF_2, and SO_2F_2, unveiling the critical role of metal doping of CTFs on gas-sensor interactions.

2 Chapter 2: Literature Review

2.1 Application of functionalized CTFs in environmental remediation

Herein, the recent advances in capturing CO_2, heavy metals (e.g., mercury, cadmium, lead, and other types of heavy metal species), and radioiodine utilizing functionalized CTF materials have been reviewed. To that effect, we mainly focus on the research works published in the last four years.

2.1.1 CO_2 capture using functionalized CTFs

As previously remarked, the ever-increasing demand for energy has led to the excessive use of fossil fuels, resulting in air pollution and other adverse environment-related consequences such as climate change and global warming [92]. Greenhouse gases (e.g., CO_2, CH_4, SO_2, NO_2, etc.) produced due to the extreme burning of fossil fuels are emitted into the atmosphere and severely deteriorate the ecosystem [93]. The global level of CO_2 concentration in the environment has risen from 415.52 to 418.19 ppm in January 2022 [94]. In particular, CO_2 significantly affects global warming and climate change as a major anthropogenic greenhouse gas. Meanwhile, the natural consumption of CO_2 through photosynthesis has declined dramatically due to the drastic decrease in forests and the sharp growth of industrial civilization [95]. As a reassuring solution, putting alternative zero-emission energy sources into practice, such as solar or hydrogen-based energy generators, has attracted interest [96].

Nevertheless, these options are long-term ambitions, and their real-world implementation is not practical for the time being as they require more research and huge investments. Hence, possible hands-on solutions for lessening the concentration of this gaseous species are urgently mandated. Amongst, carbon capture and storage (CCS) and carbon capture and utilization (CCU) have been proposed as viable resolutions [97]. In this sense, CTFs show features essential for capturing such species, including noticeable specific surface area, permanent porous structure, and pre-functionalized basic surfaces (i.e., due to nitrogen atoms in triazine rings). The latter is particularly needed when capturing acidic gas species such as CO_2. Regardless, as the triazine moieties are highly stable, they do not show a high affinity towards the gas species. Functionalization of the surface is a promising technique for enhancing the affinity towards the target gas molecules, thus increasing the adsorption capability/capacity.

It is well-known that the gas-capturing performance of a given adsorbent is directly governed by its textural, structural, topology, and chemical composition [98]. Taking into account these criteria, Liu et al. constructed a novel bifunctional nitrogen-and sulfur-rich CTF (TPFM) using bithiophene (BTCA) and melamine as primary building units through a one-pot catalyst-free Schiff-base reaction for the uptake of CO_2 [99]. The resulting CTF material possessed a sphere-like morphology with a mesopore-dominated porous structure. Benefiting from the accessible pores and abundant amine (i.e., −NH−) and triazine functional groups on the internal surfaces of TPFM, this material showed an efficient CO_2 adsorption capacity of 77.5 $cm^3\ g^{-1}$ (143 mg g^{-1}) at 273 K up to 1 bar.

Sang et al. developed carbonyl-containing CTF-based adsorbents (PHTCZ-1-MA and PHTCZ-2-MA) via an $AlCl_3$-catalyzed Friedel-Crafts alkylation reaction between benzene-1,3,5,-triyltris((9H-carbazol-9-yl) methanone) (HTCZ), and propane to prepare (poly)HTCZ precursor, followed by a Schiff-base reaction between (poly)HTCZ and melamine to afford the final CTF

adsorbents [100]. The resulting porous polymers displayed a noticeable CO_2 adsorption capacity of 180 mg g^{-1}. The good performance of PHTCZ-1-MA CTF adsorbent in CO_2 capturing is ascribed to the high reactivity of carbonyl functionalities of HTCZ precursor, which even increased by about 18% after polymerization.

To benefit from heteroatom effects, Rangaraj et al. synthesized a series of phosphazene-functionalized CTF (Pz-CTFs) using building blocks of hexakis(oxy)hexabenzonitrile phosphazene (HCPz) through the $ZnCl_2$-catalyzed ionothermal cyclotrimerization of nitrile functionalities for effective CO_2 adsorption [101]. The sample prepared at the optimized conditions utilizing a $ZnCl_2$/HCPz molar ratio of 10 with a temperature gradient (400 °C/25 h; 450 °C /13 h; 500 °C /1 h; and 600 °C /1 h) showed an ultra-microporous structure (Pz-CTF6) with high specific surface area (1009 m^2 g^{-1}). The primary aspect of the employed temperature gradient is that it causes a simultaneous reversible/irreversible trimerization of nitrile groups, leading to the reconstruction of triazine moieties and, thus, resulting in a fully-extended microporous network. Benefiting from the electron-rich phosphazene cores embedded within the structure of the highly crosslinked Pz-CTF6, enhanced CO_2 uptake capacities of 4.19 mmol g^{-1} (184 mg g^{-1}) and 2.47 mmol g^{-1} (109 mg g^{-1}) were obtained at 273 and 298 K, respectively, and 1 bar. The phosphazene units controlled the framework's architecture and thermal/chemical stability. In the meantime, the uniform distribution of electron-rich heteroatoms (N, O, P) throughout the internal surfaces of Pz-CTFs enhanced the electron density of the framework. Such high electron density, in turn, increases the dipole-quadrupole interactions between the polarizable CO_2 molecules and the CTF adsorbent.

Deng et al. reported a series of 7,7,8,8-tetracyanoquinodimethane-derived covalent triazine frameworks (TCNQ-CTFs) with various textural characteristics for efficient CO_2 capture [102]. TCNQ-CTFs exhibit maximum CO_2 uptake capacity up to 5.99 mmol g^{-1} (264 mg g^{-1}, 273 K, 1 bar). Abundant nitrogen and defects formed by annealing treatment are considered the main elements for the ultra-high uptake capacity of this material. Bagherian et al. synthesized a highly crystalline CTF adsorbent (TPT/OH CTF) via a solvothermal synthetic method through the condensation reaction between 2,4,6-tris(p-formylphenoxy)-1,3,5-triazine and oxalyl dihydrazide [103]. TPT/OH CTF surfaces were decorated with oxalyl dihydrazide and s-triazine rings, leading to a strong interaction between the framework and the CO_2 molecules. TPT/OH CTF, with a distinctive nature of the extended π-conjugated framework, N-rich surfaces, moderate specific surface area (424 m^2 g^{-1}), the abundance of micropores, and high stability of hydrazone functionalities, was capable of adsorbing CO_2 with the maximum adsorption capacity of 0.9 mmol g^{-1} (40 mg g^{-1}) at 298 K and 1 bar.

Yi et al. recently prepared a boronic acid-functionalized CTF (BCTF-1) through the $ZnCl_2$-catalyzed ionothermal copolymerization of DCB and 4-cyanophenylboronic acid [104]. BCTF-1 showed a good CO_2 adsorption capacity of 74 cm^3 g^{-1} (136 mg g^{-1}) at 298 K up to 1 bar. With a similar synthetic method, Krishnaraj et al. synthesized two rigid and highly stable urea-functionalized CTFs (urea-CTF-400-5 and urea-CTF-500-5) utilizing the pre-functionalized 1,3-bis(4-cyanophenyl) urea monomer. Due to the strong acid-base interactions between CO_2 and N-basic sites along with the hydrogen-bonding interactions between the urea functionalities and CO_2 molecules, urea-CTF-400-5 and urea-CTF-500-5 exhibited noticeable CO_2 adsorption capacities of 3.1 mmol g^{-1} (136 mg g^{-1}) and 2.8 mmol g^{-1} (123 mg g^{-1}) at 273 K and 1 bar, respectively. The

sample synthesized at the lower temperature (i.e., urea-CTF-400-5) possessed a lower specific surface area and pore volume than the sample prepared at the higher temperature (i.e., urea-CTF-500-5). Nonetheless, urea-CTF-400-5 showed higher CO_2 adsorption capacity, possibly due to its higher nitrogen content (N content of 14 wt% vs. 11.38 wt%, respectively) and higher V_{micro}/V_{total} ratio within its structure than those of urea-CTF-500-5 (0.72 vs. 0.61, respectively).

The enhancement of the electron density of a framework through incorporating π-conjugated moieties would result in stronger electrostatic (i.e., Coulombic interactions) interactions with electron-deficient CO_2 molecules. In this regard, Mohamed Gamal et al. developed two pyrene-functionalized conjugated microporous CTFs (Pyrene-CTF-10 and Pyrene-CTF-20) via the $ZnCl_2$-catalyzed ionothermal cyclotrimerization of 1,3,6,8-cyanopyrene (TCNPy) at 500 °C [105]. The former material was synthesized using a $ZnCl_2$/TCNPy molar ratio of 10, while this value was increased to 20 for the latter's preparation. Pyrene-CTF-10 showed high CO_2 adsorption capacities of 2.82 mmol g^{-1} (124 mg g^{-1}) and 5.1 mmol g^{-1} (224 mg g^{-1}) at 298 and 273 K, respectively, up to 1 bar. Meanwhile, for Pyrene-CTF-20, these values were reduced to 2.54 mmol g^{-1} (118 mg g^{-1}) and 3.43 mmol g^{-1} (151 mg g^{-1}), respectively. The superior performance of Pyrene-CTF-10 can be assigned to its higher nitrogen content (9.85 wt%), as the lower amount of catalyst leads to a lower degree of carbonization/graphitization. Namely, the higher the ratio of $ZnCl_2$/monomer, the higher the possibility of carbonization/graphitization of the framework in the ionic melt.

The negatively polarized O atoms of CO_2 can enhance the nucleophilic attacks on the adsorbents' electron-deficient and cationic moieties [106]. In this respect, Xi et al. utilized a pyrimidine-and bis(imidazolium)-containing aromatic nitrile as the monomer to prepare a bis(imidazolium)-functionalized cationic CTF (PyImCl-cCTF) by the $ZnCl_2$-catalyzed ionothermal cyclotrimerization reaction [107]. With the high content of positively charged imidazolium moieties derived from the bis(imidazolium) monomer, PyImCl-cCTF exhibited impressive CO_2 capture capacities of 235 and 133 mg g^{-1} at 273 and 298 K, respectively, up to 1 bar. Due to the presence of imidazolium cations in the structure of PyImCl-cCTF, the enhanced electrostatic interactions between CO_2 and the polymer skeleton could improve the CO_2-capturing performance of the framework. Similarly, Wu et al. synthesized a cobalt-containing porphyrin-based imidazolium-functionalized cationic CTF (Co-PCCTF) through the copolymerization of cobalt 5,10,15,20-tetrakis(4-cyanophenyl) porphyrin (Co-TPPCN) and 1,3-bis(4-cyanophenyl) imidazolium chloride ([BCIM]Cl) under ionothermal conditions [108]. The obtained bifunctional Co-PCCTF with positively charged imidazolium moieties exhibited the maximum CO_2 adsorption capacity of 37 cm^3 g^{-1} (68 mg g^{-1}) at 298 K and 1 bar.

Introducing electron-rich heteroatoms into the structure is another beneficial functionalization treatment to achieve high CO_2 adsorption capability and capacity. In this venue, Fu et al. investigated the synthesis and adjustable pore structure along with the CO_2 adsorption characteristics of hierarchically porous covalent triazine frameworks (CTF-CSUs) modified by incorporated carboxylic acid/sodium carboxylate functionalities [109]. The compactly combined functionalities with the CTF-CSUs' skeleton confer robust affinity on the as-made frameworks towards guest CO_2 molecules despite their moderate specific surface areas (333 to 491 m^2 g^{-1}). With abundant microporosity and incorporated carboxylic acid functionalities, CTF-CSU41 exhibited a strong affinity towards CO_2 with a considerably high adsorption capacity of up to 10.3 wt% at 273 K and 1 bar.

In another study, Liao et al. synthesized three CTF adsorbents comprising phenylamino (PhNH−), phenoxy (PhO−), and benzenesulfenyl (PhS−) functionalities utilizing nitrile-containing monomers, including 2,4,6-tris(4-cyanophenylamino)-1,3,5-triazine (TAT), 2,4,6-tris(4-cyanophenoxy)-1,3,5-triazine (TOT), and 2,4,6-tris(4-cyanobenzenesulfenyl)-1,3,5-triazine (TST) via the classical $ZnCl_2$-catalyzed ionothermal cyclotrimerization approach [110]. Although these CTFs possessed similar structures, the CTF material with amino functionalities (CTF-N) showed a superior CO_2 adsorption performance (5 mmol g^{-1}, 220 mg g^{-1}) in comparison with the samples functionalized with phenoxy (CTF-O, 4.5 mmol g^{-1}, 198 mg g^{-1}) and sulfenyl (CTF-S, 4 mmol g^{-1}, 176 mg g^{-1}) at 273 K and 1 bar. The observed trend in the CO_2 adsorption performance of the three PhNH−, PhO−, and PhS−functionalized CTFs might be due to the higher electron-donating ability of the N atoms, endowing CTF-N with the largest interaction energy with CO_2 molecules. On the other hand, the O atoms in PhO-functionalized CTF can enhance the electrostatic interactions between CO_2 and the framework. In contrast, the larger S atoms in PhS-containing CTF can only provide π-stacking interactions with CO_2 molecules, leading to lower complexation energy in this adsorption system.

2.1.2 Removal of heavy metals from aqueous solutions using functionalized CTFs

Heavy metal ions removal (e.g., Hg^{2+}, Pb^{2+}, Cd^{2+}, Ni^{2+}, Cu^{2+}, Cr^{6+}) from water is important due to their potential hazards and severe environmental and human health risks [111-113]. Heavy metal ions are not biodegradable and, thus, can accumulate in the environment, triggering terrible health problems for living creatures [114]. Therefore, these highly toxic species must be efficiently eliminated, in particular, from the industrial effluents before being discharged into the environment. In this respect, removing metal-based pollutants through the adsorption technique utilizing functionalized CTFs can be a promising solution for wastewater/contaminated water treatment. The uptake process is mainly governed by the ion-exchange mechanism and coordinative adsorption (i.e., chelation) [115]. The latter occurs through coordinative bonds between the positively charged metal cations and the electron-rich functional groups (e.g., S, N, O, and π-conjugated moieties) within CTFs. Various functionalized CTF adsorbents have been reported to effectively uptake heavy metal cations from aquatic solutions. In this regard, most of the research has been undertaken to remove mercury (Hg^{2+}) from contaminated wastewater owing to its high chemical reactivity and life-threatening bio-toxicity [116]. This section reviews the performance of functionalized CTF adsorbents in capturing diverse heavy metal species in the liquid phase.

Benefiting from the heteroatom effect induced by sulfur atoms, Fu et al. reported a high Hg^{2+} uptake capacity of 658 mg g^{-1} and 99.9% removal effectiveness at an extremely low initial concentration of Hg^{2+} cations in water (1 ppm) for highly stable sulfide-bridged triazine-based nanospheres (NOP-28) [117]. This sulfur-functionalized CTF (i.e., decorated with thioether functional groups (−S−) between triazine rings) was synthesized through a one-pot $AlCl_3$-catalyzed Friedel-Crafts alkylation reaction between cyanuric chloride and diphenylsulfane in o-dichlorobenzene at 180 °C for 24 h under N_2 atmosphere. The notable Hg^{2+} adsorption capacity of NOP-28 is attributed to the synergistic effects of highly accessible, chelating electron-donor thioether functional groups on the internal surfaces and porous structure of NOP-28, facilitating transport and uptake of Hg^{2+} cations.

In another study, Mondal et al. prepared a novel thioether-functionalized (−S−) covalent triazine network (SCTN-1) through the ionothermal cyclotrimerization of thioether-decorated carbonitrile-containing aromatic building units using molten $ZnCl_2$ at 400 °C for 48 h [118]. SCTN-1 showed a remarkable performance towards removing toxic Hg^{2+} and Hg (0) species from contaminated effluents with the maximum adsorption capacities of 1253 and 813 mg g^{-1}, respectively. According to this work, SCTN-1 exhibited one of the fastest mercury adsorption rates among all reported adsorbents. The exceptional performance of SCTN-1 in the uptake of Hg^{2+} is assigned to the strong charge-transfer interactions of Hg^{2+} cations with the N and S atoms with accessible lone-pair electrons. Besides, the weak hydrogen-bonding interaction (i.e., Hg^{2+}…H−C) is another stabilizing factor in the adsorption complexes.

Likewise, Yang et al. developed two novel methylthio-functionalized (−S−CH_3) CTFs (MSCTF-1 and MSCTF-2) under ionothermal synthetic conditions for selective Hg^{2+} removal from model aquatic solutions [119]. MSCTF-2, with 24.45% sulfur content, displayed a superior Hg^{2+} adsorption capacity of 840.5 mg g^{-1}, while MSCTF-1 rendered an extraordinarily high efficacy for lowering the Hg^{2+} concentration to less than 0.03 μg g^{-1}. These MSCTFs showed high selectivity towards Hg^{2+} over various competitive metal cations (e.g., Pb^{2+}, Cd^{2+}, Zn^{2+}, Mg^{2+}, Fe^{3+}, and K^{+}), noticeable chemical stability over broad pH ranges from 1 to 12, and excellent reusability with about 94% of Hg^{2+} removal effectiveness after five consecutive adsorption cycles. Based on the obtained results, it was concluded that the adsorption capacities of the MSCTF adsorbents mainly depend on the binding-site density (i.e., the sulfur content).

As another chelating electron-donor atom rendering considerable heteroatom effects, oxygen-containing functionalities have demonstrated their promising potential in the heavy metal ions adsorption systems. In this venue, Afshari et al. synthesized an oxygen-containing CTF-based nanoneedle-like superadsorbent (T-COF) equipped with anchoring organic functional groups (π-conjugated phenyl rings) and achieved an ultra-high Hg^{2+} adsorption capacity of 1826 mg g^{-1} [120]. The excellent Hg^{2+}-capturing performance of T-COF superadsorbent pertains to the soft-soft interactions between Hg^{2+} cations and nitrogen atoms of triazine rings (i.e., pyridinic nitrogen atoms with accessible lone-pair electrons), cation-π interactions between the conjugated phenyl rings (as electron-donor moieties) and Hg^{2+} cations (as electron-acceptor moieties), electrostatic interactions between negatively charged oxygen atoms and Hg^{2+} cations, and abundance of mesopores in the superadsorbent structure.

In another study, Sang et al. synthesized a carbonyl-functionalized CTF-based adsorbent (PHTCZ-1-MA) through an $AlCl_3$-catalyzed Friedel-Crafts alkylation reaction between benzene-1,3,5,-triyltris((9H-carbazol-9-yl) methanone) (HTCZ) and propane to prepare (poly)HTCZ precursor, followed by a Schiff-base reaction between (poly)HTCZ and melamine to afford the final CTF adsorbent [100]. The resulting porous polymer showed a noteworthy Hg^{2+} adsorption capacity of 335 mg g^{-1}. The good performance of PHTCZ-1-MA CTF adsorbent in Hg^{2+} capturing is attributed to the high reactivity of carbonyl functionalities of HTCZ precursor, which even increased by about 18% after polymerization.

Peng et al. synthesized three acylamino-functionalized triazine-based POP samples through a catalyst-free amidation polycondensation reaction and utilized them in Hg^{2+} removal from aqueous solutions [121]. Melamine was used as the crosslinking agent featuring triazine moieties. At the same time, phthalic acid, isophthalic acid, and terephthalic acid were employed as the secondary

building units to prepare NOM, NMM, and NPM adsorbents, respectively. NOM exhibited the most efficient performance towards Hg^{2+} removal with the maximum adsorption capacity of 229.9 mg g^{-1}. The electron-rich carbonyl (C=O) and amino (R−NH−) functional groups act as high-affinity adsorption sites through the strong chelating coordination with Hg^{2+} cations.

Recently, Shan et al. synthesized a triazine-based nitrogen-rich porous network (TBN-1) through a catalyst-free Schiff-base reaction between amino-and aldehyde-containing aromatic monomers [122]. The existence of electron-donor phenyl rings and electron-acceptor triazine rings in the structure of TBN-1 promoted electron transfer to a high extent [122]. TBN-1 rendered an ultra-high Hg^{2+} adsorption capacity of 1630 mg g^{-1} with 99.99% Hg^{2+} removal efficiency from a 10-ppm model solution within 20 min. The excellent Hg^{2+}-capturing performance of TBN-1 is related to its high specific surface area (1270 m^2 g^{-1}), considerable nitrogen content, and π-conjugated structure formed by phenyl and triazine rings bridged by amino functionalities. Besides, the coordination, robust cation-π electrostatic interactions, and high electron density of the conjugated structure of TBN-1 facilitated the formation of a stable Hg^{2+}/TBN-1 adsorption complex.

In addition to removing Hg^{2+} species, CTFs can adsorb other toxic heavy metal ions, for instance, Cd^{2+}, Cu^{2+}, Pb^{2+}, and Cr^{6+}. In this respect, Dinari et al. designed and synthesized an oxygen-containing nitrogen-rich triazine-based COF (N-rich COF) through the polycondensation of 2,4,6-tris(hydrazine)-1,3,5-triazine and 2,4,6,-tris(p-formylphenoxy)-1,3,5-triazine for Cd^{2+} uptake from contaminated solutions [123]. This imine-linked (−C=N−) porous CTF showed high efficiency in Cd^{2+} removal with a maximum adsorption capacity of 396 mg g^{-1}. The accessible lone-pair electrons of the O and N atoms within the flexible structure of N-rich COF interact readily with the Cd^{2+} cations, resulting in strong chelating and coordinative bonds in the adsorption complex.

In another study, Dinari et al. investigated the application of an imine-functionalized covalent triazine-based porous polymer (THT-TA-CTP) in capturing Cu^{2+} cations from the liquid phase [124]. THT-TA-CTP adsorbent showed a Cu^{2+} adsorption capacity of 86.95 mg g^{-1}. The good performance of this material can be attributed to the abundance of nitrogen atoms in the structure, resulting in the formation of pincer-type complexation with the metal species. Xu et al. evaluated the Pb^{2+} capturing performance of a bifunctional COF-based adsorbent (COF-Tz-OH) with triazine (aromatic C_3N_3) and hydroxyl (−OH) functionalities. Accordingly, they obtained a high Pb^{2+} uptake capacity of 476 mg g^{-1} [125]. This excellent performance is due to the high density of the accessible chelating centers resulting from the bifunctionality feature of the adsorbent, along with well-ordered mesopores, facilitating the transportation and adsorption of the Pb^{2+} cations.

Recently, Zhou et al. prepared nitrogen-doped CTF adsorbents ionothermally at different synthesis temperatures from 300 to 500 °C to control the chemical composition of the materials (i.e., the configuration of nitrogen atoms in the structure) [126]. The CTF synthesized at 500 °C (CTF500) rendered a notable Cr^{6+} adsorption capacity of 97.84 mg g^{-1} due to the strong ion exchange and electrostatic interactions between the Cr^{6+} cations and quaternary nitrogen atom adsorption sites existing on the surfaces of CTF500.

2.1.3 Radioiodine adsorption using functionalized CTFs

Energy generation from nuclear power plants is associated with disadvantages, including high risks in handling, storing, and disposal of radioactive wastes [127]. ^{129}I and ^{131}I are among the most hazardous species due to their long radioactive half-life [128]. These species harmfully affect human health and bring about severe diseases such as thyroid cancer [129]. Considering these hazards, efficient uptake of radioactive iodine is urgently required. In this regard, the adsorption

method is a promising prospect for effectively capturing and storing radioiodine. Two vital factors directly control the ability and capacity of an adsorbent in the iodine adsorption and storage process: (i) the (co)existence of high-affinity adsorption sites and appropriate functionalities in the structure, enabling iodination and evolution of (poly)iodide species (e.g., I_3^- and I_5^-) and (ii) textural characteristics of the adsorbent (i.e., specific surface area, pore-volume, and pore size distribution). Since the iodine molecule (I_2) is a Lewis acid (acting as an electron acceptor), the basicity of an adsorbent enhances the affinity of its surface towards iodine molecules through acid-base interactions [130, 131]. Hence, the capability and capacity of an adsorbent for iodine adsorption can be enhanced by introducing basic functional groups (e.g., O, S, P, $-NH_2$, $-NH-$, $-N=N-$, $-C=N-$, etc.) and electron-rich π-conjugated moieties (e.g., C=C double bond, C≡C triple bond, triazine ring, phenyl ring, porphyrin ring, etc.) into the structure [81]. Basic functional groups and electron-donating conjugated systems can share their lone-pair and π electrons with iodine molecules, leading to stronger iodine-adsorbent interactions and thus increasing the adsorption capacity [82, 99, 132]. In this section, the iodine-capturing performances of functionalized CTFs are summarized.

Feng et al. designed and developed a series of electron-rich π-conjugated triazine-based microporous polymers (TBTT-CMP@1, TBTT-CMP@2, and TBTT-CMP@3) using N^2,N^4,N^6-tris(4-bromophenyl)-1,3,5-triazine-2,4,6-triamine (TBTT) and aniline as primary building units through the Buchwald-Hartwig (BH) coupling reaction [133]. The triazine-containing TBTT building unit linked with aniline molecules led to the formation of amine-functionalized CMPs with ultra-high iodine adsorption capacities up to 4.42 g g^{-1} at 75 °C and 1 bar. Most iodine uptake occurred at $-NH-$, $-C=N-$, and aromatic rings within the electron-enriched structure of the TBTT-CMP adsorbents. Xiong et al. designed and prepared two kinds of heteroatom-rich (e.g., P and N) phosphazene-functionalized triazine-based POPs (MelPOP-2 and TatPOP-2) through a mild catalyst-free and one-step polymerization process [134]. These porous microspheres possess extended π-conjugated skeletons constructed with hexachlorocyclotriphosphazene, melamine, and 4,4',4"-(1,3,5-triazine-2,4,6-triyl) trianiline). MelPOP-2 and TatPOP-2 delivered the iodine adsorption capacities of 4.50 and 2.62 g g^{-1}, respectively, at 75 °C and atmospheric pressure. The heteroatom effect (i.e., due to the coexistence of N and P atoms with accessible lone-pair electrons in the structures) led to enhanced interactions between iodine molecules and functionalized CTFs. Besides, the conjugated nature of CTFs increased the possibilities to interact with iodine molecules, thus increasing the viable pathways through which the iodine species can be confined within the porous frameworks.

In another study, Pan et al. developed a novel sulfur-functionalized CTF (BTT-TAPT-COF) adsorbent containing abundant N atom adsorption sites and extended π-conjugated skeleton for reversible iodine adsorption [135]. BTT-TAPT-COF displayed an iodine adsorption capacity of 2.76 g g^{-1} at 78 °C and 1 bar. This noticeable value might be because of the unique characteristics of BTT-TAPT-COF, such as high specific surface area (864 m^2 g^{-1}), large pore volume (0.56 cm^3 g^{-1}), and the abundance of electron-rich heteroatoms with accessible lone-pair electrons.

Xu et al. recently prepared a series of imidazolium salt-functionalized cationic CTFs (CTF-Cl-1, CTF-Cl-2, CTF-PF-3, and CTF-PF-4) through the ionothermal cyclotrimerization method. They reported a considerable radioiodine adsorption capacity of 3.21 g g^{-1} for CTF-PF-4 at 75 °C and 1 bar [136]. Among all, the charged aromatic skeleton of CTF-PF-4, electron-rich π-conjugated moieties, and structure-based porosities (i.e., the permanent intrinsic porosity of the framework) are responsible for multiple interactions with the molecular iodine (I_2), contributing to the

satisfactory iodine-capturing performance of this material. The former characteristic of CTF-PF-4 results in more robust electrostatic interactions between the positively charged framework and the negatively charged (poly)iodide species (e.g., I_3^- and I_5^-) evolved during adsorption.

Hassan et al. reported novel triptycene-based hydroxy-functionalized covalent triazine polymers (T_COPs) from benzene-1,3,5-tricarbaldehyde derivatives [130]. Besides, these conjugated porous polymers feature abundant imine and amine functionalities (i.e., −C=N− and −NH−, respectively), bridging triptycene motifs. Among all three synthesized samples in which the density of hydroxy functionalities varied, T_COP-1 with the lowest surface area and pore volume (206 $m^2\ g^{-1}$ and 0.218 $cm^3\ g^{-1}$, respectively) showed the highest iodine uptake capacity of 4.86 g g^{-1} at 75 °C and 1 bar. This study further confirmed that the magnitude of the iodine adsorption capacity of an adsorbent is a function of its textural properties and the nature and density of functional groups within its skeleton. The main interactions between the polymer backbone and the iodine species are those between the antibonding (σ^*) orbital of iodine and the lone-pair electrons of N centers in triazine, amine, and imine linkages [137]. Conceivably, the considerable charge transfer from the electron-rich π-conjugated backbone of T_COP-1 to the molecular iodine (I_2), along with acid-base interactions between iodine as a Lewis acid and electron-donating heteroatoms such as N and O of T_COP-1 are the most critical intermolecular interactions for an efficient and reversible radioiodine adsorption.

Recently, Chang et al. explored the potential of a series of chemically stable fluorine, chlorine, and nitrogen-decorated CTFs (FCTF, ClCTF, and NCTF, respectively) as porous media for efficient and reversible radioiodine uptake [138]. Among all three samples produced under different synthetic conditions, the samples comprising F and N atoms prepared ionothermally at 400 °C with a $ZnCl_2$/monomer molar ratio of 10 (FCTF@400 and NCTF@400) displayed superior adsorption capacities, signifying that incorporating electron-rich motifs into the conjugated backbone of CTFs can improve their iodine-capturing performance noticeably. The iodine vapor adsorption capacities of FCTF@350, ClCTF@350, and NCTF@350 were 2.85, 2.31, and 2.32 g g^{-1}, while their counterparts synthesized at 400 °C with enhanced textural properties showed 3.83, 3.72, and 3.40 g g^{-1}, respectively. Embedding F and pyridinic N atoms within the structure of CTFs augmented the interactions between CTF skeleton and iodine molecules via acid-base or electrostatic interactions, which, in turn, resulted in the polarization of iodine molecules and evolution of (poly)iodide species such as I_3^- and I_5^-.

Geng et al. synthesized two multifunctional sulfur-decorated thiophene-based CTFs (TTPATTh and TTPATCz) through a Friedel-Crafts alkylation reaction between cyanuric chloride as the crosslinking unit and tris[4-(2-thienyl)phenyl]amine (TPATTh) and tris(4-carbazoyl-9-ylphenyl)amine (TPATCz) as the backbone building blocks using methanesulfonic acid (CH_3SO_3H) as the catalyst and o-dichlorobenzene as the solvent at 140 °C under nitrogen protection [139]. Despite their high specific surface areas and large pore volumes (S_{BET} and V_{tot} up to 2501 $m^2\ g^{-1}$ and 2.233 $cm^3\ g^{-1}$, respectively), TTPATTh and TTPATCz showed moderate iodine adsorption capacities of 2.58 and 3.82 g g^{-1}, respectively, at 75 °C and 1 bar. The UV-vis, XRD, Raman, and FT-IR spectra of the iodine-laden TTPATTh (I_2@TTPATTh) revealed strong interactions between the iodine molecules and the CTF skeleton, resulting in forming a charge-transfer complex, therefore leading to the evolution of (poly)iodide species. It is worth mentioning that no additional peaks were marked in all the spectroscopic characterization results, implying the predominance of physical interactions (i.e., physisorption) in the adsorption complex rather than chemisorption. Meanwhile, such strong charge-transfer interactions may lead to a conspicuous

blue shift (i.e., shifting to the shorter wavenumbers) in the FT-IR spectra of the iodine-loaded adsorbents, possibly due to the reduced electron density of the framework after iodine uptake [140-142].

Huang et al. synthesized a piperazine-functionalized CTF (n-CTP) through a solvothermal synthetic method using cyanuric chloride and piperazine as starting monomers and potassium carbonate (K_2CO_3) as the catalyst in the 1,4-dioxane solvent at 90 °C under nitrogen protection [143]. The equilibrium iodine adsorption capacity of n-CTP was 4.19 g g^{-1} at 75 °C and 1 bar. According to the characterization results of the iodine-loaded n-CTP adsorbent, the adsorbed iodine in the I_2@n-CTP complex was not in its molecular form (i.e., I_2). This observation could be because lone-pair electrons in n-CTP easily polarize the adsorbed iodine molecules, followed by a noticeable charge transfer from the conjugated framework to iodine molecules, promoting the formation of (poly)iodide species. Although no additional peaks were observed in the FT-IR spectrum of iodine-loaded n-CTP, a considerable shifting was noticed in the vibrational bands corresponding to the conjugated parts of the framework and the parts with lone-pair electrons (e.g., the N atoms of piperazine moieties). Such observation indicates that the interactions between iodine and n-CTP could simultaneously occur at the triazine and piperazine rings. In a word, the charge-transfer complex formation led to the spectral shifting elucidated earlier.

Li et al. constructed a hyper-crosslinked porous polymer (N-HCP) with dual nitrogen-containing building units, 2,4,6-triphenyl-1,3,5-triazine (as conjugated part) and pyrrole (as heterocyclic part) through a two-step $FeCl_3$-catalyzed Friedel-Crafts reaction in chloroform at 25 °C for 24 h followed by further heating at 150 °C for 48 h [144]. The N-HCP adsorbent showed a moderate iodine uptake capacity of 2.57 g g^{-1} at 75 °C and 1 bar. The main elements contributing to the obtained iodine adsorption capacity are the nitrogen content (up to 8.04 wt.%), porous media with a moderate specific surface area (222.8 m^2 g^{-1}), and the electron-rich structure of the triazine-based polymer. According to the spectral results of the iodine-loaded N-HCP, the iodine uptake occurs at the triazine, benzene, and pyrrole moieties within the framework. Besides, it was revealed that the adsorbed iodine upon the surfaces of N-HCP was in the form of (poly)iodide anion species. In another study, Pourebrahimi et al. synthesized a bipyridine-functionalized CTF (CTF-bpy) via a modified ionothermal synthetic method using molten $ZnCl_2$ at 500 °C for 40 h [145]. The resultant porous polymer showed a superior iodine adsorption capacity of 4.52 g g^{-1} at 90 °C and 1 bar. The strong acid-base interactions are considered the main governing factors affecting the iodine-capturing performance of CTF-bpy.

3 Chapter 3: Computational Methodology

3.1 Computational chemistry

Theoretical chemistry and computers are used in computational chemistry to compute the structures and characteristics of particular atoms or molecules, including their spectra, chemical reactivity, energies of molecules and transition states, and other physicochemical characteristics [146]. Computational chemistry plays a crucial role in various areas of chemistry and related disciplines, including drug discovery, materials science, environmental chemistry, and biochemistry [147]. The Schrödinger equation is a fundamental quantum mechanics equation that describes how a physical system's quantum state changes over time. It was formulated by Austrian physicist Erwin Schrödinger in 1925 and is a cornerstone of quantum chemistry. The Schrödinger equation is written in two general forms: the time-independent and time-dependent Schrödinger equations:

$$\hat{H}\psi(\bar{R},\bar{r}) = E\psi(\bar{R},\bar{r}) \qquad \text{Eq. 3-1}$$

$$\hat{H}\Psi(\bar{R},\bar{r},t) = i\hbar\frac{\partial\Psi(\bar{R},\bar{r},t)}{\partial t} \qquad \text{Eq. 3-2}$$

Here, $\hat{H}$ is the Hamiltonian operator for a molecule with M nuclei and N electrons. ψ and Ψ are the time-independent and time-dependent wave functions for electrons, respectively, and E is the eigenvalue or energy of the system. In the meantime, $\bar{R}$ and $\bar{r}$ are the positions of nuclei and electrons, respectively. The wavefunction in Schrödinger's equation represents a mathematical function that describes the quantum state of a physical system, encapsulating information about the probability distribution of particles' positions and momenta. $\hat{H}$ can be expressed as follows:

$$\hat{H} = -\frac{1}{2}\sum_{i=1}^{N}\nabla_i^2 - \frac{1}{2}\sum_{A=1}^{M}\frac{1}{M_A}\nabla_A^2 - \sum_{i=1}^{N}\sum_{A=1}^{M}\frac{Z_A}{r_{iA}} + \sum_{i=1}^{N}\sum_{j>i}^{N}\frac{1}{r_{ij}} + \sum_{A=1}^{M}\sum_{B>A}^{M}\frac{Z_A Z_B}{R_{AB}} \qquad \text{Eq. 3-3}$$

where ∇^2 is the Laplacian operator, which can be expressed as follows:

$$\nabla^2 = \frac{\partial^2}{\partial x^2} + \frac{\partial^2}{\partial y^2} + \frac{\partial^2}{\partial z^2} \qquad \text{Eq. 3-4}$$

M nuclei are represented by A and B, i and j represent N electrons, and Z is the atomic number. The kinetic energy of electrons and nuclei are the first two items. The final three items comprise the potential energy of electron-nuclear attractions, electron-electron repulsions, and nuclear-nuclear repulsions.

As a second-order differential equation, the time-dependent Schrödinger equation can only be solved analytically for the hydrogen atom. It cannot be solved exactly for other atoms having more than one electron. However, because nuclei move much more slowly than electrons, their kinetic energy may be roughly assumed to be zero, and the potential energy resulting from nucleus-nucleus repulsion is nearly constant. As a result, using the Born-Oppenheimer approximation, $\hat{H}$ can be written as follows:

$$\hat{H} = -\frac{1}{2}\sum_{i=1}^{N}\nabla_i^2 - \sum_{i=1}^{N}\sum_{A=1}^{M}\frac{Z_A}{r_{iA}} + \sum_{i=1}^{N}\sum_{j>i}^{N}\frac{1}{r_{ij}} = \hat{T} + \hat{V}_{ext} + \hat{V}_{e-e} \qquad \text{Eq. 3-5}$$

where $\hat{T}$, $\hat{V}_{ext}$, and $\hat{V}_{e-e}$ represent the kinetic energy, the external potential, and the electron-electron repulsion, respectively.

3.2 Applications of Schrodinger equation in quantum chemistry

The Schrödinger equation is used extensively in quantum chemistry for the following applications [148]:

Prediction of molecular properties: Quantum chemists use the Schrödinger equation to calculate the electronic structure of molecules. Researchers can predict properties like molecular energy, bond lengths, bond angles, and electronic spectra by solving this equation for a molecule's electrons interacting with atomic nuclei.

Chemical bonding: Quantum chemistry employs the Schrödinger equation to understand and explain chemical bonding, including covalent, ionic, and metallic bonds. It helps determine the distribution of electrons and the strength of chemical interactions.

Spectroscopy: The Schrödinger equation is central to the interpretation of spectroscopic data. It provides the theoretical foundation for understanding how molecules interact with electromagnetic radiation, leading to the interpretation of various spectroscopic techniques, such as infrared, UV-visible, and NMR spectroscopy.

Reaction Mechanisms: Quantum chemistry allows researchers to study chemical reactions at the molecular level. Solving the Schrödinger equation for reactants, intermediates, and products makes it possible to determine reaction pathways, activation energies, and rate constants.

Material Science: Quantum chemistry is applied to predict the properties of materials, including electronic conductivity, optical properties, and magnetic behavior. This helps in the development of new materials with tailored characteristics.

Catalysis: Understanding the mechanisms of catalytic reactions is essential in various industries. Quantum chemistry allows scientists to investigate how catalysts facilitate chemical reactions by solving the Schrödinger equation for reactants, intermediates, and catalysts.

3.3 Density-functional theory (DFT)

Density Functional Theory (DFT) is a highly successful and widely used quantum mechanical method in computational chemistry and condensed matter physics. It provides a framework for predicting the electronic structure and properties of atoms, molecules, and solids. DFT is based on the concept of electron density, a function of spatial coordinates that describes the distribution of electrons in a system [149].

3.3.1 Fundaments of DFT

3.3.1.1 Electron density

At the core of DFT is the concept of electron density ($\rho(\mathbf{r})$), which describes the distribution of electrons in a system as a function of position ($\mathbf{r}$). Unlike traditional quantum methods, DFT does not explicitly solve for the wave functions of individual electrons but instead focuses on the electron density.

3.3.1.2 Hohenberg-Kohn theorems

DFT is grounded in two key theorems proposed by Walter Kohn and Pierre Hohenberg in 1964 [150]. The first theorem states that the ground-state electron density uniquely determines the ground-state energy of a system. In other words, there is a one-to-one correspondence between the electron density and the total energy. The second theorem states that a universal functional, Exc [ρ(r)], called the exchange-correlation functional, accounts for all the electronic interactions

beyond the classical electrostatic repulsion. Accordingly, the electron density ($\rho(\mathbf{r})$) can determine the ground-states energy:

$$E = E(\rho(\mathbf{r})) \quad \text{Eq. 3-6}$$

3.3.2 Kohn-Sham equations

The system is divided into a set of non-interacting, fictitious electrons to apply DFT, each moving in an effective potential that accounts for the interaction with the other electrons. These fictitious electrons are called Kohn-Sham electrons. The Kohn-Sham equations are a set of equations that describe the behavior of these non-interacting electrons within this effective potential [151]. They are mathematically similar to the Schrödinger equation but are solved self-consistently to find the electron density. Accordingly, the total energy can be calculated as follows:

$$E[\rho(\mathbf{r})] = T[\rho(\mathbf{r})] + E_{ee}[\rho(\mathbf{r})] + E_{xc}[\rho(\mathbf{r})] + \int V_{ext}(\mathbf{r})\,\rho(\mathbf{r})d\mathbf{r} \quad \text{Eq. 3-7}$$

where T, E_{ee}, and E_{xc} are kinetic, electron-electron repulsion, and exchange-correction energy, respectively. According to this method, each electron moves in an effective single-particle potential, following the single-particle Schrödinger equation:

$$\left\{-\frac{\hbar^2}{2m}\nabla^2 + V_{eff}[\rho(\mathbf{r})]\right\}\psi_i(\mathbf{r}) = \epsilon_i\psi_i(\mathbf{r}) \quad \text{Eq. 3-8}$$

where V_{eff} stands for an effective potential and is expressed as:

$$V_{eff}[\rho(\mathbf{r})] = V_{ext}[\rho(\mathbf{r})] + V_{e-e}[\rho(\mathbf{r})] + V_{xc}[\rho(\mathbf{r})] \quad \text{Eq. 3-9}$$

where V_{xc} denotes the exchange-correlation potential, defined as:

$$V_{xc}[\rho(\mathbf{r})] = \frac{\partial E_{xc}[\rho(\mathbf{r})]}{\partial \rho(\mathbf{r})} \quad \text{Eq. 3-10}$$

Meanwhile, the electron density of a given quantum system can be defined as follows:

$$\rho(\mathbf{r}) = \sum_i |\psi_i \rho(\mathbf{r})|^2 \quad \text{Eq. 3-11}$$

Moreover, T and E_{xc} can be calculated through Eqs. 3-12 and 3-13, respectively:

$$T[\rho(\mathbf{r})] = \sum_i \langle \psi_i \left| -\frac{\hbar^2}{2m}\frac{1}{2}\nabla^2 \right| \psi_i \rangle \quad \text{Eq. 3-12}$$

$$E_{ee}[\rho(\mathbf{r})] = \frac{1}{2}\iint \frac{\rho(\mathbf{r})\rho(\mathbf{r}')}{|\mathbf{r}-\mathbf{r}'|}d\mathbf{r}d\mathbf{r}' \quad \text{Eq. 3-13}$$

3.3.3 Exchange-correlation functional

The exchange-correlation functional is a critical component of DFT in quantum chemistry and condensed matter physics. It plays a central role in approximating the interactions between electrons in a system when applying DFT to calculate the electronic structure and properties of atoms, molecules, and solids.

3.3.3.1 Purpose of the exchange-correlation functional

In DFT, the electron-electron interaction in a many-electron system is approximated by dividing it into exchange and correlation. Exchange accounts for the quantum mechanical phenomenon where electrons avoid each other due to their indistinguishable nature. In simple terms, it represents the tendency of electrons to be in different quantum states (spin and spatial coordinates)

to minimize their mutual electrostatic repulsion. The correlation term accounts for the electron-electron interactions beyond the exchange term, including electron-electron correlation effects like electron-electron scattering. The exchange-correlation functional combines these two contributions into a single mathematical expression. It is typically a functional of the electron density, which describes the spatial distribution of electrons in the system.

3.3.3.2 Approximations for the exchange-correlation functional

One of the key challenges in DFT is finding an accurate expression for the exchange-correlation functional. The exact functional is unknown, so various approximations have been developed to make DFT computationally tractable [152].

Local Density Approximation (LDA): The exchange-correlation energy is approximated using the electron density at each point in space. This simple approximation works well for some systems but not others, especially those with varying electron densities.

Generalized Gradient Approximation (GGA): GGAs consider the electron density and its gradient (spatial variations). This provides a more accurate description of systems with varying electron densities and is a popular choice for many applications.

Meta-Generalized Gradient Approximation (meta-GGA): Meta-GGAs go a step further and consider the electron density, gradient, and the Laplacian of the electron density. This allows for improved accuracy, particularly in describing electron correlation effects.

Hybrid Functionals: Hybrid functionals combine DFT with a fraction of the exact Hartree-Fock exchange. They can provide better accuracy for certain properties like band gaps and energetics but are computationally more demanding.

3.3.4 Basis sets

Basis sets are a fundamental component of computational chemistry, and they play a crucial role in approximating the electronic wave functions of atoms and molecules [153]. Basis sets describe the spatial distribution of electrons within a quantum mechanical framework. Each basis set comprises a set of mathematical functions, typically Gaussian-type orbitals (GTOs) or Slater-type orbitals (STOs), centered on the atomic nuclei [154]. These basis functions are combined to build the molecular orbitals that describe the electronic structure of molecules. Two widely used basis sets, also employed in this dissertation, are the Pople and Karlsruhe basis sets, each with its characteristics and applications.

3.3.4.1 Pople basis sets

Named after Nobel laureate John Pople, Pople basis sets are a hierarchy of basis sets designed to balance accuracy and computational cost [153]. They are particularly well-suited for electronic structure calculations of small to medium-sized molecules. The hierarchy includes double-zeta (DZ), triple-zeta (TZ), quadruple-zeta (QZ), and more, indicating the number of basis functions used for each electron in the system.

Components of Pople basis sets, widely used in computational chemistry, are designed to represent the electron distribution in atoms and molecules with a balance of accuracy and computational efficiency. These basis sets are often divided into different types of functions, including core functions, valence functions, polarization functions, and diffuse functions.

Core Functions: Core functions are the basis functions that closely approximate the electron distribution near the atomic nucleus. They are typically high quality, meaning they can accurately represent the electron density in the core region, where electrons are tightly bound to the nucleus. Core functions ensure that the basis set accurately captures the electron-nucleus interaction, especially for inner electrons strongly influencing the electronic structure.

Valence Functions: Valence functions are the basis functions that describe the electron distribution away from the atomic nucleus. They provide a more extended representation of the electron density and are crucial for accurately describing the bonding and chemical interactions between atoms. Valence functions are generally lower quality than core functions to balance computational efficiency with accuracy.

Polarization Functions: Polarization functions are additional basis functions that are introduced to account for electron correlation effects and electron density polarization. They allow the basis set to adapt more flexibly to the electronic distribution in a molecule, particularly in regions where electron density varies significantly. Polarization functions are often labeled as *d*, *p*, *f*, etc., denoting different levels of polarization (e.g., *d* functions provide higher polarization than *p* functions).

Diffuse functions: Diffuse functions are basis functions that describe the electron density in regions of space far away from the atomic nucleus. They are particularly useful when studying molecules with charged or highly polarized species, such as ions or molecules with large dipole moments. Diffuse functions improve the basis set's ability to describe the shape and extent of electron clouds.

Split-Valence Sets: The split-valence approach is a common strategy in Pople basis sets where the basis functions for each electron are divided into core and valence functions. As mentioned earlier, core functions are higher quality and focus on accurately describing the electron density near the nucleus. Valence functions provide a more extended description of the electron distribution, focusing on regions farther from the nucleus. Split-valence sets are designed to balance computational efficiency with accuracy. They ensure the basis set appropriately captures the core and valence electron interactions.

3.3.4.2 Karlsruhe basis sets

Karlsruhe basis sets, also known as the Karlsruhe segmented contracted basis sets, are specialized basis sets designed to accurately describe the electronic structure of molecules, particularly those containing heavy elements [155]. They include components similar to Pople basis sets, such as core, valence, polarization, and diffuse functions, but are customized for high-accuracy quantum chemical calculations.

3.3.4.3 Choice of appropriate basis sets

The 6-311+G(d,p) basis set (*used in the Computational Section of Chapters 5 and 6*) and 6-31+G(d,p) (*used in the Computational Section of Chapter 7*) are widely used basis sets in computational quantum chemistry, particularly known for its suitability for light atoms such as carbon (C), nitrogen (N), sulfur (S), fluorine (F), hydrogen (H), and oxygen (O). These versatile basis sets offer a balanced compromise between accuracy and computational cost, making them popular for modeling molecular systems containing these elements. The "6" in their names denotes the number of primitive Gaussian functions used to describe the core electrons, while "311" and "31" signify the number of primitive Gaussians employed for valence electrons. Additionally, the

"+G(d,p)" part incorporates additional diffuse (+) and polarization (d and p) functions, enhancing the basis sets' ability to describe electron correlation and polarization effects accurately. Therefore, these basis sets are well-suited for predicting the geometries, energies, and spectroscopic properties of molecules containing these light elements, offering a balance between computational efficiency and accuracy in quantum chemical calculations.

The def2-TZVPD basis set is a highly effective basis set, particularly well-suited for heavy atoms such as iodine (I) and heavy metals like cadmium (Cd), lead (Pb), and mercury (Hg) (*i.e., the main heavy atoms studied in Chapters 5 and 6*). As heavy atoms and transition metals possess complex electron structures and a greater number of electrons compared to lighter elements, they demand basis sets that can accurately capture electron correlation and relativistic effects. The def2-TZVPD basis set's name signifies its comprehensive nature, with "def2" indicating the inclusion of both polarization and diffuse functions to account for electron correlation and dispersion interactions. The "TZVP" portion encompasses the triple-ζ valence polarized basis set, providing a robust representation of valence electrons. It facilitates the reliable prediction of geometries, energetics, and spectroscopic properties in complex systems involving heavy atoms and metals.

The LANL2DZ basis set [156] is a specialized basis set designed for accurate calculations of heavy atoms like platinum (Pt) (*i.e., the main heavy atom studied in Chapter 7*). It is characterized by its two components: a small core or "double-ζ" basis set for the innermost electrons, which is particularly important for accurately capturing the core electron correlation effects, and a larger basis set for the valence electrons. This approach is essential for heavy atoms like Pt, as they possess complex electronic structures with strongly interacting core and valence electrons. The LANL2DZ basis set effectively balances computational efficiency with the precision required to describe Pt's electronic behavior in various chemical and physical contexts.

3.3.5 Difference between basis sets and exchange-correlation functionals

Basis sets and exchange-correlation functionals are essential in quantum mechanical methods for studying atoms, molecules, and solids. Basis sets are mathematical functions that approximate electron wave functions, serving as a foundation for describing electronic density and energy. Larger basis sets typically offer more accuracy but demand greater computational resources. Exchange-correlation functionals, part of DFT, address electron-electron interactions and correlation energy, which are crucial for describing electron behavior. These functionals use approximations like LDA or GGA to represent these interactions. Together, basis sets provide spatial and angular electron information, while exchange-correlation functionals account for electron interactions, allowing for precise predictions in quantum chemistry and condensed matter physics.

3.4 Methods

The ωB97XD (short for "ωB97X-D") exchange-correlation functional is a widely used hybrid density functional that incorporates a fraction of Hartree-Fock (HF) exchange, which is known for its accurate treatment of electron correlation, along with DFT exchange-correlation terms [157]. It also includes a dispersion correction (D) term, which accounts for van der Waals interactions. ωB97XD is designed to provide accurate results for systems involving dispersion forces, making it suitable for various applications, including adsorption systems. We now compare ωB97XD with other typical exchange-correlation functionals and justify its use in adsorption systems studied in Chapter 5 and Chapter 6. The mathematical expression for the ωB97XD exchange-correlation functional is as follows:

$$E_{XC}^{\omega B97XD} = E_{XC}^{GGA} + E_{dispersion}$$ Eq. 3-14

Here, $E_{XC}^{\omega B97XD}$ represents the total exchange-correlation energy calculated using the ωB97XD functional. E_{XC}^{GGA} represents the generalized gradient approximation (GGA) exchange-correlation energy, which includes terms that depend on the electron density and its gradient (spatial variation). The specific form of the GGA exchange-correlation energy is derived from the ωB97X functional. $E_{dispersion}$ accounts for dispersion or van der Waals interactions between atoms and molecules. It is often calculated using the D3 or D4 dispersion correction methods, which provide an empirical correction to the standard GGA-DFT calculations.

3.4.1 ωB97XD vs. Local Density Approximation (LDA) and Generalized Gradient Approximation (GGA)

LDA: LDA provides a simple and computationally efficient approximation for exchange-correlation effects. However, it underestimates dispersion forces and often lacks the accuracy needed for adsorption studies, especially for non-covalent interactions.

GGA: GGAs, such as the widely used Perdew-Burke-Ernzerhof (PBE) functional, improve upon LDA by considering the electron density gradient. They perform better than LDA for dispersion interactions but may still not capture them accurately in all cases.

ωB97XD: In contrast, ωB97XD includes both HF exchange (which provides accurate correlation treatment) and a dispersion correction (D) term (which accounts for van der Waals forces). This combination makes ωB97XD well-suited for systems with significant dispersion interactions, such as adsorption systems.

3.4.2 ωB97XD vs. Pure Density Functionals

Pure DFT Functionals: Functionals like B3LYP and PBE0 include a fraction of HF exchange but lack explicit dispersion correction. While they perform well for many systems, they may not adequately describe dispersion-dominated interactions in adsorption scenarios.

3.4.3 Justification for using ωB97XD in adsorption systems

Accurate dispersion correction: Including a dispersion correction in ωB97XD is particularly beneficial for adsorption systems, where non-covalent interactions like van der Waals forces and π-π stacking play a crucial role. ωB97XD's D correction significantly improves the description of these interactions.

Balanced treatment of exchange and correlation: ωB97XD combines HF exchange (which treats electron correlation more accurately) with DFT exchange-correlation terms, striking a balance between computational cost and accuracy. This makes it well-suited for adsorption systems, which often involve a compromise between accuracy and computational resources.

Good overall performance: ωB97XD has demonstrated good performance across various chemical systems, including molecular adsorption on surfaces, physisorption, and intermolecular interactions in crystal structures. It provides more reliable adsorption energies and structures than pure DFT functionals.

Benchmarking: ωB97XD has been extensively benchmarked for adsorption systems against high-level quantum chemistry methods and experimental data, further justifying its use in adsorption studies.

The TPSS (Tao-Perdew-Staroverov-Scuseria) exchange-correlation functional is a density functional that falls within the meta-generalized gradient approximation (meta-GGA) category [158]. TPSS is known for its relatively good performance across various molecular and condensed matter systems. When considering its use in adsorption systems involving transition metals like Pt and organic materials such as CTFs (Chapter 7), it's essential to compare TPSS with other typical exchange-correlation functionals and evaluate its suitability based on certain characteristics. The mathematical expression for the TPSS exchange-correlation functional is as follows:

$$E_{XC}^{TPSS} = E_{XC}^{LDA} + E_{XC}^{GGA} + E_{C}^{nl} \quad \text{Eq. 3-15}$$

Here, E_{XC}^{TPSS} represents the total exchange-correlation energy as calculated using the TPSS functional. E_{XC}^{LDA} represents the exchange-correlation energy calculated using the local density approximation (LDA). LDA is a simple and computationally efficient approximation that depends only on the local electron density at each point in space. E_{XC}^{GGA} represents the exchange-correlation energy calculated using the GGA. GGA functionals incorporate the electron density and its gradient (spatial variation), providing a more accurate description of exchange and correlation effects than LDA. E_{C}^{nl} accounts for non-local correlation effects and is a distinctive feature of the TPSS functional. It introduces additional terms that capture non-local electron correlation effects beyond what is typically included in standard GGA functionals. These terms are designed to improve the description of non-covalent interactions and non-local electronic correlations.

3.4.4 TPSS vs. Local Density Approximation (LDA) and Generalized Gradient Approximation (GGA)

LDA: LDA is a simple and computationally efficient functional but often underestimates dispersion forces and may need to capture the correct electronic structure of transition metals. TPSS typically provides more accurate results than LDA, especially for adsorption systems involving weak interactions and transition metals.

GGAs (e.g., PBE, BLYP): GGAs like PBE and BLYP improve upon LDA by considering the electron density gradient, which provides better results for non-covalent interactions. However, TPSS often offers improved accuracy over GGAs due to its inclusion of the meta-generalized gradient approximation (meta-GGA) framework.

3.4.5 TPSS vs. Hybrid Functionals (e.g., B3LYP)

Hybrid functionals, including a fraction of the Hartree-Fock exchange, are known for accurately describing electronic correlation effects. While they perform well for many systems, they may be computationally expensive for large systems. TPSS offers a good compromise between accuracy and computational cost for various adsorption scenarios.

3.4.6 Justification for using TPSS in gas adsorption and sensing systems

Inclusion of non-local correlation effects: TPSS belongs to the meta-GGA class of functionals, which includes non-local correlation terms that capture non-local electronic correlations more accurately than GGAs. This feature is particularly useful when dealing with adsorption systems

that involve weak, non-covalent interactions, such as van der Waals forces and π-π stacking between organic materials and transition metals like Pt.

Balanced treatment of exchange and correlation: TPSS provides a balanced treatment of exchange and correlation effects, which is crucial for achieving accurate adsorption energies and geometries. This balance is particularly important for systems with covalent and non-covalent interactions, such as those involving organic materials and transition metals.

Transition metal accuracy: TPSS has been shown to provide reasonably accurate results for transition metal systems. While more computationally expensive than hybrid functionals, TPSS can reasonably capture transition metals' electronic structure and energetics.

Good overall performance: TPSS has been tested and benchmarked for various systems, including adsorption systems. It performs well in predicting adsorption energies and structures, making it a reliable choice for adsorption studies involving transition metals like Pt and organic materials.

Benchmarking: TPSS has been extensively benchmarked for adsorption systems against high-level quantum chemistry methods and experimental data when characterizing the electronic properties of transition metals-containing organometallic compounds [159], further justifying its use in gas adsorption and sensing studies.

3.4.7 Solvation models

Solvation models are key tools in computational chemistry, facilitating the study of solute-solvent interactions without explicitly accounting for all solvent molecules. These models are essential for investigating the influence of solvents on electronic structures, thermodynamics, and various properties of solutes. One such solvation model of note is the Integral Equation Formalism Polarizable Continuum Model (IEFPCM) [160]. Solvation models bridge the gap between the molecular scale and macroscopic solutions, allowing for the accurate simulation and prediction of diverse chemical and physical properties. These models encapsulate the complex interaction of forces governing solute-solvent interactions, including electrostatic forces, polarization effects, dispersion forces, and steric hindrance, within the solvent environment.

The mathematical representation for the IEFPCM solvation model involves solving the Poisson equation for the solvent region's electrostatic potential ($V_{sol}(\mathbf{r})$):

$$\nabla.\left(\epsilon(\mathbf{r})\nabla V_{sol}(\mathbf{r})\right) = -4\pi\rho(\mathbf{r}) \qquad \text{Eq. 3-16}$$

In this equation, $\epsilon(\mathbf{r})$ represents the dielectric constant of the solvent at each point in space ($\mathbf{r}$), ∇ denotes the gradient operator, which operates on the dielectric constant and the electrostatic potential, $V_{sol}(\mathbf{r})$ is the electrostatic potential in the solvent region, which is the quantity being solved for, and $\rho(\mathbf{r})$ is the electron density of the solute molecule.

The goal of solving this equation is to obtain the electrostatic potential ($V_{sol}(\mathbf{r})$) throughout the solvent region, which accounts for the electrostatic interaction between the solute and the solvent. This potential is then used to calculate solvation energies and properties, such as solvation free energies.

The IEFPCM model is a prominent representative among solvation models, classified as a continuum model. Continuum models, in contrast to explicit solvent models, consider the solvent as a continuous medium with defined dielectric properties, thereby simplifying the computational complexity. IEFPCM is grounded in the principles of integral equations, effectively capturing the essence of solute-solvent interactions within this continuum framework. A distinguishing feature of the IEFPCM model is its comprehensive treatment of polarizability. It not only accounts for the polarizability of the solute but also incorporates the polarizability of the solvent. This characteristic is especially critical when studying systems comprising polarizable components, as it faithfully represents the dynamic response of both solute and solvent to changes in their surroundings.

The IEFPCM model also integrates the concept of the dielectric continuum. By considering the dielectric constant of the solvent, a measure of its ability to screen electrostatic interactions, IEFPCM accurately models electrostatic solute-solvent interactions. Furthermore, this model does not neglect non-electrostatic forces, such as dispersion and repulsion interactions, ensuring a holistic description of electrostatic and non-electrostatic solute-solvent interactions. The IEFPCM model's strength lies in its self-consistent approach. It iteratively solves the solvation problem, considering how the solute's charge distribution evolves due to solvent effects and vice versa. This self-consistency ensures a balanced treatment of the complex intermolecular forces during the solvation process. Additionally, IEFPCM provides insights into the nature of solute-solvent interactions, shedding light on molecular recognition, binding phenomena, and the stability of chemical species in solution. Hence, this dissertation uses the IEFPCM solvation model in Chapters 5 and 6.

3.4.8 Structure, intermolecular, intramolecular, and orbital interaction analyses

3.4.8.1 Natural bond orbital (NBO) analysis

NBO analysis is a powerful tool in computational chemistry for exploring charge transfer, charge delocalization, and orbital interactions within molecules. By examining the occupancy values of NBOs, one can identify regions of electron-rich and electron-poor character, shedding light on charge redistribution during chemical processes. NBO analysis also reveals the degree of delocalization of electrons across molecular frameworks, highlighting the extent to which electrons are shared or localized. Furthermore, it elucidates orbital interactions, helping us understand how various molecular orbitals interact to form bonds or stabilize reactive intermediates.

Charge distributions and stabilization energy $E(2)$ for donor-acceptor were investigated in this dissertation. The stabilization energy $E(2)$ probable interactions between filled donors (Lewis-type NBOs) and empty acceptors (non-Lewis-type NBOs) are assessed using second-order perturbation theory. $E(2)$can be calculated as follows [161]:

$$E(2) = q_i \frac{(F_{i,j})^2}{\varepsilon_i - \varepsilon_j} \qquad \text{Eq. 3-17}$$

In this equation, q_i is the orbital occupancy and ε_i and ε_j are diagonal elements (orbital energies), and $F_{i,j}$ is the off-diagonal NBO Fock matrix element. A higher $E(2)$ value signifies a more robust donor-acceptor interaction.

3.4.8.2 Non-covalent interactions (NCI) analysis

NCI analysis is a vital computational tool to investigate intermolecular interactions in diverse chemical systems. It provides valuable insights into the nature, strength, and spatial distribution of

non-covalent forces such as hydrogen bonding, van der Waals interactions, and π-π stacking. NCI analysis allows researchers to visualize and quantify regions of attractive or repulsive interactions by examining electron density properties, particularly the electron density gradient and its Laplacian. This method not only aids in characterizing the stability of molecular complexes but also assists in rationalizing the binding affinity between molecules.

NCI can be analyzed by plotting the reduced density gradient (RDG) versus the electron density multiplied by the sign of the second Hessian eigenvalue ($\mathrm{sing}(\lambda_2)\rho(\mathbf{r})$). The RDG is a dimensionless quantity and can be calculated as follows [162]:

$$\mathrm{RDG} = \frac{|\nabla\rho(\mathbf{r})|}{2(3\pi^2)^{1/3}\rho(\mathbf{r})^{4/3}} \qquad \text{Eq. 3-18}$$

In fact, NCI analysis visualizes and distinguishes between non-covalent interactions in real space, such as van der Waals forces (weak interactions, $\mathrm{sign}(\lambda_2)\rho(r)\approx 0$), strong attraction (e.g., hydrogen bonds, $\mathrm{sign}(\lambda_2)\rho(r)<0$) and steric repulsion (e.g., steric effect in rings, $\mathrm{sign}(\lambda_2)\rho(r)>0$).

3.4.8.3 Density of states (DOS) analysis

DOS analysis is a fundamental tool in computational chemistry and solid-state physics, primarily used to investigate orbital interactions within materials and molecules. DOS analysis provides crucial information about systems' electronic structure, bonding, and reactivity by analyzing the distribution of electronic states as a function of energy [163]. It allows for identifying energy levels associated with different molecular orbitals and studying their interactions, including bonding and antibonding states. DOS analysis is particularly useful in characterizing the density of electronic states near the Fermi level, aiding in predicting electronic conductivity, optical properties, and chemical reactivity in various materials, from semiconductors to catalysts. DOS can be expressed as follows:

$$\mathrm{D(E)} = \int \delta(\mathrm{E} - \mathrm{E_i})\mathrm{dE_i} \qquad \text{Eq. 3-19}$$

where $\mathrm{D(E)}$ represents the DOS, a function of energy (E), $\mathrm{E_i}$ represents the energy levels of the electronic states in the system, and δ is the Dirac delta function, which ensures that the integral selects only the energy levels that match the specified energy E.

3.4.9 Software

Gaussian 16 is a versatile software package that provides a comprehensive suite of tools for conducting DFT calculations, including geometry optimization, frequency calculations, energy calculations, and NBO analysis. In the meantime, the GaussView 6 graphical interface was used to visualize molecular structures. Additionally, the Multiwfn software package can be employed to obtain DOS plots, while RDG plots and 3D isosurfaces can be generated to better understand electron density distribution and NCI.

4 Chapter 4: Experimental Methodology

4.1 Project 1: Iodine adsorption using conjugated CTFs

4.1.1 Chemicals and reagents

Cyanuric chloride (2,4,6-trichloro-1,3,5-triazine, 99%, ACROS Organics), trans-stilbene (TS, 96%, Sigma-Aldrich), diphenylacetylene (DPA, 98%, Sigma-Aldrich), aluminum chloride ($AlCl_3$, anhydrous, 99.99%, Sigma-Aldrich), iodine (I_2, ACS reagent, 99.8+%, Sigma-Aldrich), hydrochloric acid (HCl, certified ACS Plus grade, 36.5–38 wt.%, Fisher Scientific), methanol (MeOH, ACS reagent, 99%, Fisher Scientific), ethanol (EtOH, ACS reagent, 99%, Fisher Scientific), n-hexane (ACS reagent, 99%, Sigma-Aldrich), tetrahydrofuran (THF, ACS reagent, 99+%, Alfa Aesar), dichloromethane (DCM, ACS reagent, anhydrous, 99.6%, ACROS Organics), dimethylformamide (DMF, 99.8%, Sigma-Aldrich), dimethylsulfoxide (DMSO, 99+%, Alfa Aesar), and acetone (ACS reagent, 99+%, Alfa Aesar) were used as received without further purification/treatment. Deionized water (DI water) was supplied from a local Barnstead/Sybron Nanopure II purification system.

4.1.2 Synthesis procedure for CTF-DPA and CTF-TS

Cyanuric chloride (0.184 g, 1 mmol) was firstly well mixed with anhydrous aluminum chloride (0.400 g, 3 mmol) in an argon-filled glovebox. The mixture was then transferred to a round-bottom Schlenk flask equipped with a condenser. Subsequently, 15 mL of dichloromethane (DCM) was added to the mixture under nitrogen protection, and the resulting white dispersed solution was stirred vigorously for 30 min at room temperature. Diphenylacetylene (DPA, 0.276 g, 1.55 mmol) was separately dissolved in 15 mL of DCM, and the solution was added dropwise into the reactor under nitrogen protection in 15 min. The resulting black color solution was refluxed for 18 h at 70 °C, after which the reactor was cooled down to room temperature. The insoluble black precipitate was collected by centrifugation and thoroughly washed with 1 M aqueous HCl solution, DI water, methanol, DCM, THF, and acetone, respectively, to remove the catalyst and unreacted starting materials. Ultimately, the resulting brownish paste was dried at 80 °C under vacuum (~-30 inHg) for 12 h to yield the activated CTF-DPA powder (0.417 g, ~91% yield). A similar procedure was used with diphenylacetylene replaced with trans-stilbene (0.403 g, ~87% yield) to synthesize CTF-TS.

4.1.3 Iodine vapor adsorption procedure using CTF-DPA and CTF-TS

The equilibrium and kinetic studies of iodine vapor adsorption utilizing the prepared CTF-DPA and CTF-TS adsorbents were performed as follows. Ten small glass vials were loaded with a prescribed amount (ca. 10 mg) of the CTF adsorbent. Then, the vials were placed in a conical Erlenmeyer flask containing excess iodine flakes at the bottom (ca. 1 g). The Erlenmeyer flask was then sealed using a septum rubber and heated to 75 °C under ambient pressure. Sampling from the small glass bottles was performed at different intervals to investigate the kinetics of iodine vapor adsorption. The iodine-loading weight of CTFs was obtained by directly weighing the samples and thermogravimetric measurements (see ESI for the thermogravimetric measurements and calculations). The amount of iodine vapor uptake by the CTF adsorbents was calculated as follows:

$$\text{Iodine uptake} = \frac{m_{I_2@CTF} - m_{CTF}}{m_{CTF}} \qquad \text{Eq. 4-1}$$

where m_{CTF} and $m_{I_2@CTF}$ are the masses of the CTF adsorbent before and after iodine vapor adsorption, respectively.

4.1.4 Iodine adsorption from n-hexane solution using CTF-DPA and CTF-TS

To study the iodine adsorption kinetics of CTFs in an organic solvent, an iodine/n-hexane solution with an initial concentration of 1 mg mL^{-1} was prepared by dissolving 10 mg iodine in 10 mL n-hexane. The resultant solution was ultrasonicated for 10 min to obtain a homogeneous solution and ensure that the iodine flakes were completely dissolved in n-hexane. Then, the prescribed amount (ca. 10 mg) of the activated adsorbent was added to an iodine/n-hexane solution, and the amount of iodine adsorbed upon the CTFs was monitored over time. To that effect, the iodine concentration in the supernatant was measured by UV-Vis spectrophotometry and calculated according to the Lambert-Beer law at different time intervals. The instantaneous amount of iodine adsorbed upon the CTF adsorbents (q_t: mg g^{-1}) was computed as follows:

$$q_t = \frac{(C_i - C_t)V}{W} \qquad \text{Eq. 4-2}$$

where C_i is the initial iodine concentration of the solution (1 mg mL^{-1}), C_t is that at time t, V is the volume of the iodine/n-hexane solution (10 mL), and W is the mass of the CTF adsorbent (10 mg).

4.1.5 Adsorption kinetic model

Adsorption kinetic models are important in surface chemistry and materials science, designed to describe how molecules interact with solid surfaces over time. These models help us understand the mechanisms governing adsorption processes, such as the rate at which molecules are adsorbed onto or desorbed from surfaces. By providing mathematical descriptions of these processes, adsorption kinetic models enable researchers to quantify and predict adsorption behavior under different conditions. Various models, including the pseudo-first-order (PFO), pseudo-second-order (PSO), fractal-like pseudo-first-order (FL-PFO), Elovich, and intraparticle diffusion models, among others, have been developed to capture the complex interplay of factors impacting adsorption kinetics [164]. In this dissertation, focusing on the FL-PFO kinetic model, we have predicted the kinetic behavior of iodine/CTF-DPA and iodine/CTF-TS adsorption systems in both vapor and n-hexane phases in Chapter 5.

4.1.5.1 FL-PFO kinetic model

The FL-PFO kinetic model is an advanced and specialized means that describes adsorption kinetics, particularly in complex systems where non-linear behavior is observed [164]. This model develops the traditional PFO kinetic model and is particularly suitable for characterizing complex adsorption processes on heterogeneous surfaces or porous materials. What distinguishes the FL-PFO model is its ability to capture adsorption mechanisms that exhibit fractal-like characteristics, often seen in systems with irregular surface structures or multiple adsorption sites. Incorporating a fractal dimension into the model accounts for the adsorbent's complex geometry and complicated adsorption pathways. The FL-PFO kinetic model can be mathematically expressed as follows:

$$q_t = q_e\left(1 - \exp(-kt^{\alpha})\right) \qquad \text{Eq. 4-3}$$

where q_t is the amount of adsorbed species at time t, $q_{e,cal}$ is that at equilibrium, k is the FL-PFO rate constant, and α is the fractional order parameter.

4.1.6 Recycling procedure for CTF-DPA and CTF-TS

To examine the recyclability of the synthesized CTF-DPA and CTF-TS, the iodine-loaded CTF adsorbents were first soaked in ethanol (20 mL) and stirred at room temperature for 2 h. The samples were centrifuged and thoroughly washed with ethanol (3×10 mL), heated at 120 °C under

a dynamic vacuum (~−30 inHg) for 4 h, and then used again. The extracted iodine species could be retrieved from ethanol through evaporation and stored in an environmentally stable porous material or other long-term storage systems.

4.2 Project 2: Heavy metal removal from water using functionalized CTFs

4.2.1 Chemicals and reagents

All chemicals and reagents utilized in this project were used without further purification or pre-treatment. Zinc chloride ($ZnCl_2$, reagent grade, ≥98%, Sigma-Aldrich), 1,4-dicyanobenzene (DCB, 98%, Sigma-Aldrich), 2,5-dicyanobenzoic acid (COOH-DCB, ≥96%, PJPC Ltd), hydrochloric acid (HCl, certified ACS Plus grade, 36.5-38 wt.%, Fisher Scientific), and acetone (Mojallali Laboratory, ≥99.8%) were used as received. Deionized water (DI water) was supplied from a local Barnstead/Sybron Nanopure II water purification system.

4.2.2 Synthesis procedure for CTF-1 and COOH-CTF

To synthesize CTF-1 adsorbent, 1,4-dicyanobenzene (DCB, 0.128 g, 1 mmol) and zinc chloride ($ZnCl_2$, 0.136 g, 1 mmol) are well-admixed mechanically using a mortar in an argon-filled glovebox. Then, the resulting white-color mixture is loaded in a high-temperature quartz glass tube (1.5 cm diameter×15 cm length) in the glovebox. The glass tube is sealed by a rubber septum stopper, vacuumed for 2 h, then flame-sealed, and ultimately placed in a muffle furnace vertically, heated to 400 °C with a heating rate of 1 °C min^{-1} and kept at 400 °C for 40 h. Upon the reaction completion, the glass tube is cooled to room temperature and opened carefully under a fume hood to collect the resulting black-color monolithic product. After the synthesis, the product undergoes a detailed purification procedure to remove the catalyst ($ZnCl_2$), unreacted monomer (e.g., DCB), and other impurities. In this respect, the obtained material is crushed and thoroughly ground into the fine powder using a mortar under a fume hood, added to the aqueous HCl solution (30 mL, 0.1 M), and refluxed at 100 °C under stirring at 300 rpm for 12 h. Successively, the resulting material is centrifuged and washed with the excess amount of aqueous HCl solution (3×10 mL, 0.1 M), DI water (5×50 mL), and acetone (3×10 mL), respectively. Ultimately, the resulting material is dried at 120 °C for 8 h under a dynamic vacuum to render the final activated adsorbent. A similar synthetic procedure is used with DCB replaced with COOH-DCB monomer (i.e., 2,5-dicyanobenzoic acid, 0.172 g, 1 mmol) to synthesize COOH-CTF.

4.2.3 Heavy metal adsorption onto CTF-1 and COOH-CTF in a batch system

The experiments of batch equilibrium adsorption are performed to determine the heavy metal (HM) cation-capturing performance of CTFs at the ambient temperature (i.e., 25 °C) and the constant pH value of 5.0 adjusted by NaOH and HCl solutions. The adsorption experiments are conducted by adding a prescribed amount of activated adsorbent (ca. 5 mg) in 40 mL of HM cations aqueous solutions with different initial concentrations in a set of glass vials (50 mL). Each vial is stirred at 200 rpm for 360 min. After each batch adsorption experiment, the adsorbents are separated from the solution by filtration. The remaining HM cations concentrations are acidified with 2.0% nitric acid (HNO_3) as a diluent to ensure all the HM species are dissolved. It ought to be noted that nitric acid (1% to 5%) is typically utilized for metal dissolution and stabilization for ICP-OES investigation [165]. The residual concentration of HM cations in the aqueous phase is determined using ICP-OES. The amount of adsorbed HM cations onto the CTF adsorbents (q_e) is calculated as follows:

$$q_e = \frac{C_i - C_f}{m} V \qquad \text{Eq. 4-4}$$

where C_i and C_f are the initial and final concentrations (mg L^{-1}) of HM cations, respectively, V is the volume of the aqueous solution (40 mL), and m represents the mass of the CTF adsorbent (5 mg).

4.2.4 Adsorption isotherm models

Adsorption isotherm models are essential in surface chemistry and materials science, offering valuable insights into the interactions between molecules and solid surfaces. These models provide a mathematical framework to describe how gases or liquids adhere to a surface as a function of concentration or pressure, shedding light on phenomena such as gas adsorption, catalysis, and the behavior of porous materials. Understanding adsorption isotherms is crucial for applications in gas storage, environmental remediation, and drug delivery systems. Various adsorption isotherm models, including the Langmuir, Freundlich, Sips, Toth, and BET models, among others, have been developed to capture the diverse range of adsorption behaviors observed in different systems [166]. In this dissertation, focusing on the Langmuir and Sips models, we have predicted the thermodynamic behavior of HM@CTF-1 and HM@COOH-CTF adsorption systems.

4.2.4.1 Langmuir adsorption isotherm

The Langmuir adsorption isotherm model is a fundamental concept in surface chemistry and adsorption science, named after the renowned scientist Irving Langmuir. This model describes the adsorption of molecules onto a solid surface, typically in the context of gases or liquids adhering to a solid material. The Langmuir model assumes monolayer adsorption, meaning that molecules can occupy only a single layer on the surface and that there is no interaction between the adsorbed molecules. The model's mathematical expression, known as the Langmuir equation, relates the fractional surface coverage (θ, the ratio of adsorbed molecules to the maximum possible coverage) to the pressure or concentration of the adsorbate. The Langmuir adsorption isotherm can be mathematically expressed as follows:

$$q = \frac{q_{m,cal} b C_e}{1 + b C_e} \qquad \text{Eq. 4-5}$$

where q is the amount of adsorbed species, $q_{m,cal}$ is the maximum possible amount of that species, b is the affinity coefficient (i.e., the Langmuir constant), and C_e is the equilibrium concentration of adsorbate in the aqueous phase.

4.2.4.2 Sips adsorption isotherm

The Sips adsorption isotherm model, also known as the Langmuir-Freundlich or Sips-Langmuir model, is a widely used mathematical model in surface chemistry and adsorption science [166]. It extends the Langmuir and Freundlich isotherm models, offering a more flexible approach to describing complex adsorption behaviors. The Sips isotherm accommodates situations where adsorption does not strictly follow monolayer adsorption (as in the Langmuir model) or has heterogeneous adsorption energies (as in the Freundlich model). It introduces a shape parameter (n) that allows for variations in adsorption mechanisms, ranging from cooperative adsorption ($n > 1$) to competitive adsorption ($n < 1$). When $n = 1$, the Sips model simplifies to the Langmuir model. The Sips model is particularly useful for describing adsorption on heterogeneous surfaces and when deviations are from ideal Langmuir-type behavior. The Sips adsorption isotherm can be mathematically expressed as follows:

$$q = \frac{q_{m,cal} (b C_e)^{\frac{1}{n}}}{1 + (b C_e)^{\frac{1}{n}}} \qquad \text{Eq. 4-6}$$

4.2.5 Kinetic studies of heavy metal adsorption onto CTF-1 and COOH-CTF

The amount of HM cations adsorbed onto CTF materials can be expressed as a function of time to study the kinetics associated with the adsorption process. The process followed the steps described in Section 6.4.4 for the equilibrium analyses, except for stopping the adsorption at specific times. That is, samples (4 mL) from the vials are taken at certain intervals by rapid filtration of residual adsorbent from the sample solutions. ICP-OES is also used to determine the residual concentration of the Cd^{2+}, Hg^{2+}, and Pb^{2+} cations in each sample solution. The amount of adsorbed HM cations is determined as follows:

$$q_t = \frac{C_i - C_r}{m} V \qquad \text{Eq. 4-7}$$

where C_i and C_r are the initial and instantaneous residual concentrations (mg L^{-1}) of HM cations, respectively.

4.2.6 Adsorption kinetic models

Adsorption kinetic models are important in surface chemistry and materials science, designed to describe how molecules interact with solid surfaces over time. These models help us understand the mechanisms governing adsorption processes, such as the rate at which molecules are adsorbed onto or desorbed from surfaces. By providing mathematical descriptions of these processes, adsorption kinetic models enable researchers to quantify and predict adsorption behavior under different conditions. Various models, including the pseudo-first-order (PFO), pseudo-second-order (PSO), fractal-like pseudo-first-order (FL-PFO), Elovich, and intraparticle diffusion models, among others, have been developed to capture the complex interplay of factors impacting adsorption kinetics [164]. In this dissertation, focusing on the PFO and PSO kinetic models, we have predicted the kinetic behavior of HM@CTF-1 and HM@COOH-CTF adsorption systems in Chapter 6.

4.2.6.1 PFO kinetic model

The PFO kinetic model is a widely used approach in adsorption science to describe the rate at which molecules are adsorbed onto solid surfaces [164]. This model assumes that the adsorption process follows first-order reaction kinetics, meaning that the adsorption rate is directly proportional to the number of available sites on the surface and the concentration of adsorbate in the solution. The mathematical expression for this model simplifies the adsorption process into a linear equation relating the natural logarithm of the difference between the initial and equilibrium concentrations of the adsorbate to time. While the pseudo-first-order model provides a straightforward way to estimate adsorption rates, it is important to note that it may need to accurately represent the actual mechanisms governing adsorption in complex systems. The PFO kinetic model can be mathematically expressed as follows:

$$q_t = q_{e,cal}(1 - \exp(-k_1 t)) \qquad \text{Eq. 4-8}$$

where q_t is the amount of adsorbed species at time t, $q_{e,cal}$ is that at equilibrium, and k_1 is the PFO rate constant.

4.2.6.2 PSO kinetic model

The PSO kinetic model is a prominent tool in adsorption science, particularly for elucidating the kinetics of adsorption processes on solid surfaces [164]. Unlike the simplified assumptions of the PFO model, the PSO model offers a more realistic representation of adsorption kinetics. It asserts

that the adsorption rate is directly proportional to the product of the number of available surface sites and the square of the adsorbate concentration in the solution. The mathematical expression for this model yields a linear relationship when plotting the inverse of the adsorbate concentration against time, making it suitable for estimating adsorption rate constants and predicting equilibrium adsorption capacities. The PSO kinetic model can be mathematically expressed as follows:

$$q_t = \frac{k_2 q_{e,cal}^2 t}{1+k_2 q_{e,cal} t} \quad \text{Eq. 4-9}$$

where k_2 is the PSO rate constant.

4.2.7 Recycling procedure for heavy metal-loaded CTF-1 and COOH-CTF

Desorption investigations were performed utilizing HCl solution (40 mL, 1 M) as a desorption/regeneration solution. The HM-loaded CTF is isolated from the solution, washed with DI water, and dried. Next, the CTF adsorbent is immersed in the HCl solution while stirred at room temperature for 3 h and filtered through a centrifuge. Ultimately, the recovered CTF adsorbent is used for a subsequent adsorption cycle.

4.3 Material Characterization

4.3.1 X-ray diffraction (XRD) patterns

X-ray diffraction (XRD) is a crucial technique in materials science used to analyze crystalline materials' phase structure and purity. It involves exposing a sample to X-rays and measuring the resulting diffraction patterns, revealing the arrangement of atoms within the crystal lattice. XRD identifies crystalline phases, helping determine chemical composition and crystallographic structure. Additionally, it detects impurities and undesirable phases, assessing material purity. Overall, XRD is required for understanding atomic arrangements and properties.

Several key parameters are involved in XRD analysis, and specific mathematical formulas govern them as follows:

4.3.1.1 Bragg's law

Bragg's law can be stated as follows:

$$n\lambda = 2d\sin(\theta) \quad \text{Eq. 4-10}$$

where n is integer representing the order of diffraction, λ is the wavelength of the incident X-ray, d is the interplanar spacing, and θ is the diffraction angle.

The XRD patterns of all the CTF samples synthesized in this dissertation (i.e., CTF-DPA, CTF-TS, CTF-1, and COOH-CTF) were collected on the Bruker D8 Advance diffractometer with a Cu-Kα radiation source (2.2 kW) with λ=1.5418 Å and a scanning rate of 0.1 (degree min^{-1}). The running conditions for the X-ray tube were 40 kV and 40 mA, and the power supply controlled these with a stability of better than 0.01% for the high voltage and 10% of the variation of the supply for the current. The detector was a NaI dynamic scintillation detector with a maximum count rate of 2×10^6 s^{-1}. To visualize and analyze the diffraction patterns, the DIFFRAC.SUITE software package was used. The diffraction pattern data were collected in the range of 5-70°.

4.3.2 Fourier-transform infrared (FT-IR) spectroscopy

Fourier-transform infrared (FT-IR) spectroscopy is a fundamental analytical technique in materials science that provides valuable insights into the chemical composition and molecular structure of a wide range of materials. FT-IR spectroscopy can identify functional groups, chemical bonds, and

molecular vibrations by measuring the absorption or emission of infrared radiation as it interacts with a sample. FT-IR characterization enables the detection of impurities, the assessment of material purity, and the investigation of chemical reactions. Moreover, it plays a key role in elucidating the intricate chemical composition of complex organic and inorganic materials.

In the meantime, attenuated total reflectance Fourier-transform infrared spectroscopy (ATR-FT-IR) is a powerful analytical technique widely used in materials science and chemistry. ATR-FTIR spectroscopy offers significant advantages for studying solid and liquid samples without extensive preparation. It employs total internal reflection of infrared light at the sample's interface with a high-refractive-index crystal. ATR-FT-IR is particularly valuable for its ease of use, speed, and ability to analyze samples directly. In this dissertation, all the precursors and CTF samples were characterized by ATR-FT-IR.

FT-IR spectroscopic measurements of the precursors (DPA, TS, cyanuric chloride, DCB, and COOH-DCB) and resulting CTF samples (CTF-DPA, CTF-TS, CTF-1, and COOH-CTF) were conducted on a Thermo Scientific Nicolet 6700 Analytical FTIR spectrometer (600–3600 cm^{-1}) with diamond ATR and a single room temperature DTGS detector. For each experiment, the resolution was 4 cm^{-1}, and the number of scans was 64. The OMNIC^{TM} spectra software suite was used to visualize and analyze the obtained spectra.

4.3.3 Thermogravimetric analysis (TGA)

Thermogravimetric Analysis (TGA) is a powerful thermal analysis technique used in materials science and chemistry to investigate substances' thermal stability and decomposition behavior. TGA works by subjecting a sample to controlled temperature increases while continuously measuring its weight change as a function of temperature or time. It plays a crucial role in assessing the suitability of materials for specific applications and in studying degradation processes, making it an invaluable characterization tool.

The thermal behavior and stability of all the precursors and CTF samples synthesized in this dissertation were examined using a TA Instruments TGA Q50 from 30 °C to 700 °C at a heating rate of 10 °C min^{-1} under a nitrogen atmosphere. A 100 µL platinum sample pan was used to load the samples. The nitrogen flow was set at 20 mL min^{-1}. Also, 5-10 mg of samples were used for each experiment. The Universal Analysis software was used to control and monitor the instrument during experiments.

4.3.4 N_2 adsorption-desorption isotherms

Nitrogen (N_2) adsorption-desorption isotherms are key in surface science and materials characterization. These isotherms provide valuable insights into solid materials' porous structure and surface area. By exposing a sample to varying pressures of N_2 gas at a constant temperature using a liquid nitrogen bath, researchers can measure the amount of gas adsorbed (adsorption) and desorbed from the material's surface. The resulting isotherm plot reveals critical information about pore size distribution, surface area, and the textural properties of materials, aiding in the characterization of catalysts, adsorbents, and porous solids.

In this dissertation, the N_2 adsorption-desorption isotherms were collected on a Micromeritics ASAP 2020 physisorption analyzer at 77.4 K to investigate the porous media textural properties and the pore features of the CTF samples. The analysis range of the N_2 relative pressure (i.e., P/P_0) was from 1.3×10^{-9} to 1.0. The samples were firstly degassed at 120 °C for 6-12 h under a dynamic vacuum (~−30 inHg) to ensure the pores were free and accessible to probe molecules (e.g., He

and N_2). 100-150 mg of CTF samples were used for each experiment. The ASAP 2020 V4.01 software was used to analyze and visualize the collected data.

4.3.4.1 BET specific surface area measurements

Using the data from the adsorption and desorption isotherms, one might be able to calculate the BET specific surface area employing the following equation:

$$\frac{1}{{}^{P}/_{P_0}\left(\frac{1}{q}-1\right)} = \frac{1}{B \times S_{BET}} + \frac{C-1}{B \times S_{BET}} \times \left(\frac{P}{P_0}\right) \qquad \text{Eq. 4-11}$$

In this equation, P is the N_2 relative pressure at a given point on the isotherm, P_0 is the N_2 relative pressure at the saturation point, q is the amount of gas adsorbed per unit mass of the sample, B and C are the constants derived from the BET equation, and S_{BET} is the specific surface area of the sample. One can perform linear regression analysis on the linearized data to obtain the values of B and C in the BET equation.

4.3.4.2 Pore size distribution

When using Non-Local Density Functional Theory (NLDFT) for pore size analysis, the type of pore geometry assumed can vary depending on the specific NLDFT model selected and the nature of the porous material being analyzed. NLDFT is a versatile method that can account for various pore geometries, including micropores, mesopores, and macropores. The choice of pore geometry is typically made based on the size and structure of the pores within the material. The pore size distribution in all the CTF samples synthesized in this work was estimated using N_2@77 on the Carbon Slit Pores model and non-negative method without smoothing. Applying the Carbon Slit Pores model to characterize polymeric porous materials is warranted when considering the model from a pore shape perspective. While polymeric porous materials can exhibit diverse and irregular pore structures, the Carbon Slit Pores model simplifies pore geometries. This model, which assumes the presence of slit-like pores, provides a useful means to estimate key pore properties, such as size and distribution while facilitating the analysis of specific surface areas. While it may not fully capture the intricacies of polymeric pore shapes, its simplicity and interpretability make it a valuable tool for initial investigations, offering insights into the pore structures of polymeric materials and guiding further, more comprehensive analyses as needed.

4.3.5 X-ray photoelectron spectroscopy (XPS)

X-ray photoelectron spectroscopy (XPS) is a powerful surface analysis technique widely used in materials science and chemistry. XPS provides invaluable insights into a material's surface layer's elemental composition and chemical state. By bombarding the sample with X-rays and measuring the kinetic energy of emitted photoelectrons, XPS reveals detailed information about the chemical bonds, oxidation states, and electronic structure of elements on the sample's surface.

In this dissertation, XPS spectra of iodine-loaded CTF-DPA, iodine-loaded CTF-TS, HM-loaded CTF-1, and HM-loaded COOH-CTF samples were collected on a Thermo Scientific ESCALAB 250Xi analyzer. The photon source was a monochromatic Al Kα X-ray source (aluminum anode with a characteristic wavelength of 1486.6 eV), and the spectral range was 0-1400 eV. Also, the analyzer type was a double-focusing hemispherical analyzer. Moreover, the energy step size was set at 0.1 eV.

Origin is a widely used scientific data analysis and graphing software package for analyzing and visualizing XPS data. Origin provides a user-friendly interface and a broad range of tools and

functions for effectively processing, interpreting, and presenting XPS data. Hence, we used the Origin software package to visualize and analyze the XPS results. In the meantime, the Gaussian model was selected to perform curve fitting.

4.3.6 Transmission electron microscopy (TEM)

Transmission Electron Microscopy (TEM) is an influential imaging and analytical technique in materials science and nanotechnology. TEM allows researchers to visualize and examine the microstructure of materials with unprecedented detail at the nanoscale. By passing a beam of electrons through a thin specimen, TEM generates high-resolution images that reveal the morphology, crystal structure, and defects of materials at the atomic level.

In this dissertation, the TEM characterization of the CTFs was carried out on a JEOL 2010F high-resolution transmission electron microscope at an accelerating voltage of 200 keV, with a point-to-point resolution of 0.19 nm, a focused probe of 0.2 nm, Schottky field emission source, tilt range of $\pm$15°, equipped with silicon drift EDS detector and ASTAR precession electron diffraction.

4.3.7 Raman spectroscopy

Raman spectroscopy is a non-destructive analytical technique that provides valuable insights into molecules' vibrational and rotational modes. By shining laser light on a sample, Raman spectroscopy measures the shifts in the scattered light's energy, revealing information about chemical compositions, molecular structures, and bonding arrangements. This technique is highly versatile and applicable to various fields.

In this dissertation, the iodine-loaded CTF-DPA and CTF-TS adsorbents were analyzed by Raman spectroscopy using a Bruker Optics Senterra equipped with a 532 nm (green) laser. This wavelength is commonly used for Raman spectroscopy due to its interaction with various materials. The instrument collected data with a resolution of 4 cm^{-1} and was equipped with a Grating detector. In the meantime, the OPUS spectroscopy software package was used to visualize and analyze the collected data.

4.3.8 Ultraviolet-visible spectrophotometry (UV-Vis)

Ultraviolet-visible spectrophotometry (UV-Vis) is a fundamental analytical technique widely used in various scientific fields, including chemistry, biology, and materials science. UV-Vis spectrophotometry involves the absorption of ultraviolet and visible light by molecules, providing insights into their electronic structure and concentration. By measuring the absorbance of light at different wavelengths, one can identify compounds, determine their concentrations, and study chemical reactions. UV-Vis is particularly valuable for characterizing the color, purity, and chemical composition of substances, making it an indispensable tool for quality control, environmental analysis, and research into the behavior of molecules in solution.

In this dissertation, the UV-Vis absorption spectra were recorded on a Thermo Scientific Genesys 10S UV-Vis spectrophotometer with 10 mm path-length glass cells, spectral bandwidth of 1.8 nm, a Xenon flash lamp light source, dual silicon photodetector, wavelength range of 190-1100 nm, speed scan of 3600 nm min^{-1}, and scanning data interval of 1 nm.

To calculate the concentration of iodine in n-hexane solutions, the Lamber-Beer law can be used. This law describes the linear relationship between the concentration of a substance in a solution, the path length of the sample (usually the length of the cuvette or cell), and the absorbance of light at a specific wavelength. The law is expressed mathematically as:

$$A = \log_{10} \frac{I_0}{I} = \varepsilon c l \qquad \text{Eq. 4-12}$$

where A is the absorbance of the sample at a particular wavelength, I_0 is the intensity of incident light, I is the intensity of transmitted light, ε is the molar absorptivity (also called molar extinction coefficient) of the substance at that wavelength, a constant specific to the substance, c is the concentration of the substance in the solution (in mol L^{-1} or Molarity), and l is the path length of the sample (typically in cm).

4.3.9 Scanning electron microscopy (SEM)

Scanning electron microscopy (SEM) is a cutting-edge imaging technique critical in modern materials science, nanotechnology, and biology. SEM provides high-resolution, three-dimensional images of surfaces and structures by scanning a focused electron beam over the sample's surface. By capturing secondary electrons, backscattered electrons, and characteristic X-rays emitted from the specimen, SEM reveals elaborate details at the micro- and nanoscale. This versatile tool allows the visualization of surface morphology, the study of particle size and shape, and the investigation of elemental composition.

In this dissertation, a scanning electron microscope (Zeiss model EVO MA10, OXFORD instruments) was used for the SEM/EDX analysis. The parameters used were a working distance of 8.5 mm and an accelerating voltage of 25 keV. Samples were metalized with copper (Cu) to improve the quality of images.

4.3.10 Inductively coupled plasma optical emission spectrometry (ICP-OES)

Inductively coupled plasma optical emission spectrometry (ICP-OES) is a highly versatile and sensitive analytical technique in various scientific disciplines, including chemistry, environmental science, and materials research. ICP-OES operates by creating an extremely hot and ionized argon plasma, which vaporizes and atomizes a sample, generating a high-energy environment. As the sample's atoms relax from their excited states, they emit characteristic wavelengths of light, which are then quantitatively analyzed. This method allows for the simultaneous detection of multiple elements across a broad range of concentrations, making ICP-OES an invaluable tool for elemental analysis. In this dissertation, the concentrations of HM species in water were determined using ICP-OES in Chapter 6.

The Avio 200 ICP-OES used in this dissertation has a double-spectrometer optical system. The sealed optical system can be purged with nitrogen for low UV (165-190 nm) performance. The high-dispersion echelle spectrometer has a focal length of 0.3 meters and a Stigmatic Littrow configuration. The echelle grating used for dispersion has 79 lines mm^{-1} with a blaze angle of 63.8 degrees. The spectral range is 165-900 nm with a resolution of < 0.009 nm @ 200 nm. The UV-sensitive, dual backside-illuminated Charge-Coupled Device (CCD) array detector is cooled directly using a single-stage integrated Peltier cooler at approximately -8 °C. The Avio 200 ICP-OES features a fourth-generation 40 MHz, free-running solid-state RF generator, adjustable from 1000 to 1500 watts in 1-watt increments. The power efficiency is greater than 81% with < 0.1% variation in output power stability. A compressed-air shear gas (18-25 L min^{-1}) removes the plasma tail from the optical path, minimizing interferences and extending the dynamic range.

5 Chapter 5: Highly Efficient and Reversible Iodine Adsorption Utilizing Amorphous Conjugated Covalent Triazine-Based Porous Polymers: Experimental and Computational Studies

5.1 Abstract

A robust conjugated covalent triazine framework, CTF-DPA, has been synthesized through a facile Friedel-Crafts alkylation reaction using cyanuric chloride as the cross-linking agent and diphenylacetylene (DPA) as the backbone building block. Benefiting from its unique textural and structural features, such as high specific surface area (943 $m^2 g^{-1}$), accessible pores, and abundant π-electrons, CTF-DPA exhibits outstanding iodine-capturing performance. It features an ultrahigh iodine vapor adsorption capacity of 5.12 g g^{-1} at 75 °C and 1 bar and a remarkable iodine adsorption capacity of 667 mg g^{-1} in an n-hexane solution. To the best of our knowledge, these are among the highest iodine adsorption capacities reported for porous organic polymers. In contrast, an analog CTF synthesized with trans-stilbene (TS) replacing DPA features a slight decrease in specific surface area (919 $m^2 g^{-1}$) but a noticeable reduction in iodine adsorption capacities. The iodine uptake mechanism was investigated by Fourier-transform infrared (FT-IR), X-ray photoelectron spectroscopy (XPS), energy-dispersive X-ray spectroscopy (EDX), and Raman spectroscopy as well as computationally. Density functional theory (DFT) calculations reveal that charge transfer from conjugated C≡C, phenyl, and triazine moieties to iodine molecules facilitates the generation of charged (poly)iodide species (e.g., I_3^-), enhancing the adsorption affinity/capacity. Moreover, CTF-DPA could be recycled five times while preserving above 87.6% of its initial iodine uptake capacity.

5.2 Introduction

To address the rapidly growing energy shortage and decrease the emission of greenhouse gases, viable, cost-effective, and zero-emission energies are urgently required. In this regard, many countries have steadily expanded and implemented nuclear energy [167]. Nonetheless, radioactive wastes commonly generated in nuclear power plants have become an inevitable problem, hindering further development and progress in the nuclear industry [168]. Among fission products, radioiodine species (^{129}I and ^{131}I) have particularly drawn concerns. They can accumulate in the environment, harming environmental safety and human health [169]. Therefore, effectively removing radioiodine species from both gaseous and organic phases remains a big challenge for nuclear energy's safe and sustainable development. For instance, some nuclear waste reprocessing implementations, such as PUREX/UREX, use flammable organic solvents to recover iodine-containing spent fuel products [170]. The traditional strategy for radioiodine uptake relies on chemical adsorption by robust Ag^+-doped composite materials [171]. However, this method suffers disadvantages such as low adsorption capacity (e.g., iodine uptake capacity of 132 mg g^{-1} for Ag_2O@zeolite) [172], high cost, and essentially irreversible adsorption due to chemical bonding between iodine species and silver cations. The latter hinders the regeneration of the adsorbent, consequently increasing the cost of the chemical adsorption technique. Meanwhile, physisorption (i.e., physical adsorption) is a suitable candidate for effectively removing contaminants. Physisorption possesses distinctive features such as high efficiency, low-cost and facile fabrication of adsorbents, straightforward operating and recycling procedures, etc. [173]. In this respect, significant research has been undertaken on developing robust porous adsorbents for effective and reversible radioiodine adsorption in the last two decades. Zeolites [174, 175], activated carbons [176, 177], metal-organic frameworks (MOFs) [178, 179], and microporous

polymers [180, 181] are among the most widely used adsorbents for the physisorption of iodine. Three types of well-known porous organic polymers (POPs), namely covalent organic frameworks (COFs) [141, 182], conjugated microporous polymers (CMPs) [183, 184], and covalent triazine frameworks (CTFs) [145, 185], have also attracted interest for applications related to iodine adsorption.

Two key factors directly affect the capability and capacity of an adsorbent in the iodine adsorption and storage process: (i) the (co)existence of high-affinity adsorption sites and suitable functionalities in the structure, facilitating iodination, and (ii) textural properties of the adsorbent (i.e., specific surface area, pore volume, and pore size distribution). Since the iodine molecule (I_2) is a Lewis acid, an adsorbent's basicity enhances its surface's affinity towards iodine molecules through acid-base interactions [80, 130, 131]. Hence, the capability and capacity of an adsorbent for iodine adsorption can be promoted by incorporating basic functional groups (e.g., O, S, P, $-NH_2$, $-NH-$, $-N=N-$, $-C=N-$, etc.) and/or electron-rich π-conjugated moieties (e.g., C=C double bond, C≡C triple bond, triazine ring, phenyl ring, porphyrin ring, etc.) within the structure [68, 81]. Basic functional groups and electron-donating conjugated systems can share their lone-pair electrons and/or π electrons with iodine molecules, leading to stronger iodine-adsorbent interaction and thus enhancing the adsorption capability and capacity [82, 99, 132]. In the meantime, mutual polarization of the host (i.e., adsorbent) and guest (i.e., iodine species) electronic clouds leads to stronger dispersion (i.e., London) forces and thus stronger van der Waals interactions typical in physisorption [83].

When interacting with a high-affinity adsorption site, the neutral iodine molecule (I_2) can be easily polarized and converted to (poly)iodide species through subsequent acid-base interaction with additional iodine molecule(s), following Eq. 5-1 [84].

$$(n+1)I_2 \rightleftarrows I^-.nI_2 + I^+ \qquad \text{Eq. 5-1}$$

where n is the number of additional iodine molecules interacting with the first iodine molecule adsorbed by the adsorption site (n=0, 1, 2, 3, ...). Charged (poly)iodide species such as I^-, I_3^-, and I_5^- evolved during adsorption can act as Lewis bases and form negatively charged complexes with molecular iodine (I_2). Hence, optimal adsorbents may also be equipped with acidic functional groups and/or electron-withdrawing moieties to adsorb these iodine species adequately. For instance, Yan et al. synthesized a series of conjugated porous polymers (PAF-23, PAF-24, and PAF-25) through the Sonogashira-Hagihara coupling reaction for iodine adsorption [186]. All three materials were reported to possess different high-affinity adsorption sites (including acidic Li^+, electron-rich C≡C triple bond, and phenyl ring) for iodine adsorption. PAF-23, PAF-24, and PAF-25 have iodine vapor adsorption capacities of 2.71, 2.76, and 2.60 g g^{-1}, respectively, at 75 °C and 1 bar. Li et al. synthesized an azo-bridged ($-N=N-$) porphyrin-phthalocyanine-based porous conjugated polymer and achieved an iodine vapor adsorption capacity of 2.9 g g^{-1} at 75 °C and 1 bar [187], while Liao et al. reported that amine-functionalized ($-NH-$) conjugated porous organic polymers achieved iodine vapor adsorption capacities up to 3.36 g g^{-1} at 75 °C and 1 bar [188].

Covalent triazine frameworks (CTFs) are a novel subclass of POPs constructed with conjugated triazine linkages (i.e., aromatic C=N), which endow them with exceptional thermal/chemical

stability [46]. These porous cross-linked polymers possess unique characteristics, including high specific surface area, large pore volume, low skeletal density, and considerable nitrogen content (i.e., heteroatom effect) [36]. Besides, the synthesis of CTFs requires relatively inexpensive and readily available precursors (e.g., 1,4-dicyanobenzene, 2,6-dicyanopyridine, cyanuric chloride, melamine, etc.), making them suitable candidates for scaling up production to larger volumes/masses and thus practical applications. Several synthetic methods have been developed for the preparation of CTFs, including ionothermal cyclotrimerization of carbonitrile-containing aromatic molecules [46], phosphorus pentoxide (P_2O_5)-catalyzed direct condensation of aromatic amides [58], superacid-catalyzed interfacial polymerization of carbonitrile-containing aromatic molecules [53], elemental-sulfur-and lithium-salt-mediated preparations [55, 189], and Friedel-Crafts alkylation of cyanuric chloride with phenyl species [190]. Among them, Friedel-Crafts alkylation of cyanuric chloride, which already possesses the triazine linkage, is one of the most widely used methods for preparing CTF materials [60]. The most significant advantage of this synthetic method is that it significantly expands the diversity of applicable monomers since the standard carbonitrile functionality required in the ionothermal and super acid-catalyzed synthesis methods is no longer needed. Meanwhile, the Friedel-Crafts reaction often involves more facile reaction conditions, requiring considerably lower temperatures than with the ionothermal method (e.g., 70–140 °C vs. 400–700 °C), and thus avoiding the undesired carbonization/graphitization and loss of volatile elements (e.g., nitrogen, hydrogen, halogens, etc.) that would compromise the structural integrity of the resulting CTFs.

In the present contribution, we have rationally designed and successfully synthesized a robust conjugated CTF (CTF-DPA) through the convenient one-pot $AlCl_3$-catalyzed Friedel-Crafts alkylation reaction of cyanuric chloride with diphenylacetylene (DPA), which bears a rigid and electron-rich C≡C (acetylene) bridging unit between two phenyl rings (see Figure 5.1). To demonstrate the effect of structural design on the properties and, thus, the iodine-capturing performance of the material, an analog CTF (CTF-TS) has also been synthesized with trans-stilbene (TS), in which the bridging unit between the two phenyl rings is CH=CH (ethene) (see Figure 5.1). The resulting conjugated porous CTFs have been systematically characterized for their textural and structural properties and evaluated for their performance toward iodine adsorption. The mechanism of iodine uptake by the synthesized CTFs was further investigated by density-functional theory (DFT) calculations.

5.3 Experimental section

5.3.1 Chemicals and reagents

Cyanuric chloride (2,4,6-trichloro-1,3,5-triazine, 99%, ACROS Organics), trans-stilbene (TS, 96%, Sigma-Aldrich), diphenylacetylene (DPA, 98%, Sigma-Aldrich), aluminum chloride ($AlCl_3$, anhydrous, 99.99%, Sigma-Aldrich), iodine (I_2, ACS reagent, 99.8+%, Sigma-Aldrich), hydrochloric acid (HCl, certified ACS Plus grade, 36.5–38 wt%, Fisher Scientific), methanol (MeOH, ACS reagent, 99%, Fisher Scientific), ethanol (EtOH, ACS reagent, 99%, Fisher Scientific), n-hexane (ACS reagent, 99%, Sigma-Aldrich), tetrahydrofuran (THF, ACS reagent, 99+%, Alfa Aesar), dichloromethane (DCM, ACS reagent, anhydrous, 99.6%, ACROS Organics), dimethylformamide (DMF, 99.8%, Sigma-Aldrich), dimethylsulfoxide (DMSO, 99+%, Alfa Aesar), and acetone (ACS reagent, 99+%, Alfa Aesar) were used as received without further purification/treatment. Deionized water (DI water) was supplied from a local Barnstead/Sybron Nanopure II purification system.

5.3.2 Material characterization

Fourier-transform infrared (FT-IR) spectroscopic measurements of the precursors and resulting CTF samples were conducted on a Thermo Scientific Nicolet 6700 Analytical FTIR spectrometer (600–3600 cm^{-1}) to identify functional groups and chemical bonds in the structures. The CTF samples' powder X-ray diffraction (XRD) patterns were obtained on a Bruker D8 Advance diffractometer with a Cu-Kα radiation source. Nitrogen adsorption-desorption isotherms were collected on a Micromeritics ASAP 2020 physisorption analyzer at 77.4 K to investigate the porous media textural properties and the pore features of the CTF samples. Thermogravimetric analysis (TGA) was conducted on a TA Instrument TGA Q50 from 30 °C to 700 °C at a heating rate of 10 °C min^{-1} under a nitrogen atmosphere. Transmission electron microscopy (TEM) characterization of the CTFs was carried out on a JEOL 2010F high-resolution transmission electron microscope at an accelerating voltage of 200 keV. X-ray photoelectron spectroscopy (XPS) spectra were collected on a Thermo Scientific ESCALAB 250Xi analyzer. The iodine-loaded adsorbents were also analyzed by Raman spectroscopy using a Bruker Optics Senterra equipped with a 532 nm laser. The ultraviolet-visible (UV-Vis) absorption spectra were recorded on a Thermo Scientific Genesys 10S UV-Vis spectrophotometer with 10 mm path-length cells. A scanning electron microscope (Zeiss model EVO MA10, OXFORD instruments) was used for the SEM/EDX analysis. The parameters used were a working distance of 8.5 mm and an accelerating voltage of 25 keV. Samples were metalized with copper (Cu) to improve the quality of images.

5.3.3 Preparation of CTFs

Cyanuric chloride (0.184 g, 1 mmol) was firstly well mixed with anhydrous aluminum chloride (0.400 g, 3 mmol) in an argon-filled glovebox. The mixture was then transferred to a round-bottom Schlenk flask equipped with a condenser. Subsequently, 15 mL of dichloromethane (DCM) was added to the mixture under nitrogen protection, and the resulting white dispersed solution was stirred vigorously for 30 min at room temperature. Diphenylacetylene (DPA, 0.276 g, 1.55 mmol) was separately dissolved in 15 mL of DCM, and the solution was added dropwise into the reactor under nitrogen protection in 15 min. The resulting black color solution was refluxed for 18 h at 70 °C, after which the reactor was cooled down to room temperature. The insoluble black precipitate was collected by centrifugation and thoroughly washed with 1 M aqueous HCl solution, DI water, methanol, DCM, THF, and acetone, respectively, to remove the catalyst and unreacted starting materials. Ultimately, the resulting brownish paste was dried at 80 °C under vacuum (~-30 inHg) for 12 h to yield the activated CTF-DPA powder (0.417 g, ~91% yield). A similar procedure was used with diphenylacetylene replaced with trans-stilbene (0.403 g, ~87% yield) to synthesize CTF-TS.

5.3.4 Iodine vapor adsorption

The equilibrium and kinetic studies of iodine vapor adsorption utilizing the prepared CTF-DPA and CTF-TS adsorbents were performed as follows. Ten small glass vials were loaded with a prescribed amount (ca. 10 mg) of the CTF adsorbent. Then, the vials were placed in a conical Erlenmeyer flask containing excess iodine flakes at the bottom (ca. 1 g). The Erlenmeyer flask was then sealed using a septum rubber and heated to 75 °C under ambient pressure. Sampling from the small glass bottles was performed at different intervals to investigate the kinetics of iodine vapor adsorption. The iodine-loading weight of CTFs was obtained by directly weighing the samples and thermogravimetric measurements (see ESI for the gravimetric measurements and calculations). The amount of iodine vapor uptake by the CTF adsorbents was calculated as follows:

$$\text{Iodine uptake} = \frac{m_{I_2@CTF} - m_{CTF}}{m_{CTF}} \quad \text{Eq. 5-2}$$

where m_{CTF} and $m_{I_2@CTF}$ are the masses of the CTF adsorbent before and after iodine vapor adsorption, respectively.

As pointed out in the introduction, the recyclability of the adsorbents is a significant factor for real-world applications, particularly when considering sustainability and cost-effectiveness [191]. Hence, examining the recyclability of CTF-DPA and CTF-TS in the iodine adsorption process is crucial. To that effect, the iodine-loaded CTF adsorbents were first soaked in ethanol (20 mL) and stirred at room temperature for 2 h. The samples were centrifuged and thoroughly washed with ethanol (3×10 mL), heated at 120 °C under a dynamic vacuum (∼−30 inHg) for 4 h, and then used again. The extracted iodine species could be retrieved from ethanol through evaporation and stored in an environmentally stable porous material or other long-term storage systems.

5.3.5 Iodine adsorption in n-hexane solution

To study the iodine adsorption kinetics of CTFs in an organic solvent, an iodine/n-hexane solution with an initial concentration of 1 mg mL^{-1} was prepared by dissolving 10 mg iodine in 10 mL n-hexane. The resultant solution was ultrasonicated for 10 min to obtain a homogeneous solution and ensure that the iodine flakes were completely dissolved in n-hexane. Then, the prescribed amount (ca. 10 mg) of the activated adsorbent was added to an iodine/n-hexane solution, and the amount of iodine adsorbed upon the CTFs was monitored over time. To that effect, the iodine concentration in the supernatant was measured by UV-Vis spectrophotometry and calculated according to the Lambert-Beer law at different time intervals (Figure S5.1). The instantaneous amount of iodine adsorbed upon the CTF adsorbents (q_t: mg g^{-1}) was computed as follows:

$$q_t = \frac{(C_i - C_t)V}{W} \quad \text{Eq. 5-3}$$

where C_i is the initial iodine concentration of the solution (1 mg mL^{-1}), C_t is that at time t, V is the volume of the iodine/n-hexane solution (10 mL), and W is the mass of the CTF adsorbent (10 mg). N-hexane was chosen as a typical nonpolar organic solvent unlikely to react with iodine and CTFs and/or interfere with the formation of complexes between CTFs and iodine [187] for comparison with previous similar works.

5.4 Computational methodology

The electronic structure of the organic building blocks of the CTF materials and their complexes with iodine species was characterized by DFT. The ωB97XD range-separated exchange-correlation functional is employed here with dispersion correction (often critical for weak interaction energies), together with the Pople triple-zeta 6-311+G** basis set for the N, C, and H atoms, and the Karlsruhe valence triple-ζ def2-TZVPD basis set for the I atom. These basis sets include a balanced polarization function on all atoms and a diffuse function on all heavy atoms (i.e., those with more than one electron). Molecular geometries were optimized with no constraints, and the obtained structures were verified to be energy-minima (no imaginary frequencies) through vibrational analysis. In addition, natural bond orbital (NBO) analysis is performed to evaluate charge delocalization and transfer between the iodine species and CTF adsorbents and gain insight into the intermolecular interactions that stabilize the complexes. All calculations were carried out

using the Gaussian16 software package [192]. The adsorption energy for each system was computed as follows:

$$E_{ads} = E_{Complex} - E_{Iodine\ species} - E_{Framework} \quad \text{Eq. 5-4}$$

where $E_{Complex}$, $E_{Iodine\ species}$, and $E_{Framework}$ are the energies of the optimized adsorption complex, iodine species, and CTF framework model, respectively.

5.5 Results and discussion

Figure 5.1 describes the synthesis procedure for the conjugated CTFs. These porous cross-linked polymers were prepared through the one-step and convenient $AlCl_3$-catalyzed Friedel-Crafts alkylation reaction in anhydrous DCM under nitrogen protection at 70 °C (see Figure 5.1). This reaction involves mild conditions without toxic and expensive catalysts and solvents, paving a low-cost and sustainable way to prepare novel CTFs. The obtained triazine-based polymers were insoluble and highly stable in common organic solvents, e.g., DCM, DMSO, DMF, THF, and acetone, due to the formation of rigid frameworks and the existence of highly stable triazine linkages in their structures.

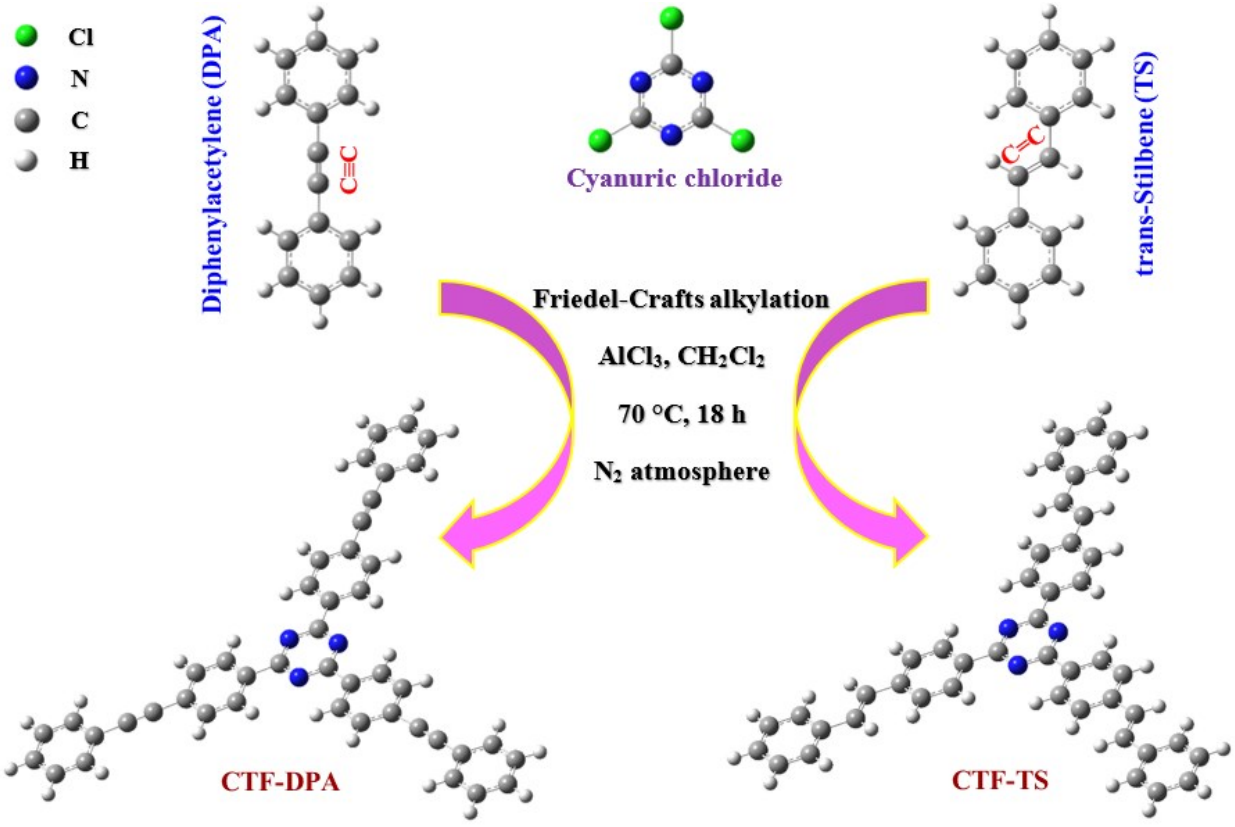

Figure 5.1. Schematic representation of the synthesis procedure for the conjugated CTFs through the $AlCl_3$-catalyzed Friedel-Crafts alkylation reaction.

5.5.1 Characterization of the prepared CTF samples

5.5.1.1 FT-IR spectroscopy of the precursors and prepared CTF samples

To further examine the structural properties and confirm the successful formation of the CTF samples, FT-IR spectroscopy was employed on the precursors and their corresponding CTFs (Figure 5.2-a). The characteristic spectral bands of triazine moieties in CTF-DPA are observed at 1351 cm^{-1} (1356 cm^{-1} for CTF-TS) and 1509 cm^{-1} (1515 cm^{-1} for CTF-TS) and are assigned to the C-N and in-plane triazine ring stretching vibration modes, respectively (see Figure 5.2-a and Figure S5.2) [109, 193]. In addition, the spectral peaks located at around 1495 and 1599 cm^{-1} (1606 cm^{-1} for CTF-TS) can be assigned to C=C stretching vibrations in the aromatic phenyl rings of the organic building units and their corresponding CTFs (see Figure 5.2-a and Figure S5.2) [194]. Besides, the weak peak at 2160 cm^{-1} in the spectrum of CTF-DPA is related to the stretching vibration of C≡C (see Figure 5.2-a) [94]. When compared with the spectrum of the cyanuric chloride reactant, the sharp peak at 848 cm^{-1} corresponding to the C-Cl stretching vibration is absent from the spectra of the CTF samples, demonstrating successful reaction between the backbone building blocks (i.e., trans-stilbene and diphenylacetylene) and $AlCl_3$-activated cyanuric chloride through the Friedel-Crafts alkylation (see Figure 5.2-a and Figure S5.3) [60]. The FT-IR spectra focusing on 700-900 cm^{-1} and 1300-1800 cm^{-1} wavenumber ranges are shown in Figure S5.2 & Figure S5.3.

5.5.1.2 PXRD patterns of the prepared CTF samples

As shown through the powder X-ray diffraction patterns (Figure 5.2-b), the broad peaks at approximately 23.10° and 20.05° 2Θ in the patterns of CTF-DPA and CTF-TS, respectively, suggest amorphous structures for the obtained CTFs. Such observation implies a low degree of structural order in the CTF frameworks, and indeed no reflection band of ordered structures was detected. The fast, irreversible, and random alkylation reaction might be the possible reason for obtaining amorphous CTFs synthesized through the Friedel-Crafts preparation method [60, 190]. Besides, no peak indicative of the presence of secondary solid phases such as unreacted precursors (e.g., unreacted DPA, TS, and cyanuric chloride) and unremoved $AlCl_3$ was observed (see Figure 5.2-b), demonstrating completion of the alkylation reaction and effectiveness of the purification/activation procedure.

5.5.1.3 N_2 adsorption-desorption isotherms on the prepared CTF samples

The textural properties and pore features of the CTF samples were studied utilizing nitrogen adsorption-desorption isotherms at 77.4 K and the N_2 relative vapor pressure (P/P_0) (i.e., N_2 pressure/N_2 saturation vapor pressure at 77.4 K) up to 1 (Figure 5.2-c & Figure 5.2-d). It ought to be noted that the samples were firstly degassed at 120 °C for 12 h under a dynamic vacuum (~−30 inHg) to make sure the pores were free and accessible to probe molecules (e.g., He and N_2). Figure 5.2-c indicates that the synthesized CTF samples feature a combination of the I and IV isotherm types, according to the International Union of Pure and Applied Chemistry (IUPAC) classification [195]. The adsorption isotherms of the CTF samples exhibit a sharp and rapid uptake at low relative pressures (i.e., P/P_0 up to 0.01), indicating the presence of micropores (i.e., pores smaller than 2 nm) in the structures [28]. In addition, the hysteresis loops in the high-pressure region (i.e., $P/P_0 >$ 0.1) implicate the presence of mesopores (i.e., pores with diameter between 2 and 50 nm) in the structures (see Figure 5.2-c) [14, 29]. The hysteresis loops in the isotherms can be attributed to the pore geometry of the porous amorphous pure organic polymers with soft pore walls and/or narrow slit-like pores [60]. In the meantime, the pore size distributions were obtained from N_2 adsorption branches utilizing the non-local density functional theory (NLDFT) (Figure 5.2-d). The obtained

data reveals that the average pore sizes in the structure of CTF-DPA and CTF-TS are 2.49 and 2.54 nm, respectively (see Table S5.1). As mentioned earlier, the results explicitly indicate the coexistence of micropores and mesopores in the CTF structures. Also, CTF-DPA and CTF-TS feature Brunauer-Emmett-Teller (BET) specific surface areas of 943 and 919 $m^2 g^{-1}$, respectively (for BET specific surface area plots, see Figure S5.4 & Figure S5.5). The detailed textural properties and pore features of the CTF samples are summarized in Table S5.1.

5.5.1.4 Thermal analysis of the precursors and prepared CTF samples

The thermal behavior and stability of the precursors and the obtained CTF samples are compared in Figure 5.2-e. The CTF materials do not show any conspicuous weight loss from 30 to 100 °C, indicating the excellent hydrophobicity of their pure organic structures. Despite all the precursors that totally decomposed at temperatures lower than 200 °C, CTF-DPA is highly stable up to about 280 °C with negligible weight loss (see Figure 5.2-e). However, slight weight loss is observed for CTF-TS at temperatures above 220 °C. This may be due to the loss of hydrogen atoms from the ethene bridges between the phenyl rings of CTF-TS, resulting in more weight loss at lower temperatures than CTF-DPA. Moreover, it may be inferred from Figure 5.2-e that at temperatures higher than 280 °C for CTF-DPA and 220 °C for CTF-TS, some pores collapse, and thus the structure of CTFs starts to decompose. Besides, the residual weights of the CTF-DPA and CTF-TS samples when heated up to 700 °C under N_2 atmosphere were about 63 and 59 wt.%, respectively (see Figure 5.2-e). Such exceptional thermal stability of the CTF samples can be attributed to their networks' highly stable triazine rings and rigid fused π-conjugated structures [196].

5.5.1.5 XPS and elemental analysis of the prepared CTF samples

Through XPS analyses (Figure 5.2-f), we could obtain the detailed surface chemical compositions and electronic states of the elements existing in the structure of CTFs. As indicated in the XPS survey spectra (see Figure 5.2-f), three prominent peaks corresponding to C1s, N1s, and O1s can be observed in both spectra, suggesting the successful introduction of triazine rings to the organic backbone units through the Friedel-Crafts alkylation (i.e., no peaks relevant to Cl1s possibly due to unreacted cyanuric chloride were observed). The O1s peak might be attributed to adsorbed CO_2 and/or oxygen [132]. High-resolution XPS C1s spectra of CTFs (Figure 5.2-g) exhibit two distinct peaks at 284.6 and 286.9 eV corresponding to C atoms from benzene (C=C) and triazine (C=N) rings, respectively [197]. In the N1s spectra (Figure 5.2-h), two peaks at 398.6 and 402.1 eV can be assigned to the N atoms of the triazine rings (i.e., N=C, pyridinic nitrogen) and oxygenated nitrogen species (N-O), respectively [198]. Besides, elemental analysis (EA) of CTF-DPA and CTF-TS showed that the C, H, and N contents were in good agreement with the theoretical values corresponding to the fully-condensed frameworks (Table S5.2).

5.5.1.6 TEM images of the prepared CTF samples

The morphology and microstructure of the synthesized amorphous conjugated CTFs were further investigated through TEM analysis. As shown in Figure 5.3 (a-d), CTF-DPA and CTF-TS samples exhibit homogeneous nanosheet-like morphologies (Figure 5.3-a and Figure 5.3-c), while the microstructures of the CTF samples correspond to the aggregation/assembly of a few nanosheets (Figure 5.3-b and Figure 5.3-d). Besides, the lack of long-range ordered parallel channels in the structure of CTFs is in excellent agreement with the obtained PXRD results (see Figure 5.2-b). TEM analysis of CTF samples thus confirms the absence of a crystalline region, possibly due to

the fast, irreversible, and random Friedel-Crafts alkylation reaction, which leads to the formation of amorphous structures.

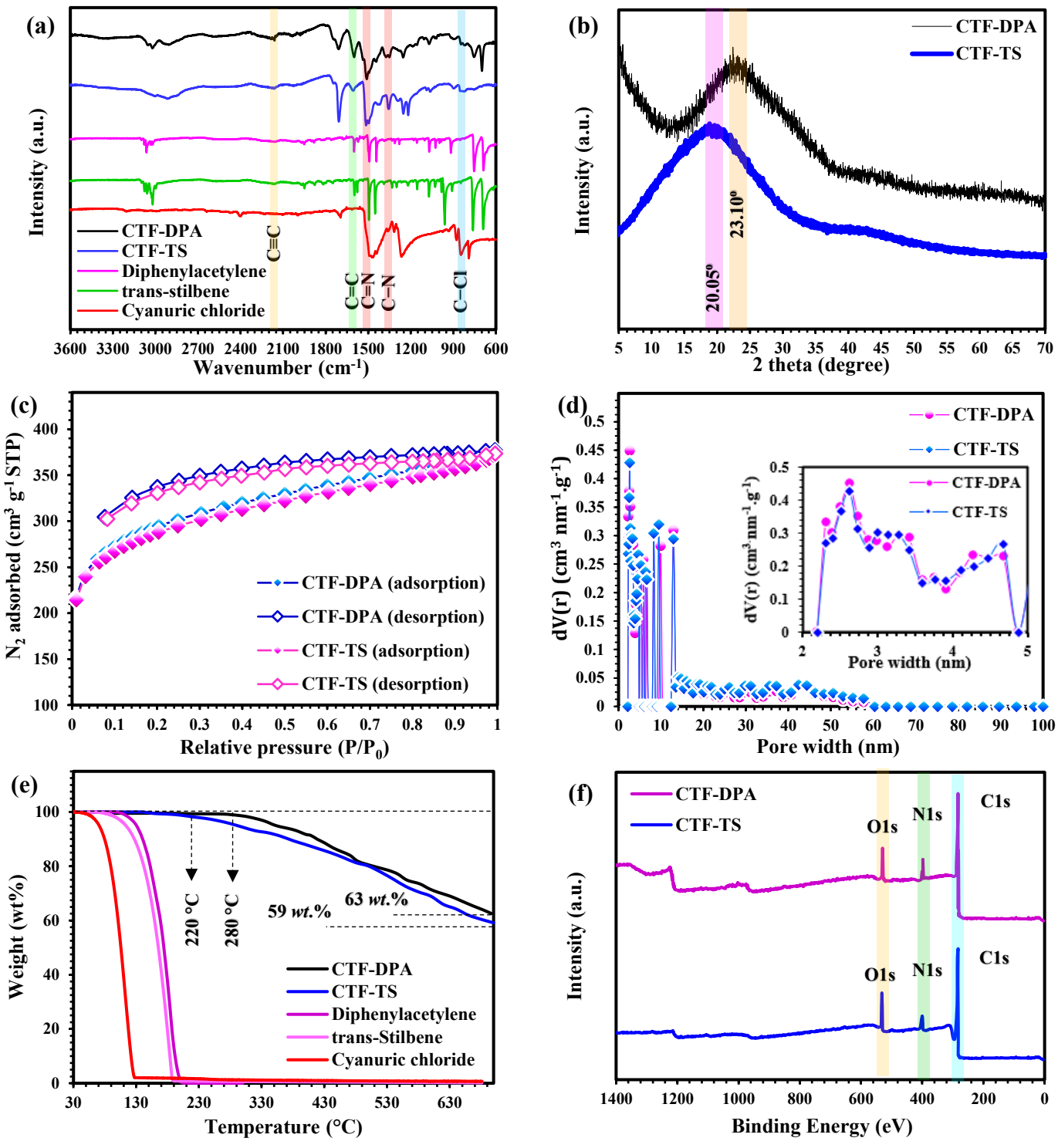

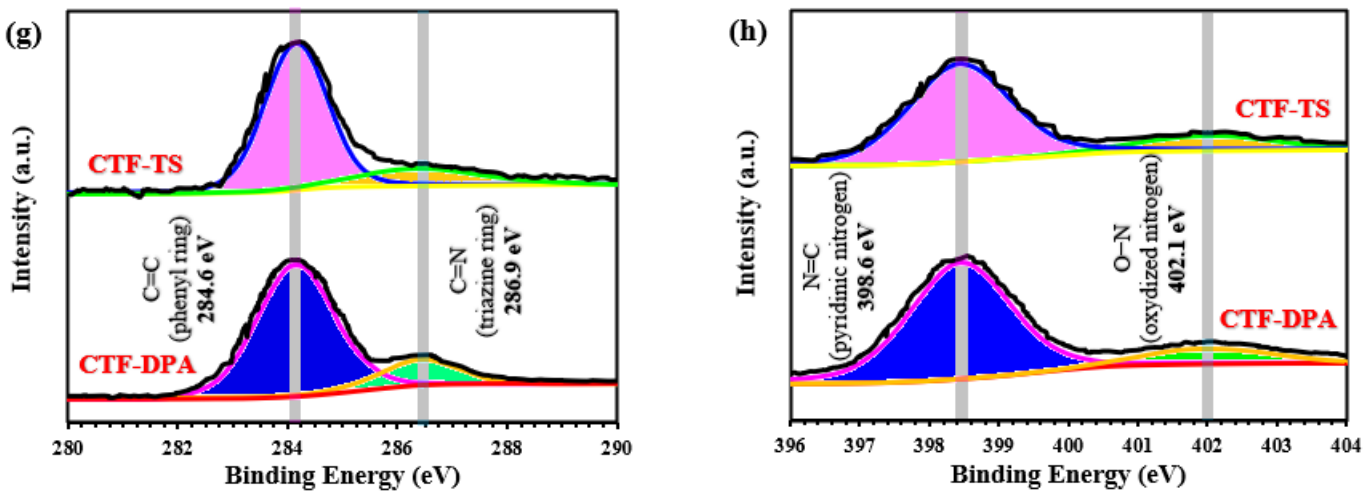

Figure 5.2. Characterization results for the precursors and conjugated CTFs synthesized in this project. (a) FT-IR spectra of the precursors and the synthesized CTFs. (b) X-ray diffraction patterns of the amorphous CTFs. (c) N_2 adsorption-desorption isotherms on the CTFs at 77.4 K up to 1 bar. (d) Pore size distribution plots of CTFs. (e) TGA plots of the precursors and the obtained CTFs. (f) XPS survey spectra of CTFs. (g) High-resolution C1s and (h) N1s XPS spectra for CTFs.

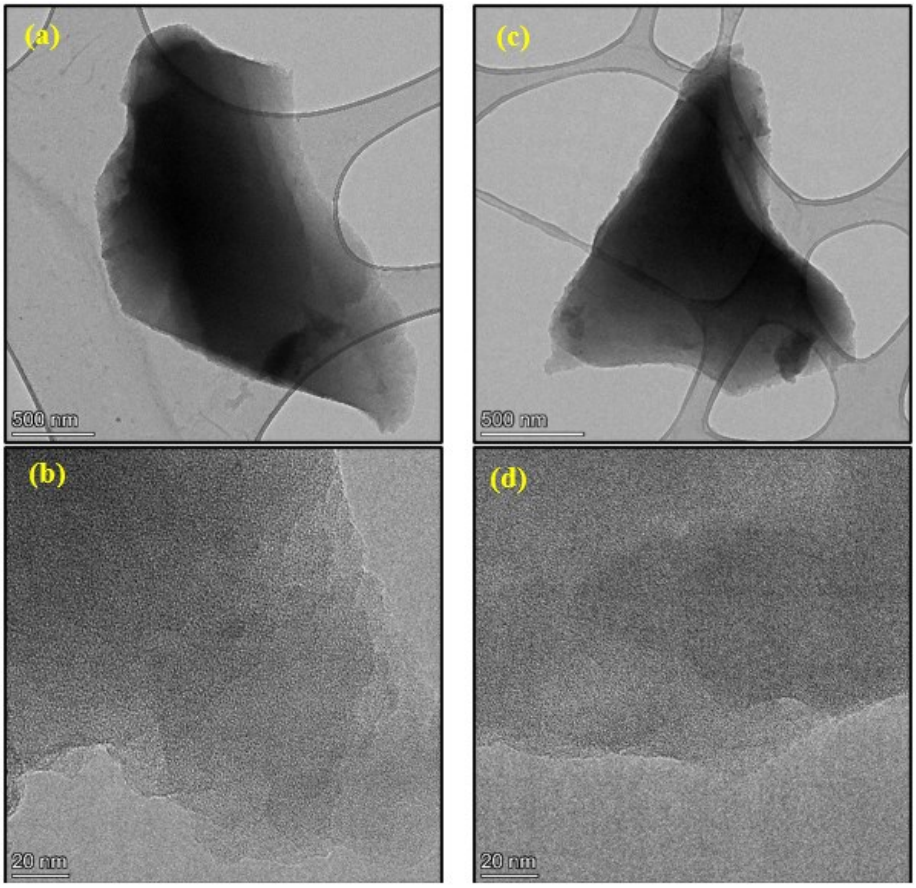

Figure 5.3. TEM images of conjugated CTFs.
(a, b) CTF-DPA and (c, d) CTF-TS.

5.5.2 Iodine vapor adsorption studies

To explore the iodine vapor-capturing performance of the synthesized CTFs, we performed gravimetric (Figure 5.4-a) and thermogravimetric (Figure S5.6) measurements. The gravimetric measurements were performed at different time intervals and showed that iodine adsorption by CTFs increased significantly during the first 2 h (see Figure 5.4-a), followed by a slower increase until the iodine adsorption systems reached equilibrium (see Figure 5.4-a). Also, no marked weight change was observed after 4 h contact time, implying that the surfaces of CTFs were essentially saturated with iodine species. The observed high iodine vapor adsorption by the CTFs can be attributed to the abundance of accessible micro-and mesopores in their frameworks and their high specific surface areas featuring high-affinity adsorption sites suitable for trapping iodine species.

Quantitatively, iodine adsorption capacities were calculated to be 5.12 and 3.75 g g^{-1} for CTF-DPA and CFT-TS, respectively. Further, the quantities of sublimed iodine from the iodine-loaded CTFs determined by thermogravimetric measurements (Figure S5.6) are in good agreement with the gravimetric measurements (Figure 5.4-a). To the best of our knowledge, the iodine uptake capacity of CTF-DPA (5.12 g g^{-1}) is one of the highest values reported for POPs in the open literature; a detailed comparison is presented in Table S5.3, where the iodine adsorption capacity of CTF-DPA is seen to exceed that of most of the previously reported porous adsorbents [136, 199-206]. CTF-DPA saturated with iodine could preserve its weight (91 wt.% after 24 h) upon exposure to air at room temperature and atmospheric pressure. This further demonstrates that most iodine species managed to penetrate the porous framework and are strongly adsorbed on CTF-DPA surfaces, which feature high-affinity adsorption centers.

Figure 5.4-b, which collects the results of the recyclability of CTF-DPA and CTF-TS in the iodine vapor adsorption process, shows that after five consecutive cycles, the iodine vapor adsorption capacities of CTF-DPA and CTF-TS samples remain at 91.9 and 89.8% of their initial iodine uptake capacities, respectively (Figure 5.4-b). These high values make the CTF adsorbents promising candidates as recyclable iodine vapor-capturing sorbents. The layered structure of CTF-DPA and the uniform and dense distribution of iodine throughout the surfaces of CTF-DPA can be observed from the SEM and EDX elemental mapping images (Figure 5.4-c). Figure 5.4-d shows that in addition to the peaks corresponding to CTF-DPA carbon and nitrogen elements, strong iodine peaks are also observed in the EDX results of the iodine-loaded CTF-DPA sample. It ought to be noted that the peaks corresponding to copper (Cu) in the EDX profile (Figure 5.4-d) are due to the copper support grids. These results further confirm the excellent performance of CTF-DPA in capturing iodine vapor. During iodine adsorption upon internal and external surfaces of CTFs, the color of the adsorbent gradually changed from brown to black (see Figure 5.4-e). This color change is typically observed in the charge transfer interacting complexes.

Overall, such remarkable iodine vapor-capturing performance of CTF-DPA can be attributed to (i) its high specific surface area (943 m^2 g^{-1}), providing iodine species with a large contact area, (ii) the high nitrogen content of the framework, leading to enhanced interactions between iodine molecules and the framework (i.e., heteroatom effect), and (iii) the abundance of π electrons (as a result of the coexistence of electron-rich C≡C triple bond, triazine, and phenyl moieties, see Figure 5.1), resulting in noticeable stabilizing charge transfer between the framework and iodine species. The latter results in favorable electrostatic interactions between adsorbates and adsorbents, leading to the generation of charged (poly)iodide species (e.g., I^- and I_3^-), and thus an increase in the

adsorption affinity/capacity. In addition, nitrogen atoms with lone-pair electrons (i.e., the pyridinic nitrogen atoms of the triazine ring, see Figure 5.2-h) can act as a Lewis base, amplifying the framework's affinity towards the iodine molecule (as a Lewis acid) and propensity to form a stable state according to Lewis acid-base theory [207, 208]. Interaction between the lone-pair orbitals (n, i.e., LP as defined in Section 5.4.5) of the nitrogen atoms of the triazine rings and the antibonding I_2 molecular-orbital (σ^*, i.e., BD* as defined in Section 5.4.5) also has a stabilizing effect on the iodine-CTF systems [137, 209, 210].

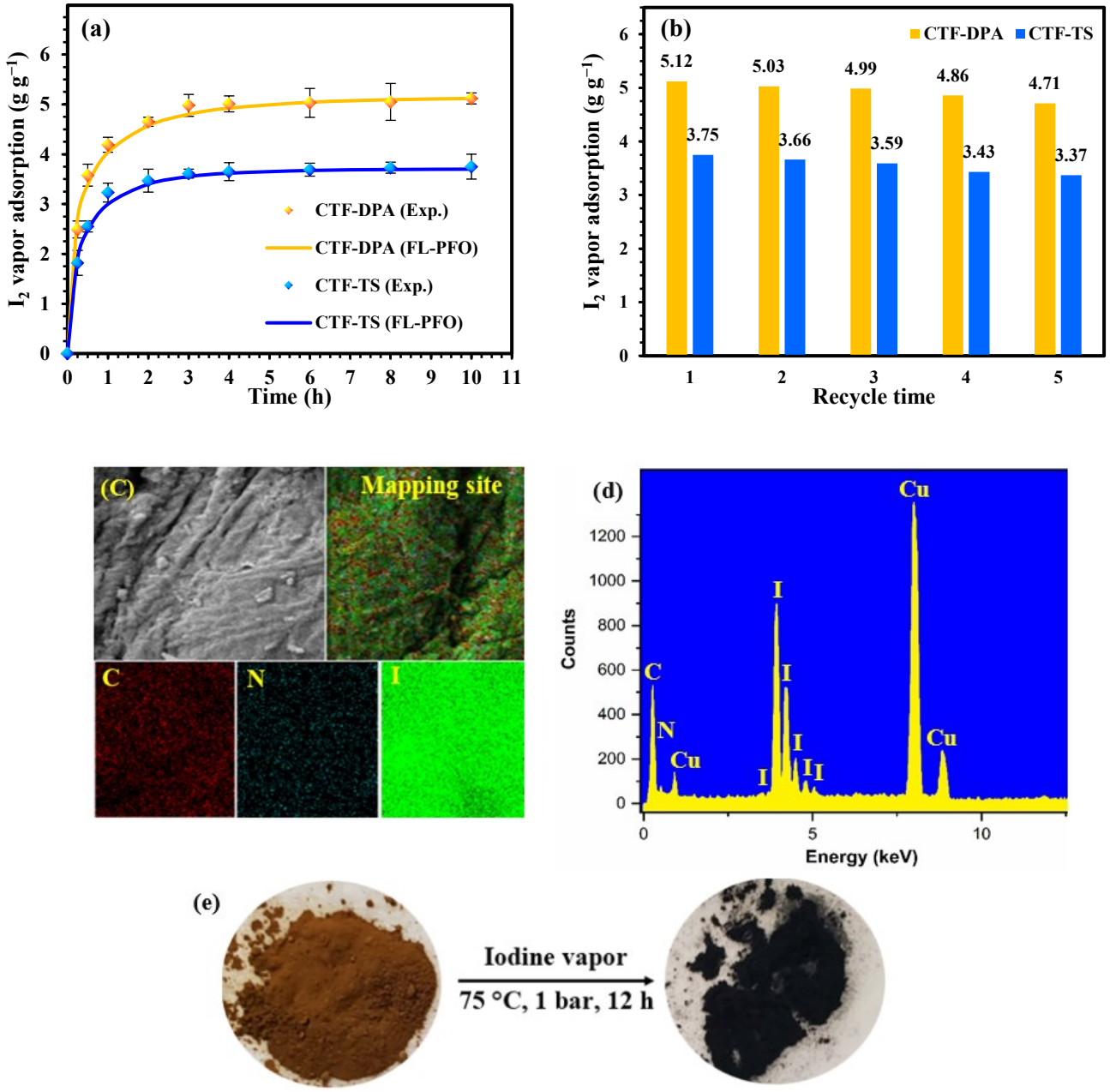

Figure 5.4. Iodine vapor adsorption studies.
(a) Gravimetric measurements of the iodine vapor adsorption capacities of the CTFs derived in this work as a function of time at 75 °C and 1 bar (Error bars represent the standard deviation from the average value

of two independent experiments). (b) Recyclability of the synthesized CTFs for iodine vapor adsorption. (c) SEM and EDX elemental mapping images of the iodine-loaded CTF-DPA. (d) EDX profile of CTF-DPA exposed to iodine vapor. (e) Photographs of CTF-DPA before and after iodine vapor adsorption.

5.5.3 Iodine adsorption from n-hexane solution

The adsorption performance of the synthesized CTFs in iodine/n-hexane solution was explored by monitoring the changes in the absorption intensity at the wavelength of 522 nm in the corresponding UV-Vis spectra (Figure 5.5-a and Figure S5.7). Upon iodine adsorption from n-hexane, the color of the solution changed from purple to pink (Figure 5.5-b). The isotherms for iodine adsorption on CTF samples are shown in Figure 5.5-c. As anticipated, CTF-DPA offers superior iodine adsorption performance in n-hexane solution at room temperature (667 mg g^{-1}) when compared with CTF-TS (518 mg g^{-1}) and literature reports (for a detailed comparison, see Table S5.4) [211-217]. Our results further support the fact that the iodine-capturing performance of a given adsorbent is a function of not only its textural properties (e.g., specific surface area and pore volume) but also the nature and number of high-affinity adsorption sites in its structure. Hence, it is reasonable to consider the synergistic effects of the coexistence of high-affinity adsorption sites (i.e., the conjugated C≡C triple bond, triazine, and phenyl moieties), accessible pores, and high specific surface area, which, in turn, enhance the adsorption of iodine upon the surfaces of CTF-DPA. After regenerating the CTF adsorbents using the method described in Section 5.3.4, the reversibility of iodine adsorption from the n-hexane solution on CTFs was also investigated (Figure 5.5-d). The CTF samples showed high recyclability at a relatively stable value after five consecutive regeneration cycles, with a slight decrease in iodine adsorption capacity (adsorption capacity retention of 87.6% for CTF-DPA and 83.9% for CTF-TS, see Figure 5.5-d).

The adsorption kinetics are important for new sorbents when addressing environmental problems. To gain better insight into the kinetics of iodine adsorption on the CTFs synthesized in this work, the fractal-like pseudo-first-order (FL-PFO) kinetic model [21] was fitted to the experimental data for vapor as well as liquid phases (see Figure 5.4-a and Figure 5.5-a). The optimized parameters of this kinetic model are presented in Table S5.5, where it is seen that the adsorption rates in the liquid phase are lower than those in the gas phase (see Table S5.4). This might be due to the higher diffusion coefficient in the gas phase at a higher temperature (i.e., 75 °C in the gas phase vs. room temperature in the liquid phase) relative to that in the liquid phase. Besides, the obtained iodine adsorption capacities from n-hexane are lower than those for iodine vapor uptake (i.e., 667 and 518 mg g^{-1} in the liquid phase vs. 5120 and 3750 mg g^{-1} in the gas phase for CTF-DPA and CTF-TS, respectively), which could be attributed to solvent encapsulation effects [218].

The influence of n-hexane on the iodine adsorption process can vary depending on the specific adsorbent material and the conditions of the adsorption system. N-hexane is a nonpolar hydrocarbon solvent commonly used in various chemical processes, and its impact on iodine adsorption is primarily related to its solvency properties and competitive adsorption effects.

Solubility and Competitive Adsorption: n-hexane is a nonpolar solvent, and iodine is a nonpolar molecule in its elemental form (I_2). As a result, n-hexane can effectively dissolve iodine, forming iodine-hexane complexes in solution. This solubility can reduce the concentration of free iodine molecules available for adsorption onto the adsorbent material. In essence, n-hexane competes with the adsorbent for iodine molecules, potentially decreasing the overall adsorption capacity for iodine.

Solvent Effects: n-hexane can alter the chemical environment and interactions within the iodine adsorption system. It can affect the kinetics and thermodynamics of iodine adsorption on the adsorbent surface. The solvent's impact on the adsorption rate and the equilibrium adsorption capacity depends on factors such as the adsorbent's pore structure, the nature of the iodine species, and the strength of iodine-solvent interactions.

Selectivity: The selectivity of the adsorbent material for iodine versus n-hexane is a critical consideration. If the adsorbent exhibits a higher affinity for iodine than n-hexane, it may still preferentially adsorb iodine despite the presence of the solvent. Conversely, if n-hexane has a higher affinity for the adsorbent, it may displace iodine from the adsorption sites.

System Specificity: The specific effects of n-hexane on iodine adsorption vary depending on the adsorption system's characteristics. Researchers must consider factors such as the choice of adsorbent, solvent concentration, temperature, and pressure to fully understand how n-hexane impacts iodine adsorption in a given context.

Hence, the impact of n-hexane on iodine adsorption processes is multifaceted and depends on the interplay of solubility, competitive adsorption, solvent effects, and selectivity. The degree of influence varies based on the specific adsorbent material and the conditions of the adsorption system.

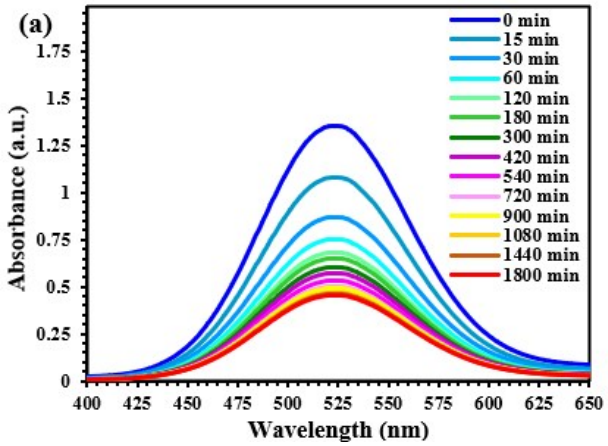

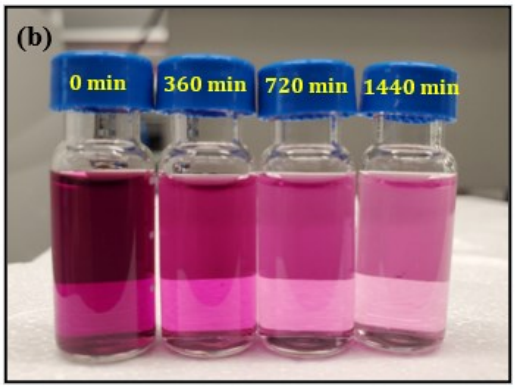

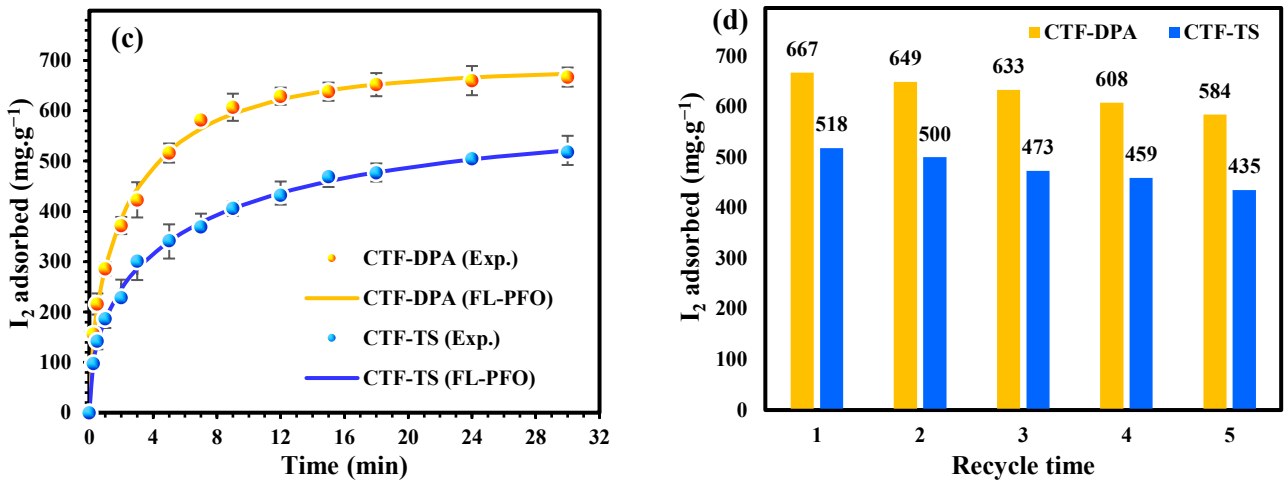

Figure 5.5. Iodine adsorption from n-hexane solution studies.
(a) Time-dependent UV-Vis spectra of CTF-DPA in iodine/n-hexane solution. (b) Photographs of the supernatants sampled from the iodine/n-hexane solution/CTF-DPA at different contact times. (c) Iodine adsorption from n-hexane solution isotherms on the CTFs (Error bars represent the standard deviation from the average value of two independent experiments). (d) Recyclability of the obtained CTFs for the iodine adsorption from n-hexane solution.

A detailed calculation and explanation of mass transfer and diffusion mechanism is provided in the Appendix.

5.5.4 Experimental investigation of the iodine adsorption mechanism

We also employed PXRD, N_2 adsorption-desorption isotherms (BET specific surface area measurements), FT-IR, XPS, and Raman spectroscopy techniques to examine the textural and structural properties of the iodine-loaded CTFs and the existing form of iodine adsorbed by the CTF adsorbents. The XRD analyses of the iodine-loaded CTFs reveal that the CTF adsorbents maintain their amorphous structure without any conspicuous crystalline diffraction peaks (see Figure S5.8), an observation that suggests the presence of (poly)iodide species and molecular iodine confined within the porous frameworks (no peaks corresponding to the crystalline form of iodine are observed in the PXRD patterns of the iodine-loaded CTFs). The N_2 adsorption-desorption isotherms for the iodine-loaded CTFs unveil a dramatic decrease in the specific surface area and pore volume of the CTF adsorbents upon capturing iodine (see Figure S5.9). Accordingly, the iodine-loaded CTF-TS showed a considerably lowered specific surface area (154 vs. 919 m^2 g^{-1}) and pore volume (0.153 vs. 0.579 cm^3 g^{-1}), while the iodine-loaded CTF-DPA exhibited a higher extent of reduction in its specific surface area (61 vs. 943 m^2 g^{-1}) and pore volume (0.074 vs. 0.584 cm^3 g^{-1}) in comparison with their pristine counterparts. These observations demonstrate the higher pore efficiency in the porous structure of CTF-DPA (with C≡C triple bond) in capturing iodine species compared to CTF-TS (with C=C double bond). The FT-IR spectra of CTF-DPA and CTF-TS before and after iodine uptake are compared in Figure S5.10. Accordingly, no new spectral band was observed compared to the spectra of the pristine materials, suggesting that no strong chemical bond is formed between the skeleton of CTF adsorbents and iodine species. Therefore, the iodine uptake process is essentially physical in nature [81]. Meanwhile, a comparison of the FT-IR spectra of pristine adsorbents (CTF-DPA and CTF-TS) and those of their iodine-loaded counterparts (I_2@CTF-DPA and I_2@CTF-TS) reveals that the peaks corresponding to the skeletal vibration of conjugated moieties (i.e., C=C double bond, C≡C triple bond, triazine,

and phenyl rings) are slightly shifted upon iodine uptake, which may be due to the electrostatic interactions arising from charge transfer (see Figure S5.10) [209]. For instance, in the case of CTF-DPA, the bands around 1351 (triazine), 1495 (phenyl), 1509 (triazine), 1599 (phenyl), and 2160 cm^{-1} (C≡C triple bond) shift to 1363, 1521, 1530, 1613, and 2169 cm^{-1}, respectively, upon iodine uptake. A similar trend is observed for iodine-loaded CTF-TS (see Figure S5.10).

The nature of the iodine species inside the pores of CTFs was further investigated by Raman spectroscopy (Figure 5.6-a). Interestingly, the spectra of iodine-loaded CTFs exhibit three distinct bands. The symmetric and asymmetric stretching vibrations of I_3^- (poly)iodide anions were detected at 111 and 144 cm^{-1}, respectively [140]. Meanwhile, the band located at 180 cm^{-1} can be ascribed to the iodine molecules (I_2) physically adsorbed on the adsorption sites of CTFs [219]. As seen in Figure 5.6-a, the percentage of I_3^- (poly)iodide species in the iodine-loaded CTF-DPA (77% in total) is much higher than in the iodine-loaded CTF-TS sample (24% total). In the meantime, most iodine trapped by CTF-TS is molecular iodine (i.e., I_2, 76%). CTF-DPA consisting of conductive DPA building blocks may thus have a higher tendency to share a negative charge with the adsorbed iodine molecules (I_2), stabilizing most of them as I_3^- (poly)iodide anion species [220]. Similar findings are obtained from XPS spectra (Figure 5.6-b). As shown in Figure 5.6-b, two types of characteristic bands assigned to molecular iodine (I_2, 620.1 and 631.7 eV) and I_3^- (poly)iodide anion species (618.6 and 630.2 eV) are observed in the XPS spectra of CTFs. We speculate that some of the adsorbed molecular iodine (I_2) sublimed under high vacuum conditions during XPS analysis, resulting in a larger I_3^-/I_2 ratio than that inferred from the Raman spectra [140].

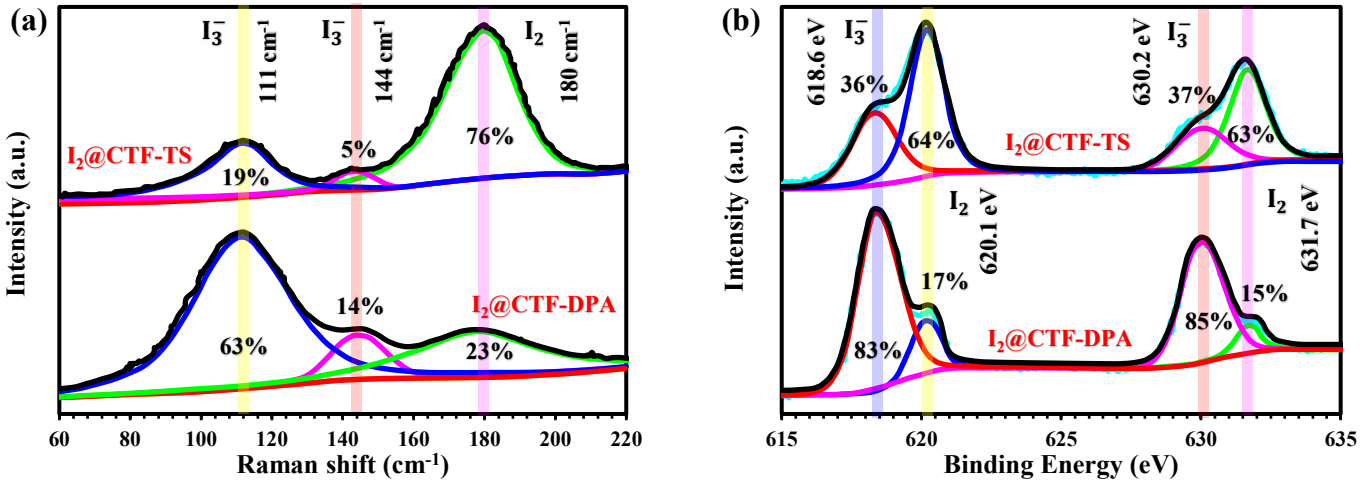

Figure 5.6. (a) Raman and (b) XPS spectra of the iodine-loaded conjugated CTFs.

5.5.5 Computational investigation of the iodine adsorption mechanism

To further unveil details of the intermolecular interactions between iodine species and the adsorption sites of the CTF adsorbents, DFT calculations were performed to obtain molecular geometries and adsorption energies for iodine on CTF building blocks. Figure 5.7 displays the resulting CTF building blocks, iodine complex geometries, and relevant partial atomic charges and interaction energies information. Moreover, the most significant donor-acceptor interactions obtained from NBO analysis, highest occupied molecular orbitals (HOMO), and lowest

unoccupied molecular orbitals (LUMO) are presented in Table 5.1 and Table S5.6. The HOMO is the outermost electron-containing orbital that tends to give/share electrons, acting as an electron donor, while the LUMO is the innermost orbital that can accommodate electrons and thus acts as an electron acceptor [221]. The red and green colors represent the positive and negative signs of the molecular orbital wave function, respectively. The molecular orbital population analysis shows localization of the HOMO electron density on the C=C double bond, C≡C triple bond, phenyl rings, and triazine ring (see Table 5.1), thus suggesting enhancement of reactivity by the electrophilic attack of iodine molecules onto these electron-donating conjugated moieties. The calculated interaction energies in I_2@DPA and I_2@TS are −0.23 eV and −0.25 eV, respectively. These values indicate that both CTFs can adsorb iodine in its molecular form, consistent with the obtained XPS and Raman results (see Figure 5.6-a and Figure 5.6-b).

Meanwhile, DFT calculations further predict that I^- species can adsorb readily upon the organic building blocks of CTF-DPA and CTF-TS (i.e., negative values for the calculated interaction energies, Figure 5.7). However, the adsorption of I^- upon TS is much more favorable (i.e., more negative or higher magnitude interaction energies) than that upon DPA (i.e., −0.26 eV vs. −0.15 eV, see Figure 5.7). As a result, I^- species in the more stable I^-@TS adsorption complex shows a lower propensity for the formation of I_3^- species upon adsorption of an additional I_2 molecule (i.e., less negative interaction energy, see Figure 5.7).

As seen from Table S5.6, the I^- species adsorbed upon the C≡C adsorption site of CTF-DPA can interact easily with an additional iodine molecule by transferring charge from its lone-pair (LP) electrons to the antibonding (BD*) orbital of the newly adsorbed I_2 molecule, forming the stable I_3^-@DPA adsorption complex (interaction energy of −0.18 eV, see Figure 5.7) [222]. Hence, both the C=C double and C≡C triple bonds show high affinity towards the iodine molecule (I_2), with the latter exhibiting a higher tendency to form I_3^- (poly)iodide species (see Figure 5.7). Iodine molecules adsorbed upon C≡C could form outer charge-transfer (i.e., electron-donor-acceptor) complexes via partial charge transfer between the C≡C triple bond and I_2 molecule, which would, in turn, be capable of adsorbing additional iodine molecules (i.e., through the acid-base interactions) and form (poly)iodide species such as I_3^-. These results align with the obtained XPS and Raman results (see Figure 5.6-a and Figure 5.6-b).

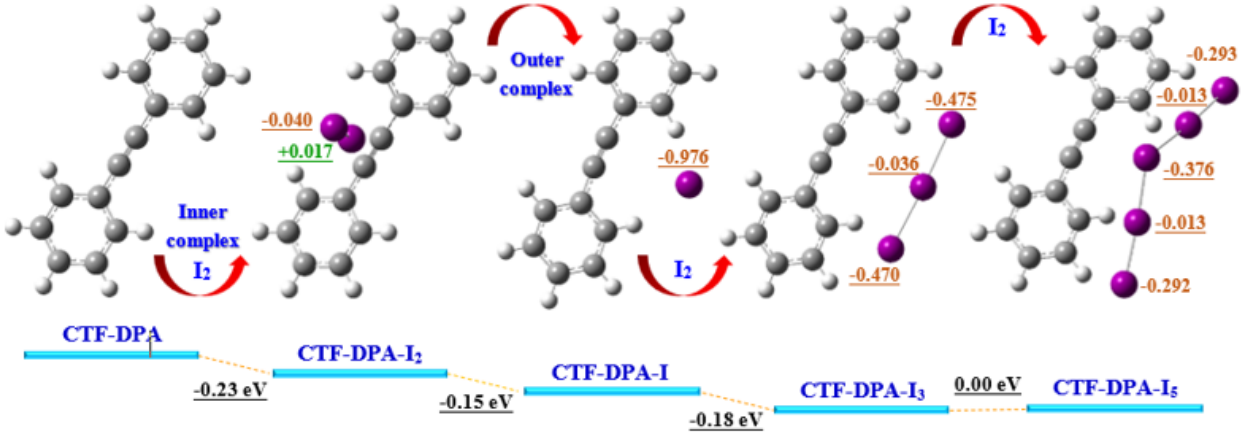

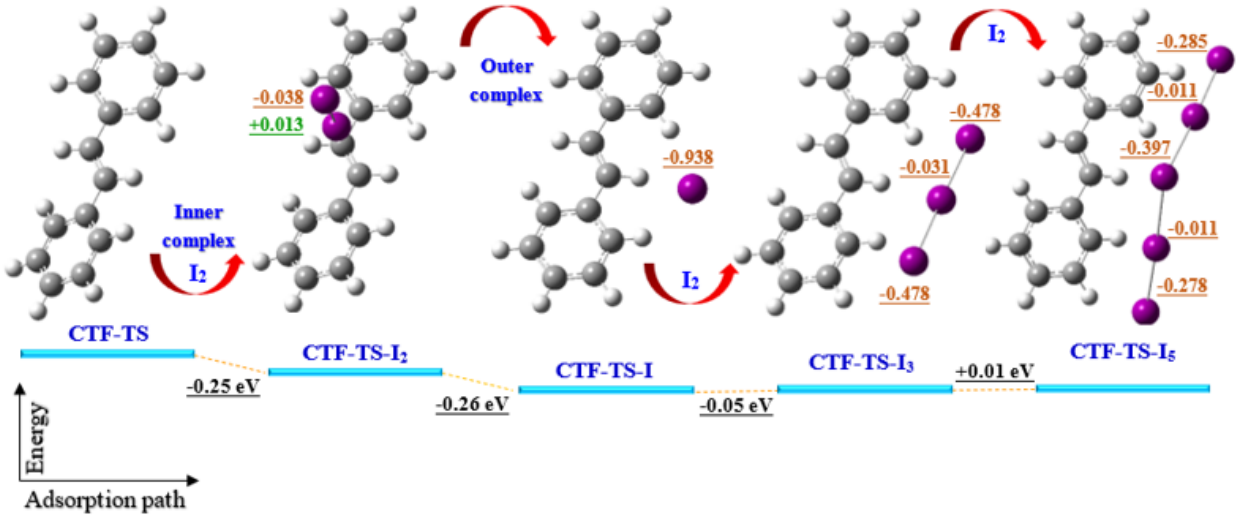

Figure 5.7. Molecular geometries of DPA and TS building blocks and their complexes with iodine species in the gas phase calculated with ωB97XD/6-311+G**/def2-TZVPD.

In the meantime, other conjugated parts of the frameworks, such as triazine and phenyl rings, play a significant role in charge transfer to the iodine molecules and thus promote the formation of (poly)iodide species. To demonstrate this, we also performed DFT calculations on a triphenyl-triazine (TPhTAz) CTF model consisting of a triazine ring connecting three phenyl rings (see Figure 5.8). As expected, some charge is transferred from TPhTAz to the iodine molecule (−0.033 e), facilitating the formation of the outer charge-transfer complex and the evolution of the charged (poly)iodine species. The majority of this charge transfer occurs from the lone-pair (LP) electrons of the N atoms as well as the bonding orbitals (σ, i.e., BD) of the conjugated moieties of the frameworks to the antibonding (BD*) orbital of the iodine molecule (as inferred from the corresponding donor-acceptor orbital interaction energies in Table 5.1).

Meanwhile, the CTF materials synthesized in this research, i.e., CTF-DPA, CTF-TS, exhibit an amorphous phase (i.e., according to their corresponding XRD and TEM characterization results), signifying that their structural arrangement lacks the well-defined structural characteristic of crystalline materials with long-range parallel channels or pores. Consequently, there is a significant probability of π interactions between the conjugated components of CTF materials, encompassing phenyl rings, triazine rings, double bonds, and triple bonds, with adsorbate species. In other words, these π-conjugated components are not arranged and thus confined in a stacked fashion, as observed in highly crystalline materials where layers are organized through π–π interactions. Thus, these conjugated moieties would be accessible to efficiently interact with the adsorbate species. Therefore, the CTF models examined in this dissertation closely mimic the actual adsorption sites found in CTF materials.

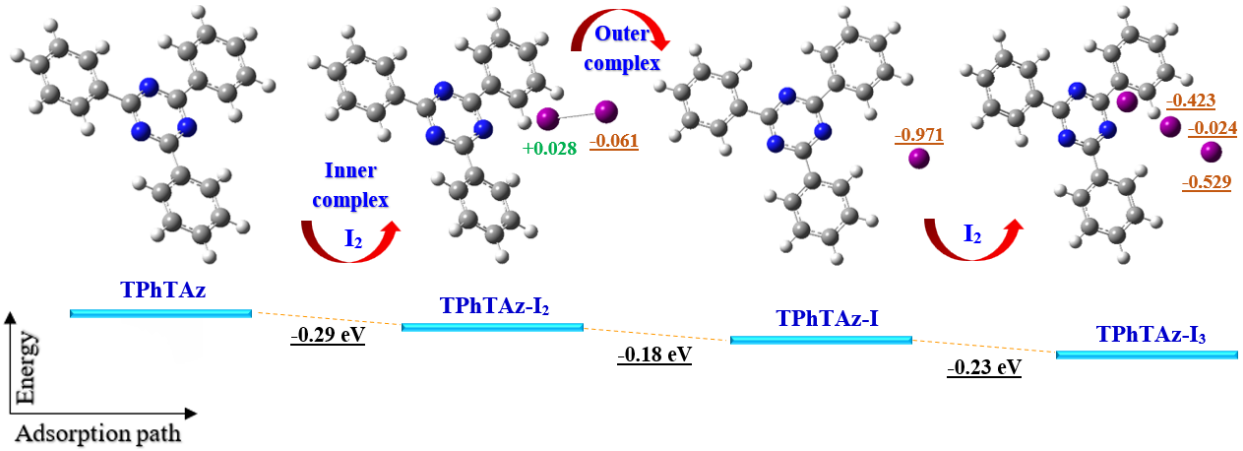

Figure 5.8. Molecular geometries of the conjugated TPhTAz trimer cut of CTFs and its complexes with iodine species in the gas phase calculated with ωB97XD/6-311+G**/def2-TZVPD.

Donor NBOs can serve as adsorption sites in certain adsorption processes, particularly when the NBOs possess chemical properties conducive to interactions with adsorbate species. NBOs represent localized electron density associated with specific atoms or groups within a molecule. Hence, according to Figures 5.7 and 5.8, donor NBOs of CTF materials, including bonding orbitals of π-conjugated moieties such as C=C double bond, C≡C triple bond, C=N double bond, and lone-pair electrons of the N atoms in triazine rings can act as adsorption sites interacting with adsorbate species (e.g., iodine molecules) through charge transfer interactions (i.e., acid-base interactions).

Table 5.1. Selected NBO population analysis results for CTF-iodine complexes [a].

Adsorption system	Donor NBO	Acceptor NBO	E(2) (eV)	HOMO	LUMO
DPA-I_2	BD (C−C)	BD* (I−I)	0.003	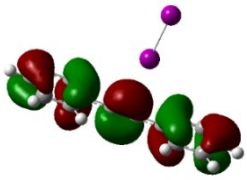	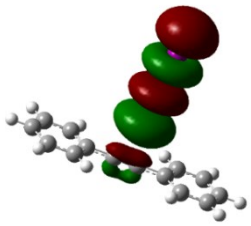
	BD (C−C)	BD* (I−I)	0.003		
	BD (C−C)	BD* (I−I)	0.007		
	BD (C≡C)	BD* (I−I)	0.251		
TS-I_2	BD (C−C)	BD* (I−I)	0.003	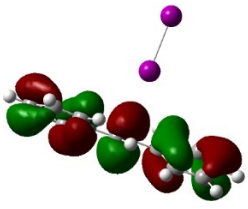	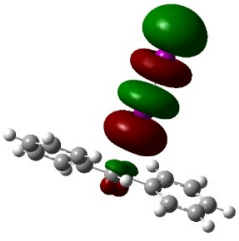
	BD (C=C)	BD* (I−I)	0.252		
	BD (C−H)	BD* (I−I)	0.005		
	BD (C−H)	BD* (I−I)	0.005		
TPhTAz-I_2	BD (C−N)	BD* (I−I)	0.004		
	BD (C=N)	BD* (I−I)	0.083		
	BD (C=C)	BD* (I−I)	0.083		

LP (N)	BD* (I–I)	0.247		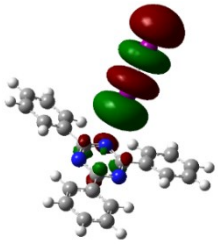

[a]. E(2) is the orbital interaction donor-acceptor second-order perturbation energy. Calculated with ωB97XD/6-311+G**/def2-TZVPD. LP, BD, and BD* refer to lone-pair, bonding, and antibonding orbitals, respectively.

5.6 Conclusion

In summary, novel conjugated CTFs were designed and synthesized through one-step and convenient Friedel-Crafts alkylation using cyanuric chloride as the cross-linking agent and DPA as well as TS as backbone building units. The structure of each polymer possesses abundant π-conjugated moieties essential for efficient iodine−π interactions. Moreover, large quantities of heteroatoms (N) were deliberately embedded within the frameworks in triazine moieties to enhance the iodine adsorption capacity through Lewis acid-base interactions. Compared to the CTF-TS adsorbent, CTF-DPA exhibits a higher affinity towards iodine species. After washing with ethanol and heat treatment under a dynamic vacuum, CTFs can still preserve their remarkable iodine adsorption capacities. The C≡C triple bond, conjugated triazine, and phenyl moieties are able to share π-electrons with the adsorbed molecular iodine, promoting the evolution of charged (poly)iodide species. That is, charge transfer from the frameworks to the iodine molecule affects its electronic structure and promotes the formation of (poly)iodide species to achieve a high iodine adsorption capacity. The C≡C triple bond is found to be even more effective in adsorbing and stabilizing the (poly)iodide species than the C=C double bond, making CTF-DPA a more efficient platform for capturing iodine. These results are paramount for efficiently designing optimum CTF adsorbents for treating toxic vapors and contaminated organic solutions.

6 Chapter 6: Removal of heavy metal cations (Cd^{2+}, Hg^{2+}, and Pb^{2+}) from water using functionalized covalent triazine frameworks: Computational design and experimental validation

6.1 Abstract

The search for efficient adsorbents for capturing harmful heavy metal cations is a timely and crucial topic for environmental remediation. Nanoporous adsorbents are a target of choice for this purpose, especially owing to the possibility of further functionalizing them to optimize their adsorption performance. In that respect, the molecular-level understanding of host-guest interactions that such materials may implicate is key to the rational design of functionalized nanoporous adsorbents. Covalent triazine frameworks (CTFs) with high chemical/thermal stability, particularly under severe conditions, and their fascinating textural and structural properties, such as high specific surface area, considerable pore volume, and designability, are suitable adsorbents. This work investigates the adsorption performance of pristine (i.e., unfunctionalized) and functionalized CTFs toward eliminating Cd^{2+}, Hg^{2+}, and Pb^{2+} cations from water by combining computational and experimental means. Density-functional theory (DFT) calculations at the ωB97XD level predict complexation energies of the cations on model CTF fragments in the order of $E_{Pb^{2+}@CTF} > E_{Hg^{2+}@CTF} > E_{Cd^{2+}@CTF}$. After careful computational screening, the carboxylic (COOH)-functionalized CTF (COOH-CTF) is selected as an optimal adsorbent. COOH-CTF is synthesized via the ($ZnCl_2$)-catalyzed ionothermal cyclotrimerization of cyano functionalities of the 2,5-dicyanobenzoic acid monomer, and further characterized by XRD, FT-IR, BET, and XPS techniques. The prepared COOH-CTF adsorbent exhibits medium to high adsorption capacities for the heavy metal cations investigated in this work, highlighting the role of rational computational design of modern materials for environmental remediation.

6.2 Introduction

In the 21st century, anthropogenic activities such as mining operations, alkaline batteries, textile printing, steelmaking, fertilizers, metallurgy, and paper industries have extensively released heavy metal (HM) species (e.g., Cd^{2+}, Hg^{2+}, and Pb^{2+}) into water resources, resulting in severe environmental pollution [223]. One definition of HMs includes elements with atomic masses between 63.5 and 200.6 a.u. and a density of more than 5 g cm^{-3} [224]. The imposed severe hazards to humankind and the environment arise from the HMs' non-biodegradability and high biotoxicity, even at very low concentrations [225]. Hence, worldwide attention and concern about eliminating HM micropollutants from water/wastewater have increased.

Several remediation techniques for HMs from the aqueous phase have been proposed, including adsorption, flotation, electrocoagulation, chemical precipitation, membrane separation, and ion exchange [226]. Among these remediation techniques, adsorption is considered a promising strategy for removing HMs from water, relying on the benefits of high removal efficiency, recyclability of adsorbent, and low-cost operation [227]. In this respect, various adsorbents have been utilized to remove HMs from contaminated water bodies, including metal-oxides (MOs) [228], activated carbons (ACs) [229], covalent organic frameworks (COFs) [230], metal-organic frameworks (MOFs) [231], minerals [232], agricultural wastes [233], graphene oxide (GO) [234], biosorbents [235], and conjugated microporous polymers (CMPs) [236]. However, some adsorbents show low adsorption capacity besides their high cost. Thus, exploring efficient and inexpensive adsorbents for removing biotoxic HM species from polluted waters is crucial. One

practical solution is to design an optimum and task-specific adsorbent. There are various material design tools and strategies of which density-functional theory (DFT) calculations stand out [237].

First-principles calculations, particularly DFT calculations, have become progressively significant in both the development and discovery of novel materials and the modification/investigation of existing materials [238]. From the material design point of view, DFT and other computational methods offer important theoretical predictions and guidance. First-principles studies can be performed before experimental investigations to find the optimal synthetic conditions/methods and starting materials to obtain difficult and expensive materials to synthesize. Meanwhile, DFT calculations provide significant information for better insights into case studies when interpreting the experimental results. DFT calculations are key for adsorption processes to help reveal the role of different adsorption sites and discover the effect of element doping and functionalization of the structure [239].

DFT calculations are powerful tools for studying the interactions between various components in adsorption systems (i.e., adsorbent-adsorbate and adsorbate-adsorbate interactions). DFT simulations may be employed to determine, in particular, the adsorption energy between adsorbate and functional building blocks, and from a wide range of organic compounds, the optimal/more suitable functional monomers can be selected as the adsorbent's building blocks. In most cases, the larger absolute values of adsorption energy calculated through DFT will result in higher adsorption capability and, thus, the adsorption capacity of a given adsorbent [240].

An emerging subclass of porous organic polymers (POPs), CTFs comprise properly assembled organic building blocks with well-defined pores [210]. Since Kuhn et al.'s initial report in 2008 on their preparation through the ionothermal polymerization of carbonitrile-containing (i.e., cyano-functionalized) monomers, triazine-linked CTFs have drawn more and more attention [46]. Except for the C−H bonds appended to phenyl rings, CTFs lack weak bonds in their skeleton and possess exceptionally strong and stable aromatic C=N bonds (i.e., conjugated triazine rings) [45]. Similar to MOFs and COFs, designability is one of the characteristics that sets CTFs apart. In practice, the organic monomers' geometry, size, and functional groups regulate the resultant porous structure's textural, structural, and physicochemical characteristics. For effective interaction with photons, electrons, and ions (such as HM cations and other guest species), CTFs provide tailor-made supramolecular architectures. Particularly, CTFs exhibit outstanding thermal/chemical stability (due to the presence of extremely stable triazine moieties in their skeleton), significant nitrogen content, increased specific surface area, and considerable pore volume, which renders them many possibilities for addressing growing energy-and environment-related challenges in areas such as adsorption [48], separation [241], energy storage and conversion [242], and catalysis [243].

This study presents an efficient adsorbent carboxylic acid-functionalized covalent triazine framework (COOH-CTF) to eliminate Cd^{2+}, Hg^{2+}, and Pb^{2+} metal cations from water. The design process of functionalized CTFs was inspired by incorporating negatively-charged electron-rich moieties (e.g., sulfur, nitrogen, and oxygen atoms with accessible lone pair electrons) into the skeleton of CTF-1. It has been shown through DFT calculations that the COOH functional group, accompanied by triazine moieties of the framework, induces a high binding ability to the framework, thus enabling strong coordination with HM cations and forming stable complexes through strong electrostatic interactions.

6.3 DFT-assisted computational screening of functionalized monomers

6.3.1 Computational methodology

Complexation energies (i.e., interaction energies) in various HM cation-adsorbent complexes are evaluated using the DFT approach implemented in the Gaussian 16 software package linked with GaussView 6 graphical interface [192]. This is to explore the high-affinity functional groups for developing the optimum HM-capturing CTF-based adsorbents. First, DFT analyzes the electronic structure of the organic fragments (such as triazine-containing functionalized trimers) of the CTF materials and their complexes with HM cations. In this respect, the ωB97XD range-separated exchange-correlation energy functional [157] is utilized with the Pople triple-ζ 6-311+G** basis set [244] for the non-metal atoms and the Karlsruhe valence triple-ζ def2-TZVPD basis set [245] for the HM cations. On all atoms, these basis sets employ balanced diffuse and polarization functions. The integral equation formalism polarizable continuum model (IEF-PCM) implicitly accounts for the solvent (i.e., water) effect [160]. No constraints are applied during the optimization of the molecular geometries, and vibrational analysis is used to confirm that the resulting structures are energy-minima (i.e., no imaginary frequencies). To realize the charge delocalization and intermolecular interactions caused by the adsorption of HM cations onto the CTF surface, natural bond orbital (NBO) population analysis [246] is also carried out at the same level of theory to calculate the charge transfer and delocalization between the HM cations and organic fragments of CTF adsorbents. The adsorption energy for each system is computed as follows:

$$E_{ads} = E_{Complex} - E_{Metal\ species} - E_{CTF\ fragment} \quad \text{Eq. 6-1}$$

where $E_{Complex}$, $E_{Matal\ species}$, and $E_{CTF\ fragment}$ are the energies of the optimized adsorption complex (i.e., HM-loaded CTF fragment), HM species, and CTF fragment model, respectively.

6.4 Experimental section

6.4.1 Chemicals and reagents

All chemicals and reagents utilized in this research are used without further purification or pre-treatment. Zinc chloride ($ZnCl_2$, Sigma-Aldrich, reagent grade, ≥98%), 1,4-dicyanobenzene (DCB, Sigma-Aldrich, 98%), 2,5-dicyanobenzoic acid (COOH-DCB, PJPC Ltd, ≥96%), hydrochloric acid (HCl, certified ACS Plus grade, 36.5-38 wt.%, Fisher Scientific), and acetone (Mojallali Laboratory, ≥99.8%) are used as received. Deionized water (DI water) is supplied from a local Barnstead/Sybron Nanopure II water purification system.

6.4.2 Material characterization

Fourier-transform infrared (FT-IR) spectra of the precursors (i.e., DCB and COOH-DCB) and resulting CTF samples (i.e., CTF-1 and COOH-CTF) are collected on a Thermo Scientific Nicolet 6700 Analytical FTIR spectrometer (600–3600 cm^{-1}) to determine the polymerization conversion, functional groups, and chemical bonds. The CTF samples' powder X-ray diffraction (XRD) patterns are obtained on a Bruker D8 Advance diffractometer with a Cu-Kα radiation source (λ=1.5418 Å). Nitrogen adsorption-desorption isotherms are collected on a Micromeritics ASAP 2020 physisorption analyzer at 77.4 K to investigate the porous media textural properties and the pore features of the CTF samples. X-ray photoelectron spectroscopy (XPS) is performed on a Thermo Scientific ESCALAB 250Xi analyzer to examine the surface chemical composition and the oxidation states of elements in the CTF samples. The concentrations of HM cations are

measured using an inductively coupled plasma optical emission spectrometer (ICP-OES) (AVIO 200, Perkin Elmer).

6.4.3 Ionothermal synthesis of functionalized CTFs

To synthesize CTF-1 adsorbent, 1,4-dicyanobenzene (DCB, 0.128 g, 1 mmol) and zinc chloride ($ZnCl_2$, 0.136 g, 1 mmol) are well-admixed mechanically using a mortar in an argon-filled glovebox. Then, the resulting white-color mixture is loaded in a high-temperature quartz glass tube (1.5 cm diameter×15 cm length) in the glovebox. The glass tube is sealed by a rubber septum stopper, vacuumed for 2 h, then flame-sealed, and ultimately placed in a muffle furnace vertically, heated to 400 °C with a heating rate of 1 °C min^{-1} and kept at 400 °C for 40 h. Upon the reaction completion, the glass tube is cooled to room temperature and opened carefully under a fume hood to collect the resulting black-color monolithic product. After the synthesis, the product undergoes a detailed purification procedure to remove the catalyst ($ZnCl_2$), unreacted monomer (e.g., DCB), and other impurities. In this respect, the obtained material is crushed and thoroughly ground into the fine powder using a mortar under a fume hood, added to the aqueous HCl solution (30 mL, 0.1 M), and refluxed at 100 °C under stirring at 300 rpm for 12 h. Successively, the resulting material is centrifuged and washed with the excess amount of aqueous HCl solution (3×10 mL, 0.1 M), DI water (5×50 mL), and acetone (3×10 mL), respectively. Ultimately, the resulting material is dried at 120 °C for 8 h under a dynamic vacuum to render the final activated adsorbent. A similar synthetic procedure is used with DCB replaced with COOH-DCB monomer (i.e., 2,5-dicyanobenzoic acid, 0.172 g, 1 mmol) to synthesize COOH-CTF.

6.4.4 Batch equilibrium studies

The experiments of batch equilibrium adsorption are performed to determine the HM cation-capturing performance of CTFs at the ambient temperature (i.e., 25 °C) and the constant pH value of 5.0. The adsorption experiments are conducted by adding a prescribed amount of activated adsorbent (ca. 5 mg) in 40 mL of HM cations aqueous solutions with different initial concentrations in a set of glass vials (50 mL). Each vial is stirred at 200 rpm for 360 min. After each batch adsorption experiment, the adsorbents are separated from the solution by filtration. The remaining HM cations concentrations are acidified with 2.0% nitric acid (HNO_3) as a diluent to ensure all the HM species are dissolved. It ought to be noted that nitric acid (1% to 5%) is typically utilized for metal dissolution and stabilization for ICP-OES investigation [165]. The residual concentration of HM cations in the aqueous phase is determined using ICP-OES. The amount of adsorbed HM cations onto the CTF adsorbents (q_e) is calculated as follows:

$$q_e = \frac{C_i - C_f}{m} V \qquad \text{Eq. 6-2}$$

where C_i and C_f are the initial and final concentrations (mg L^{-1}) of HM cations, respectively, V is the volume of the aqueous solution (40 mL), and m represents the mass of the CTF adsorbent (5 mg).

6.4.5 Adsorption kinetics

The amount of HM cations adsorbed onto CTF materials might be expressed as a function of time to study the kinetics associated with the adsorption process. The process followed the steps described in Section 6.4.4 for the equilibrium analyses, except for stopping the adsorption at specific times. That is, samples (4 mL) from the vials are taken at certain intervals by rapid filtration of residual adsorbent from the sample solutions. ICP-OES is also used to determine the

residual concentration of the Cd^{2+}, Hg^{2+}, and Pb^{2+} cations in each sample solution. The amount of adsorbed HM cations is determined as follows:

$$q_t = \frac{C_i - C_r}{m} V \qquad \text{Eq. 6-3}$$

where C_i and C_r are the initial and instantaneous residual concentrations (mg L^{-1}) of HM cations, respectively.

It has been proven in many studies that the pH range of 4.5−5.2 is the optimal range for HMs adsorption, as at values below 4.0, there is a competition between the HM cations and hydronium ions (H_3O^+) for the active sites of adsorbent, while at values higher than 5.2, various HM species (such as $HM(OH)^+$, $HM(OH)_3^-$, and $HM(OH)_2$, when dealing with a divalent HM), will be present in the aqueous phase [247-249]. As a result, some of these species will be adsorbed by the negatively charged adsorbent moieties, decreasing the overall HM cations removal efficiency. The precipitation of insoluble $HM(OH)_2$ also inhibits or interferes with the adsorption of HM cations. Therefore, the pH value of all experiments is adjusted to 5.0 using the NaOH and HCl solutions.

6.4.6 HM desorption and CTFs regeneration

Desorption investigations were performed utilizing HCl solution (40 mL, 1 M) as a desorption/regeneration solution. The HM-loaded CTF is isolated from the solution, washed with DI water, and dried. Next, the CTF adsorbent is immersed in the HCl solution while stirred at room temperature for 3 h and filtered through a centrifuge. Ultimately, the recovered CTF adsorbent is used for a subsequent adsorption cycle.

6.5 Results and discussion

6.5.1 DFT-assisted design of functionalized CTF adsorbents

To prepare an optimal adsorbent, we analyzed the synergistic adsorption configurations of CTFs with different functional groups (i.e., SH, OH, COH, and COOH) and HM cations, including Cd^{2+}, Hg^{2+}, and Pb^{2+} (Figure 6.1). As mentioned in the Introduction Section, one significant criterion for selecting an optimal adsorbent is the binding energy (i.e., complexation energy or interaction energy) between adsorbent (e.g., CTF) and adsorbate (e.g., HM cations). Hence, according to the DFT calculations results presented in Table 6.1, one might conclude that the CTF featuring the carboxylic acid functional group (i.e., COOH-CTF) shows the best performance in terms of complexation energy and net charge transfer from the framework to HM cations, among other functionalized CTF materials. These results indicate that the synergistic interactions between the HM cations, N atoms in the triazine rings, and O atoms in the COOH functional group are the strongest, and the resultant HM@COOH-CTF adsorption complexes are the most stable configurations (i.e., the highest absolute values of complexation energy, see Table 6.1). The more negative interaction energy values result in a higher possibility of efficient adsorption, leading to a more stable adsorption complex. Thus, based on the DFT calculations results, it is anticipated that using the COOH-functionalized CTF adsorbent for eliminating HM cations will result in maximum adsorption capacities.

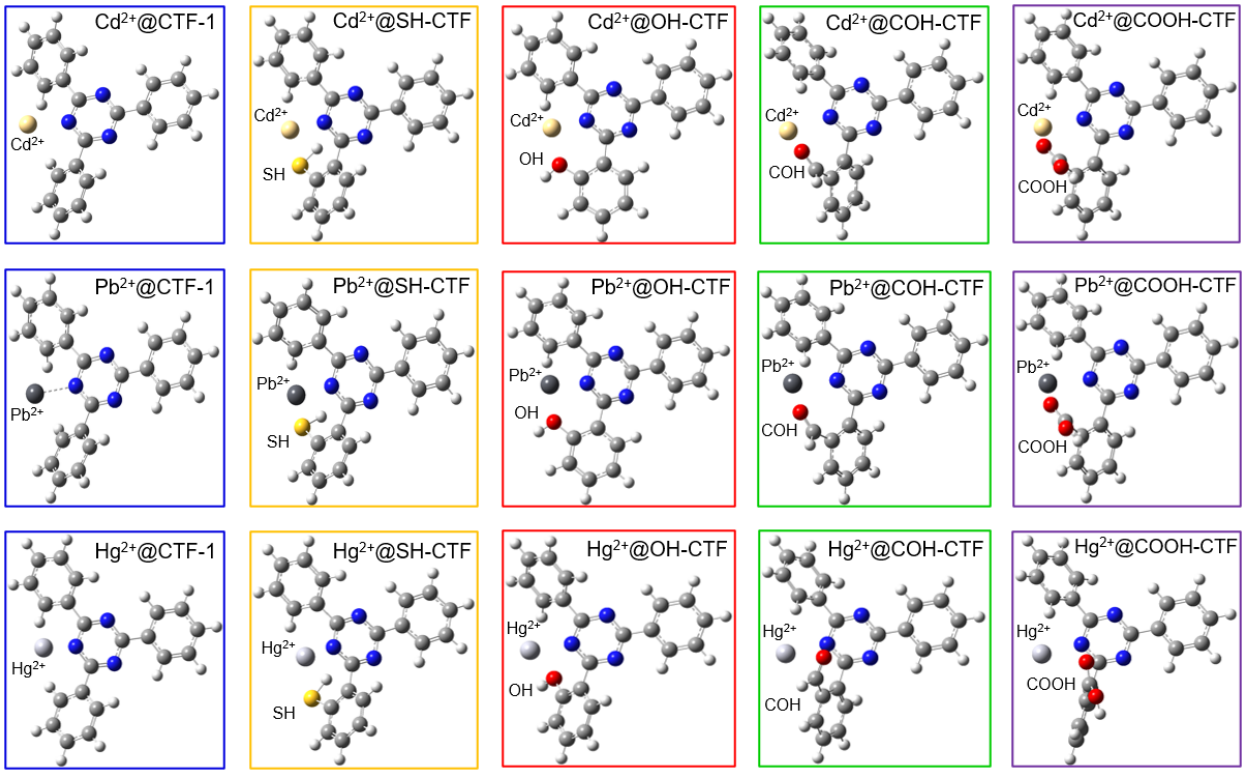

Figure 6.1. Molecular geometries of trimer cuts of CTFs.
CTFs featuring thiol (SH), hydroxyl (OH), aldehyde (COH), and carboxylic acid (COOH) functionalities and their complexes with HM cations in the aqueous phase calculated with ωB97XD/6-311+G**/ def2-TZVPD/IEF-PCM model chemistry.

Table 6.1. Thermochemical properties of HM-loaded functionalized CTFs.
Adsorption energy (E_{ads}), Gibbs free energy (ΔG_{ads}), enthalpy (ΔH_{ads}), and net NBO charge transfer for the adsorption complexes calculated with ωB97XD/6-311+G**/ def2-TZVPD/IEF-PCM model chemistry. All calculations were performed at 298 K.

Adsorbent	Adsorbate	E_{ads} (kcal mol^{-1})	ΔG_{ads} (kcal mol^{-1})	ΔH_{ads} (kcal mol^{-1})	ΔS_{ads} (kcal mol^{-1} K^{-1})	Net CT (e)
CTF-1	Cd^{+2}	−7.5	1.4	−7.9	−0.031	0.043
	Pb^{2+}	−36.7	−28.0	−39.0	−0.037	0.196
	Hg^{2+}	−10.9	−1.4	−11.4	−0.033	0.098
SH-CTF	Cd^{+2}	−8.1	−1.1	−8.3	−0.024	0.060
	Pb^{2+}	−37.1	−29.2	−37.3	−0.027	0.074
	Hg^{2+}	−22.1	−14.1	−21.9	−0.026	0.144
OH-CTF	Cd^{+2}	−9.3	−2.4	−9.5	−0.024	0.086
	Pb^{2+}	−43.9	−33.1	−44.1	−0.037	0.126
	Hg^{2+}	−22.1	−13.7	−23.5	−0.033	0.146
COH-CTF	Cd^{+2}	−9.5	−2.7	−9.7	−0.023	0.096
	Pb^{2+}	−51.7	−44.9	−51.8	−0.023	0.158
	Hg^{2+}	−23.3	−14.0	−23.8	−0.033	0.148
COOH-CTF	Cd^{+2}	−9.9	−2.9	−10.1	−0.024	0.080
	Pb^{2+}	−53.9	−46.3	−53.2	−0.023	0.257
	Hg^{2+}	−24.8	−12.8	−24.4	−0.039	0.159

A negative entropy change (ΔS) within a given adsorption system signifies reduced disorder or randomness due to adsorption. Specifically, this entails that, during adsorption, the adsorbate species, e.g., heavy metal cations, become more organized and ordered in relation to the adsorbent surface. Consequently, the freedom and randomness associated with the motion and arrangement of these adsorbate species diminish, resulting in a lower entropy value. This phenomenon is a characteristic feature of adsorption processes that bind molecules or ions to solid surfaces and is an integral aspect of the thermodynamic considerations governing such interactions. It is worth noting that while a negative ΔS indicates a decrease in entropy, the overall spontaneity and thermodynamic feasibility of the adsorption process are determined by the interplay of ΔS with changes in enthalpy (ΔH) and temperature (T), as reflected in the Gibbs free energy equation ($\Delta G = \Delta H - T\Delta S$).

6.5.2 Characterization of the prepared CTF samples

6.5.2.1 PXRD patterns of the prepared CTF samples

Figure 6.2-a represents the powder X-ray diffraction (PXRD) patterns of the synthesized CTF-1 and COOH-CTF materials. One might infer that CTF-1 possesses a crystalline structure while the COOH-CTF sample is partially crystalline. The CTF-1 sample shows a high extent of crystallinity, as demonstrated by the sharp (100) peak at 7.4° and two other peaks around 13.3° and 14.4° related to the (110) and (200) facets, respectively (see Figure 6.2-a). In the meantime, the 2D structure of CTF materials in a crystalline and/or π-π stacked arrangement could be proved by a broad peak typically observable in the 2Θ range of 24-26° corresponding to the (001) plane [210, 250].

6.5.2.2 FT-IR spectroscopy of the precursors and prepared CTF samples

Comparing the Fourier-transform infrared (FT-IR) spectra of precursors (i.e., DCB and COOH-DCB) with those of corresponding CTF materials (Figure 6.2-b), one might confirm the successful conversion of carbonitrile functionalities (i.e., C≡N) into triazine moieties (i.e., aromatic C=N). That is, the strong spectral peaks at 2230 and 2245 cm^{-1} attributing to the C≡N functionalities within the structure of DCB and COOH-DCB monomers, respectively, disappeared completely after the ionothermal cyclotrimerization (see Figure 6.2-b) [145, 251]. In the meantime, two spectral peaks related to the stretching vibrational modes of triazine rings appeared around 1510 and 1352 cm^{-1} in the absorption spectra of CTFs [210, 252]. The former corresponds to the triazine ring's C−N stretching vibration, whereas the latter pertains to the in-plane stretching vibration of the triazine ring [253]. In the case of COOH-CTF, spectral peaks at 3436, 1613, and 1394 cm^{-1} signify the presence of carboxylic acid functionalities in the structure (see Figure 6.2-b) [254-256].

6.5.2.3 N_2 adsorption-desorption isotherms on the prepared CTF samples

The CTF-1 material displays a porous structure with a type of I isotherm, typically occurring in microporous materials, according to the N_2 adsorption-desorption isotherms on the CTF materials (Figure 6.2-c). The CTF-1 adsorption isotherm shows a sharp uptake at low relative pressures (i.e., P/P_0 up to 0.01) followed by a plateau, which denotes an abundance of micropores (i.e., pores smaller than 2 nm). The isotherms of CTF-1 also reveal a small yet fully reversible hysteresis loop, further demonstrating the dominance of micropores over meso-and macropores.

The synthesized COOH-CTF sample, on the other hand, exhibits the combined isotherm types I and IV (see Figure 6.2-c). The adsorption isotherm of COOH-CTF shows an intense uptake at low relative pressures due to micropores followed by continued N_2 uptake to high relative pressures, indicating the presence of mesopores (i.e., pores with a diameter between 2 and 50 nm) in the

structures. Additionally, the presence of mesopores in the COOH-CTF structure is also implied by the H4-type hysteresis loop in the high-pressure area (i.e., P/P_0>0.1). The observed hysteresis loop in the COOH-CTF isotherm can be attributed to the distortion of the COOH-CTF structure to some extent due to the loss of heteroatoms at elevated temperatures during the prolonged synthesis, resulting in the formation of meso-and macropores.

Meanwhile, the pore size distributions are realized using the non-local density-functional theory (NL-DFT) (Figure 6.2-d). According to the results collected, the average pore diameters of CTF-1 and COOH-CTF are 2.19 and 4.18 nm, respectively. The BET specific surface area (S_{BET}) and the total pore volume (V_{tot}) of CTF-1 and COOH-CTF synthesized in this work are 756 and 599 $m^2\ g^{-1}$ and 0.414 and 0.626 $cm^3\ g^{-1}$, respectively.

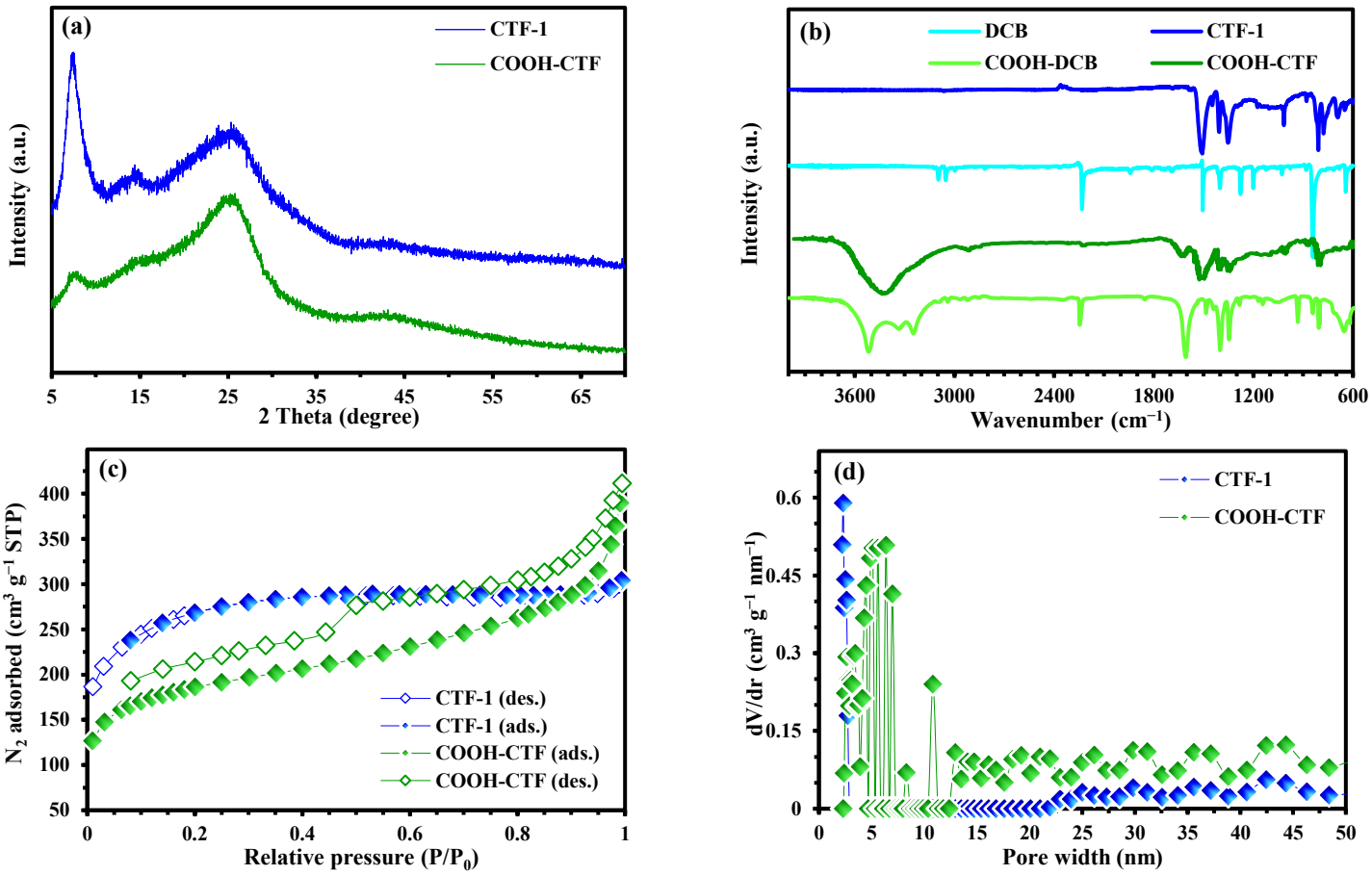

Figure 6.2. Characterization results for the precursors and prepared functionalized CTFs.
(a) PXRD patterns of CTF-1 and COOH-CTF. (b) FT-IR spectra of the precursors and the synthesized CTFs. (c) N_2 adsorption-desorption isotherms on the CTFs at 77.4 K up to 1 bar. (d) Pore size distribution plots of CTFs obtained through the NL-DFT method.

6.5.3 Adsorption kinetics of HM cations onto CTFs

An essential factor in assessing the efficacy of adsorbents is the adsorption equilibrium time and how fast the adsorbent adsorbs the pollutants (e.g., HM cations) from the environment (e.g., water/wastewater). The adsorption capacities of CTFs for HM cations at various contact times up

to 180 min are investigated to understand the HMs' adsorption process and equilibration period. The findings are shown in Figure 6.3 (a-c). As can be seen, COOH-CTF adsorbs HM cations (i.e., Cd^{2+}, Hg^{2+}, and Pb^{2+}) more quickly than CTF-1, which is likely due to the former's mesoporous structure as opposed to the latter's microporous framework (see Section 6.5.2.3 & Figure 6.2-d for pore size distributions).

Moreover, the prevalence of high-affinity adsorption sites (such as carboxylic acid functionalities) within the structure of COOH-CTF is a feature that favorably influences the adsorption kinetics of HM cations. Hence, the superior kinetic performance of COOH-CTF can be due to the synergistic effects of its mesoporous structure featuring high-affinity adsorption sites. Among three HM cations, Pb^{2+} shows faster kinetics than Hg^{2+} (see Figure 6.3-b & Figure 6.3-c), while the latter is adsorbed onto the CTF surfaces faster than Cd^{2+} (see Figure 6.3-a). This observation is consistent with the adsorption energy hierarchy of these HM species (see Table 6.1 for E_{ads}).
The pseudo-first-order (PFO) and pseudo-second-order (PSO) kinetic models are utilized to describe the adsorption kinetics, and the results are presented in Table 6.2. In light of this, both models are well-fitted with the experimental adsorption data (see Figure 6.3 (a-c) for fitted curves & Table 6.2 for R^2 values). While the PFO model slightly better fits the HM@CTF-1 adsorption systems, the PSO model more accurately describes the HM@COOH-CTF adsorption systems' kinetic behavior.

The HM cations' adsorption kinetic profiles show that adsorption occurred in two stages depending on the adsorption complex. HM cations' rapid and remarkable uptake is observed within 30-60 min after contact with the CTF adsorbents (see Figure 6.3 (a-c)). An equilibrium or quasi-stabilized state is subsequently thought to have been established after a sluggish phase of HM cation elimination developed after the rapid initial phase. The two-stage kinetic profile for HM cations can be related to the nature and types of accessible high-affinity adsorption sites on the CTFs' surfaces.

The initial abundance of accessible sites for adsorption, particularly in COOH-CTF, accounts for the rapid initial phase of the HM cations uptake. Nonetheless, as the adsorption continues and HM cations occupy the readily accessible high-affinity centers, the further adsorption rate is reduced due to several factors, including the repulsive forces between the already adsorbed and the additional HM cations and the fewer available sites for occupation. Thus, compared to plenty of adsorption sites at the beginning of the adsorption, this progressive occupation of the remaining vacant sites will move along more slowly (i.e., the sluggish second phase).

6.5.4 Equilibrium adsorption isotherms

For Cd^{2+} cation adsorption, an analysis of Figure 6.3-d reveals that the amount of Cd^{2+} adsorbed onto CTF-1 increased from 24.14 mg g^{-1} for an initial Cd^{2+} concentration of 11.9 mg L^{-1} to 68.45 mg g^{-1} for 201.7 mg L^{-1}. The corresponding values for the adsorption of Cd^{2+} cations onto COOH-CTF are 39.64 and 88.02 mg g^{-1} (see Figure 6.3-d).

From Figure 6.3-e, the loading amount of Hg^{2+} on CTF-1 increased with an increase in the initial Hg^{2+} concentration from 72.20 mg g^{-1} for 11.8 mg L^{-1} to 180.43 mg g^{-1} for 203.6 mg L^{-1}. As expected, the corresponding adsorption capacity values for the adsorption of Hg^{2+} cation onto COOH-CTF increased to 102.23 and 247.28 mg g^{-1}, respectively (see Figure 6.3-e).

For Pb^{2+} cations adsorption, according to Figure 6.3-f, it is revealed that the quantity of Pb^{2+} uptaken by CTF-1 raised from 92.24 mg g^{-1} for an initial Pb^{2+} concentration of 12.3 mg L^{-1} to 258.25 mg g^{-1} for 204.7 mg L^{-1}. In the meantime, Pb^{2+} cations are adsorbed onto COOH-CTF with capacities of 121.69 and 360.39 mg g^{-1} when the initial Pb^{2+} concentration increased from 12.3 to 204.7 mg L^{-1}, respectively (see Figure 6.3-f).

Although COOH-CTF possesses a lower specific surface area than CTF-1 (i.e., 599 vs. 756 m^2 g^{-1}), the superior HM adsorption performance of COOH-CTF might be due to its higher pore volume (0.626 vs. 0.414 cm^3 g^{-1}) along with the abundance of accessible high-affinity adsorption sites (i.e., negatively charged oxygen atoms in carboxylic acid functionalities and nitrogen atoms of triazine rings). It is speculated that there are strong electrostatic interactions and charge transfer between the HM cations and these high-affinity adsorption sites, resulting in an enhanced HM cations adsorption capacity.

Adsorption is a dynamic process in which molecules or ions from a fluid phase adhere to the surface of a solid material, the adsorbent. In the case of a single-component stream, only one type of adsorbate is present in the fluid phase. The adsorbent's surface contains sites with an affinity for these adsorbate molecules or ions. As the fluid contacts the solid adsorbent, interactions such as electrostatic attraction, chemical bonding, or dipole-dipole forces can facilitate the adsorption, leading to charge transfer between the adsorbate and adsorbent. This dynamic process continues until equilibrium is reached, where the adsorption rate equals the desorption rate.

In a multiple-component stream, the fluid phase contains various adsorbates, resulting in competitive adsorption. Different adsorbates compete for available adsorption sites on the adsorbent surface. Charge transfer in such systems becomes more complex, involving interactions between multiple species. The selectivity of the adsorbent dictates which components are preferentially adsorbed, with charge transfer occurring due to both the interactions between adsorbate molecules and the adsorbent surface and interactions among adsorbate species themselves. The dynamic nature of these processes is central to understanding the adsorption behavior in complex, multicomponent systems.

Adsorption system design requires an understanding of the interaction between the adsorbent and the adsorbate at equilibrium, and one favored method to obtain this knowledge is the use of equilibrium adsorption isotherms. It is crucial to comprehend the precise relation between the pollutant concentration (i.e., HM concentration) and its adsorption capacity by the solid adsorbent at a certain temperature, which is used to develop adsorption isotherms. In this respect, equilibrium adsorption experiments are performed employing various HM cations' initial concentrations to remedy the HM cations-contaminated water samples, and the results are presented in Figure 6.3 (d-f). The quantities of HM cations adsorbed by the CTF adsorbents are attained from the experiments, and in this work, the adsorption process is described using the Langmuir and Sips isotherms (see Figure 6.3 (d-f) for fitted curves and Table 6.3 for adjustable parameters of isotherm models).

The non-linear technique, a trial-and-error process, is used to evaluate the Langmuir and Sips isotherms. This method uses the Solver add-in in Microsoft Excel to derive the isotherms' adjustable parameters from the models by maximizing the corresponding coefficient of

determination (R^2) between experimental data and those predicted by isotherm models. The isotherms' adjustable parameters are presented in Table 6.3. The Langmuir isotherm model best explains the experimental adsorption data of HM@CTF-1 complexes, as inferred from the R^2 values in Table 6.3. However, while analyzing the adsorption behavior of the HM@COOH-CTF, the Sips isotherm model performed better than the Langmuir isotherm model (see Table 6.3 for corresponding R^2 values). This finding is likely caused by the COOH-CTF surface's increased heterogeneity, which features various high-affinity adsorption sites. Higher affinity values (i.e., b parameter, see Table 6.3) are achieved in these systems compared to HM@CTF-1 adsorption systems due to more robust intermolecular interactions in the HM@COOH-CTF adsorption complexes. In the meantime, stronger interactions between Pb^{2+} and CTF adsorbents are suggested by the higher b values for Pb^{2+} adsorption systems than those for Hg^{2+} and Cd^{2+} (see Table 6.3).

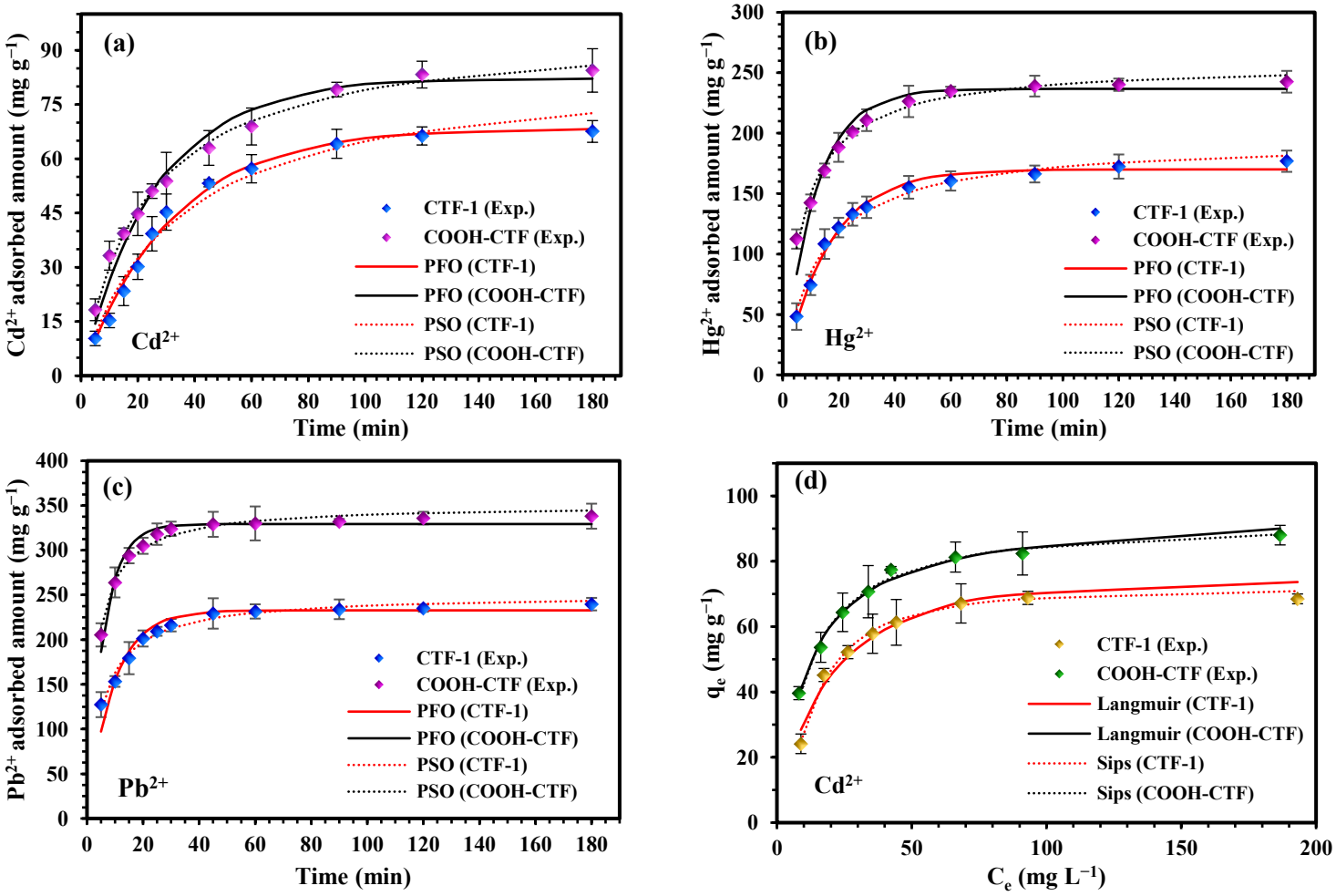

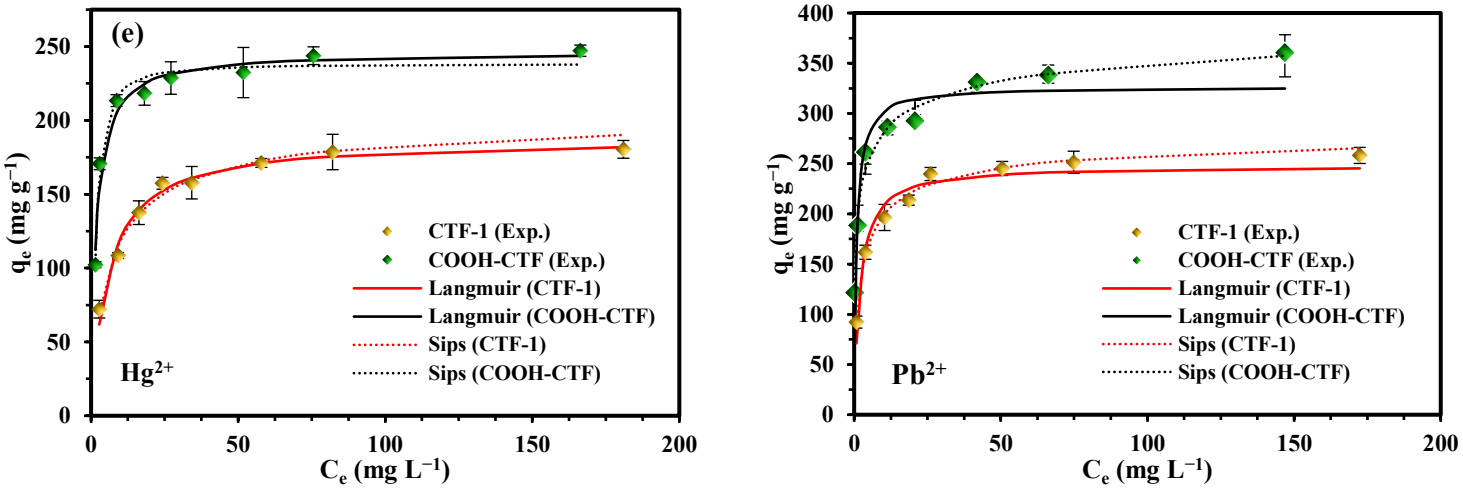

Figure 6.3. The HM cations adsorption performance of functionalized CTF adsorbents.
Adsorption kinetics of (a) Cd^{2+}, (b) Hg^{2+}, and (c) Pb^{2+}. The equilibrium adsorption of (d) Cd^{2+}, (e) Hg^{2+}, and (f) Pb^{2+}. (Error bars represent the standard deviation from the average value of two independent experiments)

Table 6.2. Adjustable parameters of the PFO and PSO kinetic models for HM cations adsorption onto the CTF-1 and COOH-CTF adsorbents at 25 °C.

Kinetic model	Adsorbent	Adsorbate	$q_{e,cal}$ (mg g^{-1})	$k_1 \times 10$ (min^{-1})	$k_2 \times 10^2$ (min^{-1}g mg^{-1})	R^2
PFO $q_t = q_{e,cal}(1-\exp(-k_1 t))$	CTF-1	Cd^{2+}	65.92	1.302	–	0.9881
		Hg^{2+}	174.51	0.476	–	0.9933
		Pb^{2+}	240.65	0.293	–	0.9809
	COOH	Cd^{2+}	81.31	1.571	–	0.8314
		Hg^{2+}	233.43	0.623	–	0.9309
		Pb^{2+}	320.69	0.372	–	0.9423
PSO $q_t = \frac{k_2 q_{e,cal}^2 t}{1+k_2 q_{e,cal} t}$	CTF-1	Cd^{2+}	71.37	–	0.297	0.9563
		Hg^{2+}	206.56	–	0.026	0.9418
		Pb^{2+}	306.20	–	0.009	0.9520
	COOH-CTF	Cd^{2+}	85.37	–	0.388	0.9728
		Hg^{2+}	261.79	–	0.033	0.9940
		Pb^{2+}	380.48	–	0.011	0.9971

Table 6.3. Adjustable parameters of the Langmuir and Sips isotherm models for HM cations adsorption onto the CTF-1 and COOH-CTF adsorbents at 25 °C.
The equilibrium time for each measurement was 360 min.

Isotherm model	Adsorbent	Adsorbate	$q_{m,cal}$ (mg g^{-1})	b (L mg^{-1})	n	R^2
Langmuir $q = \frac{q_{m,cal} b C_e}{1+bC_e}$	CTF-1	Cd^{2+}	73.65	0.056	–	0.9679
		Hg^{2+}	187.55	0.177	–	0.9759
		Pb^{2+}	248.06	0.518	–	0.9563
	COOH	Cd^{2+}	90.86	0.089	–	0.9506
		Hg^{2+}	248.73	0.474	–	0.9271
		Pb^{2+}	331.54	1.046	–	0.9412
Sips	CTF-1	Cd^{2+}	72.10	0.074	0.856	0.9752

$$q = \frac{q_{m,cal}(bC_e)^{\frac{1}{n}}}{1 + (bC_e)^{\frac{1}{n}}}$$

	Hg^{2+}	205.14	0.148	1.293	0.9855
	Pb^{2+}	285.77	0.379	1.629	0.9811
	Cd^{2+}	88.34	0.198	0.788	0.9834
COOH-CTF	Hg^{2+}	234.32	0.511	0.532	0.9643
	Pb^{2+}	370.55	0.812	1.703	0.9812

6.5.5 HM desorption and CTFs regeneration

The reversibility of HM removal from water by CTFs was also examined after recycling the CTF adsorbents using the method described in Section 6.4.6 (Figure 6.4 (a-b)). After five successive regeneration cycles, the CTF adsorbents demonstrated significant recyclability at a comparatively steady value with a small reduction in HM adsorption capacity.

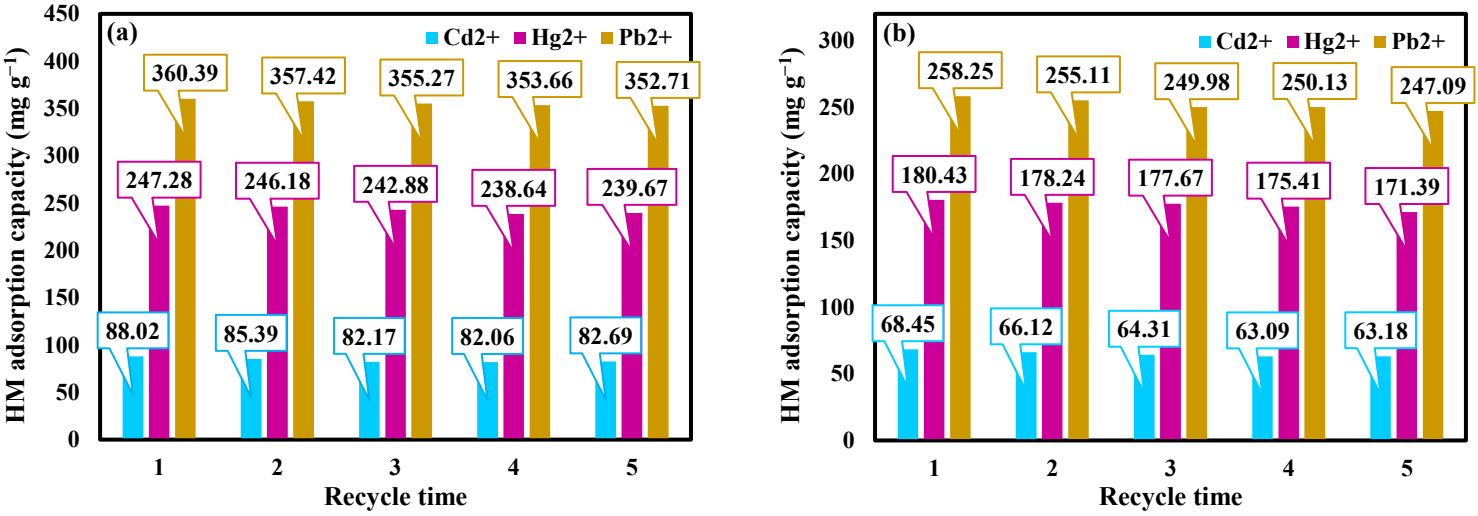

Figure 6.4. Recyclability of (a) CTF-1 and (b) COOH-CTF for removing HM cations from water. HM initial concentrations of 200 mg L^{-1}, pH of 5, and temperature of 25 °C.

6.6 Adsorption mechanism

6.6.1 XPS analysis of HM cations-loaded CTF adsorbents

XPS characterization results are used to analyze the interactions between HM cations and the functional groups acting as high-affinity adsorption sites in CTF adsorbents. In this respect, XPS survey spectra are collected before and after HM adsorption onto the CTF surfaces (Figure S6.1). Three main characteristic peaks can be deconvoluted from the N1s XPS spectra of CTF-1 (Figure 6.5-a). The peaks deconvoluted at 398.66, 399.88, and 400.86 eV are attributed to pyridinic, pyrrolic, and quaternary nitrogen species (see Figure 6.5-a). In the meantime, due to charge transfer from pyridinic and pyrrolic nitrogen species to HM cations, their corresponding peaks slightly shifted to higher binding energy values (see Figure 6.5-a). In addition to the nitrogen species mentioned above, the peak at 402.75 eV observed in the N1s XPS spectra of COOH-CTF adsorbent can be assigned to the oxidized N species (Figure 6.5-b). Two main characteristic peaks can be deconvoluted from the O1s XPS spectra of COOH-CTF (Figure 6.5-c). The peaks deconvoluted at 531.58 and 532.95 eV can be assigned to the oxygen species of the carboxylic acid functional group. The shift in peak position is also observable in the O1s XPS spectra of COOH-CTF upon HM adsorption (see Figure 6.5-c). Hence, nitrogen atoms of triazine rings and

oxygen atoms of carboxylic acid act as high-affinity adsorption sites to adsorb HM cations from water through the charge transfer mechanism.

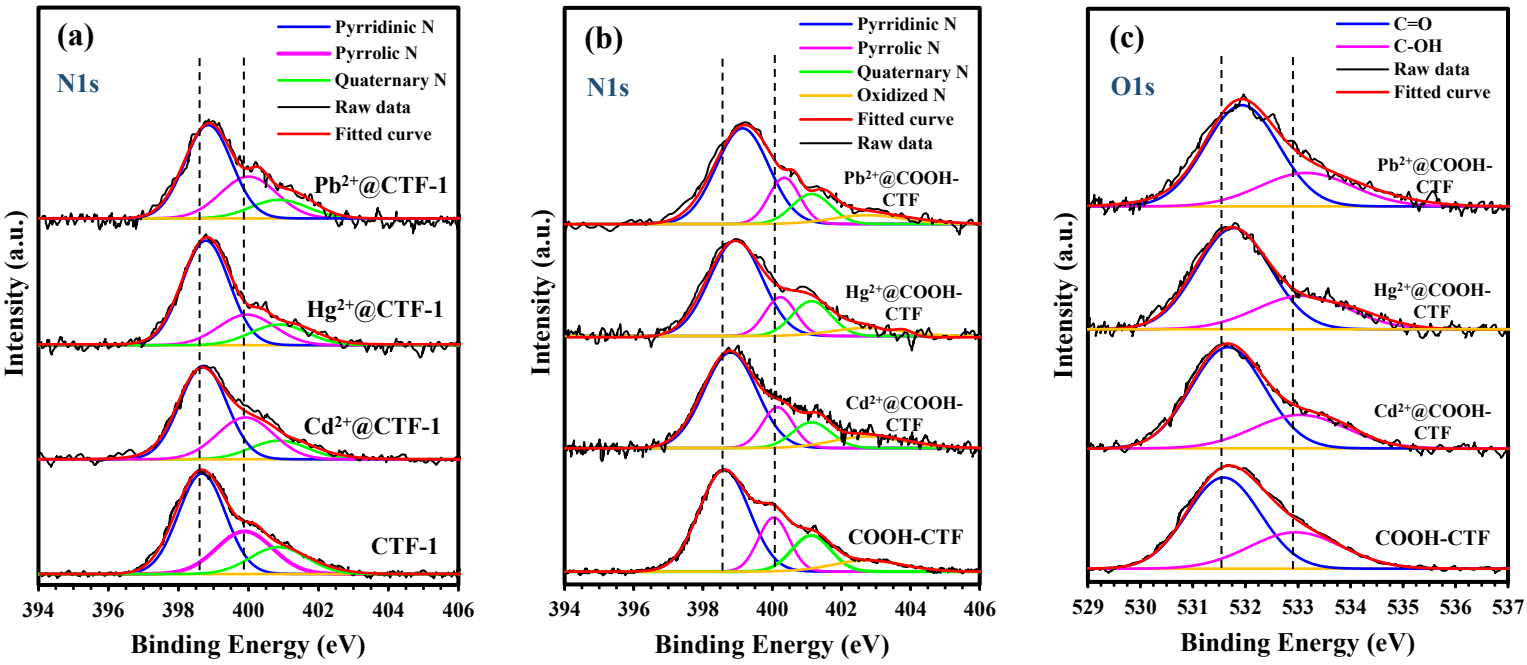

Figure 6.5. XPS spectra of the HM-loaded CTFs.
High-resolution deconvoluted N1s XPS spectra for (a) CTF-1 and HM-loaded CTF-1 and (b) COOH-CTF and HM-loaded COOH-CTF. High-resolution deconvoluted O1s XPS spectra for COOH-CTF and HM-loaded COOH-CTF.

6.6.2 Non-covalent interactions (NCI) analysis

Using NCI analysis, which includes 2D RDG (i.e., reduced density gradient) plots and 3D isosurfaces, it is possible to understand the nature of non-bonding interactions, particularly intermolecular interactions. The non-covalent interactions can be marked in regions with low electron density and RDG. The electron density ($\rho(r)$) and the sign of the second eigenvalue of the electron density Hessian matrix ($\text{sign}(\lambda_2)$) correlate with the intensity of the interaction. In fact, NCI analysis visualizes and distinguishes between non-covalent interactions in real space, such as Van der Waals forces (weak interactions, $\text{sign}(\lambda_2)\rho(r)\approx 0$), strong attraction (e.g., hydrogen bonds, $\text{sign}(\lambda_2)\rho(r)<0$) and steric repulsion (e.g., steric effect in rings, $\text{sign}(\lambda_2)\rho(r)>0$). Three color codes evaluate the nature of interactions in 3D isosurfaces. London dispersion interactions (weak forces) and strong non-bonding interactions (e.g., strong Coulombic forces and hydrogen bonding) are presented as green and blue patches, respectively. At the same time, the steric repulsive interactions appear red. With RDG on the y-axis and $\text{sign}(\lambda_2)\rho(r)$ on the x-axis, the 2D NCI graph is produced. Similar to 3D isosurfaces, strong electrostatic interactions, repulsive interactions, and weak non-bonding Van der Waals forces, in that order, are accompanied by spikes (i.e., where both the electron density, $\rho(r)$, and its reduced gradient, RDG, are small) in the colors blue, red, and green.

As inferred from Figure 6.6 (a-c), the main intermolecular interactions in the HM@CTF-1 adsorption system are weak Van der Waals and strong electrostatic interactions (the green and blue

patches in Figure 6.6 (a-b)) between HM cations and one of the N atoms of the triazine ring. This might be due to electrostatic interactions between the positively charged HM cations and the negatively charged N atom of the triazine ring. However, in addition to the strong electrostatic interactions between HM cations and the nitrogen atom of the triazine ring, further strong electrostatic interaction is also observable between the HM species and the O atom of the carboxylic acid functionality of COOH-CTF (Figure 6.6 (d-f)). Hence, a synergistic electrostatic interaction occurs in the HM @ COOH-CTF adsorption system where the negatively charged O and N atoms are high-affinity adsorption sites.

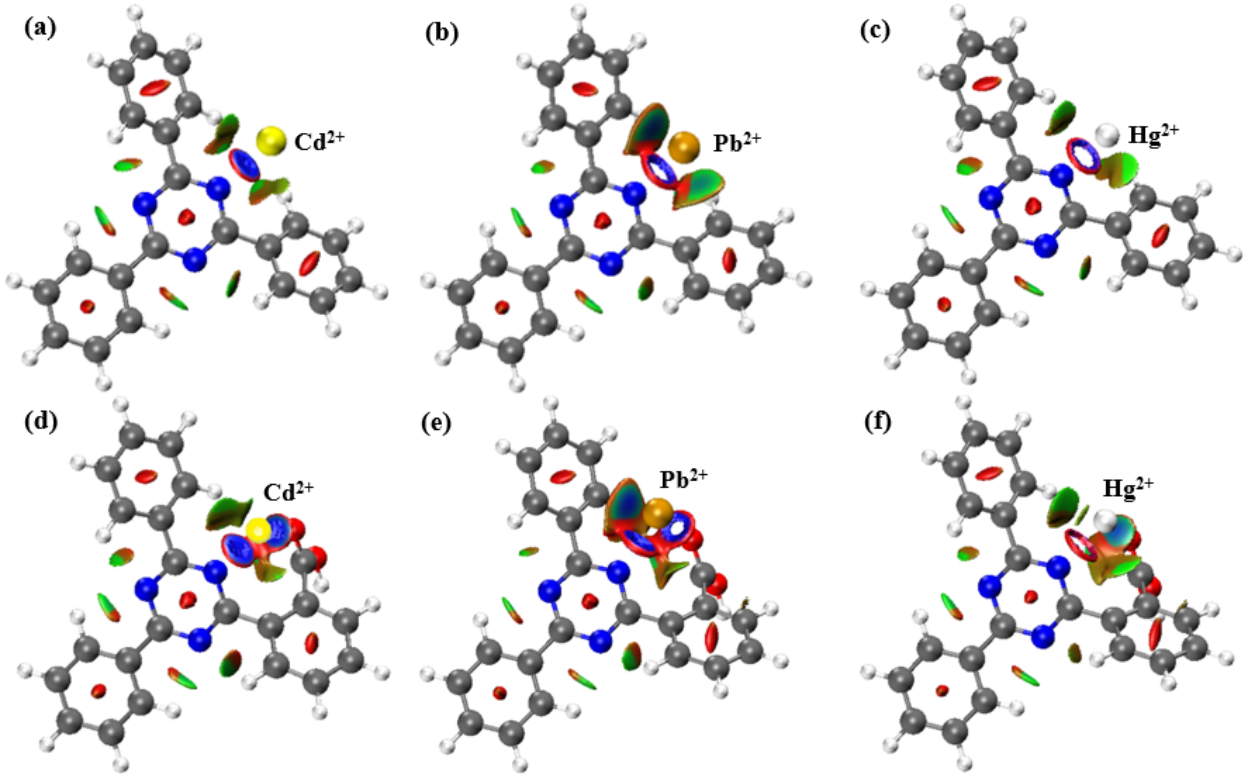

Figure 6.6. 3D isosurfaces for HM cations-loaded CTF adsorbents.
(a) Cd^{2+}@CTF-1, (b) Pb^{2+}@CTF-1, (c) Hg^{2+}@CTF-1, (d) Cd^{2+}@COOH-CTF, (e) Pb^{2+}@COOH-CTF, and (f) Hg^{2+}@COOH-CTF. All calculations are performed using ωB97XD/6-311+G**/ def2-TZVPD/IEF-PCM model chemistry.

6.7 Conclusion

In summary, we computationally designed functionalized CTF adsorbents for efficient HM removal from water. The designed COOH-CTF was synthesized successfully through ionothermal cyclotrimerization of the cyano functionalities of the COOH-DCB monomer. The structure of COOH-CTF material possesses abundant π-conjugated moieties and negatively charged N and O atoms suitable for interacting with HM cations through strong electrostatic interactions. Compared to unfunctionalized CTF-1, COOH-CTF showed a higher affinity towards capturing HM cations from water. After washing with HCl, CTFs could preserve their good HM adsorption capacities to a high extent. The charge transfer from the frameworks to the HM cations facilitates adsorption and stabilizes the resultant complexes. COOH-CTF possessing COOH functionalities on top of triazine rings is more effective in adsorbing and stabilizing the adsorption complexes than CTF-1.

7 Chapter 7: Adsorption of SF_6 decomposition products (H_2S, SO_2, SOF_2, and SO_2F_2) onto Pt-doped CTF-1 covalent triazine framework for gas sensing applications: A DFT study

7.1 Abstract

In the present study, we have investigated the gas adsorption and sensing properties of pristine covalent triazine framework CTF-1 and its platinum atom (Pt)-doped counterpart theoretically towards SF_6 decomposition products (*i.e.*, H_2S, SO_2, SOF_2, and SO_2F_2 gases). For this purpose, density-functional theory (DFT) calculations are employed at the TPSS level of theory corrected by the Grimme D3 empirical dispersion correction for Van der Waals interactions to examine the gas adsorption and sensing capability of the designed materials. The results reveal that the bandgap of the pristine CTF-1 lowers noticeably following surface doping with a Pt atom (3.48 vs. 1.06 eV for pristine vs. Pt-doped CTF-1, respectively), enhancing the electrical conductivity of the gas sensor. The gas@adsorbent complexes are geometrically optimized to assess the systems' electronic characteristics and adsorption parameters. In contrast to pristine CTF-1, which has weak adsorption performance, Pt-doped CTF-1 exhibits strong interaction with the gas species, particularly with SOF_2 and SO_2F_2, along with high sensitivity toward detecting the target gas species under study. Moreover, the density of state (DOS) analysis illustrates the gas adsorption and sensing mechanisms. It has been concluded that Pt-doped CTF-1 could be a novel SF_6 decomposition gas adsorbent and sensor and provides experimentalists with the essential physicochemical characteristics of the designed materials.

7.2 Introduction

With its fascinating characteristics of compact design, durability, and long lifecycle, the gas-insulated switchgear (GIS) is an important component of power transmission and distribution systems [257]. As an inexpensive insulating or arc-extinguishing agent, sulfur hexafluoride (SF_6) gas is typically loaded in the GIS at high pressures (0.1−0.6 MPa) [85]. Nevertheless, the long-term operation of a GIS ultimately results in insulation deficiencies, leading to partial discharge. The resultant partial discharge promotes the breakdown of SF_6 to different sulfur fluoride species (SF_x, $1 \leq x \leq 5$) [86]. Trace impurities such as H_2O and O_2, often present in GIS, will react rapidly with SF_x and produce different decomposition species (e.g., H_2S, SO_2, SOF_2, and SO_2F_2) [258]. Most of these decomposition products are corrosive gases that, upon interacting with H_2O and O_2, promote the corrosion of the insulating chambers [87]. These gas species are also highly toxic to the environment and human health [88]. Hence, it is crucial to monitor and manage the evolution of SF_6 breakdown products from the viewpoints of process control, environment, and human health. This objective can be accomplished by devising high-tech, sensitive, and effective gas sensors.

Important aspects must be considered when developing and selecting appropriate gas sensors. Various two-dimensional (2D) nanomaterials have been prepared and employed as suitable gas sensors [259]. Two essential characteristics of 2D nanomaterials' sensing capability are their high surface-to-volume ratio which provides sufficient and efficient contact area, and proper bandgap (i.e., the energy difference between the top of the valence band and the bottom of the conduction band) [260]. In the meantime, heteroatom doping of sensing nanomaterials, mostly with metal atoms, is a common approach for enhancing the performance of gas sensors [261]. The basic concept of metal doping is to improve surface activity, customize chemical properties, and adjust the electrical conductivity of the pristine (i.e., intrinsic) material [262]. In particular, it is anticipated that doping the substrate with transition metal (TM) atoms (e.g., Pt, Pd, Au, Ag, Fe,

Cu, etc.) will magnify substrate-adsorbate interactions, rendering unique gas-sensing properties [263]. In this respect, FePc monolayers [264], Pt_3 cluster-doped SnS_2 monolayers [265], Sc-doped MoS_2 monolayers [266], Fe-doped single-walled carbon nanotubes (SWCNTs) [267], Rh-doped 2D hexagonal boron nitride (h-BN) nanosheets [268], metal-oxide cluster-modified graphene nanosheets [269], Ni-doped $MoTe_2$ monolayers [270], Pd-doped GaN monolayers [271], among many others, have been theoretically investigated as potential electrochemical gas sensors for SF_6 decomposition products.

Covalent triazine frameworks (CTFs) are an emerging subcategory of porous organic polymers (POPs) that consist of properly assembled organic building units resulting in nanostructures with tailor-made pores [210]. Ionothermal cyclotrimerization of carbonitriles catalyzed by molten $ZnCl_2$ [145], super acid-catalyzed polymerization of carbonitriles [252], and Lewis acid-catalyzed Friedel-Crafts alkylation reaction between cyanuric chloride and phenyl species [210] are among the most widely utilized preparation methods for CTFs. The existence of electron-rich π-conjugated moieties, e.g., phenyl and triazine rings, in the structure of CTFs, their high specific surface area, and considerable thermal/chemical stability make them promising candidates for gas adsorption and sensing applications [89]. In CTFs, the triazine ring can serve as an electron-accepting moiety and the phenyl ring as an electron-donating one [90]. Among various CTF materials, CTF-1, a crystalline 2D nanoporous type of CTFs that exclusively comprises phenyl and triazine rings, is a promising material for several practical applications [45]. More interestingly, CTF-1 can reportedly be delaminated/exfoliated through ultrasonication-assisted mild oxidation, producing single-layered nanosheets with high surface-to-volume ratios [91], highly suitable for gas sensing applications.

These findings inspired us to investigate the wider applications of CTF-based electrochemical sensors for detecting SF_6 decomposition products. The single-layered CTF-1 surface is selected due to its high thermal stability, electron-rich structure, and high nitrogen content, with the latter enabling efficient metal doping and thus anticipated superior gas sensing capability. As mentioned earlier, metal doping significantly affects a given material's gas adsorption and sensing properties, especially those with poor electrical conductivity. Platinum (Pt) stands out among other metal atoms for its exceptional carrier mobility and gas interaction ability [272]. Therefore, the use of Pt as an appropriate doping metal to enhance the adsorption and sensing capabilities of CTF-1 nanomaterial is explored. This work highlights the adsorption characteristics and sensing mechanism of pristine and Pt-doped CTF-1 single-layered nanosheet gas sensors upon interaction with H_2S, SO_2, SOF_2, and SO_2F_2, unveiling the critical roles of metal doping of CTFs on effective gas-sensor interactions through increasing the electrical conductivity, charge transfer, and adsorption energy.

7.3 Computational methodology

7.3.1 Molecular structure modeling

The representative structure for the CTF-1 surface selected for gas adsorption and sensing investigations consists of three hydrogen-caped phenyl rings connected by one triazine ring as cross-linking agent (Figure 7.1). The phenyl rings are hydrogen-capped to offset the dangling bonds of carbon atoms (i.e., immobilized free radicals) at the phenyl ring ends. The pristine CTF-1 model saturated by hydrogen atoms possesses 21 carbon (C) atoms, 3 nitrogen (N) atoms, and 15 hydrogen (H) atoms. The structure of Pt-doped CTF-1 is also shown in Figure 7.1. It should be

noted that the Pt atom is initially placed on top of the phenyl and triazine rings, with the former possessing a π-conjugated structure with the electron-donating ability and the latter possessing N atoms with lone pairs as potential adsorption sites for the Pt-doped CTF-1 optimized structure. All structures are visualized by the GaussView 6 graphical interface [273] linked to the Gaussian 16 software [192]. The total density of states (TDOS) and partial density of states (PDOS) plots are generated using the open-source Multiwfn wavefunction analyzer program [274].

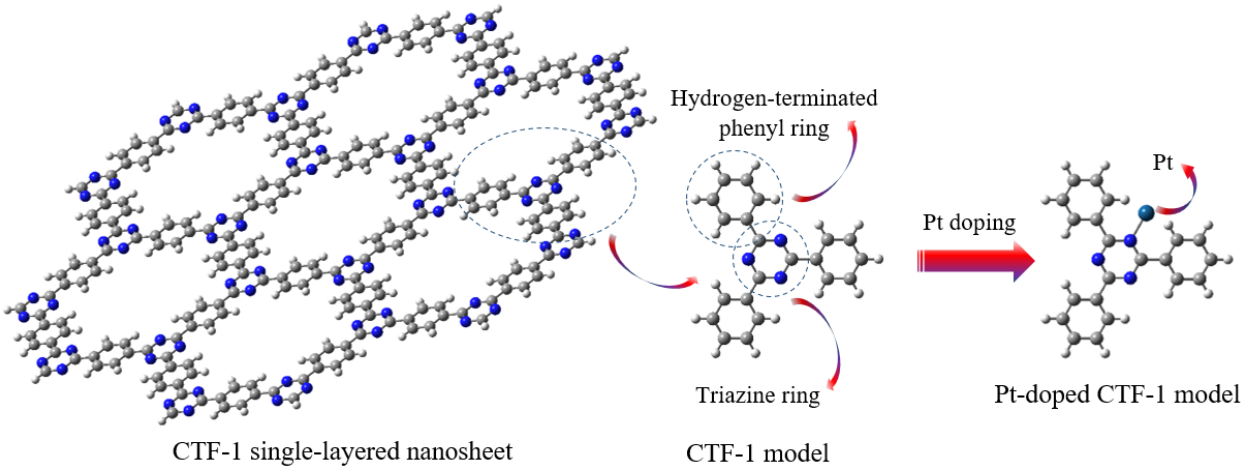

Figure 7.1. Schematic representation of the CTF-1 single-layered nanosheet, CTF-1 model, and Pt-doped CTF-1 model.

7.3.2 DFT method and basis sets

The geometries of the gas species, the pristine and Pt-doped CTF-1 models, are optimized before and after gas adsorption using density-functional theory (DFT). DFT characterization of the electronic structure of gas species (i.e., H_2S, SO_2, SOF_2, and SO_2F_2), the pristine CTF-1, the Pt-doped CTF-1, the gas@CTF-1, and the gas@Pt-doped CTF-1 complexes is performed utilizing the TPSS meta-generalized gradient approximation (meta-GGA) exchange-correlation energy functional [158] with the Grimme-D3 empirical dispersion correction (essential for capturing weak interaction energies, e.g., Van der Waals interactions) [275]. The Pople double-ζ 6-31+G** split valence basis set with polarization functions on heavy atoms and H atoms and diffuse functions on heavy atoms is used for C, N, O, S, F, and H atoms [276]. In the meantime, the effective-core potential (ECP)-based Los Alamos National Laboratory 2 double-ζ (Lanl2DZ) basis set is used for the Pt atom [277]. The TPSS exchange-correlation energy functional with the 6-31+G**/Lanl2DZ mixed basis set has been shown to provide an appropriate description of the electronic structure of TM-containing complexes [278]. Molecular geometries are fully optimized, and subsequent vibrational analysis is performed to confirm that the resulting structures are indeed energy-minima (i.e., only real frequency). Ultimately, natural bond orbital (NBO) analysis is carried out to assess the extent of charge delocalization and transfer between the adsorbates and the gas sensor models and unveil the intermolecular interactions that stabilize the complexes.

7.3.3 Calculations

The heat of formation (E_{form}) of the Pt-doped CTF-1 gas sensor is calculated as:

$$E_{form} = E_{Pt@CTF-1} - (E_{CTF-1} + E_{Pt}) + E_{BSSE}^{CP} \quad \text{Eq. 7-1}$$

where $E_{Pt@CTF-1}$, E_{CTF-1}, and E_{Pt} are the total energies of Pt-doped CTF-1, CTF-1, and the Pt atom, respectively. E_{BSSE}^{CP} is the basis set superposition error correction calculated through the counterpoise (CP) method on the basis of Pt atom and pristine CTF-1 fragments. Large heats of formation imply high levels of structural stability. In the meantime, gas adsorption energies (E_{ads}) are calculated as:

$$E_{ads} = E_{gas@sensor} - (E_{sensor} + E_{gas}) + E_{BSSE}^{CP} \quad \text{Eq. 7-2}$$

where $E_{gas@sensor}$, E_{sensor}, and E_{gas} are the total energies of the adsorbed gas-sensor system, the gas sensor (i.e., the Pt-doped CTF-1 or pristine CTF-1 gas sensors) and the adsorbed gas molecule, respectively.

Eq. 7-3 is employed to calculate the bandgap (E_{BG}):

$$E_{BG} = E_{LUMO} - E_{HOMO} \quad \text{Eq. 7-3}$$

where E_{LUMO} and E_{HOMO} are the energies of the lowest unoccupied molecular orbital (LUMO) and the highest occupied molecular orbital (HOMO), respectively. This approach is useful for assessing the change in electrical conductivity induced by metal doping and gas adsorption.
The sensitivity of the gas sensor (i.e., pristine and Pt-doped CTF-1) towards the target adsorbate is determined as [272]:

$$S = \exp\left(\frac{\left(\left|E_{BG_{gas@sensor}} - E_{BG_{sensor}}\right|\right)}{2k_BT}\right) - 1 \quad \text{Eq. 7-4}$$

where k_B is the Boltzmann constant (8.617×10^{-5} eV K^{-1}), and T is the temperature. $E_{BG_{gas@sensor}}$ and $E_{BG_{sensor}}$ are the bandgap for gas@sensor and sensor, respectively.

7.4 Results and discussion

7.4.1 Geometry optimization of gas molecules

It is essential to establish the most stable structures for gas molecules prior to proceeding with the process of adsorption of gas molecules onto the surface of gas sensors. In this sense, the optimized structures of H_2S, SO_2, SOF_2, and SO_2F_2 are obtained and exhibited in Figure 7.2 a-d. The four gas molecules are positioned around the S atom with the multivalent characteristic. The partial charges of the H and S atoms in H_2S are +0.159 e and −0.318 e, respectively (see Figure 7.2-a). The O and S atoms in SO_2 possess partial charges of −0.749 e and +1.498 e, respectively (see Figure 7.2-b). The partial charges of the O, F, and S atoms in SOF_2 are −0.785, −0.478, and +1.740 e, respectively (see Figure 7.2-c). In the meantime, the O, F, and S atoms in SO_2F_2 carry partial charges of −0.787 e, −0.454 e, and +2.482 e, respectively (see Figure 7.2-d). Only in H_2S the S atom is negatively charged, probably because it has a higher electronegativity than the H atom. Due to the increased electronegativity of the O and F atoms, the S atom is positively charged in the remaining gas species (i.e., SO_2, SOF_2, and SO_2F_2). Hence, the S atom is more positively charged in gas molecules with more electronegative atoms.

In the H_2S structure (Figure 7.2-a), the S−H bond has a length of 1.348 Å, and the H−S−H bond angle equals 92.55°, showing a bent molecule (i.e., the bond angle deviated from 180°). The bent structure of SO_2 (Figure 7.2-b) resembles that of H_2S while possessing a longer S−O bond length of 1.482 Å due to the higher oxygen atom's radius than that of the hydrogen atom in H_2S. Besides, a larger O−S−O bond angle of 118.95° is observed in the optimized structure of SO_2 than that in H_2S (92.55°), which can be ascribed to the fact that both the oxygen atoms have lone pair (sometimes called an unshared pair or non-bonding pair), which induce lone pair-lone pair repulsion. Comparing the optimized structure of SO_2F_2 shown in Figure 7.2-d with that of SOF_2 in Figure 7.2-c, it can be observed that the addition of the oxygen atom slightly shortens the lengths of S−O and S−F bonds, from 1.458 Å and 1.664 Å to 1.448 Å and 1.615 Å, respectively. In the meantime, when adding an oxygen atom to SOF_2, the F−S−F bond angle increases from 92.89° to 94.45° in SO_2F_2. These findings are in good accord with previously reported results [266, 279, 280].

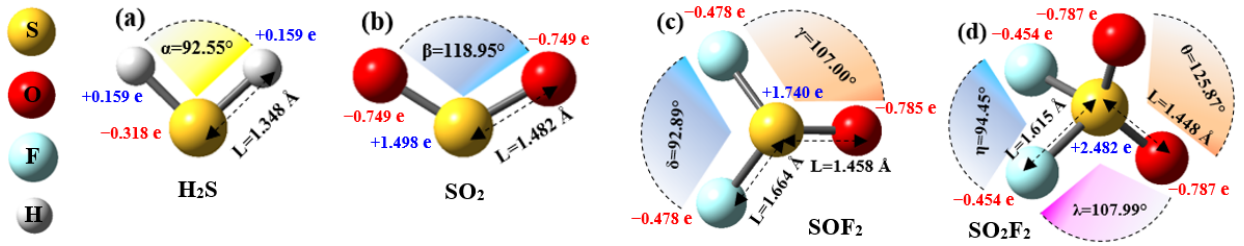

Figure 7.2. The ball-and-stick model representation of the optimized structures of gas molecules.
(a) H_2S, (b) SO_2, (c) SOF_2, and (d) SO_2F_2 with NBO charge distribution calculated with TPSS-D3/6-31+G**. Sulfur (yellow), oxygen (red), fluorine (turquoise), and hydrogen (white).

7.4.2 Electronic properties of the optimized pristine and Pt-doped CTF-1

The most stable structures of the pristine and Pt-doped CTF-1 are shown in Figure 7.3-a & Figure 7.3-b, respectively, along with some critical partial charges on the N atoms and Pt atom obtained through NBO population analysis. The pristine CTF-1 planar structure (see Figure 7.3-a, side view) is distorted/deformed noticeably due to Pt doping (see Figure 7.3-b, side view), demonstrating a strong interaction between the Pt atom and CTF-1. In the Pt-doped structure (Figure 7.3-b), one Pt atom is initially placed in different positions, including on top of the triazine ring and then relaxed with no restrictions/constraints to obtain the optimal structure with minimal energy.

DFT calculations reveal that the Pt atom prefers to be adsorbed onto an N atom of the triazine ring with the formation energy (E_{form}, see Eq. 7-1) of about 2.90 eV. This high value further confirms the strong interactions between the Pt atom and the pristine CTF-1. Besides, the change in Gibbs free energy through the Pt doping in CTF-1 ($\Delta G_{Pt\ doping}$) is calculated to be −2.02 eV. The negative sign of $\Delta G_{Pt\ doping}$ implies a spontaneous doping process.

The distance between the Pt atom and the closest N atom of the triazine ring is 1.935 Å. Besides, NBO population analysis reveals that some charge (−0.061 e) is transferred from the CTF-1 fragment to the Pt atom due to complexation, stabilizing the resultant organometallic structure. According to NBO population analysis, most of this charge transfer occurs between the lone pairs of N atoms of the triazine ring and the Pt atom. Also, a polar sigma (σ) bond is formed between

the closest N atom of the triazine ring and the Pt atom with the occupancy of 1.95936 and approximate composition of 0.8981 N($sp^{2.57}$)+0.4397 Pt($sd^{0.52}$). Hence, the strong interaction between the Pt atom and the pristine CTF-1 results in chemisorption. These findings, in turn, suggest an effective Pt doping capability of CTF materials possessing triazine rings as immobilizing sites.

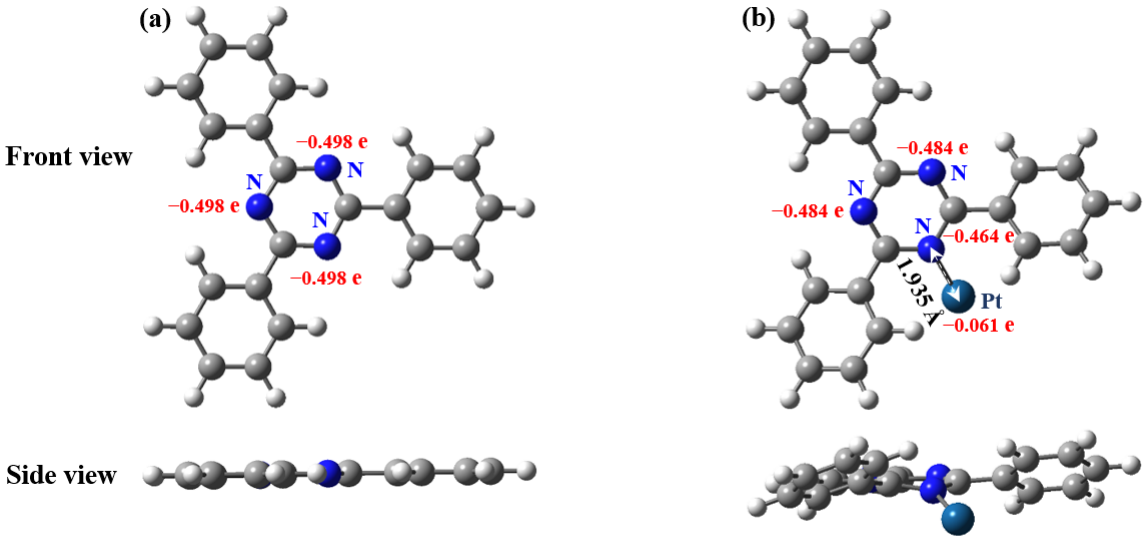

Figure 7.3. The ball-and-stick model representation of the gas sensors.
(a) Pristine CTF-1 structure optimized at TPSS-D3/6-31+G** and (b) Pt-doped CTF-1 structure optimized at TPSS-D3/6-31+G**/Lanl2DZ (b) with some critical partial charges obtained through NBO population analysis. Carbon (gray), nitrogen (blue), hydrogen (white), and platinum (dark teal).

The TDOS and PDOS analyses are also performed to further compare the electronic behavior of the pristine CTF-1 with that of the Pt-doped CTF-1, and the results are presented in Figure 7.4 (a-d). In these figures, the dashed lines represent the Fermi level. The considerable semiconducting characteristic of the pristine CTF-1 is associated with a large bandgap of 3.48 eV (see Figure 7.4-a). In contrast, the Pt-doped CTF-1 possesses a smaller bandgap of 1.06 eV (see Figure 7.4-b). The Pt atom contributes significantly to the DOS of the Pt-doped CTF-1, particularly near the Fermi level (see Figure 7.4-c).

More interestingly, some new states are created near the Fermi level due to the Pt doping, lowering the bandgap and thus facilitating the electron transfer from the valence band into the conduction band. As the bandgap of the Pt-doped CTF-1 is much lower than that of the pristine CTF-1 (1.06 vs. 3.48 eV), the Pt atom can notably enhance the electrical conductivity and thus promote the gas adsorption and sensing performance of CTF-1. Furthermore, the PDOS projected on the Pt atom's 5d and 6s orbitals and the N atom's 2p orbital suggests a significant overlap in the energy range of −2 to 2 eV (i.e., around the Fermi level), demonstrating the Pt atom's capability in hybridization with the N atom of the triazine ring of CTF-1 (see Figure 7.4-d).

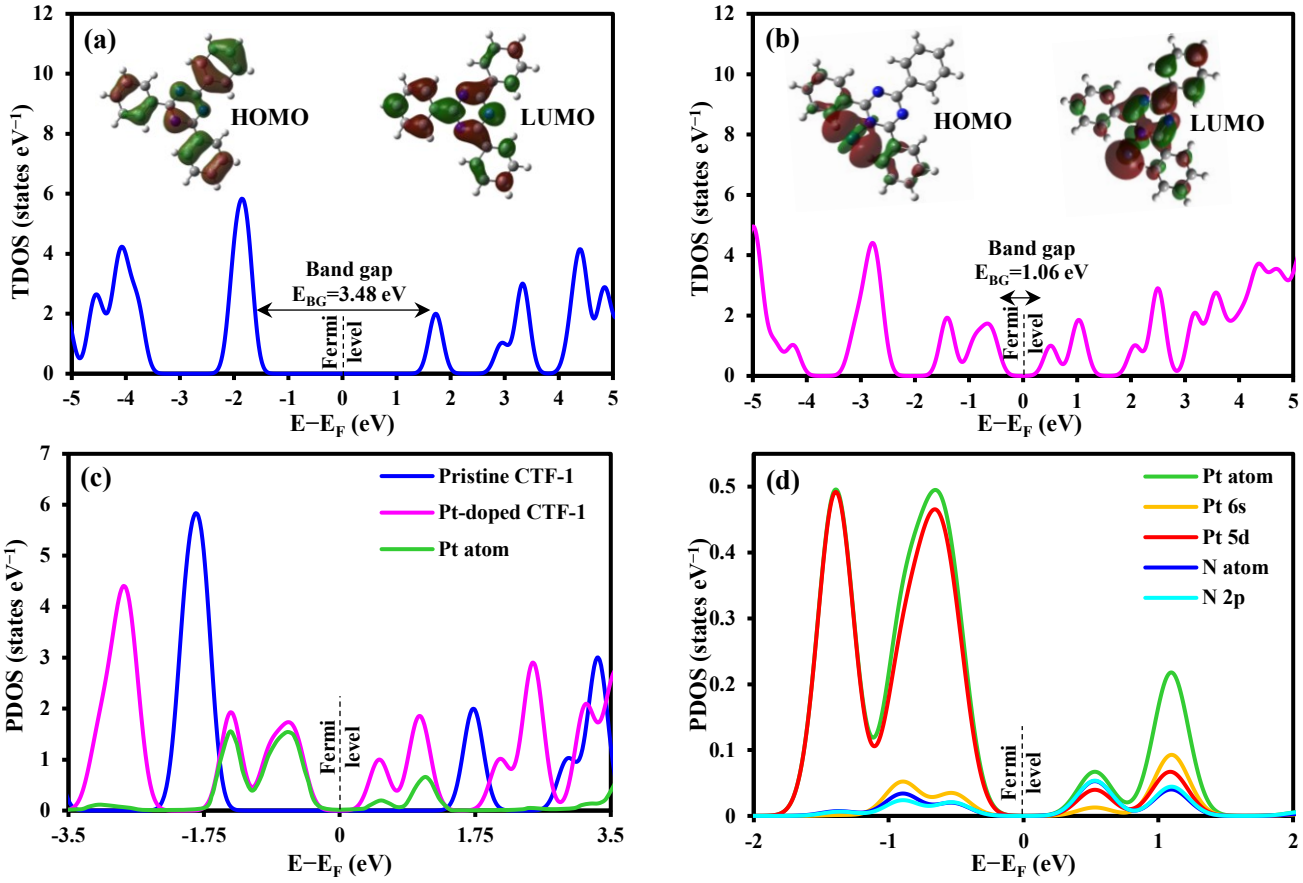

Figure 7.4. DOS plots for the gas sensors.
TDOS of (a) pristine CTF-1 calculated at TPSS-D3/6-31+G**, (b) Pt-doped CTF-1 calculated at TPSS-D3/6-31+G**/Lanl2DZ (b), PDOS of (c) the Pt atom in the Pt-doped CTF-1, and (d) projected on the Pt's 5d and 6s orbitals and the N's 2p orbital. Insets in (a) & (b) show the HOMO and LUMO of the systems visualized at the isovalue of 0.025. The Fermi level is set to zero.

7.4.3 Gas adsorption onto pristine CTF-1

Figure 7.5 (a-d) represents the adsorption models of the pristine CTF-1 for SF_6 decomposition gases (i.e., H_2S, SO_2, SOF_2, and SO_2F_2). Besides, the adsorption parameters, including adsorption energy (E_{ads}, see Eq. 7-2) and net charge transfer (Q_T) for these systems are shown in Table 7.1. The adsorbing distances (D) representing the shortest distance between the adsorbent and the atom in the adsorbate species (i.e., gas molecules), along with some of the geometric characteristics of the adsorbed gas molecules (e.g., bond lengths and bond angles), are also presented in Table 7.1. E_{ads} values for H_2S, SO_2, SOF_2, and SO_2F_2 due to adsorption onto the pristine CTF-1 surface are 0.25, 0.27, 0.31, and 0.18 eV, respectively. These small values indicate that the pristine CTF-1 is incapable of adsorbing the gas species efficiently. Meanwhile, according to NBO population analysis, due to adsorption, a small amount of charge is transferred between the pristine CTF-1 and H_2S (−0.019 e), SO_2 (−0.027 e), SOF_2 (−0.022 e), and SO_2F_2 (+0.006 e). A positive sign denotes a charge transfer from the gas species to the pristine CTF-1, whereas a negative sign denotes a charge transfer from the pristine CTF-1 to the gas species. In the meantime, the adsorbed gas molecules' geometric characteristics (see Table 7.1) and partial charges (see Figure 7.5) are

approximately identical to those of the isolated gas molecules shown in Figure 7.2 (i.e., before adsorption), demonstrating weak interactions in the gas@CTF-1 adsorption systems.

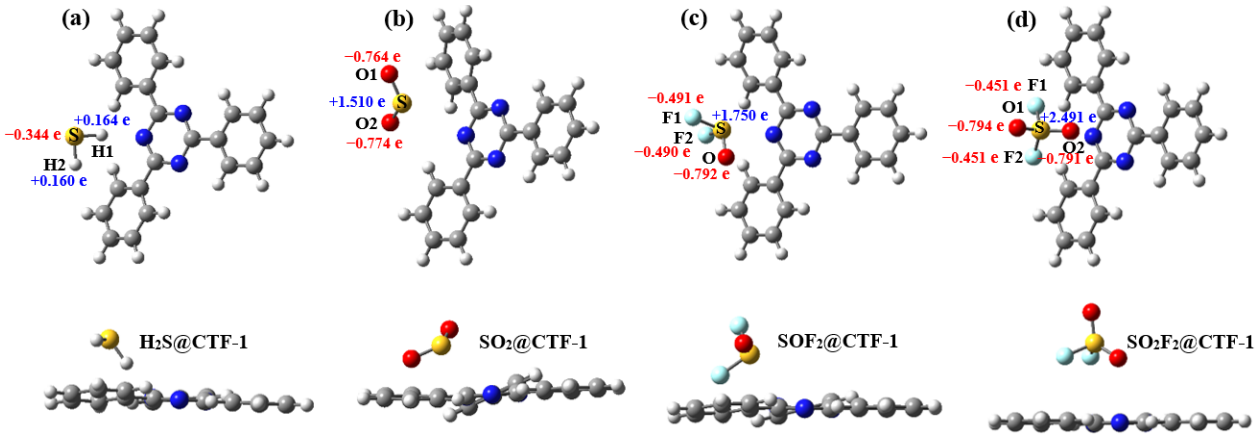

Figure 7.5. The adsorption models of the pristine CTF-1 for (a) H_2S, (b) SO_2, (c) SOF_2, and (d) SO_2F_2 optimized at TPSS-D3/6-31+G**.
Front view (top row) and side view (bottom row). Partial charges are calculated based on NBO population analysis.

Table 7.1. The adsorption parameters and the adsorbed gas molecules' geometric characteristics for the gas@CTF-1 adsorption systems calculated at TPSS/6-31+G**.
(Gas molecules: H_2S, SO_2, SOF_2, and SO_2F_2).

System	D (Å)	Bond length (Å)	Bond angle (degree)	E_{ads} (eV)	Q_T (e)
H_2S@CTF-1	2.094 (H2−S−H1···N)	1.363 (H1−S) 1.349 (H2−S)	92.08 (H−S−H)	0.25	−0.019
SO_2@CTF-1	3.332 (O−S···N)	1.485 (O1−S) 1.486 (O2−S)	117.90 (O−S−O)	0.27	−0.027
SOF_2@CTF-1	2.850 (OF2−S···N)	1.460 (O−S) 1.675 (F1−S) 1.681 (F2−S)	106.67 (O−S−F) 91.69 (F−S−F)	0.31	−0.022
SO_2F_2@CTF-1	3.273 (O1F2S−O2···N)	1.447 (O1−S) 1.449 (O2−S) 1.613 (F1−S) 1.613 (F2−S)	125.54 (O−S−O) 108.22 (O−S−F) 94.73 (F−S−F)	0.18	+0.006

7.4.4 Gas adsorption onto Pt-doped CTF-1

After geometry optimization and calculating the adsorption energies, the most stable adsorption complexes of the SF_6 decomposition gas species onto the Pt-doped CTF-1 are shown in Figure 7.6 (a-d). Similar to the gas@CTF-1 adsorption systems, the adsorption parameters for the gas@Pt-doped CTF-1 adsorption systems, along with the adsorbed molecules' geometric characteristics and partial charges, are shown in Table 7.2. E_{ads} for H_2S, SO_2, SOF_2, and SO_2F_2 due to adsorption onto the Pt-doped CTF-1 surface are 1.93, 2.41, 6.27, and 7.98 eV, respectively. These high values demonstrate that the Pt-doped CTF-1 can efficiently adsorb the gas species. Besides, based on NBO population analysis, due to adsorption, a considerable charge is transferred between the Pt-doped CTF-1 and H_2S (+0.234 e), SO_2 (+0.047 e), SOF_2 (−0.582 e), and SO_2F_2 (−0.225 e). NBO

population analysis also shows that H_2S and SO_2 are physically adsorbed onto the Pt-doped CTF-1 (i.e., no new bond is formed), whereas SOF_2 and SO_2F_2 are essentially chemisorbed by forming new bonds between the Pt and S atoms. The newly formed sigma (σ) bonds between the Pt and S atoms in the SOF_2@Pt-doped CTF-1 and SO_2F_2@Pt-doped CTF-1 adsorption systems possess the approximate composition of 0.6969 $Pt(sp^{0.08}d^{3.4})$+0.7172 $S(sp^{0.99}d^{0.09})$ with an occupancy of 1.96902, and 0.6243 $Pt(sp^{0.49}d^{3.31})$+0.7812 $S(sp^{2.13}d^{0.03})$ with an occupancy of 1.95161, respectively. In the meantime, the values for adsorbed gas molecules' geometric characteristics (see Table 7.2) and partial charges (see Figure 7.6) deviated from those of the isolated gas molecules shown in Figure 7.2 (i.e., before adsorption), signifying strong interactions in the gas@Pt-doped CTF-1 adsorption systems. This deviation is more severe for the chemically adsorbed SOF_2 and SO_2F_2 gas species.

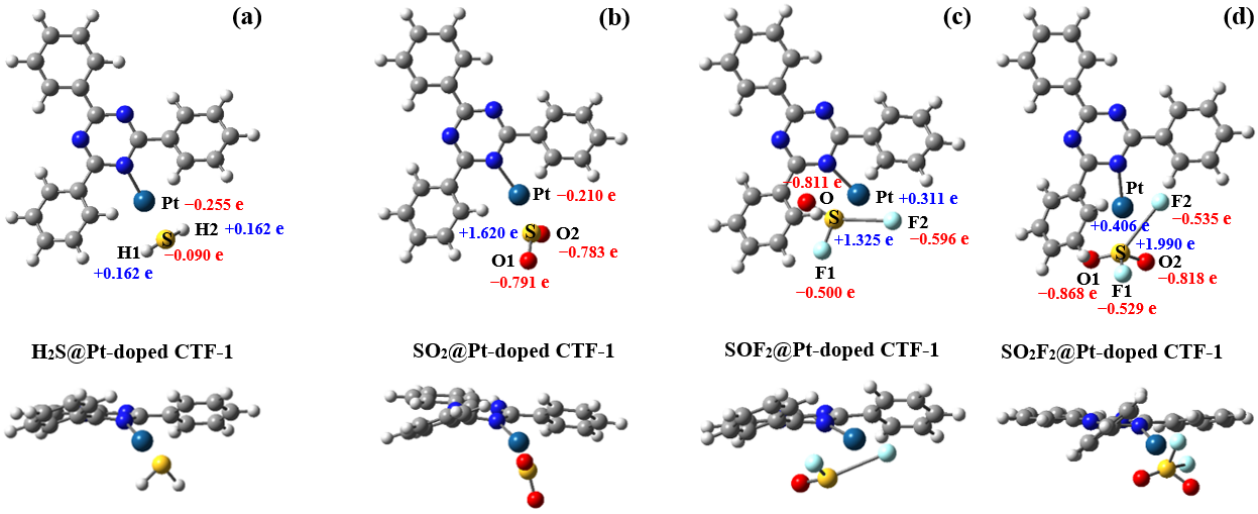

Figure 7.6. The adsorption models of the Pt-doped CTF-1 for (a) H_2S, (b) SO_2, (c) SOF_2, and (d) SO_2F_2 optimized at TPSS-D3/6-31+G**/Lanl2DZ.
Front view (top row) and side view (bottom row). Partial charges are calculated based on NBO population analysis.

Table 7.2. The adsorption parameters and the adsorbed gas molecules' geometric characteristics for the gas@Pt-doped CTF-1 adsorption systems obtained at TPSS/6-31+G**/Lanl2DZ.
(Gas molecules: H_2S, SO_2, SOF_2, and SO_2F_2).

System	D (Å)	Bond length (Å)	Bond angle (degree)	E_{ads} (eV)	Q_T (e)
H_2S@Pt-doped CTF-1	2.236 (H−S···Pt)	1.364 (H1−S) 1.364 (H2−S)	91.84 (H−S−H)	1.93	+0.234
SO_2@Pt-doped CTF-1	2.130 (O−S···Pt)	1.489 (O1−S) 1.491 (O2−S)	117.25 (O−S−O)	2.41	+0.047
SOF_2@Pt-doped CTF-1	1.982 (OF1S−F2···Pt)	1.498 (O−S) 1.714 (F1−S) 2.894 (F2−S)	105.41 (O−S−F) 93.72 (F−S−F)	6.27	−0.582
SO_2F_2@Pt-doped CTF-1	1.969 (O_2F1S−F2···Pt)	1.482 (O1−S) 1.471 (O2−S) 1.714 (F1−S) 2.988 (F2−S)	119.69 (O−S−O) 103.74 (O−S−F) 112.82 (F−S−F)	7.98	−0.225

7.4.5 Investigation of gas sensing properties and mechanisms utilizing DOS analysis

Superior adsorption characteristics, such as high adsorption energy and marked change in physicochemical properties (e.g., conductivity) due to adsorption, are the foundation for efficient sensing of the desired gas species. In this respect, sensitivity (S) based on bandgap change is often employed to assess the sensing capability of the designed gas sensors, such as the pristine and Pt-doped CTF-1 gas sensors. Figure 7.7 through Figure 7.10 illustrate the TDOS and PDOS curves of gas@CTF-1 and gas@Pt-doped CTF-1 adsorption systems. It is evident from these figures that the bandgaps have altered to some extent after the adsorption of gas species. As a result, the adsorption systems' conductivity varies following gas adsorption. The changes in sensitivity of the gas sensors towards the SF_6 breakdown gases are caused by variances in TDOS.

7.4.5.1 H_2S sensing

After the adsorption of H_2S onto the pristine and Pt-doped CTF-1 gas sensors, the change in TDOS is studied in the range of −5 to 5 eV (see Figure 7.7 (a-b)). As seen from Figure 7.7-a, the TDOS curves before and after the H_2S adsorption onto the pristine CTF-1 virtually resemble each other, except for the appearance of a new state around the Fermi level, indicating an increase in the electrical conductivity of the H_2S@CTF-1 adsorption system. Moreover, TDOS moves slightly to the left due to the H_2S adsorption. In the meantime, the bandgap decreases from 3.48 to 2.89 eV (see Figure 7.7-a).

In the case of the Pt-doped CTF-1 gas sensor, TDOS moves slightly to the right after the H_2S adsorption (see Figure 7.7-b). Meanwhile, the bandgap of the system increases from 1.06 to 1.28 eV, decreasing the system's conductivity. In this case, no conspicuous new states appear near the Fermi level (see Figure 7.7-b). Hence, it is expected that the pristine CTF-1 with a larger ΔE_{BG} (0.59 eV vs. 0.22 eV) shows a better performance toward sensing H_2S than the Pt-doped CTF-1.

Since the electrons in the atoms' outer orbitals significantly impact TDOS, PDOS in certain outer orbitals (e.g., S 3p, Pt 6s, and Pt 5d) is also investigated (see Figure 7.7 (c-d)). As seen from Figure 7.7-c, there is no overlap between the DOS curves of H_2S and the pristine CTF-1 near the Fermi level. Meanwhile, the newly formed state around the Fermi level in the DOS curve of H_2S@CTF-1 (see Figure 7.7-a & Figure 7.7-c) emerges from that of the adsorbed H_2S molecule (see Figure 7.7-c). Additionally, a close overlap between the DOS curve of the H_2S molecule and that of the S atom's 3p orbital in H_2S is observed in Figure 7.7-c, further confirming that the outer orbitals significantly influence the TDOS.

While the majority of states of the H_2S@Pt-doped CTF-1 adsorption system near the Fermi level is due to the Pt atom's 5d orbital (see Figure 7.7-d), small overlaps between the PDOS of the Pt 5d and 6s orbitals and the S 3p orbital can be pinpointed (see Figure 7.7-d). These results imply that the pristine and Pt-doped CTF-1 gas sensors adsorb H_2S physically with different strengths.

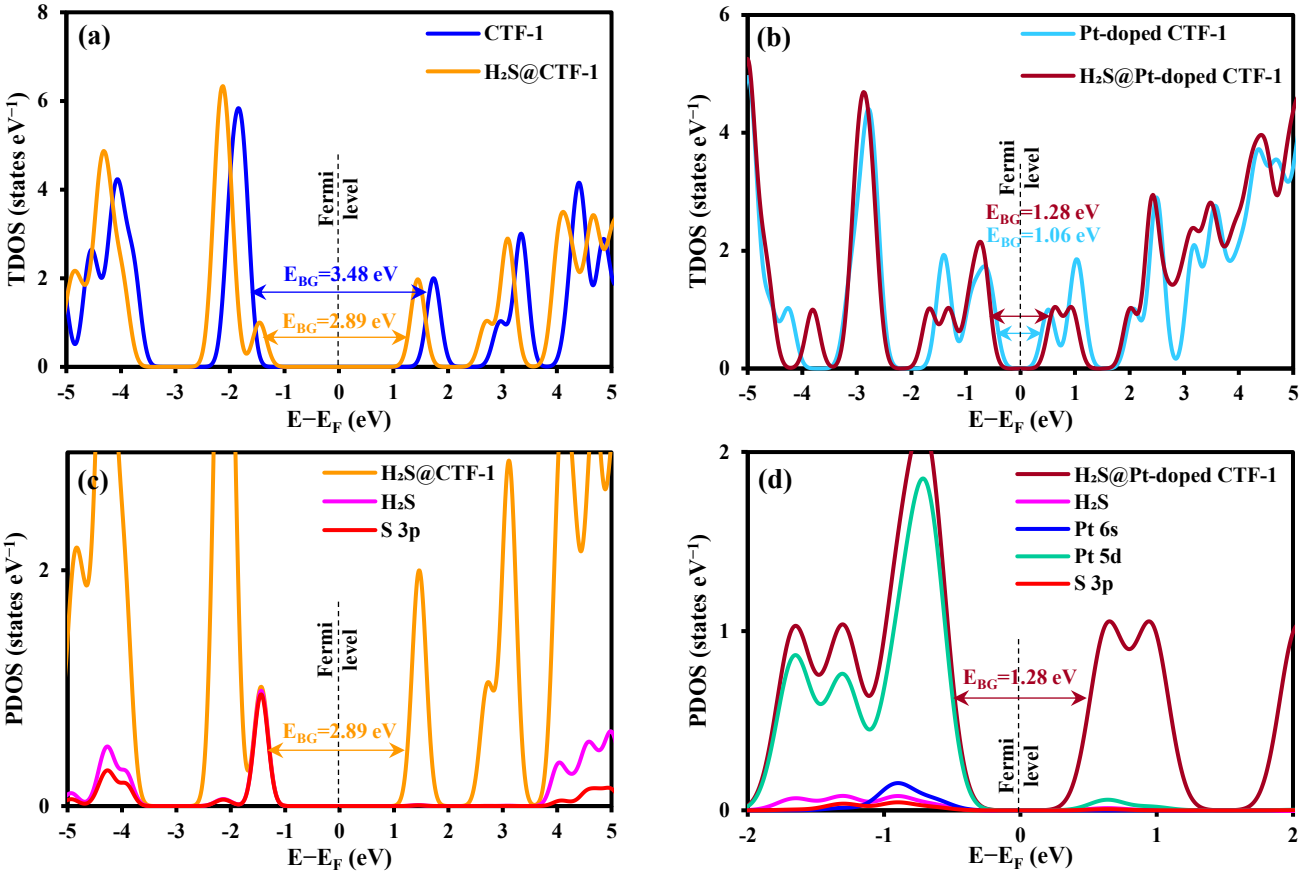

Figure 7.7. DOS plots for H_2S sensing using pristine and Pt-doped CTFs.
(a) TDOS of the pristine CTF-1 before and after H_2S adsorption, (b) TDOS of the Pt-doped CTF-1 before and after H_2S adsorption, (c) PDOS of H_2S and PDOS projected on the S' 3p atomic orbital for the H_2S@CTF-1 adsorption system, and (d) PDOS of H_2S and PDOS projected on the Pt's 5d and 6s atomic orbitals and S's 3p atomic orbital for the H_2S@Pt-doped CTF-1 adsorption system.

7.4.5.2 SO_2 sensing

After the adsorption of SO_2 onto the pristine and Pt-doped CTF-1 gas sensors, the change in TDOS is investigated in the range of −5 to 5 eV (see Figure 7.8 (a-b)). The TDOS curves before and after SO_2 adsorption onto the pristine CTF-1 are relatively comparable, as shown in Figure 7.8-a. However, a new state emerged around the Fermi level, which denotes an increase in the electrical conductivity of the SO_2@CTF-1 adsorption system. Furthermore, TDOS moves to the right due to SO_2 adsorption. In the meantime, the bandgap is lowered from 3.48 to 2.14 eV (see Figure 7.8-a). In the case of the Pt-doped CTF-1 gas sensor, TDOS moves to the right after the SO_2 adsorption (see Figure 7.8-b). Meanwhile, the bandgap of the system increases from 1.06 to 1.73 eV, decreasing the system's conductivity. In this case, no noticeable new states are formed around the Fermi level (see Figure 7.8-b). Therefore, it is expected that the pristine CTF-1 with a larger ΔE_{BG} (1.34 eV vs. 0.67 eV) performs better than the Pt-doped CTF-1 in sensing SO_2.

PDOS curves projected on the S 3p, O 2p, Pt 6s, and Pt 5d atomic orbitals are also examined (see Figure 7.8 (c-d)). As seen from Figure 7.8-c, there is no marked overlap between the DOS curves of SO_2 and the pristine CTF-1 near the Fermi level. Meanwhile, the newly formed state around the

Fermi level in the DOS curve of SO_2@CTF-1 (see Figure 7.8-a & Figure 7.8-c) arises from that of the adsorbed SO_2 molecule (see Figure 7.8-c). Similar to the H_2S@Pt-doped CTF-1 adsorption system, the majority of states of the SO_2@Pt-doped CTF-1 adsorption system near the Fermi level is due to the Pt atom's 5d orbital (see Figure 7.8-d). Besides, slight overlaps between the PDOS of the Pt 5d and 6s orbitals and the S 3p orbital are observed (see Figure 7.8-d). These results imply that the pristine and Pt-doped CTF-1 gas sensors adsorb SO_2 physically.

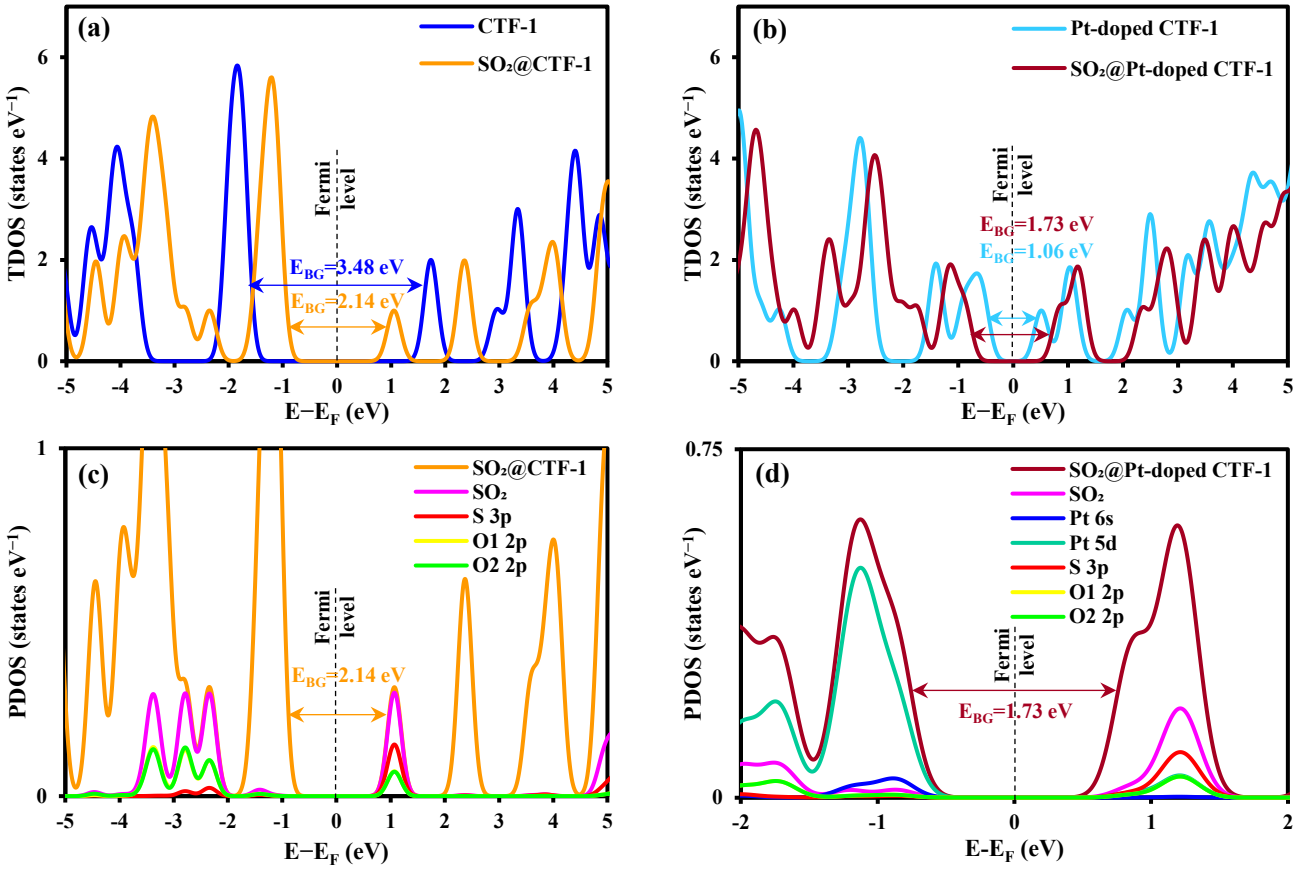

Figure 7.8. DOS plots for H_2S sensing using pristine and Pt-doped CTFs.
(a) TDOS of the pristine CTF-1 before and after SO_2 adsorption, (b) TDOS of the Pt-doped CTF-1 before and after SO_2 adsorption, (c) PDOS of SO_2 and PDOS projected on the S' 3p and O' 2p atomic orbitals for the SO_2@CTF-1 adsorption system, and (d) PDOS of SO_2 and PDOS projected on the Pt's 5d and 6s atomic orbitals and the S's 3p and O' 2p atomic orbitals for the SO_2@Pt-doped CTF-1 adsorption system.

7.4.5.3 SOF_2 sensing

Figure 7.9 (a-b) shows the changes in TDOS of the pristine and Pt-doped CTF-1 in the range of −5 to 5 eV before and after SOF_2 adsorption. Although the TDOS curve of the SOF_2@CTF-1 adsorption system minimally differs from that of the pristine CTF-1; however, these two curves closely overlap near the Fermi level with no additional new states due to the SOF_2 adsorption (see Figure 7.9-a). The bandgap is slightly reduced from 3.48 to 3.28 eV due to SOF_2 adsorption (see Figure 7.9-a). When adsorbed onto the Pt-doped CTF-1 gas sensor, SOF_2 causes significant changes in the TDOS (see Figure 7.9-b). The bandgap of the system rises from 1.06 to 1.96 eV, lowering the system's electrical conductivity. In this case, no additional states are created around

the Fermi level (see Figure 7.9-b). Thus, it is expected that the Pt-doped CTF-1 with a larger ΔE_{BG} (0.90 eV vs. 0.20 eV) outperforms the pristine CTF-1 in sensing SOF_2.

Figures 7.9 (c-d) represent the PDOS curves projected on the S 3p, O 2p, F 2p, Pt 6s, and Pt 5d atomic orbitals. As seen from Figure 7.9-c, there is no notable overlap between the DOS curves of SOF_2 and that of the pristine CTF-1 around the Fermi level. However, as seen from Figure 7.9-d, the considerable orbital hybridization around the Fermi level for the SOF_2 adsorption onto the Pt-doped CTF-1 is predominantly caused by the significant overlapping of the Pt 5d, Pt 6s, S 3p, O 2p, and F2 2p atomic orbitals. These results suggest that the pristine CTF-1 has a decreased tendency toward sensing SOF_2. At the same time, the Pt-doped CTF-1 robustly adsorbs SOF_2 with a high degree of orbital hybridization near the Fermi level, forming new chemical bonds. In light of the obtained partial charges (see Figure 7.6-c) and different electronegativity between the Pt and F, O, and S atoms, as well as the results of NBO population analysis, we speculate that the Pt atom adsorbs the F2 atom in an ionic binding nature where the electrostatic interactions play a key role [281]. In the meantime, the S atom is covalently bonded to the Pt atom.

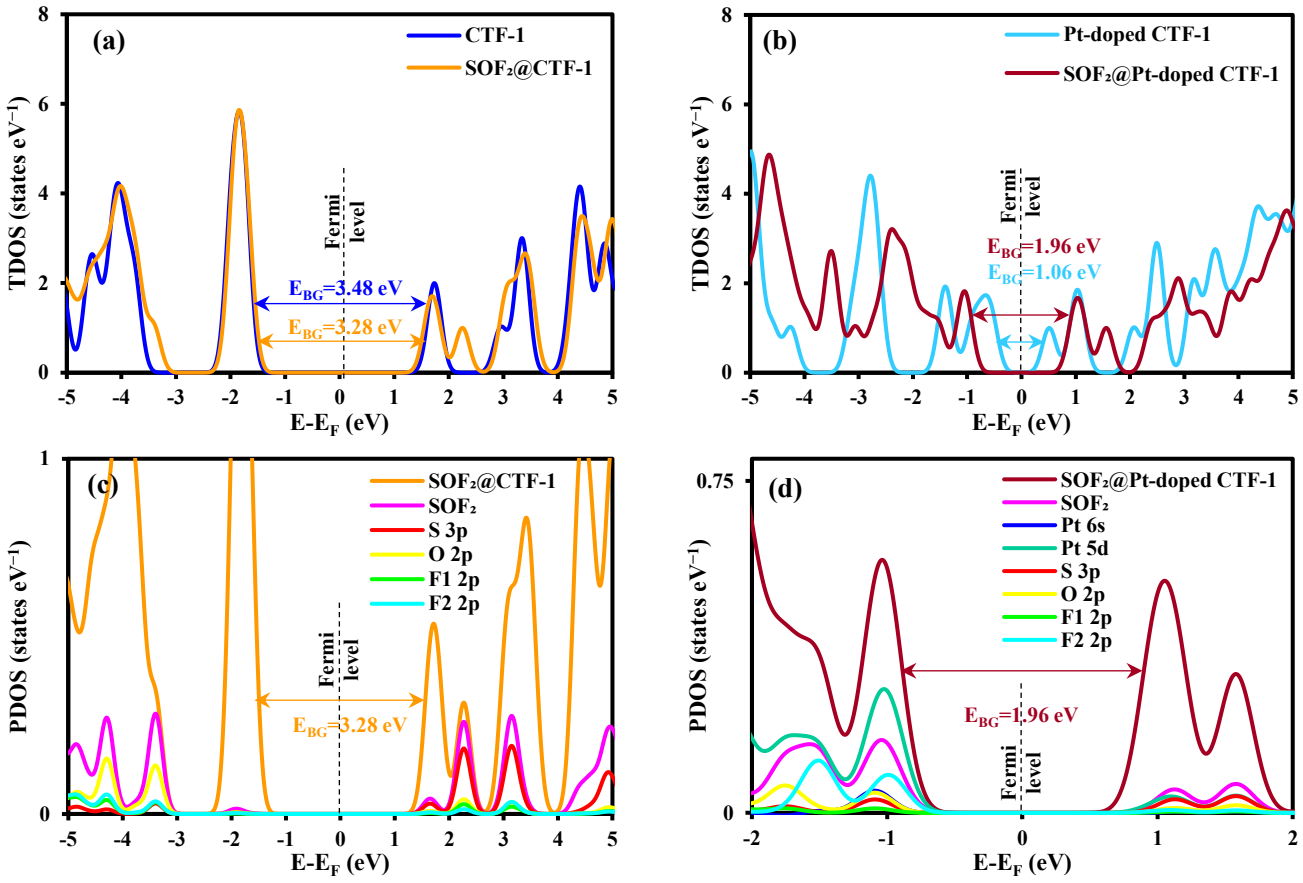

Figure 7.9. DOS plots for H_2S sensing using pristine and Pt-doped CTFs.
(a) TDOS of pristine CTF-1 before and after SOF_2 adsorption, (b) TDOS of Pt-doped CTF-1 before and after SOF_2 adsorption, (c) PDOS of SOF_2 and PDOS projected on the S 3p, O 2p, and F 2p atomic orbitals for SOF_2@CTF-1, and (d) PDOS of SOF_2 and PDOS projected on the Pt 5d and 6s atomic orbitals and the S 3p, O 2p, and F 2p atomic orbitals for SOF_2@Pt-doped CTF-1.

7.4.5.4 SO_2F_2 sensing

Figures 7.10 (a-b) display the variations in TDOS of pristine and Pt-doped CTF-1 in the range of −5 to 5 eV before and after SO_2F_2 adsorption. As seen from Figure 7.10-a, the TDOS curve of SO_2F_2@CTF-1 resembles that of pristine CTF-1 with no additional new states due to the SO_2F_2 adsorption. Besides, the bandgap remains constant with a negligible reduction from 3.48 to 3.46 eV after the SO_2F_2 adsorption. Due to SO_2F_2 adsorption onto Pt-doped CTF-1, substantial changes in TDOS occurred (Figure 7.10-b). The bandgap of the system increases from 1.06 to 2.32 eV, decreasing the system's conductivity. It is anticipated that Pt-doped CTF-1 would perform better than pristine CTF-1 in detecting SO_2F_2 due to its higher ΔE_{BG} (1.26 eV vs. 0.02 eV).

The PDOS curves projected on the S 3p, O 2p, F 2p, Pt 6s, and Pt 5d atomic orbitals are shown in Figures 7.10 (c-d). The DOS curves of SO_2F_2 and pristine CTF-1 do not overlap at the Fermi level, as shown in Figure 7.10-c. However, as can be observed from Figure 7.10-d, the significant overlapping of the Pt 5d, Pt 6s, S 3p, O1 2p, O2 2p, and F2 2p atomic orbitals causes considerable orbital hybridizations around the Fermi level for the SO_2F_2 adsorption onto Pt-doped CTF-1. These findings show that SO_2F_2 sensing by pristine CTF-1 is subpar. We hypothesize that the Pt atom binds the F2 atom by electrostatic interactions similar to that described for SOF_2 adsorption.

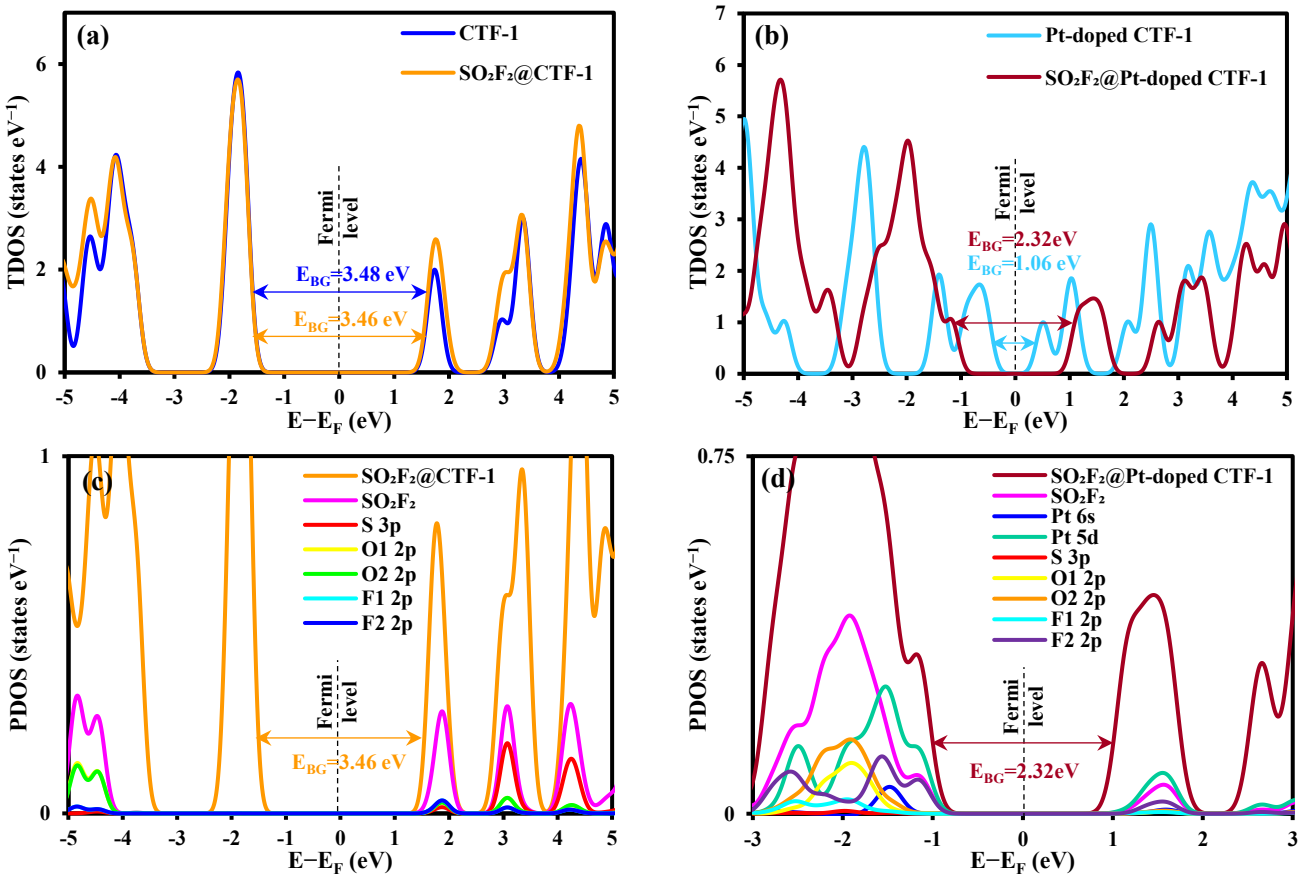

Figure 7.10. DOS plots for H_2S sensing using pristine and Pt-doped CTFs.
(a) TDOS of the pristine CTF-1 before and after SO_2F_2 adsorption, (b) TDOS of the Pt-doped CTF-1 before and after SO_2F_2 adsorption, (c) PDOS of SO_2F_2 and PDOS projected on the S 3p, O 2p, and F 2p atomic orbitals for SO_2F_2@CTF-1, and (d) PDOS of SO_2F_2 and PDOS projected on the Pt 5d and 6s atomic orbitals and the S 3p, O 2p, and F 2p atomic orbitals for SO_2F_2@Pt-doped CTF-1.

7.4.6 Non-covalent interactions (NCI) analysis

The nature of non-bonding interactions, particularly intermolecular interactions, may be comprehended utilizing NCI analysis, which includes 2D RDG (i.e., reduced density gradient) plots and 3D isosurfaces [162]. The non-covalent interactions can be marked in regions with low electron density and RDG. The electron density ($\rho(r)$) and the sign of the second eigenvalue of the electron density Hessian matrix ($sign(\lambda_2)$) correlate with the intensity of the interaction. NCI analysis visualizes and distinguishes between non-covalent interactions in real space, such as Van der Waals forces (weak interactions, $sign(\lambda_2)\rho(r)\approx 0$), strong attraction (e.g., hydrogen bonds, $sign(\lambda_2)\rho(r)<0$) and steric repulsion (e.g., steric effect in rings, $sign(\lambda_2)\rho(r)>0$). Three color codes evaluate the nature of interactions in 3D isosurfaces. London dispersion interactions (weak forces) and strong non-bonding interactions (e.g., strong Coulombic forces and hydrogen bonding) are presented as green and blue patches, respectively. At the same time, the steric repulsive interactions appear red. Similar to 3D isosurfaces, strong electrostatic interactions, repulsive interactions, and weak non-bonding Van der Waals forces, in that order, are accompanied by spikes (i.e., where both the electron density, $\rho(r)$, and its reduced gradient, RDG, are small) in the colors blue, red, and green.

As inferred from Figure 7.11-a and Figure 7.11-e, the main intermolecular interaction in the H_2S@CTF-1 adsorption system is hydrogen bonding (i.e., H-bonding, the greenish-blue spikes in Figure 7.11-a and its corresponding greenish-blue patch in Figure 7.11-e) between one hydrogen atom of H_2S and one of the N atoms of the triazine ring with the adsorbing distance of 2.094 Å (see Table 7.1). The more negative the $sign(\lambda_2)\rho(r)$ value at low RDG values, the stronger the H-bonding interactions. Hence, one might conclude that the H-bonding observed in the H_2S@CTF-1 adsorption system can be categorized as a weak to medium-strength interaction. Such greenish-blue spikes and their corresponding greenish-blue patches are also observable in the 2D RDG plot and 3D isosurface of the SOF_2@CTF-1 adsorption system (see Figure 7.11-c and Figure 7.11-g). This might be due to electrostatic interactions between the positively charged S atom and the negatively charged N atom of the triazine ring with the adsorbing distance of 2.850 Å (see Figure 7.5 and Table 7.1). Moreover, weak Van der Waals interactions) are observed in all four adsorption systems (i.e., the green spikes and their corresponding green patches in Figure 7.11 a-h). Besides, the red spikes in the 2D RDG plots and their corresponding red patches (e.g., mainly observed inside the triazine and phenyl rings) in the 3D isosurfaces demonstrate the presence of strong steric repulsion in all the systems under study.

Similar to the gas@CTF-1 adsorption systems, weak Van der Waals interactions can be observed for the gas@Pt-doped CTF-1 adsorption systems (i.e., the existence of green spikes and green patches in Figure 7.12 (a-d) and Figure 7.12 (e-h), respectively). However, strong steric repulsions have occurred near the adsorption site (i.e., the Pt atom) in all four adsorption systems (i.e., red spikes and red patches in Figure 7.12 (a-d) and Figure 7.12 (e-h), respectively), which might be due to the reduced adsorbing distances compared to those of gas@CTF-1 adsorption systems (compare the results of Table 7.1 with those of Table 7.2 for adsorbing distances). In other words, due to strong Coulombic (i.e., electrostatic) interactions in these systems, the distance between the adsorbate and adsorbent is reduced, resulting in repulsive interactions between the electronic clouds of the interacting atoms. In the meantime, the blue spikes in Figure 7.12 (a-d) and their corresponding blue patches in Figure 7.12 (e-h) demonstrate the existence of electrostatic interactions in these adsorption systems.

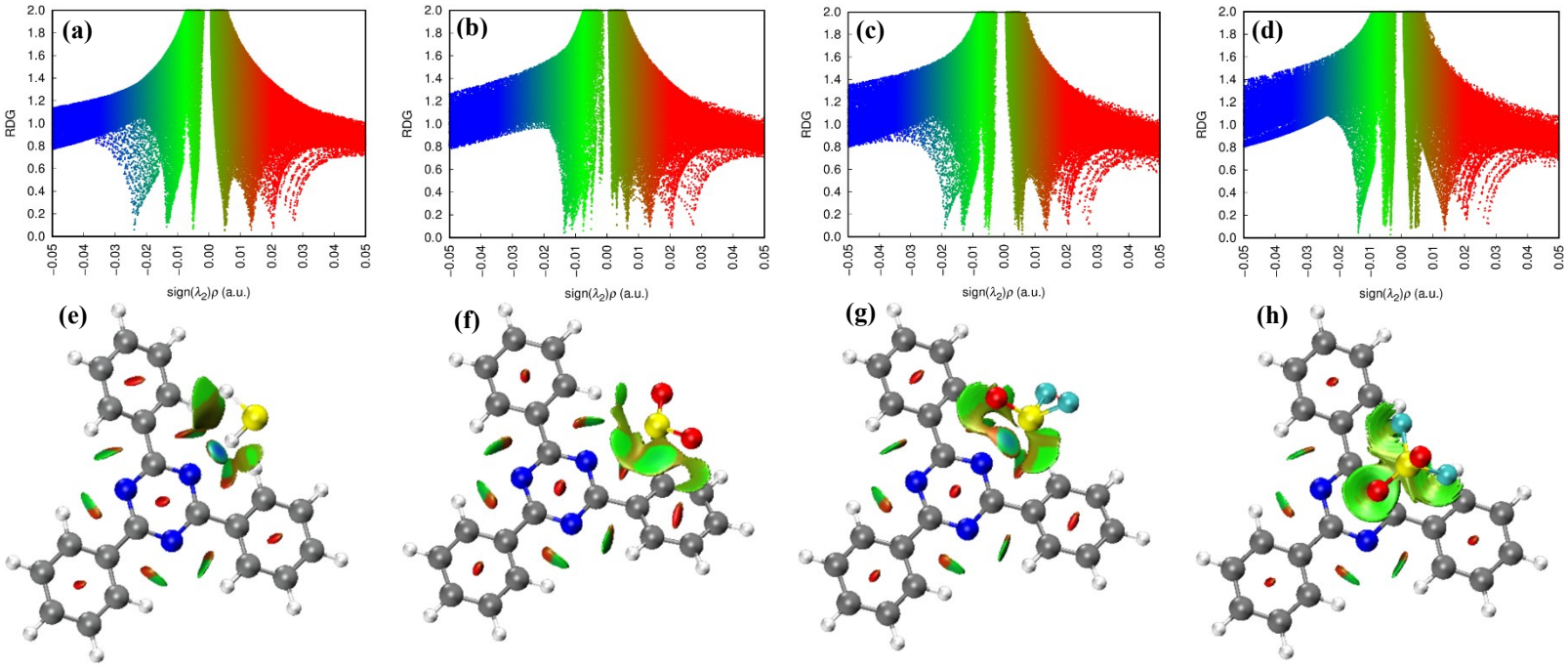

Figure 7.11. 2D RDG scatter plots and 3D isosurfaces of gas@CTF-1.
(a, e) H_2S@CTF-1, (b, f) SO_2@CTF-1, (c, g) SOF_2@CTF-1, and (d, h) SO_2F_2@CTF-1.

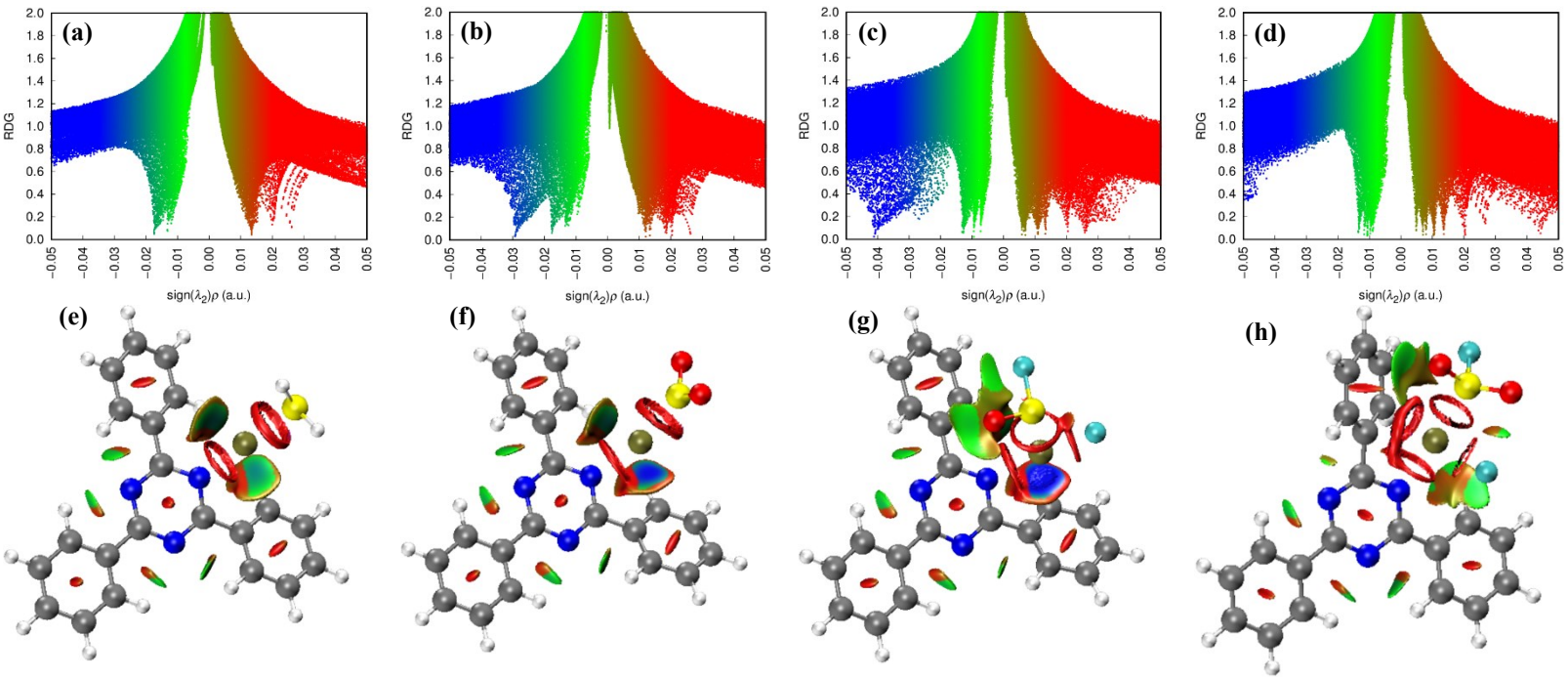

Figure 7.12. 2D RDG scatter plots and 3D isosurfaces of gas@Pt-doped CTF-1.
(a, e) H_2S@Pt-doped CTF-1, (b, f) SO_2@Pt-doped CTF-1, (c, g) SOF_2@Pt-doped CTF-1, and (d, h) SO_2F_2@Pt-doped CTF-1.

7.4.7 Sensor sensitivity

Based on the change in electrical conductivity (i.e., bandgap) of a given gas sensor before and after contact with the gas species, its sensitivity can be computed using Eq. 7-4. Accordingly, the sensitivity values of the pristine and Pt-doped CTF-1 gas sensors for detecting various SF_6 decomposition products is shown in Figure 7.13 (a-b). When detecting H_2S and SO_2, the pristine CTF-1 with a higher change in its bandgap (see Figure 7.7-a and Figure 7.8-a) shows higher sensitivity values than the Pt-doped CTF-1 (see Figure 7.7-b and Figure 7.8-b). For the same reason, the latter outperforms the former in detecting SOF_2 and SO_2F_2 gas species. Furthermore, the sensitivity of sensors toward detecting different gases alters to a certain degree, facilitating the selective detection of understudied gases. In light of the calculated sensitivity values, the Pt-doped CTF-1 exhibits a superior overall sensing capability than the pristine CTF-1.

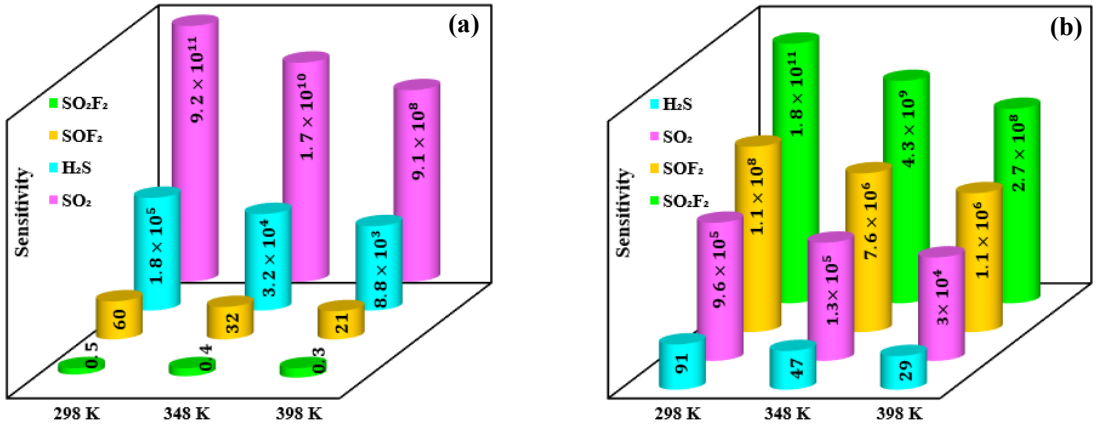

Figure 7.13. Sensitivity of gas sensors.
(a) Pristine CTF-1 and (b) Pt-doped CTF-1 gas sensors.

7.5 Conclusion

This study investigated the sensing capability of pristine and Pt-doped CTF-1 for SF_6 decomposition gas products. To improve the gas adsorption and detection, Pt was doped into CTF-1, increasing its charge carrier mobility and, thus, electrical conductivity. DFT calculations revealed that the Pt atom prefers to be strongly adsorbed onto an N atom of the triazine ring with a high formation energy of about 2.90 eV. E_{ads} for H_2S, SO_2, SOF_2, and SO_2F_2 due to adsorption onto the pristine CTF-1 surface were 0.25, 0.27, 0.31, and 0.18 eV, respectively. These small values indicated that the pristine CTF-1 is incapable of adsorbing the gas species efficiently. On the other hand, E_{ads} for H_2S, SO_2, SOF_2, and SO_2F_2 due to adsorption onto the Pt-doped CTF-1 surface were 1.93, 2.41, 6.27, and 7.98 eV, respectively. These high values demonstrated that the Pt-doped CTF-1 could efficiently adsorb the gas species. The CTF-1 showed superior sensing performance for H_2S and SO_2, while the Pt-doped CTF-1 displayed better sensing performance for SOF_2 and SO_2F_2, based on the DOS studies and the change in the energy bandgap of the gas sensors upon gas adsorption. According to NCI analysis, the gas@CTF-1 and gas@Pt-doped CTF-1 adsorption systems exhibited weak Van der Waals interactions.

8 Chapter 8: General Conclusions

Covalent triazine frameworks (CTFs) have shown fascinating textural, structural, thermal, and physicochemical properties with the potential to be implemented in real-world applications. CTFs with triazine rings comprising N atoms are pre-functionalized supramolecular structures. The existence of the N atoms in their skeleton endows them with a high potential to be used as an adsorbent for capturing acidic/electron-deficient micropollutants from various phases/environments. In the meantime, due to their electron-rich conjugated architectures along with their inherent basicity, CTFs have the potential to be further functionalized and, thus, task-specific materials.

In the first phase of this dissertation (Chapter 5), benefiting from the electron-rich structure of conjugated CTFs further functionalized by π-conjugated C=C double and C≡C triple bonds, we succeeded in capturing radioiodine in both the gas and liquid phases with ultrahigh adsorption efficiency. Therefore, further functionalization of CTF materials is possible and highly beneficial for enhancing their adsorption performance toward the uptake of target species. In brief, we created novel conjugated CTFs using a straightforward Friedel-Crafts alkylation process, employing cyanuric chloride as the cross-linking agent and incorporating DPA and TS as backbone components. Each polymer's structure contains abundant π-conjugated segments crucial for effective iodine−π interactions.

We consciously introduced nitrogen atoms within the frameworks, i.e., in the triazine moieties, to enhance iodine adsorption through Lewis acid-base interactions. When compared to CTF-TS, CTF-DPA exhibited a stronger attraction to iodine species. Even after washing with ethanol and subjecting the CTFs to heat treatment in a dynamic vacuum, their exceptional iodine adsorption capabilities remained intact. The C≡C triple bond, conjugated triazine, and phenyl groups shared π-electrons with the adsorbed molecular iodine, promoting the generation of charged (poly)iodide species. This means the charge transfer from the frameworks to the iodine molecule influenced its electronic structure, facilitating the formation of (poly)iodide species and achieving a high iodine adsorption capacity in both vapor and organic phases. The C≡C triple bond proved more effective at adsorbing and stabilizing (poly)iodide species than the C=C double bond, making CTF-DPA a superior platform for iodine adsorption. These findings are crucial for designing optimal CTF adsorbents to efficiently treat toxic vapors and contaminated organic solutions.

Meanwhile, DFT calculations further predict that both the C=C double and C≡C triple bonds show high affinity towards the iodine molecule (I_2), with the latter exhibiting a higher tendency to form I_3^- (poly)iodide species. Iodine molecules adsorbed upon C≡C could form outer charge-transfer (i.e., electron-donor-acceptor) complexes via partial charge transfer between the C≡C triple bond and the I_2 molecule, which would, in turn, be capable of adsorbing additional iodine molecules (i.e., through the acid-base interactions) and form (poly)iodide species such as I_3^-. These results align with the obtained XPS and Raman results. In the meantime, other conjugated parts of the frameworks, such as triazine and phenyl rings, play a significant role in charge transfer to the iodine molecules and thus promote the formation of (poly)iodide species. Most of this charge transfer occurs from the lone-pair (LP) electrons of the N atoms and the bonding orbitals of the conjugated moieties of the frameworks to the antibonding orbital of the iodine molecule.

The commercialization of CTF-DPA and CTF-TS as efficient adsorbents for radioiodine adsorption is highly justified based on their unique properties and the practicality of their synthesis method. These materials offer a promising solution for addressing the pressing need to remove radioactive iodine contaminants effectively.

First and foremost, both CTF-DPA and CTF-TS exhibit an exceptional adsorption capacity for iodine, as highlighted in Chapter 5. This attribute is of paramount importance in radioiodine adsorption applications, where the goal is to efficiently trap and immobilize radioactive iodine species from various sources, including nuclear power plants and medical facilities. The high adsorption capacity ensures that a substantial amount of radioiodine can be effectively adsorbed and removed from the environment, thereby mitigating potential health and environmental hazards.

Furthermore, the relatively fast adsorption kinetics these materials display is a significant advantage. In radioiodine adsorption scenarios, time is often of the essence, as swift adsorption can prevent the release and dispersion of radioactive iodine into the surroundings. The ability of CTF-DPA and CTF-TS to rapidly adsorb iodine species enhances their suitability for real-time applications and emergency response situations.

The synthesis of CTF-DPA and CTF-TS is facilitated by a facile, safe, and scalable Friedel-Crafts alkylation method, which adds to their appeal for commercialization. The availability of readily accessible precursors further simplifies the production process. These factors collectively contribute to the feasibility of large-scale manufacturing, making CTF-DPA and CTF-TS cost-effective options for widespread deployment in radioiodine adsorption systems.

Therefore, the utilization of CTF-DPA and CTF-TS as commercial adsorbents in radioiodine adsorption is justified by their impressive adsorption capacity, rapid kinetics, and the convenience of their synthesis method. These materials promise to effectively address radioiodine contamination issues, safeguarding public health and the environment.

In the second project (Chapter 6), thanks to the bottom-up functionalization method applicable to CTF materials, we successfully synthesized a computationally-designed task-specific CTF adsorbent to adsorb biohazardous heavy metal cations from water efficiently. Computational investigations, particularly the DFT method, are powerful tools in designing novel CTF-based materials and predicting/simulating the adsorption mechanism of micropollutants onto CTFs. The DFT method successfully designed functionalized CTF materials in this framework, as confirmed by experimental results.

We successfully synthesized the computationally designed COOH-CTF material using ionothermal cyclotrimerization, involving the transformation of cyano functionalities within the COOH-DCB monomer. The structure of COOH-CTF was characterized by an abundance of π-conjugated segments and negatively charged nitrogen and oxygen atoms, making it well-suited for engaging in robust electrostatic interactions with heavy metal cations in water. Compared to the unfunctionalized CTF-1, COOH-CTF demonstrated an elevated affinity for capturing heavy metal

ions from water. Even after undergoing an HCl washing procedure, CTFs retained a significant portion of their heavy metal adsorption capabilities. Transferring charge from the CTF frameworks to the heavy metal cations was key in promoting adsorption and stabilizing the resulting complexes. Notably, COOH-CTF, with its carboxylic acid functionalities positioned atop triazine rings, exhibited superior effectiveness in adsorbing and stabilizing these adsorption complexes compared to CTF-1.

The commercialization of COOH-CTF as an efficient adsorbent for heavy metal removal from water is strongly justified due to its exceptional properties and suitability for practical applications. COOH-CTF offers a promising solution to address the critical issue of heavy metal contamination in water sources.

One of the most compelling reasons to consider COOH-CTF for commercialization is its relatively high adsorption capacity for heavy metals. As highlighted in Chapter 6, COOH-CTF possesses abundant π-conjugated moieties and negatively charged nitrogen and oxygen atoms. These features create a favorable environment for strong electrostatic interactions with heavy metal cations in water. The high adsorption capacity ensures that a significant quantity of heavy metal contaminants can be efficiently adsorbed and removed from water, improving water quality.

Furthermore, COOH-CTF exhibits rapid adsorption kinetics, a crucial attribute for practical water treatment applications. The rapid uptake of heavy metal ions by COOH-CTF means that it can promptly remove contaminants from water. This is particularly important in scenarios where quick and efficient removal of heavy metals is essential to prevent further environmental damage or protect human health.

Another significant advantage of COOH-CTF is its high chemical stability under highly acidic conditions commonly encountered in water treatment processes. In the meantime, acidic conditions are often employed to regenerate and clean adsorbents after heavy metal adsorption. The ability of COOH-CTF to maintain its structural integrity and adsorption capacity in such harsh environments enhances its practicality and longevity as an adsorbent.

Hence, the commercialization of COOH-CTF as an efficient adsorbent for heavy metal removal from water is well-justified based on its high adsorption capacity, fast adsorption kinetics, and excellent chemical stability under acidic conditions. These characteristics make COOH-CTF a promising candidate for addressing the pressing challenges of heavy metal contamination in water sources, offering a reliable and effective solution for water treatment applications.

In the meantime, the DFT method is a tremendous tool to predict and thus adjust the electronic properties of CTF material to a desired level (Chapter 7). We employed this feature of the DFT method to develop novel and highly sensitive gas detectors. Overall, combining experimental and theoretical approaches for developing, synthesizing, performance testing, and analyzing mechanisms would be an ideal research path through which one may address most issues that usually occur during research projects. Based on our findings, we have concluded that CTF-based materials, such as those investigated in this dissertation, can be utilized in various applications. We have accomplished the objective of designing and developing multi-purpose materials.

In Chapter 7, we investigated the sensing capability of pristine and Pt-doped CTF-1 for SF_6 decomposition gas products. To improve the gas adsorption and detection, Pt was doped into CTF-1, increasing its charge carrier mobility and, thus, electrical conductivity. DFT calculations revealed that the Pt atom prefers to be strongly adsorbed onto an N atom of the triazine ring with a high formation energy. Meanwhile, the small values obtained for adsorption energies in the gas@CTF-1 sensing and adsorption systems indicated that the pristine CTF-1 could not efficiently adsorb the gas species. On the other hand, the high adsorption energy values in the gas@Pt-doped CTF-1 sensing and adsorption systems demonstrated that the Pt-doped CTF-1 could efficiently adsorb the gas species. The CTF-1 showed superior sensing performance for H_2S and SO_2, while the Pt-doped CTF-1 displayed better sensing performance for SOF_2 and SO_2F_2, based on the DOS studies and the change in the energy bandgap (here defined as the energy gap between the HOMO and LUMO levels) of the gas sensors upon gas adsorption.

The fabrication of Pt-doped CTF-1 gas sensors is supported by various favorable factors that render them a promising option for gas detection. These benefits include their elevated sensitivity to various gas species, the inherent chemical and thermal stability found in CTF materials, the distinctive high aspect ratio of CTF-based nanosheets, and the capability to adjust the bandgap of CTF materials by introducing metal dopants.

Foremost, the significant sensitivity demonstrated by Pt-doped CTF-1 in detecting gas species is a primary motivating factor. The integration of Pt dopant enhances the material's receptivity to specific gas molecules, resulting in an elevated level of sensitivity. This increased responsiveness is critical in ensuring precise and effective gas detection, rendering it suitable for various applications, from environmental monitoring to industrial safety protocols.

Moreover, CTF materials' impressive chemical and thermal stability further supports the feasibility of producing Pt-doped CTF-1 as a gas sensor. CTFs have exhibited robust resilience against chemical deterioration and exposure to high-temperature conditions. This resilience ensures the long-term durability and dependability of the gas sensor across diverse operational settings. Such stability is essential for achieving sustained and consistent gas detection without the risk of material degradation.

The unique high aspect ratio of CTF-based nanosheets constitutes another beneficial feature contributing to the potential synthesis of Pt-doped CTF-1 gas sensors. This morphology facilitates a substantial surface area relative to volume, enabling enhanced gas adsorption and interaction with gas molecules. Consequently, this characteristic supports the overall sensitivity and receptiveness of the gas sensor, enabling it to effectively identify even minute quantities of target gases.

Furthermore, the capacity to modify the bandgap of CTF materials through metal doping provides a paramount advantage. Including Pt dopant enables the tailoring of CTF-1's bandgap to optimize its gas-sensing capabilities for specific gas species. This adjustability permits customization, guaranteeing that the gas sensor can be fine-tuned to accurately detect particular gases with precision and selectivity.

Thus, the synthesis of Pt-doped CTF-1 gas sensors is substantiated by their potential for elevated sensitivity, inherent chemical and thermal stability, the distinctive morphology of CTF-based nanosheets, and the adaptability of their bandgap through metal doping. These collective attributes position Pt-doped CTF-1 as a promising candidate for developing advanced gas sensors with extensive applicability in gas detection and monitoring systems.

To put the work presented in this thesis in a broader context, it is useful to compare it with metal-organic frameworks (MOFs), a popular class of materials studied for similar applications, as discussed here. CTFs are more difficult to synthesize than MOFs and, therefore, more expensive in practice. However, CTFs have advantages that compensate and, in many cases, will fully offset this disadvantage. In particular, CTFs are much more stable and can be used in a much wider range of conditions than MOFs. MOFs have low moisture resistance and low heat resistance. Hence, they cannot be used in aqueous solution or humid air. CTFs, in contrast, can be used in the aqueous phase and humid air. They can also be treated with strong acids. Hence, CTFs used as adsorbents can be regenerated with little or no performance loss, even if the regeneration requires hostile conditions such as heat treatment or acid washing. As a result, higher synthesis costs can be offset by reusability.

Reusability may not be an option for platinum-doped CTFs as sensors for SF_6 degradation products because platinum interacts irreversibly with sulfur (poisoning). However, the purpose of these sensors is to monitor the safety and integrity of large electric components such as high-power converters or inverters. Once the integrity and safety of these components are compromised, they must be repaired or replaced, and this would normally lead to the replacement of the sensor with a new one. Hence, the lack of reusability of the sensor is not an issue in practice.

The experimental and theoretical studies presented in this thesis show that CTFs hold much promise as adsorbents for contaminants of health concern, such as radioactive iodine isotopes, and environmental concerns, such as heavy metals. The work has also demonstrated the power of DFT studies in accelerating materials discovery.

9 Chapter 9: Recommendations for Future Studies

Based on the findings of this research, the following recommendations can be made further to develop CTF-based materials for environmental remediation through adsorption:

Building on our extensive investigation into using π-conjugated covalent organic frameworks (CTFs) to capture iodine species across gas and liquid phases, we recognize the significant potential for expanding the applicability of CTF materials in nuclear science. Our findings suggest that CTFs exhibit promising properties for radionuclide capture, raising intriguing possibilities for their utilization in capturing other types of radionuclide species, such as uranium, a critical radioactive element with numerous applications and challenges in nuclear industries. Furthermore, the concept of simultaneous capturing of fission by-products presents a fascinating avenue of research. It offers the prospect of developing multifunctional CTF-based materials capable of selectively isolating various radionuclides within a complex mixture. We anticipate that different variants of conjugated CTF materials may demonstrate unique selectivity profiles, providing tailored solutions for capturing specific radionuclides and addressing diverse nuclear waste management and environmental remediation challenges. This research recommendation stems from our conviction that CTFs hold great promise in advancing the field of nuclear chemistry and addressing pressing issues related to radioactive waste containment and clean-up.

Our investigation into iodine adsorption mechanisms, utilizing Density Functional Theory (DFT) as our primary simulation tool, has yielded valuable insights. However, we recognize a compelling opportunity for future research to advance our understanding further. One avenue worth exploring involves adopting alternative simulation software, such as Quantum Espresso, which may offer distinct advantages. By employing Quantum Espresso, we can delve deeper into the adsorption behavior of iodine on CTF materials by simulating three-dimensional adsorption systems. This approach will enable us to construct a more comprehensive and accurate representation of the complex internal surfaces and active adsorption sites within CTF adsorbents. This enhanced spatial resolution can reveal subtle adsorption sites, shedding light on the details of iodine-CFT interactions and elucidating key factors influencing adsorption capacity and kinetics. Although we have conducted investigations into iodine adsorption in both vapor and organic phases, it could be beneficial to explore the adsorption of iodine in the aqueous phase in future studies. In light of this, we propose incorporating hydrophilic functionalities into the CTF structure to facilitate proper dispersion and enhance the interaction between the sorbent surfaces and the aqueous phase.

An expansive research strategy can be devised to comprehensively explore the influence of pore size on the adsorption behavior of covalent triazine frameworks (CTFs) in adsorbing environmental micropollutants. This involves systematically varying the building blocks used to synthesize CTFs to generate various materials with diverse dimensions and pore sizes. By employing this approach, we can construct an array of CTFs, each characterized by its unique pore size distribution and structure, ranging from microporous to mesoporous. The advantage of such a multifaceted investigation lies in its ability to discern the correlation between pore size and adsorption performance. We can interpret the complex interplay between pore size, adsorption capacity, and kinetics by rigorously characterizing the synthesized CTFs and subjecting them to adsorption experiments with various environmental micropollutants. This approach will provide a comprehensive understanding of how different pore sizes impact the accessibility of adsorption

sites, the diffusion rates of pollutants, and, ultimately, the overall adsorption efficiency. Furthermore, the resulting data can inform the rational design of CTF materials optimized for the selective removal of specific micropollutants, tailoring them to meet the unique challenges of different environmental contaminants. This research strategy advances our fundamental knowledge of CTF behavior and holds great potential for developing more effective and versatile adsorbents for water purification and environmental remediation efforts.

Our research efforts thus far have yielded valuable insights into the adsorption of three biohazardous heavy metal cations from water using CTFs functionalized with nitrogen (N) and oxygen (O) groups developed via a bottom-up approach. However, in our pursuit of understanding the potential of CTFs as versatile adsorbents for heavy metal removal, we acknowledge a promising avenue for further exploration lies in diversifying our functionalization strategies. For example, we have yet to investigate the efficacy of incorporating silicon (Si)-containing functionalities, which could introduce novel electron-donor groups into the CTF structure. This endeavor aligns with post-synthetic functionalization, allowing us to tailor CTFs with diverse electron-donor moieties. Such an approach can offer several advantages, including increased active sites for heavy metal binding and improved selectivity for specific metal ions. Through systematic investigations of various functional groups, one aims to broaden the toolkit of CTF-based adsorbents, allowing for designing tailored materials optimized for efficiently removing a wide spectrum of heavy metal contaminants from water sources. This research direction not only expands the application of CTF materials but also holds the potential to significantly advance water purification technologies and environmental protection efforts in the face of growing heavy metal pollution concerns.

While our research has been beneficial in functionalizing CTFs with diverse functionalities, we recognize the untapped potential for further elevating their adsorption capabilities by integrating complementary nanomaterials. In this pursuit, we propose an innovative approach involving the incorporation of various nanomaterials, including carbon nanotubes (CNTs), reduced graphene oxide (rGO), metal-organic frameworks (MOFs), and ionic liquids (ILs), into the porous structure of CTFs. This synergistic composing of CTFs with nanomaterials opens up exciting avenues for enhancing their adsorption performance and expanding their versatility in environmental remediation. Carbon nanotubes, with their exceptional mechanical strength and high surface area, can serve as robust scaffolds within CTF matrices, providing additional adsorption sites and facilitating the rapid transport of target contaminants to the active sites. Reduced graphene oxide, known for its exceptional conductivity and chemical stability, can support the structural integrity of CTFs and augment their adsorption capacity through synergistic interactions. Incorporating MOFs can introduce tailored pore structures and unique binding sites, enriching the adsorption capabilities of CTFs for specific pollutants. Meanwhile, introducing ionic liquids, with their tunable properties, can enhance the selectivity and solvation capabilities of CTFs for a wide range of target species. By strategically blending these nanomaterials with CTFs, we can engineer hybrid adsorbents with multifunctional attributes, ultimately leading to materials that excel in removing diverse environmental contaminants. Furthermore, this research direction aligns with the emerging trend of harnessing synergistic effects between various nanomaterials, offering a holistic and comprehensive approach to addressing complex environmental challenges.

While our research has provided valuable insights into synthetic methods for CTFs, exploring additional avenues that may offer new perspectives and broaden the synthetic toolkit is critical. In

Chapter 1, we explored several catalysts for the cyclotrimerization of cyano functionalities, but an exciting uncharted territory lies in the realm of basic catalysts, including KOH, NaOH, phosphorous-based compounds, and superbases like organolithium compounds. Exploring these alternative catalytic systems can revolutionize CTF synthesis by opening up novel synthetic routes and expanding the scope of achievable CTF structures. Basic catalysts are known for their exceptional reactivity and the ability to initiate unconventional chemical transformations. Investigating the cyano trimerization process under the influence of basic catalysts introduces a paradigm shift in CTF synthesis. This approach can develop CTFs with distinct structural characteristics, potentially leading to materials with unique porosity, surface functionality, and adsorption properties. Moreover, using basic catalysts offers opportunities to fine-tune the synthesis conditions, enabling precise control over the polymerization process. This level of control is paramount for tailoring CTF properties to meet specific application requirements, such as enhanced adsorption performance, catalytic activity, or electrical conductivity. Incorporating basic catalysts into CTF synthesis also aligns with the broader goals of sustainability and green chemistry. It may facilitate more environmentally friendly and cost-effective synthetic pathways, minimizing the need for hazardous reagents and energy-intensive procedures.

Our exploration into the impact of Pt as a dopant in CTF-1 has yielded valuable insights into the modulation of electronic properties within this covalent organic framework. However, the universe of transition metals presents a rich array of potential candidates for doping CTF materials, each with unique electronic and physicochemical attributes waiting to be harnessed for gas sensing applications. In light of this, it is imperative to extend our investigations beyond Pt and consider alternative transition metals, such as Au, Pd, Ni, Fe, and others, as promising dopants that can bestow CTF-based gas sensors with diverse and tailor-made characteristics. With its excellent conductivity and catalytic properties, Au promises to enhance the gas-sensing capabilities of CTF materials, enabling the detection of specific gases with high sensitivity and selectivity. Pd, renowned for its high surface area and affinity for hydrogen, could open doors to developing highly responsive hydrogen sensors. With its magnetic properties, Ni may pave the way for magneto resistive gas sensors based on CTFs. Meanwhile, introducing Fe, known for its redox activity, could enable the creation of electrochemically driven gas sensors with unique operational mechanisms. Exploring these transition metal dopants in the context of CTF materials allows us to tailor the gas sensor's performance by fine-tuning its electrical and physicochemical properties. Each transition metal offers a distinct electrochemical fingerprint, allowing us to engineer gas sensors optimized for specific target analytes or environmental conditions. Moreover, this research direction enriches our understanding of transition metal-doped CTFs and advances the field of gas sensing by expanding the repertoire of materials and sensor designs available for practical applications.

While we have made significant strides in the conceptual design of a Pt-doped CTF-based gas sensor tailored for detecting toxic gas species, it is essential to acknowledge that this envisioned material's synthesis and empirical testing remain uncharted territory. This realization underscores the potential for a pivotal research endeavor in the future – the synthesis, characterization, and comprehensive evaluation of Pt-doped CTF materials, or more broadly, transition metal (TM)-doped CTFs, for their gas sensing performance. Translating our theoretical design into a tangible and functional gas sensor holds immense promise. As a dopant, Pt brings its unique catalytic and electronic properties to the CTF matrix, potentially augmenting the sensor's responsiveness,

sensitivity, and selectivity to toxic gases. However, this potential can only be unlocked through the meticulous synthesis of the envisioned Pt-doped CTF and a thorough assessment of its gas-sensing capabilities. Expanding our focus to encompass a broader spectrum of transition metals, including but not limited to Pt, opens the door to a comprehensive exploration of TM-doped CTF materials as versatile platforms for gas sensing applications. Each transition metal offers distinct chemical reactivity and electronic attributes that can be harnessed to tailor the sensor's response to specific gas analytes. To accomplish this, a rigorous synthesis strategy must be devised to effectively incorporate transition metal dopants into the CTF framework. The resulting materials should then be subjected to a battery of gas-sensing experiments to evaluate their performance, encompassing sensitivity, selectivity, response time, and stability. Such empirical data will provide critical insights into TM-doped CTF gas sensors' practical viability and applicability.

Bibliography

[1] A. Hassan, S.Z. Ilyas, A. Jalil, Z. Ullah, Monetization of the environmental damage caused by fossil fuels, Environmental Science and Pollution Research 28(17) (2021) 21204-21211.
[2] J. Inauen, N. Contzen, V. Frick, P. Kadel, J. Keller, J. Kollmann, J. Mata, A.M. van Valkengoed, Environmental Issues Are Health Issues, European Psychologist (2021).
[3] J. Inumaru, T. Hasegawa, H. Shirai, H. Nishida, N. Noda, S. Ohyama, Fossil fuels combustion and environmental issues, Advances in Power Boilers, Elsevier2021, pp. 1-56.
[4] S. Vadera, S. Khan, A critical analysis of the rising global demand of plastics and its adverse impact on environmental sustainability, J. Environ. Pollut. Manag 3 (2021) 105.
[5] H. Ritchie, M. Roser, CO_2 and greenhouse gas emissions, Our World in Data (2020).
[6] C. Zamora-Ledezma, D. Negrete-Bolagay, F. Figueroa, E. Zamora-Ledezma, M. Ni, F. Alexis, V.H. Guerrero, Heavy metal water pollution: A fresh look about hazards, novel and conventional remediation methods, Environmental Technology & Innovation 22 (2021) 101504.
[7] Y. Sheth, S. Dharaskar, V. Chaudhary, M. Khalid, R. Walvekar, Prospects of titanium carbide-based MXene in heavy metal ion and radionuclide adsorption for wastewater remediation: A review, Chemosphere (2022) 133563.
[8] A. Razmjoo, L.G. Kaigutha, M.V. Rad, M. Marzband, A. Davarpanah, M. Denai, A Technical analysis investigating energy sustainability utilizing reliable renewable energy sources to reduce CO2 emissions in a high potential area, Renewable Energy 164 (2021) 46-57.
[9] F.D. Guerra, M.F. Attia, D.C. Whitehead, F. Alexis, Nanotechnology for environmental remediation: materials and applications, Molecules 23(7) (2018) 1760.
[10] G. Prasad, J.P. Kumar, L. Pandey, B. Singh, Nanoporous materials for the remediation of industrial toxic chemicals, Advanced Porous Materials 5(1) (2017) 1-16.
[11] K. Jie, Y. Zhou, E. Li, F. Huang, Nonporous adaptive crystals of pillararenes, Accounts of Chemical Research 51(9) (2018) 2064-2072.
[12] L. Zhang, M. Jaroniec, Strategies for development of nanoporous materials with 2D building units, Chemical Society Reviews 49(16) (2020) 6039-6055.
[13] G.S. Day, H.F. Drake, H.-C. Zhou, M.R. Ryder, Evolution of porous materials from ancient remedies to modern frameworks, Communications Chemistry 4(1) (2021) 1-4.
[14] S. Pourebrahimi, M. Kazemeini, A kinetic study of facile fabrication of MIL-101 (Cr) metal-organic framework: Effect of synthetic method, Inorganica Chimica Acta 471 (2018) 513-520.
[15] M. Thommes, C. Schlumberger, Characterization of nanoporous materials, Annual Review of Chemical and Biomolecular Engineering 12 (2021) 137-162.
[16] N. El Messaoudi, M. El Khomri, E.-H. Ablouh, A. Bouich, A. Lacherai, A. Jada, E.C. Lima, F. Sher, Biosynthesis of SiO2 nanoparticles using extract of Nerium oleander leaves for the removal of tetracycline antibiotic, Chemosphere 287 (2022) 132453.
[17] F. Sher, S.Z. Iqbal, T. Rasheed, K. Hanif, J. Sulejmanović, F. Zafar, E.C. Lima, Coupling of electrocoagulation and powder activated carbon for the treatment of sustainable wastewater, Environmental Science and Pollution Research (2021) 1-12.
[18] F. Sher, K. Hanif, A. Rafey, U. Khalid, A. Zafar, M. Ameen, E.C. Lima, Removal of micropollutants from municipal wastewater using different types of activated carbons, Journal of Environmental Management 278 (2021) 111302.
[19] M.R. Cunha, E.C. Lima, D.R. Lima, R.S. da Silva, P.S. Thue, M.K. Seliem, F. Sher, G.S. dos Reis, S.H. Larsson, Removal of captopril pharmaceutical from synthetic pharmaceutical-industry wastewaters: Use of activated carbon derived from Butia catarinensis, Journal of Environmental Chemical Engineering 8(6) (2020) 104506.

[20] P. Sherugar, M. Padaki, N.S. Naik, S.D. George, D.H. Murthy, Biomass-derived versatile activated carbon removes both heavy metals and dye molecules from wastewater with near-unity efficiency: Mechanism and kinetics, Chemosphere 287 (2022) 132085.
[21] S. Pourebrahimi, M. Kazemeini, M. Zaroudi, H. Bozorgzadeh, Methane adsorption on carbonaceous microporous materials prepared from cellulose and lignin: Equilibrium and kinetic studies, Scientia Iranica 25(6) (2018) 3368-3380.
[22] G. Sharma, M. Naushad, Adsorptive removal of noxious cadmium ions from aqueous medium using activated carbon/zirconium oxide composite: isotherm and kinetic modelling, Journal of Molecular Liquids 310 (2020) 113025.
[23] C.D. Williams, Application of zeolites to environmental remediation, Urban Pollution: Science and Management (2018) 249-258.
[24] C. Belviso, Zeolite for potential toxic metal uptake from contaminated soil: a brief review, Processes 8(7) (2020) 820.
[25] N. Ali, M. Bilal, A. Khan, F. Ali, Y. Yang, S. Malik, S.U. Din, H.M. Iqbal, Deployment of metal-organic frameworks as robust materials for sustainable catalysis and remediation of pollutants in environmental settings, Chemosphere (2021) 129605.
[26] X. Zhang, S. Tong, D. Huang, Z. Liu, B. Shao, Q. Liang, T. Wu, Y. Pan, J. Huang, Y. Liu, Recent advances of Zr based metal organic frameworks photocatalysis: Energy production and environmental remediation, Coordination Chemistry Reviews 448 (2021) 214177.
[27] Y. Wen, P. Zhang, V.K. Sharma, X. Ma, H.-C. Zhou, Metal-organic frameworks for environmental applications, Cell Reports Physical Science (2021) 100348.
[28] S. Pourebrahimi, M. Kazemeini, E.G. Babakhani, A. Taheri, Removal of the CO2 from flue gas utilizing hybrid composite adsorbent MIL-53 (Al)/GNP metal-organic framework, Microporous and Mesoporous Materials 218 (2015) 144-152.
[29] S. Pourebrahimi, M. Kazemeini, L. Vafajoo, Embedding graphene nanoplates into MIL-101 (Cr) pores: synthesis, characterization, and CO2 adsorption studies, Industrial & Engineering Chemistry Research 56(14) (2017) 3895-3904.
[30] A.A. Alqadami, M. Naushad, Z.A. Alothman, A.A. Ghfar, Novel metal–organic framework (MOF) based composite material for the sequestration of U (VI) and Th (IV) metal ions from aqueous environment, ACS Applied Materials & Interfaces 9(41) (2017) 36026-36037.
[31] A.R. Bagheri, N. Aramesh, F. Sher, M. Bilal, Covalent organic frameworks as robust materials for mitigation of environmental pollutants, Chemosphere 270 (2021) 129523.
[32] J. Wang, S. Zhuang, Covalent organic frameworks (COFs) for environmental applications, Coordination Chemistry Reviews 400 (2019) 213046.
[33] J. Gan, X. Li, K. Rizwan, M. Adeel, M. Bilal, T. Rasheed, H.M. Iqbal, Covalent organic frameworks-based smart materials for mitigation of pharmaceutical pollutants from aqueous solution, Chemosphere 286 (2022) 131710.
[34] N. Zhang, A. Ishag, Y. Li, H. Wang, H. Guo, P. Mei, Q. Meng, Y. Sun, Recent investigations and progress in environmental remediation by using covalent organic framework-based adsorption method: A review, Journal of Cleaner Production (2020) 123360.
[35] X. Liu, H. Pang, X. Liu, Q. Li, N. Zhang, L. Mao, M. Qiu, B. Hu, H. Yang, X. Wang, Orderly porous covalent organic frameworks-based materials: superior adsorbents for pollutants removal from aqueous solutions, The Innovation (2021) 100076.
[36] C. Krishnaraj, H.S. Jena, K. Leus, P. Van Der Voort, Covalent triazine frameworks–a sustainable perspective, Green Chemistry 22(4) (2020) 1038-1071.
[37] E. Kim, R. Patel, Recent advances in covalent triazine framework based separation membranes, Membrane Journal 31(3) (2021) 184-199.

[38] H. Zhu, W. Lin, Q. Li, Y. Hu, S. Guo, C. Wang, F. Yan, Bipyridinium-based ionic covalent triazine frameworks for CO2, SO2, and NO capture, ACS Applied Materials & Interfaces 12(7) (2020) 8614-8621.
[39] M. Sun, S. Han, J. Feng, C. Li, X. Ji, J. Feng, H. Sun, Recent advances of triazine-based materials for adsorbent based extraction techniques, Topics in Current Chemistry 379(4) (2021) 1-34.
[40] J. Szerement, A. Szatanik-Kloc, R. Jarosz, T. Bajda, M. Mierzwa-Hersztek, Contemporary applications of natural and synthetic zeolites from fly ash in agriculture and environmental protection, Journal of Cleaner Production 311 (2021) 127461.
[41] B.J. Sikora, R. Winnegar, D.M. Proserpio, R.Q. Snurr, Textural properties of a large collection of computationally constructed MOFs and zeolites, Microporous and Mesoporous Materials 186 (2014) 207-213.
[42] L. Zhu, L. Meng, J. Shi, J. Li, X. Zhang, M. Feng, Metal-organic frameworks/carbon-based materials for environmental remediation: A state-of-the-art mini-review, Journal of Environmental Management 232 (2019) 964-977.
[43] S. Yuan, L. Feng, K. Wang, J. Pang, M. Bosch, C. Lollar, Y. Sun, J. Qin, X. Yang, P. Zhang, Stable metal–organic frameworks: design, synthesis, and applications, Advanced Materials 30(37) (2018) 1704303.
[44] C.S. Diercks, O.M. Yaghi, The atom, the molecule, and the covalent organic framework, Science 355(6328) (2017).
[45] M. Liu, L. Guo, S. Jin, B. Tan, Covalent triazine frameworks: synthesis and applications, Journal of Materials Chemistry A 7(10) (2019) 5153-5172.
[46] P. Kuhn, M. Antonietti, A. Thomas, Porous, covalent triazine-based frameworks prepared by ionothermal synthesis, Angewandte Chemie International Edition 47(18) (2008) 3450-3453.
[47] Z. Yang, H. Chen, S. Wang, W. Guo, T. Wang, X. Suo, D.-e. Jiang, X. Zhu, I. Popovs, S. Dai, Transformation strategy for highly crystalline covalent triazine frameworks: from staggered AB to eclipsed AA stacking, Journal of the American Chemical Society 142(15) (2020) 6856-6860.
[48] H. Wang, D. Jiang, D. Huang, G. Zeng, P. Xu, C. Lai, M. Chen, M. Cheng, C. Zhang, Z. Wang, Covalent triazine frameworks for carbon dioxide capture, Journal of Materials Chemistry A 7(40) (2019) 22848-22870.
[49] Y. Zhang, S. Jin, Recent advancements in the synthesis of covalent triazine frameworks for energy and environmental applications, Polymers 11(1) (2019) 31.
[50] J. Artz, Covalent triazine-based frameworks—Tailor-made catalysts and catalyst supports for molecular and nanoparticulate species, ChemCatChem 10(8) (2018) 1753-1771.
[51] Y. Zhang, S. Jin, Recent advancements in the synthesis of covalent triazine frameworks for energy and environmental applications, Polymers 11(1) (2018) 31.
[52] X. Suo, F. Zhang, Z. Yang, H. Chen, T. Wang, Z. Wang, T. Kobayashi, C.L. Do-Thanh, D. Maltsev, Z. Liu, Highly perfluorinated covalent triazine frameworks derived from a low-temperature ionothermal approach towards enhanced CO2 electroreduction, Angewandte Chemie International Edition 60(49) (2021) 25688-25694.
[53] J. Liu, P. Lyu, Y. Zhang, P. Nachtigall, Y. Xu, New layered triazine framework/exfoliated 2D polymer with superior sodium-storage properties, Advanced Materials 30(11) (2018) 1705401.
[54] S. Ren, M.J. Bojdys, R. Dawson, A. Laybourn, Y.Z. Khimyak, D.J. Adams, A.I. Cooper, Porous, fluorescent, covalent triazine-based frameworks via room-temperature and microwave-assisted synthesis, Advanced Materials 24(17) (2012) 2357-2361.
[55] S.N. Talapaneni, T.H. Hwang, S.H. Je, O. Buyukcakir, J.W. Choi, A. Coskun, Elemental-sulfur-mediated facile synthesis of a covalent triazine framework for high-performance lithium–sulfur batteries, Angewandte Chemie International Edition 55(9) (2016) 3106-3111.
[56] T. Zhou, Y. Zhao, J.W. Choi, A. Coskun, Lithium-salt mediated synthesis of a covalent triazine framework for highly stable lithium metal batteries, Angewandte Chemie 131(47) (2019) 16951-16955.

[57] S. Zhang, G. Cheng, L. Guo, N. Wang, B. Tan, S. Jin, Strong-base-assisted synthesis of a crystalline covalent triazine framework with high hydrophilicity via benzylamine monomer for photocatalytic water splitting, Angewandte Chemie 132(15) (2020) 6063-6070.
[58] S.Y. Yu, J. Mahmood, H.J. Noh, J.M. Seo, S.M. Jung, S.H. Shin, Y.K. Im, I.Y. Jeon, J.B. Baek, Direct synthesis of a covalent triazine-based framework from aromatic amides, Angewandte Chemie International Edition 57(28) (2018) 8438-8442.
[59] K. Wang, L.M. Yang, X. Wang, L. Guo, G. Cheng, C. Zhang, S. Jin, B. Tan, A. Cooper, Covalent triazine frameworks via a low-temperature polycondensation approach, Angewandte Chemie International Edition 56(45) (2017) 14149-14153.
[60] P. Puthiaraj, S.-M. Cho, Y.-R. Lee, W.-S. Ahn, Microporous covalent triazine polymers: efficient Friedel–Crafts synthesis and adsorption/storage of CO2 and CH4, Journal of Materials Chemistry A 3(13) (2015) 6792-6797.
[61] K. Geng, T. He, R. Liu, S. Dalapati, K.T. Tan, Z. Li, S. Tao, Y. Gong, Q. Jiang, D. Jiang, Covalent organic frameworks: design, synthesis, and functions, Chemical Reviews 120(16) (2020) 8814-8933.
[62] H. Deng, M.A. Olson, J.F. Stoddart, O.M. Yaghi, Robust dynamics, Nature Chemistry 2(6) (2010) 439-443.
[63] J. Wen, Y. Liu, H. Chen, M. Yang, H. Li, Synthesis and characterization of phenanthroimidazole-containing triazine frameworks and their performance in CO2 capture, Microporous and Mesoporous Materials 316 (2021) 110939.
[64] H. Liang, H. Li, Z. Wang, F. Wu, L. Chen, X. Huang, New binary room-temperature molten salt electrolyte based on urea and LiTFSI, The Journal of Physical Chemistry B 105(41) (2001) 9966-9969.
[65] X. Zhu, C. Tian, S.M. Mahurin, S.-H. Chai, C. Wang, S. Brown, G.M. Veith, H. Luo, H. Liu, S. Dai, A superacid-catalyzed synthesis of porous membranes based on triazine frameworks for CO2 separation, Journal of the American Chemical Society 134(25) (2012) 10478-10484.
[66] S.H. Je, H.J. Kim, J. Kim, J.W. Choi, A. Coskun, Perfluoroaryl-elemental sulfur SNAr chemistry in covalent triazine frameworks with high sulfur contents for lithium–sulfur batteries, Advanced Functional Materials 27(47) (2017) 1703947.
[67] H. Eshghi, A. Hassankhani, Phosphorus pentoxide supported on silica gel and alumina (P2O5/SiO2, P2O5/Al2O3) as useful catalysts in organic synthesis, Journal of the Iranian Chemical Society 9(4) (2012) 467-482.
[68] S.-Y. Yu, J.C. Kim, H.-J. Noh, Y.-K. Im, J. Mahmood, I.-Y. Jeon, S.K. Kwak, J.-B. Baek, Direct conversion of aromatic amides into crystalline covalent triazine frameworks by a condensation mechanism, Cell Reports Physical Science (2021) 100653.
[69] S. Cao, J. Low, J. Yu, M. Jaroniec, Polymeric photocatalysts based on graphitic carbon nitride, Advanced Materials 27(13) (2015) 2150-2176.
[70] P. Puthiaraj, S.-M. Cho, Y.-R. Lee, W.-S. Ahn, Microporous covalent triazine polymers: efficient Friedel–Crafts synthesis and adsorption/storage of CO 2 and CH 4, Journal of Materials Chemistry A 3(13) (2015) 6792-6797.
[71] T. Geng, M. Liu, C. Zhang, C. Hu, H.Y. Xia, The preparation of covalent triazine-based framework via Friedel-Crafts reaction of 2, 4, 6-trichloro-1, 3, 5-triazine with N, N'-diphenyl-N, N'-di (m-tolyl) benzidine for capturing and sensing to iodine, Polymers for Advanced Technologies 31(6) (2020) 1388-1394.
[72] X.-C. Fang, T.-M. Geng, F.-Q. Wang, W.-H. Xu, The synthesis of conjugated microporous polymers via Friedel–Crafts reaction of 2, 4, 6-trichloro-1, 3, 5-triazine with thienyl derivatives for fluorescence sensing to 2, 4-dinitrophenol and capturing iodine, Journal of Solid State Chemistry 307 (2022) 122818.
[73] B. Dong, D.-Y. Wang, W.-J. Wang, X.-L. Tian, G. Ren, Post synthesis of a glycine-functionalized covalent triazine framework with excellent CO2 capture performance, Microporous and Mesoporous Materials 306 (2020) 110475.

[74] Q. Liu, S. Yang, H. Repich, Y. Zhai, X. Xu, Y. Liang, H. Li, H. Wang, F. Xu, Porous functionalized covalent-triazine frameworks for enhanced adsorption toward polysulfides in Li-S batteries and organic dyes, Frontiers in Chemistry (2020) 1009.
[75] Y. Li, C.-X. Yang, H.-L. Qian, X. Zhao, X.-P. Yan, Carboxyl-functionalized covalent organic frameworks for the adsorption and removal of triphenylmethane dyes, ACS Applied Nano Materials 2(11) (2019) 7290-7298.
[76] L. Chen, L. Wang, Y. Wan, Y. Zhang, Z. Qi, X. Wu, H. Xu, Acetylene and diacetylene functionalized covalent triazine frameworks as metal-free photocatalysts for hydrogen peroxide production: a new two-electron water oxidation pathway, Advanced Materials 32(2) (2020) 1904433.
[77] B. Dong, D.-Y. Wang, W.-J. Wang, Post-functionalization of hydroxyl-appended covalent triazine framework via borrowing hydrogen strategy for effective CO2 capture, Microporous and Mesoporous Materials 292 (2020) 109765.
[78] H. Ding, A. Mal, C. Wang, Tailored covalent organic frameworks by post-synthetic modification, Materials Chemistry Frontiers 4(1) (2020) 113-127.
[79] D.W. Kang, M. Kang, C.S. Hong, Post-synthetic modification of porous materials: superprotonic conductivities and membrane applications in fuel cells, Journal of Materials Chemistry A 8(16) (2020) 7474-7494.
[80] J. Wang, D. Fan, C. Jiang, L. Lu, Host-guest interaction-mediated nanointerface engineering for radioiodine capture, Nano Today 36 (2021) 101034.
[81] R. Chen, T. Hu, W. Zhang, C. He, Y. Li, Synthesis of nitrogen-containing covalent organic framework with reversible iodine capture capability, Microporous and Mesoporous Materials 312 (2021) 110739.
[82] X. Li, G. Chen, H. Xu, Q. Jia, Task-specific synthesis of cost-effective electron-rich thiophene-based hypercrosslinked polymer with perylene for efficient iodine capture, Separation and Purification Technology 228 (2019) 115739.
[83] A. Gavezzotti, Efficient computer modeling of organic materials. The atom–atom, Coulomb–London–Pauli (AA-CLP) model for intermolecular electrostatic-polarization, dispersion and repulsion energies, New Journal of Chemistry 35(7) (2011) 1360-1368.
[84] Y. Sun, S. Song, D. Xiao, L. Gan, Y. Wang, Easily constructed imine-bonded COFs for iodine capture at ambient temperature, ACS Omega 5(38) (2020) 24262-24271.
[85] A. Purnomoadi, A.R. Mor, J. Smit, Health index and risk assessment models for Gas Insulated Switchgear (GIS) operating under tropical conditions, International Journal of Electrical Power & Energy Systems 117 (2020) 105681. https://doi.org/10.1016/j.ijepes.2019.105681.
[86] Z. Peng, L.-Q. Tao, K. Zheng, J. Yu, G. Wang, H. Sun, C. Zhu, S. Zou, X. Chen, Gas Sensor Based on Semihydrogenated and Semifluorinated h-BN for SF_6 Decomposition Components Detection, IEEE Transactions on Electron Devices 68(4) (2021) 1878-1885. https://doi.org/10.1109/TED.2021.3058034.
[87] Y. Gui, J. Shi, P. Yang, T. Li, C. Tang, L. Xu, Platinum modified MoS_2 monolayer for adsorption and gas sensing of SF_6 decomposition products: A DFT study, High Voltage 5(4) (2020) 454-462. https://doi.org/10.1049/hve.2019.0170.
[88] T.-Y. Sang, T. Li, Y. Yang, Y. Song, H. Tian, R. Song, C. Wang, X. Hu, Z. Yang, Y. Lu, Pd, Rh-decorated Se-vacancy $MoSe_2$ monolayer: A promising candidate for sensing and detecting SO_2F_2, SOF_2, H_2S and SO_2, Surfaces and Interfaces 33 (2022) 102269. https://doi.org/10.1016/j.surfin.2022.102269.
[89] X. Liu, D. Huang, C. Lai, G. Zeng, L. Qin, H. Wang, H. Yi, B. Li, S. Liu, M. Zhang, Recent advances in covalent organic frameworks (COFs) as a smart sensing material, Chemical Society Reviews 48(20) (2019) 5266-5302. https://doi.org/10.1039/C9CS00299E.
[90] T. Skorjanc, D. Shetty, M. Valant, Covalent organic polymers and frameworks for fluorescence-based sensors, ACS Sensors 6(4) (2021) 1461-1481. https://doi.org/10.1021/acssensors.1c00183.

[91] C. Yin, Z. Zhang, J. Zhou, Y. Wang, Single-layered nanosheets of covalent triazine frameworks (CTFs) by mild oxidation for molecular-sieving membranes, ACS Applied Materials & Interfaces 12(16) (2020) 18944-18951. https://doi.org/10.1021/acsami.0c03246.
[92] L. Cordroch, S. Hilpert, F. Wiese, Why renewables and energy efficiency are not enough-the relevance of sufficiency in the heating sector for limiting global warming to 1.5° C, Technological Forecasting and Social Change 175 (2022) 121313.
[93] J.-P. Birat, Materials, greenhouse gas emissions and climate change, Sustainable materials science-Environmental metallurgy, EDP Sciences2021, pp. 43-120.
[94] P. Purushothaman, N. Durairaj, G. Mani, S. Kalainathan, Fluorescence emission, life time, thermal properties of trans-stilbene mixed diphenylacetylene scintillator crystal, Journal of Materials Science: Materials in Electronics 32(7) (2021) 8366-8374.
[95] R.K. Upadhyay, Markers for global climate change and its impact on social, biological and ecological systems: A review, American Journal of Climate Change 9(03) (2020) 159.
[96] P.P. Singh, M. Verma, Recent Advances in Alternative Sources of Energy, Energy: Crises, Challenges and Solutions (2021) 55-71.
[97] T.T. da Cruz, J.A.P. Balestieri, J.M. de Toledo Silva, M.R. Vilanova, O.J. Oliveira, I. Ávila, Life cycle assessment of carbon capture and storage/utilization: From current state to future research directions and opportunities, International Journal of Greenhouse Gas Control 108 (2021) 103309.
[98] H. Sharma, A. Dhir, Capture of carbon dioxide using solid carbonaceous and non-carbonaceous adsorbents: a review, Environmental Chemistry Letters 19(2) (2021) 851-873.
[99] L. Liu, C. Song, A. Kong, Nitrogen and sulfur-enriched porous bithiophene-melamine covalent organic polymers for effective capture of CO2 and iodine, Materials Letters 277 (2020) 128291.
[100] Y. Sang, Y. Cao, L. Wang, W. Yan, T. Chen, J. Huang, Y.-N. Liu, N-rich porous organic polymers based on Schiff base reaction for CO2 capture and mercury (II) adsorption, Journal of Colloid and Interface Science 587 (2021) 121-130.
[101] V.M. Rangaraj, K.S.K. Reddy, G.N. Karanikolos, Ionothermal synthesis of phosphonitrilic-core covalent triazine frameworks for carbon dioxide capture, Chemical Engineering Journal 429 (2022) 132160.
[102] Q.-W. Deng, G.-Q. Ren, Y.-J. Li, L. Yang, S.-L. Zhai, T. Yu, L. Sun, W.-Q. Deng, A. Li, Y.-H. Zhou, Hydrogen and CO2 storage in high surface area covalent triazine–based frameworks, Materials Today Energy 18 (2020) 100506.
[103] N. Bagherian, A.R. Karimi, A. Amini, Chemically stable porous crystalline macromolecule hydrazone-linked covalent organic framework for CO2 capture, Colloids and Surfaces A: Physicochemical and Engineering Aspects 613 (2021) 126078.
[104] X. Wei, X. Wang, Y. Pu, A. Liu, C. Chen, W. Zou, Y. Zheng, J. Huang, Y. Zhang, Y. Yang, Facile ball-milling synthesis of CeO2/g-C3N4 Z-scheme heterojunction for synergistic adsorption and photodegradation of methylene blue: characteristics, kinetics, models, and mechanisms, Chemical Engineering Journal 420 (2021) 127719.
[105] M.G. Mohamed, A.F. EL-Mahdy, Y. Takashi, S.-W. Kuo, Ultrastable conductive microporous covalent triazine frameworks based on pyrene moieties provide high-performance CO2 uptake and supercapacitance, New Journal of Chemistry 44(20) (2020) 8241-8253.
[106] H. Zhou, R. Zhang, X.B. Lu, Isolable CO2 adducts of polarized alkenes: high thermal stability and catalytic activity for CO2 chemical transformation, Advanced Synthesis & Catalysis 361(2) (2019) 326-334.
[107] S.-C. Xi, H.-N. Guo, C.-Y. Yang, R. Wang, D.-Y. Wang, B. Dong, A bisimidazolium-based cationic covalent triazine framework for CO2 capture and dye adsorption, European Polymer Journal 161 (2021) 110821.

[108] Q.-J. Wu, M.-J. Mao, J.-X. Chen, Y.-B. Huang, R. Cao, Integration of metalloporphyrin into cationic covalent triazine frameworks for the synergistically enhanced chemical fixation of CO 2, Catalysis Science & Technology 10(23) (2020) 8026-8033.
[109] Y. Fu, Z. Wang, S. Li, X. He, C. Pan, J. Yan, G. Yu, Functionalized covalent triazine frameworks for effective CO2 and SO2 removal, ACS Applied Materials & Interfaces 10(42) (2018) 36002-36009.
[110] C. Liao, Z. Liang, B. Liu, H. Chen, X. Wang, H. Li, Phenylamino-, phenoxy-, and benzenesulfenyl-linked covalent triazine frameworks for CO2 capture, ACS Applied Nano Materials 3(3) (2020) 2889-2898.
[111] Z. Fu, S. Xi, The effects of heavy metals on human metabolism, Toxicology Mechanisms and Methods 30(3) (2020) 167-176.
[112] J. Sulejmanović, M. Memić, E. Šehović, R. Omanović, S. Begić, M. Pazalja, A. Ajanović, O. Azhar, F. Sher, Synthesis of green nano sorbents for simultaneous preconcentration and recovery of heavy metals from water, Chemosphere (2022) 133971.
[113] M. Naushad, Surfactant assisted nano-composite cation exchanger: development, characterization and applications for the removal of toxic Pb2+ from aqueous medium, Chemical Engineering Journal 235 (2014) 100-108.
[114] S. Afroze, T.K. Sen, A review on heavy metal ions and dye adsorption from water by agricultural solid waste adsorbents, Water, Air, & Soil Pollution 229(7) (2018) 1-50.
[115] S. Gupta, S. Sireesha, I. Sreedhar, C.M. Patel, K. Anitha, Latest trends in heavy metal removal from wastewater by biochar based sorbents, Journal of Water Process Engineering 38 (2020) 101561.
[116] L.C. Abbott, F. Nigussie, Mercury Toxicity and Neurogenesis in the Mammalian Brain, International Journal of Molecular Sciences 22(14) (2021) 7520.
[117] Y. Fu, W. Yu, W. Zhang, Q. Huang, J. Yan, C. Pan, G. Yu, Sulfur-rich covalent triazine polymer nanospheres for environmental mercury removal and detection, Polymer Chemistry 9(30) (2018) 4125-4131.
[118] S. Mondal, S. Chatterjee, S. Mondal, A. Bhaumik, Thioether-functionalized covalent triazine nanospheres: a robust adsorbent for mercury removal, ACS Sustainable Chemistry & Engineering 7(7) (2019) 7353-7361.
[119] Z. Yang, Y. Gu, B. Yuan, Y. Tian, J. Shang, D.C. Tsang, M. Liu, L. Gan, S. Mao, L. Li, Thio-groups decorated covalent triazine frameworks for selective mercury removal, Journal of Hazardous Materials 403 (2021) 123702.
[120] M. Afshari, M. Dinari, K. Zargoosh, H. Moradi, Novel triazine-based covalent organic framework as a superadsorbent for the removal of mercury (II) from aqueous solutions, Industrial & Engineering Chemistry Research 59(19) (2020) 9116-9126.
[121] R. Peng, G. Chen, F. Zhou, R. Man, J. Huang, Catalyst-free synthesis of triazine-based porous organic polymers for Hg2+ adsorptive removal from aqueous solution, Chemical Engineering Journal 371 (2019) 260-266.
[122] H. Shan, S. Li, Z. Yang, X. Zhang, Y. Zhuang, Q. Zhu, D. Cai, P. Qin, J. Baeyens, Triazine-based N-rich porous covalent organic polymer for the effective detection and removal of Hg (II) from an aqueous solution, Chemical Engineering Journal (2021) 130757.
[123] M. Dinari, M. Hatami, Novel N-riched crystalline covalent organic framework as a highly porous adsorbent for effective cadmium removal, Journal of Environmental Chemical Engineering 7(1) (2019) 102907.
[124] M. Dinari, N. Mokhtari, M. Hatami, Covalent triazine based polymer with high nitrogen levels for removal of copper(II) ions from aqueous solutions, Journal of Polymer Research 28(4) (2021) 1-11.
[125] T. Xu, L. Zhou, Y. He, S. An, C. Peng, J. Hu, H. Liu, Covalent organic framework with triazine and hydroxyl bifunctional groups for efficient removal of lead (ii) ions, Industrial & Engineering Chemistry Research 58(42) (2019) 19642-19648.

[126] S. Zhou, Z. Zhou, D. Zhu, H. Jiang, Y. Qi, S. Wang, Y. Jia, W. Wang, Preparation of covalent triazine-based framework for efficient Cr (VI) removal from water, Colloids and Surfaces A: Physicochemical and Engineering Aspects 632 (2022) 127757.
[127] T.S. Rao, S. Panigrahi, P. Velraj, Transport and disposal of radioactive wastes in nuclear industry, Microbial Biodegradation and Bioremediation, Elsevier2022, pp. 419-440.
[128] X.Q. Xu, L.H. Cao, Y. Yang, X.T. Bai, F. Zhao, Z.H. He, Z. Yin, Y.M. Ma, Cationic nonporous macrocyclic organic compounds for multimedia iodine capture, Chemistry–An Asian Journal 16(2) (2021) 142-146.
[129] L. Jia, Y. Chen, F. Chen, J. Lv, Y. Li, F. Hou, Z. Yang, Z. Deng, Small activating RNA-activated NIS gene promotes 131I uptake and inhibits thyroid cancer via AMPK/mTOR pathway, Pathology-Research and Practice (2021) 153735.
[130] A. Hassan, A. Alam, M. Ansari, N. Das, Hydroxy functionalized triptycene based covalent organic polymers for ultra-high radioactive iodine uptake, Chemical Engineering Journal 427 (2022) 130950.
[131] P. Wang, Q. Xu, Z. Li, W. Jiang, Q. Jiang, D. Jiang, Exceptional iodine capture in 2D covalent organic frameworks, Advanced Materials 30(29) (2018) 1801991.
[132] T.-H. Niu, C.-C. Feng, C. Yao, W.-Y. Yang, Y.-H. Xu, Bisimidazole-based conjugated polymers for excellent iodine capture, ACS Applied Polymer Materials 3(1) (2020) 354-361.
[133] C. Feng, G. Xu, W. Xie, S. Zhang, C. Yao, Y. Xu, Polytriazine porous networks for effective iodine capture, Polymer Chemistry 11(16) (2020) 2786-2790.
[134] S. Xiong, J. Tao, Y. Wang, J. Tang, C. Liu, Q. Liu, Y. Wang, G. Yu, C. Pan, Uniform poly (phosphazene–triazine) porous microspheres for highly efficient iodine removal, Chemical Communications 54(61) (2018) 8450-8453.
[135] X. Pan, X. Qin, Q. Zhang, Y. Ge, H. Ke, G. Cheng, N-and S-rich covalent organic framework for highly efficient removal of indigo carmine and reversible iodine capture, Microporous and Mesoporous Materials 296 (2020) 109990.
[136] G. Xu, Y. Zhu, W. Xie, S. Zhang, C. Yao, Y. Xu, Porous cationic covalent triazine-based frameworks as platforms for efficient CO2 and iodine capture, Chemistry–An Asian Journal 14(19) (2019) 3259-3263.
[137] D.K. Harijan, V. Chandra, T. Yoon, K.S. Kim, Radioactive iodine capture and storage from water using magnetite nanoparticles encapsulated in polypyrrole, Journal of Hazardous Materials 344 (2018) 576-584.
[138] S. Chang, W. Xie, C. Yao, G. Xu, S. Zhang, Y. Xu, Preparation of covalent triazine frameworks with multiactive sites for efficient and reversible iodine capture, European Polymer Journal 159 (2021) 110753.
[139] T.M. Geng, X.C. Fang, F.Q. Wang, F. Zhu, The synthesis of covalent triazine-based frameworks via Friedel–Crafts reactions of cyanuric chloride with thienyl and carbazolyl derivatives for fluorescence sensing to picric acid, iodine and capturing iodine, Macromolecular Materials and Engineering 306(11) (2021) 2100461.
[140] W. Zhang, Y. Mu, X. He, P. Chen, S. Zhao, C. Huang, Y. Wang, J. Chen, Robust porous polymers bearing phosphine oxide/chalcogenide ligands for volatile iodine capture, Chemical Engineering Journal 379 (2020) 122365.
[141] J. Li, H. Zhang, L. Zhang, K. Wang, Z. Wang, G. Liu, Y. Zhao, Y. Zeng, Two-dimensional covalent–organic frameworks for ultrahigh iodine capture, Journal of Materials Chemistry A 8(19) (2020) 9523-9527.
[142] A. Mohan, M.H. Al-Sayah, A. Ahmed, O.M. El-Kadri, Triazine-based porous organic polymers for reversible capture of iodine and utilization in antibacterial application, Scientific Reports 12(1) (2022) 1-10.
[143] Y. Huang, W. Li, Y. Xu, M. Ding, J. Ding, Y. Zhang, Y. Wang, S. Chen, Y. Jin, C. Xia, Rapid iodine adsorption from vapor phase and solution by a nitrogen-rich covalent piperazine–triazine-based polymer, New Journal of Chemistry 45(12) (2021) 5363-5370.
[144] X. Li, Y. Peng, Q. Jia, Construction of hypercrosslinked polymers with dual nitrogen-enriched building blocks for efficient iodine capture, Separation and Purification Technology 236 (2020) 116260.

[145] S. Pourebrahimi, M. Pirooz, Reversible iodine vapor capture using bipyridine-based covalent triazine framework: Experimental and computational investigations, Chemical Engineering Journal Advances 8 (2021) 100150.
[146] M. Bursch, J.M. Mewes, A. Hansen, S. Grimme, Best-Practice DFT Protocols for Basic Molecular Computational Chemistry, Angewandte Chemie International Edition 61(42) (2022) e202205735.
[147] J. Gasteiger, Chemistry in times of artificial intelligence, ChemPhysChem 21(20) (2020) 2233-2242.
[148] C. Chidiebere, C. Duru, J.C. Mbagwu, Application of computational chemistry in chemical reactivity: A review, Journal of the Nigerian Society of Physical Sciences 3 (2021) 292–297.
[149] P. Verma, D.G. Truhlar, Status and challenges of density functional theory, Trends in Chemistry 2(4) (2020) 302-318.
[150] A. Sharma, G.R. Nishad, P. Vishwakarma, P. Jaget, Density functional theory (DFT)-based molecular modeling, Computational Modelling and Simulations for Designing of Corrosion Inhibitors, Elsevier2023, pp. 115-133.
[151] Y. Shi, A. Wasserman, Inverse Kohn–Sham density functional theory: Progress and challenges, The Journal of Physical Chemistry Letters 12(22) (2021) 5308-5318.
[152] M.F. Kasim, S.M. Vinko, Learning the exchange-correlation functional from nature with fully differentiable density functional theory, Physical Review Letters 127(12) (2021) 126403.
[153] F. Jensen, Atomic orbital basis sets, Wiley Interdisciplinary Reviews: Computational Molecular Science 3(3) (2013) 273-295.
[154] J.G. Hill, Gaussian basis sets for molecular applications, International Journal of Quantum Chemistry 113(1) (2013) 21-34.
[155] J. Zheng, X. Xu, D.G. Truhlar, Minimally augmented Karlsruhe basis sets, Theoretical Chemistry Accounts 128 (2011) 295-305.
[156] S. Chiodo, N. Russo, E. Sicilia, LANL2DZ basis sets recontracted in the framework of density functional theory, The Journal of Chemical Physics 125(10) (2006).
[157] J.-D. Chai, M. Head-Gordon, Long-range corrected hybrid density functionals with damped atom–atom dispersion corrections, Physical Chemistry Chemical Physics 10(44) (2008) 6615-6620.
[158] V.N. Staroverov, G.E. Scuseria, J. Tao, J.P. Perdew, Comparative assessment of a new nonempirical density functional: Molecules and hydrogen-bonded complexes, The Journal of Chemical Physics 119(23) (2003) 12129-12137.
[159] Y. Yang, M.N. Weaver, K.M. Merz Jr, Assessment of the "6-31+ G**+ LANL2DZ" mixed basis set coupled with density functional theory methods and the effective core potential: prediction of heats of formation and ionization potentials for first-row-transition-metal complexes, The Journal of Physical Chemistry A 113(36) (2009) 9843-9851.
[160] E. Cances, B. Mennucci, J. Tomasi, A new integral equation formalism for the polarizable continuum model: Theoretical background and applications to isotropic and anisotropic dielectrics, The Journal of Chemical Physics 107(8) (1997) 3032-3041.
[161] E.D. Glendening, C.R. Landis, F. Weinhold, NBO 6.0: Natural bond orbital analysis program, Journal of Computational Chemistry 34(16) (2013) 1429-1437.
[162] E.R. Johnson, S. Keinan, P. Mori-Sánchez, J. Contreras-García, A.J. Cohen, W. Yang, Revealing noncovalent interactions, Journal of the American Chemical Society 132(18) (2010) 6498-6506.
[163] M.Y. Toriyama, A.M. Ganose, M. Dylla, S. Anand, J. Park, M.K. Brod, J.M. Munro, K.A. Persson, A. Jain, G.J. Snyder, How to analyse a density of states, Materials Today Electronics 1 (2022) 100002.
[164] J. Wang, X. Guo, Adsorption kinetic models: Physical meanings, applications, and solving methods, Journal of Hazardous Materials 390 (2020) 122156.
[165] S.V. Smirnova, D.V. Ilin, I.V. Pletnev, Extraction and ICP-OES determination of heavy metals using tetrabutylammonium bromide aqueous biphasic system and oleophilic collector, Talanta 221 (2021) 121485. https://doi.org/10.1016/j.talanta.2020.121485.

[166] N. Ayawei, A.N. Ebelegi, D. Wankasi, Modelling and Interpretation of Adsorption Isotherms, Journal of Chemistry 2017 (2017) 3039817. https://doi.org/10.1155/2017/3039817.
[167] D. Xia, Y. Li, Y. He, T. Zhang, Y. Wang, J. Gu, Exploring the role of cultural individualism and collectivism on public acceptance of nuclear energy, Energy Policy 132 (2019) 208-215.
[168] M. Ramana, Technical and social problems of nuclear waste, Wiley Interdisciplinary Reviews: Energy and Environment 7(4) (2018) e289.
[169] Z. Tian, T.-S. Chee, L. Zhu, T. Duan, X. Zhang, L. Lei, C. Xiao, Comprehensive comparison of bismuth and silver functionalized nickel foam composites in capturing radioactive gaseous iodine, Journal of Hazardous Materials 417 (2021) 125978.
[170] S. Edwards, F. Andrieux, C. Boxall, M. Sarsfield, R. Taylor, D. Woodhead, Neptunium (IV)-hydroxamate complexes: their speciation, and kinetics and mechanism of hydrolysis, Dalton Transactions 48(2) (2019) 673-687.
[171] B.J. Riley, J.D. Vienna, D.M. Strachan, J.S. McCloy, J.L. Jerden Jr, Materials and processes for the effective capture and immobilization of radioiodine: A review, Journal of Nuclear Materials 470 (2016) 307-326.
[172] V.J. Inglezakis, A. Satayeva, A. Yagofarova, Z. Tauanov, K. Meiramkulova, J. Farrando-Pérez, J.C. Bear, Surface interactions and mechanisms study on the removal of iodide from water by use of natural zeolite-based silver nanocomposites, Nanomaterials 10(6) (2020) 1156.
[173] J. Huve, A. Ryzhikov, H. Nouali, V. Lalia, G. Augé, T.J. Daou, Porous sorbents for the capture of radioactive iodine compounds: a review, RSC Advances 8(51) (2018) 29248-29273.
[174] T.C.T. Pham, S. Docao, I.C. Hwang, M.K. Song, D. Moon, P. Oleynikov, K.B. Yoon, Capture of iodine and organic iodides using silica zeolites and the semiconductor behaviour of iodine in a silica zeolite, Energy & Environmental Science 9(3) (2016) 1050-1062.
[175] L. Chen, J.-Y. Qian, D.-D. Zhu, S. Yang, J. Lin, M.-Y. He, Z.-H. Zhang, Q. Chen, Mesoporous zeolitic imidazolate framework-67 nanocrystals on siliceous mesocellular foams for capturing radioactive iodine, ACS Applied Nano Materials 3(6) (2020) 5390-5398.
[176] H. Sun, P. La, R. Yang, Z. Zhu, W. Liang, B. Yang, A. Li, W. Deng, Innovative nanoporous carbons with ultrahigh uptakes for capture and reversible storage of CO_2 and volatile iodine, Journal of Hazardous Materials 321 (2017) 210-217.
[177] Q.M. Zhang, T.L. Zhai, Z. Wang, G. Cheng, H. Ma, Q.P. Zhang, Y.H. Zhao, B. Tan, C. Zhang, Hyperporous carbon from triptycene-based hypercrosslinked polymer for iodine capture, Advanced Materials Interfaces 6(9) (2019) 1900249.
[178] W. Xie, D. Cui, S.-R. Zhang, Y.-H. Xu, D.-L. Jiang, Iodine capture in porous organic polymers and metal–organic frameworks materials, Materials Horizons 6(8) (2019) 1571-1595.
[179] B. Li, X. Dong, H. Wang, D. Ma, K. Tan, S. Jensen, B.J. Deibert, J. Butler, J. Cure, Z. Shi, Capture of organic iodides from nuclear waste by metal-organic framework-based molecular traps, Nature Communications 8(1) (2017) 1-9.
[180] S. Wang, Q. Hu, Y. Liu, X. Meng, Y. Ye, X. Liu, X. Song, Z. Liang, Multifunctional conjugated microporous polymers with pyridine unit for efficient iodine sequestration, exceptional tetracycline sensing and removal, Journal of Hazardous Materials 387 (2020) 121949.
[181] X. Qian, Z.-Q. Zhu, H.-X. Sun, F. Ren, P. Mu, W. Liang, L. Chen, A. Li, Capture and reversible storage of volatile iodine by novel conjugated microporous polymers containing thiophene units, ACS Applied Materials & Interfaces 8(32) (2016) 21063-21069.
[182] S. An, X. Zhu, Y. He, L. Yang, H. Wang, S. Jin, J. Hu, H. Liu, Porosity modulation in two-dimensional covalent organic frameworks leads to enhanced iodine adsorption performance, Industrial & Engineering Chemistry Research 58(24) (2019) 10495-10502.

[183] L. Wang, C. Yao, W. Xie, G. Xu, S. Zhang, Y. Xu, A series of thiophene-and nitrogen-rich conjugated microporous polymers for efficient iodine and carbon dioxide capture, New Journal of Chemistry 45(42) (2021) 19636-19640.
[184] C. Yao, T. Yu, Y. Xu, Synthesis of conjugated microporous polymers based on θ-Al_2O_3 substrate for enhanced iodine capture, Materials Letters 280 (2020) 128588.
[185] Q. Jiang, H. Huang, Y. Tang, Y. Zhang, C. Zhong, Highly porous covalent triazine frameworks for reversible iodine capture and efficient removal of dye, Industrial & Engineering Chemistry Research 57(44) (2018) 15114-15121.
[186] Z. Yan, Y. Yuan, Y. Tian, D. Zhang, G. Zhu, Highly efficient enrichment of volatile iodine by charged porous aromatic frameworks with three sorption sites, Angewandte Chemie 127(43) (2015) 12924-12928.
[187] H. Li, X. Ding, B.H. Han, Porous azo-bridged porphyrin–phthalocyanine network with high iodine capture capability, Chemistry–A European Journal 22(33) (2016) 11863-11868.
[188] Y. Liao, J. Weber, B.M. Mills, Z. Ren, C.F. Faul, Highly efficient and reversible iodine capture in hexaphenylbenzene-based conjugated microporous polymers, Macromolecules 49(17) (2016) 6322-6333.
[189] T. Zhou, Y. Zhao, J.W. Choi, A. Coskun, Lithium-salt mediated synthesis of a covalent triazine framework for highly stable lithium metal batteries, Angewandte Chemie International Edition 131(47) (2019) 16951-16955.
[190] P. Puthiaraj, S.-S. Kim, W.-S. Ahn, Covalent triazine polymers using a cyanuric chloride precursor via Friedel–Crafts reaction for CO_2 adsorption/separation, Chemical Engineering Journal 283 (2016) 184-192.
[191] Z. Feng, T. Danjo, K. Odelius, M. Hakkarainen, T. Iwata, A.-C. Albertsson, Recyclable fully biobased chitosan adsorbents spray-dried in one pot to microscopic size and enhanced adsorption capacity, Biomacromolecules 20(5) (2019) 1956-1964.
[192] M.J. Frisch, G.W. Trucks, H.B. Schlegel, G.E. Scuseria, M.A. Robb, J.R. Cheeseman, G. Scalmani, V. Barone, G.A. Petersson, H. Nakatsuji, X. Li, M. Caricato, A.V. Marenich, J. Bloino, B.G. Janesko, R. Gomperts, B. Mennucci, H.P. Hratchian, J.V. Ortiz, A.F. Izmaylov, J.L. Sonnenberg, Williams, F. Ding, F. Lipparini, F. Egidi, J. Goings, B. Peng, A. Petrone, T. Henderson, D. Ranasinghe, V.G. Zakrzewski, J. Gao, N. Rega, G. Zheng, W. Liang, M. Hada, M. Ehara, K. Toyota, R. Fukuda, J. Hasegawa, M. Ishida, T. Nakajima, Y. Honda, O. Kitao, H. Nakai, T. Vreven, K. Throssell, J.A. Montgomery Jr., J.E. Peralta, F. Ogliaro, M.J. Bearpark, J.J. Heyd, E.N. Brothers, K.N. Kudin, V.N. Staroverov, T.A. Keith, R. Kobayashi, J. Normand, K. Raghavachari, A.P. Rendell, J.C. Burant, S.S. Iyengar, J. Tomasi, M. Cossi, J.M. Millam, M. Klene, C. Adamo, R. Cammi, J.W. Ochterski, R.L. Martin, K. Morokuma, O. Farkas, J.B. Foresman, D.J. Fox, Gaussian 16 Rev. C.01, Wallingford, CT, 2016.
[193] X. He, S.-Y. Zhang, X. Tang, S. Xiong, C. Ai, D. Chen, J. Tang, C. Pan, G. Yu, Exploration of 1D channels in stable and high-surface-area covalent triazine polymers for effective iodine removal, Chemical Engineering Journal 371 (2019) 314-318.
[194] S. Xiong, X. Tang, C. Pan, L. Li, J. Tang, G. Yu, Carbazole-bearing porous organic polymers with a mulberry-like morphology for efficient iodine capture, ACS Applied Materials & Interfaces 11(30) (2019) 27335-27342.
[195] M. Thommes, K. Kaneko, A.V. Neimark, J.P. Olivier, F. Rodriguez-Reinoso, J. Rouquerol, K.S. Sing, Physisorption of gases, with special reference to the evaluation of surface area and pore size distribution (IUPAC Technical Report), Pure and Applied Chemistry 87(9-10) (2015) 1051-1069.
[196] Y. Zhu, Y.-J. Ji, D.-G. Wang, Y. Zhang, H. Tang, X.-R. Jia, M. Song, G. Yu, G.-C. Kuang, BODIPY-based conjugated porous polymers for highly efficient volatile iodine capture, Journal of Materials Chemistry A 5(14) (2017) 6622-6629.
[197] Q. Liu, S. Yang, H. Repich, Y. Zhai, X. Xu, Y. Liang, H. Li, H. Wang, F. Xu, Porous Functionalized Covalent-Triazine Frameworks for Enhanced Adsorption Toward Polysulfides in Li-S Batteries and Organic Dyes, Frontiers in chemistry 8 (2020) 1009.

[198] Q.-Q. Dang, C.-Y. Liu, X.-M. Wang, X.-M. Zhang, Novel covalent triazine framework for high-performance CO2 capture and alkyne carboxylation reaction, ACS Applied Materials & Interfaces 10(33) (2018) 27972-27978.
[199] L. Zhai, D. Han, J. Dong, W. Jiang, R. Nie, X. Yang, X. Luo, Z. Li, Constructing stable and porous covalent organic frameworks for efficient iodine vapor capture, Macromolecular Rapid Communications 42(13) (2021) 2100032.
[200] L. Shao, Y. Sang, N. Liu, Q. Wei, F. Wang, P. Zhan, W. Luo, J. Huang, J. Chen, One-step synthesis of N-containing hyper-cross-linked polymers by two crosslinking strategies and their CO_2 adsorption and iodine vapor capture, Separation and Purification Technology 262 (2021) 118352.
[201] L. Shao, N. Liu, L. Wang, Y. Sang, P. Zhan, L. Zhang, J. Huang, J. Chen, Facile preparation of oxygen-rich porous polymer microspheres from lignin-derived phenols for selective CO_2 adsorption and iodine vapor capture, Chemosphere 288 (2022) 132499.
[202] M. Ansari, A. Hassan, A. Alam, N. Das, A mesoporous polymer bearing 3D-Triptycene,–OH and azo-functionalities: Reversible and efficient capture of carbon dioxide and iodine vapor, Microporous and Mesoporous Materials 323 (2021) 111242.
[203] Y. Yu, L. Ren, M. Liu, S. Huang, X. Xiao, R. Liu, L. Wang, W. Xu, Polyphenylene sulfide ultrafine fibrous membrane modified by nanoscale ZIF-8 for highly effective adsorption, interception, and recycling of iodine vapor, ACS Applied Materials & Interfaces 11(34) (2019) 31291-31301.
[204] D. Dai, J. Yang, Y.C. Zou, J.R. Wu, L.L. Tan, Y. Wang, B. Li, T. Lu, B. Wang, Y.W. Yang, Macrocyclic arenes-based conjugated macrocycle polymers for highly selective CO_2 capture and iodine adsorption, Angewandte Chemie 133(16) (2021) 9049-9057.
[205] M.A. Sabri, M.H. Al-Sayah, S. Sen, T.H. Ibrahim, O.M. El-Kadri, Fluorescent aminal linked porous organic polymer for reversible iodine capture and sensing, Scientific Reports 10(1) (2020) 1-11.
[206] D. Chen, Y. Fu, W. Yu, G. Yu, C. Pan, Versatile Adamantane-based porous polymers with enhanced microporosity for efficient CO_2 capture and iodine removal, Chemical Engineering Journal 334 (2018) 900-906.
[207] C. Pei, T. Ben, S. Xu, S. Qiu, Ultrahigh iodine adsorption in porous organic frameworks, Journal of Materials Chemistry A 2(20) (2014) 7179-7187.
[208] J. Wang, K. Ai, L. Lu, Flame-retardant porous hexagonal boron nitride for safe and effective radioactive iodine capture, Journal of Materials Chemistry A 7(28) (2019) 16850-16858.
[209] Y. Wang, J. Tao, S. Xiong, P. Lu, J. Tang, J. He, M.U. Javaid, C. Pan, G. Yu, Ferrocene-based porous organic polymers for high-affinity iodine capture, Chemical Engineering Journal 380 (2020) 122420.
[210] S. Pourebrahimi, M. Pirooz, Functionalized Covalent Triazine Frameworks as Promising Platforms for Environmental Remediation: A Review, Cleaner Chemical Engineering 2 (2022) 100012.
[211] G. Li, Y. Huang, J. Lin, C. Yu, Z. Liu, Y. Fang, Y. Xue, C. Tang, Effective capture and reversible storage of iodine using foam-like adsorbents consisting of porous boron nitride microfibers, Chemical Engineering Journal 382 (2020) 122833.
[212] H. Wang, H. Hu, Q. Peng, A facile one-step in-situ template strategy on the synthesis of cyclophosphazene-based amino-linked porous polymer and efficient removal of iodine, Microporous and Mesoporous Materials 323 (2021) 111249.
[213] Y. Zhao, X. Liu, Y. Li, M. Xia, T. Xia, H. Sun, Z. Sui, X.-M. Hu, Q. Chen, Ultra-stable fluorescent 2D covalent organic framework for rapid adsorption and selective detection of radioiodine, Microporous and Mesoporous Materials 319 (2021) 111046.
[214] X. Pan, C. Ding, Z. Zhang, H. Ke, G. Cheng, Functional porous organic polymer with high S and N for reversible iodine capture, Microporous and Mesoporous Materials 300 (2020) 110161.
[215] F. Ren, Z. Zhu, X. Qian, W. Liang, P. Mu, H. Sun, J. Liu, A. Li, Novel thiophene-bearing conjugated microporous polymer honeycomb-like porous spheres with ultrahigh iodine uptake, Chemical Communications 52(63) (2016) 9797-9800.

[216] K. Wu, Y.-L. Huang, J. Zheng, D. Luo, M. Xie, Y.Y. Li, W. Lu, D. Li, A microporous shp-topology metal–organic framework with an unprecedented high-nuclearity Co 10-cluster for iodine capture and histidine detection, Materials Chemistry Frontiers 5(11) (2021) 4300-4309.
[217] W. Huan, H. Huiping, P. Qifan, Superior removal of iodine via cyclophosphazene-based conjugation-enriched cross-linking hybrid polymers, Colloids and Surfaces A: Physicochemical and Engineering Aspects 627 (2021) 127185.
[218] Z. Guo, P. Sun, X. Zhang, J. Lin, T. Shi, S. Liu, A. Sun, Z. Li, Amorphous porous organic polymers based on Schiff-Base chemistry for highly efficient iodine capture, Chemistry–An Asian Journal 13(16) (2018) 2046-2053.
[219] T.-S. Chee, Z. Tian, X. Zhang, L. Lei, C. Xiao, Efficient capture of radioactive iodine by a new bismuth-decorated electrospinning carbon nanofiber, Journal of Nuclear Materials 542 (2020) 152526.
[220] P. Chen, X. He, M. Pang, X. Dong, S. Zhao, W. Zhang, Iodine capture using Zr-based metal–organic frameworks (Zr-MOFs): adsorption performance and mechanism, ACS Applied Materials & Interfaces 12(18) (2020) 20429-20439.
[221] A. Bendjeddou, T. Abbaz, A. Gouasmia, D. Villemin, Molecular structure, HOMO-LUMO, MEP and Fukui function analysis of some TTF-donor substituted molecules using DFT (B3LYP) calculations, Int. Res. J. Pure Appl. Chem 12(1) (2016) 1-9.
[222] B. Cao, S. Liu, D. Du, Z. Xue, H. Fu, H. Sun, Experiment and DFT studies on radioiodine removal and storage mechanism by imidazolium-based ionic liquid, Journal of Molecular Graphics and Modelling 64 (2016) 51-59.
[223] J.P. Vareda, A.J. Valente, L. Durães, Assessment of heavy metal pollution from anthropogenic activities and remediation strategies: A review, Journal of Environmental Management 246 (2019) 101-118. https://doi.org/10.1016/j.jenvman.2019.05.126.
[224] E.A. Gendy, J. Ifthikar, J. Ali, D.T. Oyekunle, Z. Elkhlifia, I.I. Shahib, A.I. Khodair, Z. Chen, Removal of heavy metals by covalent organic frameworks (COFs): A review on its mechanism and adsorption properties, Journal of Environmental Chemical Engineering 9(4) (2021) 105687. https://doi.org/10.1016/j.jece.2021.105687.
[225] K. Yin, Q. Wang, M. Lv, L. Chen, Microorganism remediation strategies towards heavy metals, Chemical Engineering Journal 360 (2019) 1553-1563. https://doi.org/10.1016/j.cej.2018.10.226.
[226] R. Shrestha, S. Ban, S. Devkota, S. Sharma, R. Joshi, A.P. Tiwari, H.Y. Kim, M.K. Joshi, Technological trends in heavy metals removal from industrial wastewater: A review, Journal of Environmental Chemical Engineering 9(4) (2021) 105688. https://doi.org/10.1016/j.jece.2021.105688.
[227] S. Rajendran, A. Priya, P.S. Kumar, T.K. Hoang, K. Sekar, K.Y. Chong, K.S. Khoo, H.S. Ng, P.L. Show, A critical and recent developments on adsorption technique for removal of heavy metals from wastewater-A review, Chemosphere 303 (2022) 135146. https://doi.org/10.1016/j.chemosphere.2022.135146.
[228] K. Gupta, P. Joshi, R. Gusain, O.P. Khatri, Recent advances in adsorptive removal of heavy metal and metalloid ions by metal oxide-based nanomaterials, Coordination Chemistry Reviews 445 (2021) 214100. https://doi.org/10.1016/j.ccr.2021.214100.
[229] C. Duan, T. Ma, J. Wang, Y. Zhou, Removal of heavy metals from aqueous solution using carbon-based adsorbents: A review, Journal of Water Process Engineering 37 (2020) 101339. https://doi.org/10.1016/j.jwpe.2020.101339.
[230] M.-A. Gatou, P. Bika, T. Stergiopoulos, P. Dallas, E.A. Pavlatou, Recent advances in covalent organic frameworks for heavy metal removal applications, Energies 14(11) (2021) 3197. https://doi.org/10.3390/en14113197.
[231] N. Abdollahi, G. Moussavi, S. Giannakis, A review of heavy metals' removal from aqueous matrices by Metal-Organic Frameworks (MOFs): State-of-the art and recent advances, Journal of Environmental Chemical Engineering 10 (2022) 107394. https://doi.org/10.1016/j.jece.2022.107394.

[232] S. Gu, X. Kang, L. Wang, E. Lichtfouse, C. Wang, Clay mineral adsorbents for heavy metal removal from wastewater: a review, Environmental Chemistry Letters 17 (2019) 629-654. https://doi.org/10.1007/s10311-018-0813-9.
[233] H.I. Syeda, I. Sultan, K.S. Razavi, P.-S. Yap, Biosorption of heavy metals from aqueous solution by various chemically modified agricultural wastes: A review, Journal of Water Process Engineering 46 (2022) 102446. https://doi.org/10.1016/j.jwpe.2021.102446.
[234] X. Liu, R. Ma, X. Wang, Y. Ma, Y. Yang, L. Zhuang, S. Zhang, R. Jehan, J. Chen, X. Wang, Graphene oxide-based materials for efficient removal of heavy metal ions from aqueous solution: A review, Environmental Pollution 252 (2019) 62-73. https://doi.org/10.1016/j.envpol.2019.05.050.
[235] H. Qin, T. Hu, Y. Zhai, N. Lu, J. Aliyeva, The improved methods of heavy metals removal by biosorbents: A review, Environmental Pollution 258 (2020) 113777. https://doi.org/10.1016/j.envpol.2019.113777.
[236] H. Masoumi, A. Ghaemi, H.G. Gilani, Evaluation of hyper-cross-linked polymers performances in the removal of hazardous heavy metal ions: A review, Separation and Purification Technology 260 (2021) 118221. https://doi.org/10.1016/j.seppur.2020.118221.
[237] N. Marzari, A. Ferretti, C. Wolverton, Electronic-structure methods for materials design, Nature Materials 20(6) (2021) 736-749. https://doi.org/10.1038/s41563-021-01013-3.
[238] J. Luo, D. Yu, K.D. Hristovski, K. Fu, Y. Shen, P. Westerhoff, J.C. Crittenden, Critical review of advances in engineering nanomaterial adsorbents for metal removal and recovery from water: mechanism identification and engineering design, Environmental Science & Technology 55(8) (2021) 4287-4304. https://doi.org/10.1021/acs.est.0c07936.
[239] M. Du, Y. Zhang, Z. Wang, M. Lv, A. Tang, Y. Yu, X. Qu, Z. Chen, Q. Wen, A. Li, Insight into the synthesis and adsorption mechanism of adsorbents for efficient phosphate removal: Exploration from synthesis to modification, Chemical Engineering Journal 442 (2022) 136147. https://doi.org/10.1016/j.cej.2022.136147.
[240] R. Saadi, Z. Saadi, R. Fazaeli, N.E. Fard, Monolayer and multilayer adsorption isotherm models for sorption from aqueous media, Korean Journal of Chemical Engineering 32 (2015) 787-799. https://doi.org/10.1007/s11814-015-0053-7.
[241] J. Yan, H. Sun, Q. Wang, L. Lu, B. Zhang, Z. Wang, S. Guo, F. Han, Covalent triazine frameworks for the dynamic adsorption/separation of benzene/cyclohexane mixtures, New Journal of Chemistry 46(16) (2022) 7580-7587. https://doi.org/10.1039/D2NJ00727D.
[242] F. Jiang, Y. Wang, T. Qiu, G. Yang, C. Yang, J. Huang, Z. Fang, J. Li, Synthesis of biphenyl-linked covalent triazine frameworks with excellent lithium storage performance as anode in lithium ion battery, Journal of Power Sources 523 (2022) 231041. https://doi.org/10.1016/j.jpowsour.2022.231041.
[243] R. Luo, W. Xu, M. Chen, X. Liu, Y. Fang, H. Ji, Covalent triazine frameworks obtained from nitrile monomers for sustainable CO_2 catalysis, ChemSusChem 13(24) (2020) 6509-6522. https://doi.org/10.1002/cssc.202002422.
[244] M.J. Frisch, J.A. Pople, J.S. Binkley, Self-consistent molecular orbital methods 25. Supplementary functions for Gaussian basis sets, The Journal of Chemical Physics 80(7) (1984) 3265-3269. https://doi.org/10.1063/1.447079.
[245] F. Weigend, R. Ahlrichs, Balanced basis sets of split valence, triple zeta valence and quadruple zeta valence quality for H to Rn: Design and assessment of accuracy, Physical Chemistry Chemical Physics 7(18) (2005) 3297-3305. https://doi.org/10.1039/B508541A.
[246] a.J. Foster, F. Weinhold, Natural hybrid orbitals, Journal of the American Chemical Society 102(24) (1980) 7211-7218. https://doi.org/10.1021/ja00544a007.
[247] S.-T. Lin, H.N. Tran, H.-P. Chao, J.-F. Lee, Layered double hydroxides intercalated with sulfur-containing organic solutes for efficient removal of cationic and oxyanionic metal ions, Applied Clay Science 162 (2018) 443-453. https://doi.org/10.1016/j.clay.2018.06.011.

[248] M. Zbair, H.A. Ahsaine, Z. Anfar, A. Slassi, Carbon microspheres derived from walnut shell: Rapid and remarkable uptake of heavy metal ions, molecular computational study and surface modeling, Chemosphere 231 (2019) 140-150. https://doi.org/10.1016/j.chemosphere.2019.05.120.
[249] S. Ryu, G. Naidu, H. Moon, S. Vigneswaran, Selective copper recovery by membrane distillation and adsorption system from synthetic acid mine drainage, Chemosphere 260 (2020) 127528. https://doi.org/10.1016/j.chemosphere.2020.127528.
[250] Y. Zou, S. Abednatanzi, P. Gohari Derakhshandeh, S. Mazzanti, C.M. Schüßlbauer, D. Cruz, P. Van Der Voort, J.-W. Shi, M. Antonietti, D.M. Guldi, Red edge effect and chromoselective photocatalysis with amorphous covalent triazine-based frameworks, Nature Communications 13(1) (2022) 2171. https://doi.org/10.1038/s41467-022-29781-9.
[251] Y. Chen, X. Hu, J. Guo, Z. Guo, H. Zhan, S. Du, Optimizing CO_2 capture and separation in pyrene derived covalent triazine frameworks, European Polymer Journal 171 (2022) 111215. https://doi.org/10.1016/j.eurpolymj.2022.111215.
[252] S. Pourebrahimi, M. Pirooz, Synthesis of a novel freestanding conjugated triazine-based microporous membrane through superacid-catalyzed polymerization for superior CO_2 separation, Chemical Engineering Journal Advances 11 (2022) 100315. https://doi.org/10.1016/j.ceja.2022.100315.
[253] M. Yang, H. Guo, L. Sun, N. Wu, M. Wang, F. Yang, T. Zhang, J. Zhang, Z. Pan, W. Yang, Simultaneous electrochemical detection of hydroquinone and catechol using MWCNT-COOH/CTF-1 composite modified electrode, Colloids and Surfaces A: Physicochemical and Engineering Aspects 625 (2021) 126917. https://doi.org/10.1016/j.colsurfa.2021.126917.
[254] X.-F. Lu, W.-H. Ji, L. Yuan, S. Yu, D.-S. Guo, Preparation of carboxy-functionalized covalent organic framework for efficient removal of Hg^{2+} and Pb^{2+} from water, Industrial & Engineering Chemistry Research 58(38) (2019) 17660-17667. https://doi.org/10.1021/acs.iecr.9b03138.
[255] Q. Lu, Y. Ma, H. Li, X. Guan, Y. Yusran, M. Xue, Q. Fang, Y. Yan, S. Qiu, V. Valtchev, Postsynthetic functionalization of three-dimensional covalent organic frameworks for selective extraction of lanthanide ions, Angewandte Chemie 130(21) (2018) 6150-6156. https://doi.org/10.1002/ange.201712246.
[256] P. Liu, L. Niu, Y.-L. Men, C. Peng, Z. Liu, X.-Y. Meng, Y.-X. Pan, Overturning photoreduction product of CO_2 by defect-and COOH-functionalized multi-wall carbon nanotubes, Applied Catalysis B: Environmental 320 (2023) 121985. https://doi.org/10.1016/j.apcatb.2022.121985.
[257] F. Zeng, H. Li, H. Cheng, J. Tang, Y. Liu, SF_6 decomposition and insulation condition monitoring of GIE: A review, High Voltage 6(6) (2021) 955-966. https://doi.org/10.1049/hve2.12160.
[258] Q. Li, D. Chen, Y. Liu, J. Miao, C. Zhang, X. Chen, D. Cui, Ru doped aluminum nitride monolayer for detecting and scavenging SF_6 decomposition components, Surfaces and Interfaces 36 (2023) 102514. https://doi.org/10.1016/j.surfin.2022.102514.
[259] M. Kiani, M.U. Rehman, X. Tian, B. Yakobson, Two-Dimensional Nanomaterials for the Development of Efficient Gas Sensors: Recent Advances, Challenges, and Future Perspectives, Advanced Materials Technologies 7(7) (2022) 2101252. https://doi.org/10.1002/admt.202101252.
[260] X. Liu, T. Ma, N. Pinna, J. Zhang, Two-dimensional nanostructured materials for gas sensing, Advanced Functional Materials 27(37) (2017) 1702168. https://doi.org/10.1002/adfm.201702168.
[261] S. Kaushal, M. Kaur, N. Kaur, V. Kumari, P.P. Singh, Heteroatom-doped graphene as sensing materials: A mini review, RSC Advances 10(48) (2020) 28608-28629. https://doi.org/10.1039/D0RA04432F.
[262] D. Degler, U. Weimar, N. Barsan, Current understanding of the fundamental mechanisms of doped and loaded semiconducting metal-oxide-based gas sensing materials, ACS Sensors 4(9) (2019) 2228-2249. https://doi.org/10.1021/acssensors.9b00975.
[263] X. Tang, A. Du, L. Kou, Gas sensing and capturing based on two-dimensional layered materials: Overview from theoretical perspective, Wiley Interdisciplinary Reviews: Computational Molecular Science 8(4) (2018) e1361. https://doi.org/10.1002/wcms.1361.

[264] Z. Nie, C. Wang, R. Xue, G. Xie, H. Xiong, Two-dimensional FePc and MnPc monolayers as promising materials for SF_6 decomposition gases detection: Insights from DFT calculations, Applied Surface Science 608 (2023) 155119. https://doi.org/10.1016/j.apsusc.2022.155119.
[265] J. Chen, Q. Zhou, L. Jia, X. Cui, W. Zeng, The gas-sensing mechanism of Pt_3 cluster doped SnS_2 monolayer for SF_6 decomposition: A DFT study, Applied Surface Science 597 (2022) 153693. https://doi.org/10.1016/j.apsusc.2022.153693.
[266] B. Li, Q. Zhou, R. Peng, Y. Liao, W. Zeng, Adsorption of SF_6 decomposition gases (H_2S, SO_2, SOF_2 and SO_2F_2) on Sc-doped MoS_2 surface: A DFT study, Applied Surface Science 549 (2021) 149271. https://doi.org/10.1016/j.apsusc.2021.149271.
[267] H. Huang, Y. Yu, M. Zhang, Analysis of adsorption properties of SF_6 decomposed gases (SOF_2, SO_2F_2, SF_4, CF_4, and HF) on Fe-doped SWCNT: A DFT study, Applied Surface Science 505 (2020) 144622. https://doi.org/10.1016/j.apsusc.2019.144622.
[268] S.-Y. Xia, L.-Q. Tao, T. Jiang, H. Sun, J. Li, Rh-doped h-BN monolayer as a high sensitivity SF_6 decomposed gases sensor: A DFT study, Applied Surface Science 536 (2021) 147965. https://doi.org/10.1016/j.apsusc.2020.147965.
[269] Q. Zhang, Y. Gui, H. Qiao, X. Chen, L. Cao, Theoretical study of SF_6 decomposition products adsorption on metal oxide cluster-modified single-layer graphene, Journal of Industrial and Engineering Chemistry 105 (2022) 278-290. https://doi.org/10.1016/j.jiec.2021.09.025.
[270] M. Wang, Q. Zhou, W. Zeng, Theoretical study on adsorption of SF_6 decomposition gas in GIS gas cell based on intrinsic and Ni-doped $MoTe_2$ monolayer, Applied Surface Science 591 (2022) 153167. https://doi.org/10.1016/j.apsusc.2022.153167.
[271] P. Jia, S. Qiao, Y. Wang, Y. Liu, Pd-decorated GaN monolayer as a promising scavenger for SO_2 and SOF_2 in SF_6 insulation equipment: A first-principles study, Computational and Theoretical Chemistry 1201 (2021) 113276. https://doi.org/10.1016/j.comptc.2021.113276.
[272] J.-Y. Li, P. Wang, S. Akram, Adsorption and sensing for SF_6 decomposed gases by Pt-BN monolayer: a DFT study, Molecular Physics 119(14) (2021) e1950856. https://doi.org/10.1080/00268976.2021.1950856.
[273] T.A.K. Roy Dennington, John M. Millam, GaussView, Version 6.1, Semichem Inc., Shawnee Mission, KS (2016).
[274] T. Lu, F. Chen, Multiwfn: a multifunctional wavefunction analyzer, Journal of Computational Chemistry 33(5) (2012) 580-592. https://doi.org/10.1002/jcc.22885.
[275] S. Grimme, J. Antony, S. Ehrlich, H. Krieg, A consistent and accurate ab initio parametrization of density functional dispersion correction (DFT-D) for the 94 elements H-Pu, The Journal of Chemical Physics 132(15) (2010) 154104. https://doi.org/10.1063/1.3382344.
[276] W.J. Hehre, R. Ditchfield, J.A. Pople, Self—consistent molecular orbital methods. XII. Further extensions of Gaussian—type basis sets for use in molecular orbital studies of organic molecules, The Journal of Chemical Physics 56(5) (1972) 2257-2261. https://doi.org/10.1063/1.1677527.
[277] P.J. Hay, W.R. Wadt, Ab initio effective core potentials for molecular calculations. Potentials for K to Au including the outermost core orbitals, The Journal of Chemical Physics 82(1) (1985) 299-310. https://doi.org/10.1063/1.448975.
[278] Y. Yang, M.N. Weaver, K.M. Merz Jr, Assessment of the "6-31+G** + LANL2DZ" mixed basis set coupled with density functional theory methods and the effective core potential: prediction of heats of formation and ionization potentials for first-row-transition-metal complexes, The Journal of Physical Chemistry A 113(36) (2009) 9843-9851. https://doi.org/10.1021/jp807643p.
[279] X. Peng, D. Liu, F. Zhao, C. Tang, Gas sensing properties of Mg-doped graphene for H_2S, SO_2, SOF_2, and SO_2F_2 based on DFT, International Journal of Quantum Chemistry 122(22) (2022) e26989. https://doi.org/10.1002/qua.26989.

[280] W. Cao, Y. Gui, T. Chen, L. Xu, Z. Ding, Adsorption and gas-sensing properties of Pt_2–GaNNTs for SF_6 decomposition products, Applied Surface Science 524 (2020) 146570. https://doi.org/10.1016/j.apsusc.2020.146570.
[281] H. Cui, X. Zhang, D. Chen, J. Tang, Adsorption mechanism of SF_6 decomposed species on pyridine-like PtN_3 embedded CNT: a DFT study, Applied Surface Science 447 (2018) 594-598. https://doi.org/10.1016/j.apsusc.2018.03.232.

Appendix

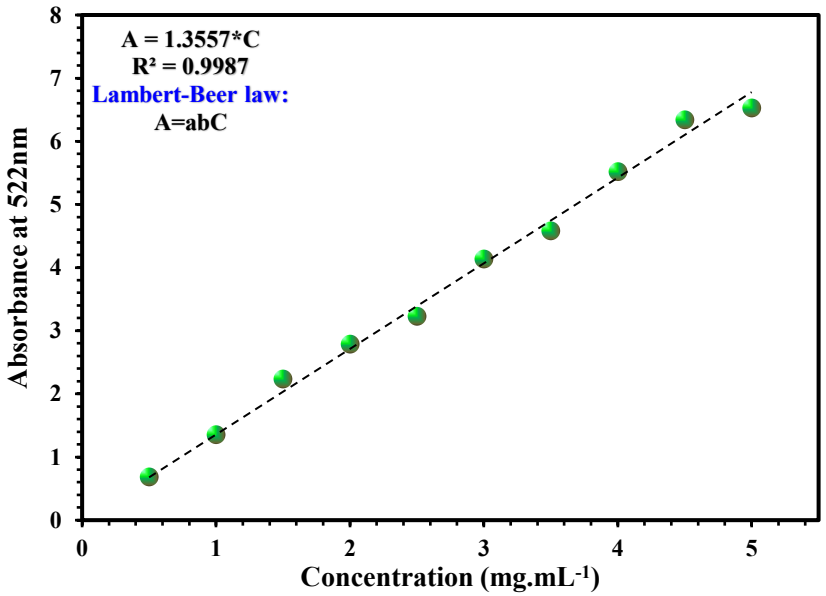

Figure S5.1. Working curve for the estimation of molar absorption coefficient.

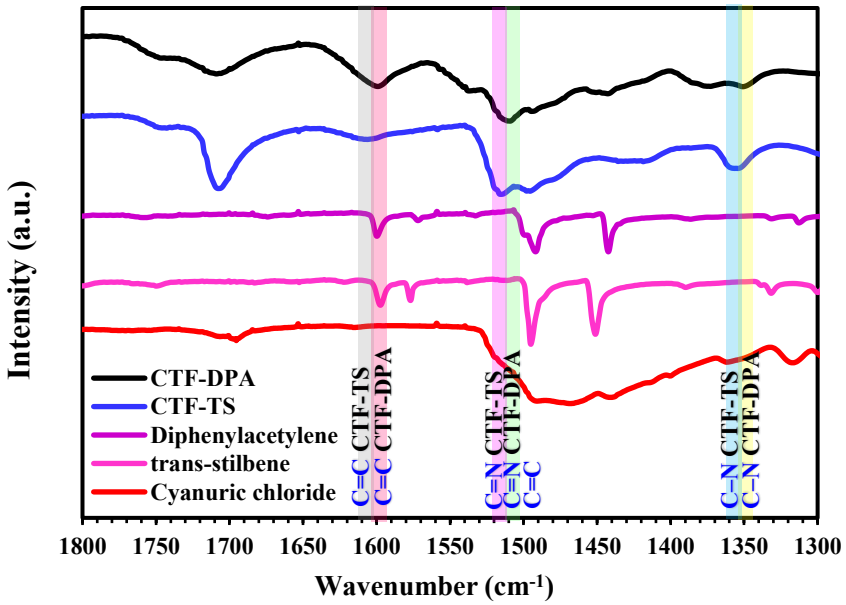

Figure S5.2. FT-IR spectra of the precursors and CTFs zoomed over the 1300-1800 cm^{-1} wavenumber range.

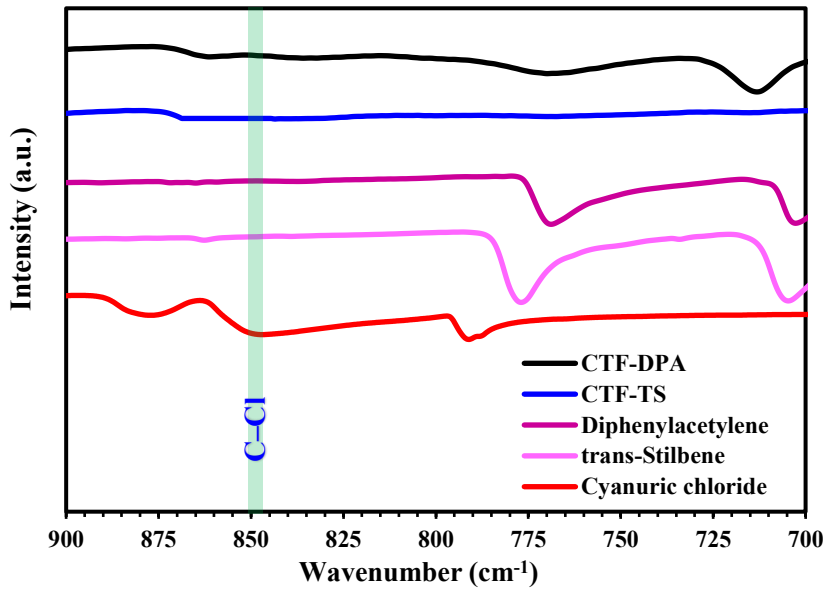

Figure S5.3. FT-IR spectra of the precursors and CTFs zoomed over the 700-900 cm^{-1} wavenumber range.

Table S5.1. Textural properties and pore features of the CTFs.

Sample ID	Surface area (m^2 g^{-1})			Pore volume (cm^3 g^{-1})			Average pore size (nm)
	S_{BET}	S_{micro}	$S_{meso/macro}$	V_{total}	V_{micro}	$V_{meso/macro}$	
CTF-DPA	943	472	471	0.584	0.251	0.333	2.49
CTF-TS	919	462	457	0.579	0.250	0.329	2.54

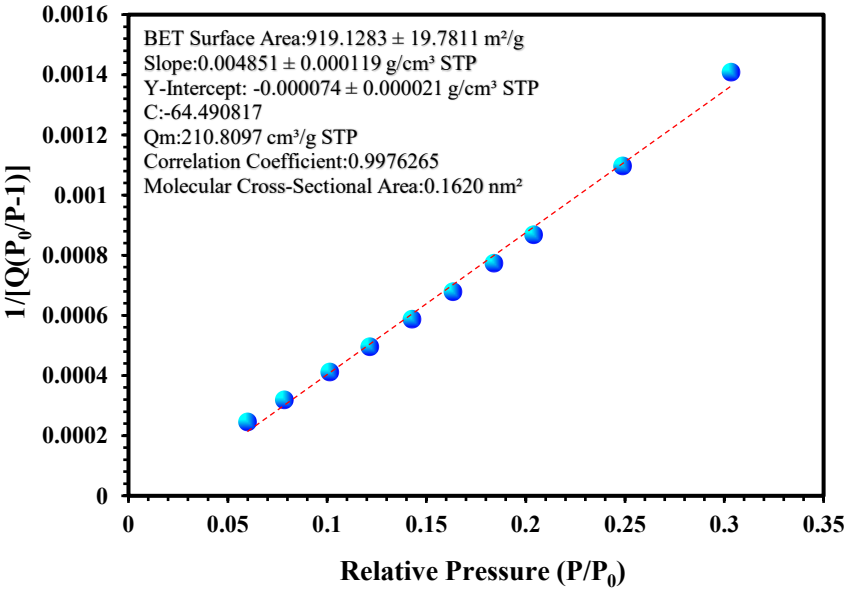

Figure S5.4. BET surface area linear plot for CTF-TS.

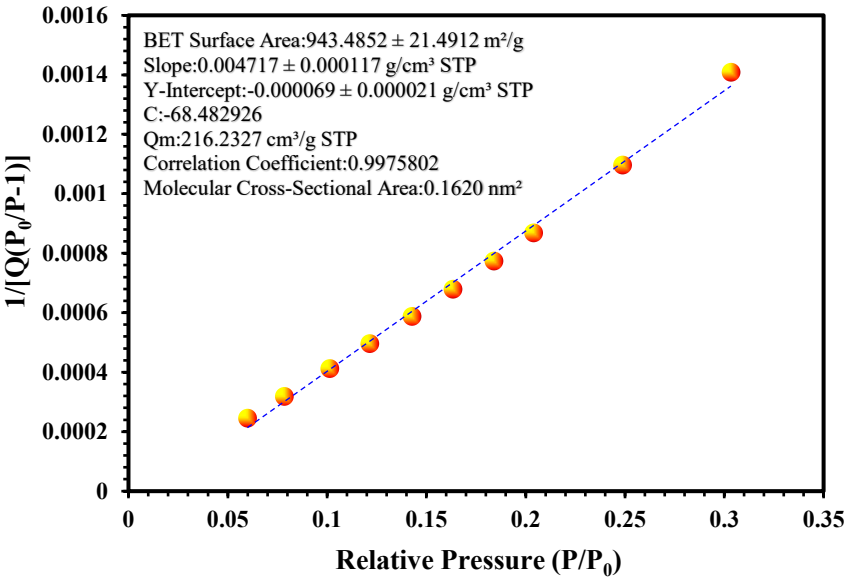

Figure S5.5. BET surface area linear plot for CTF-DPA.

Table S5.2. Elemental analysis (EA) results.

Sample	Experimental %			Theoretical %		
	% C	% H	% N	% C	% H	% N
CTF-DPA	81.36	4.24	11.79	84.21	3.51	12.28
CTF-TS	80.19	4.97	11.25	83.48	4.35	12.17

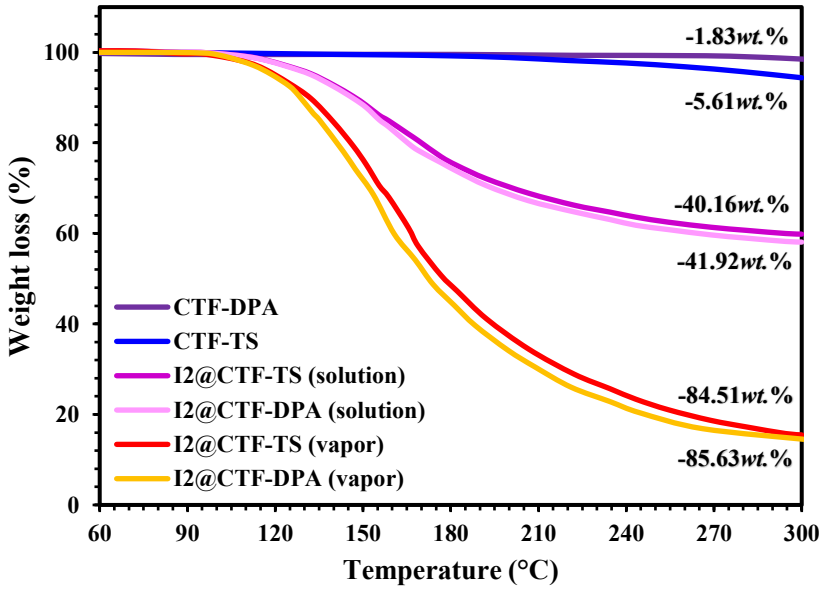

Figure S5.6. TGA curves of the iodine-loaded CTFs.

Iodine-loading weight of CTFs:

$$\frac{(40.16_{\text{CTF-TS+iodine weight loss}} - 5.61_{\text{CTF-TS weight loss}})}{(100-40.16-5.61)} = 0.528\ \frac{\text{g iodine}}{\text{g CTF-TS}}\ \text{(solution)}$$

$$\frac{(84.51_{\text{CTF-TS+iodine weight loss}} - 5.61_{\text{CTF-TS weight loss}})}{(100-84.51-5.61)} = 3.739\ \frac{\text{g iodine}}{\text{g CTF-TS}}\ \text{(vapor)}$$

$$\frac{(41.92_{\text{CTF-DPA+iodine weight loss}} - 1.83_{\text{CTF-DPA weight loss}})}{(100-41.92-1.83)} = 0.669\ \frac{\text{g iodine}}{\text{g CTF-DPA}}\ \text{(solution)}$$

$$\frac{(85.63_{\text{CTF-DPA+iodine weight loss}} - 1.83_{\text{CTF-DPA weight loss}})}{(100-85.63-1.83)} = 5.173\ \frac{\text{g iodine}}{\text{g CTF-DPA}}\ \text{(vapor)}$$

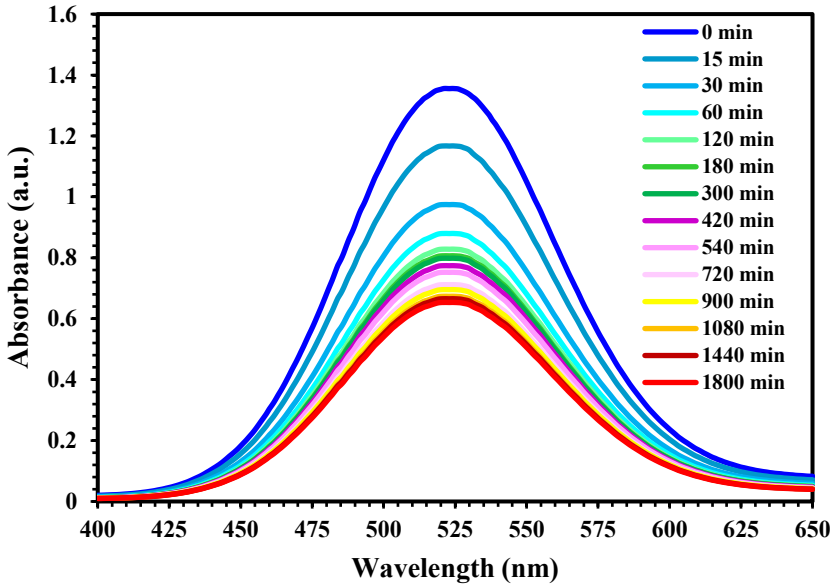

Figure S5.7. Time-dependent UV-Vis spectra of CTF-TS in n-hexane solution.

Table S5.3. Detailed iodine vapor adsorption characteristics comparison.

Sample ID	BET ($m^2\ g^{-1}$)	Pore volume ($cm^3\ g^{-1}$)	High-affinity species	I_2 uptake ($g\ g^{-1}$)	Ref.
CTF-DPA	943	0.584	C≡C, phenyl, triazine	5.12	This work
CTF-TS	919	0.579	C=C, phenyl, triazine	3.75	This work
CTF-PF-4	889	0.580	imidazole, triazine, phenyl	3.12	[55]
TTA-TMTA-COF	801	0.690	imine, phenyl, triazine, methoxy	3.21	[56]
HCP6	30.3	0.061	triphenylamine, carbazole	3.25	[57]
H-C-CTPs	20.6	0.033	ethoxy, hydroxyl, phenyl	1.92	[58]
TBHCP-OH	234.9	0.066	triptycene, hydroxyl, azo	2.60	[59]
PPS-ZIF-8	-	-	polyphenylene sulfide	2.51	[60]
CMP-4	9.5	-	C≡C, biphenyl	2.08	[61]
TALPOP	401	0.871	amine, anthracene, triazine	3.14	[62]
NOP-54	1178	1.320	adamantane, phenyl	2.02	[63]

Table S5.4. Detailed iodine adsorption in n-hexane solution characteristics comparison.

Sample ID	BET ($m^2\ g^{-1}$)	Pore volume ($cm^3\ g^{-1}$)	High-affinity species	I_2 uptake ($mg\ g^{-1}$)	Ref.
CTF-DPA	943	0.584	C≡C, phenyl, triazine	667	This work
CTF-TS	919	0.579	C=C, phenyl, triazine	518	This work
BN foam	562	0.450	boron nitride	61	[69]
CPP-2	32.7	0.121	amine, phenyl, phosphazene	347	[70]
COF-PA	1471	-	amine, phenyl, methoxy	820	[71]
P-TzTz	132	-	thiophene, N, S	494	[72]
SCMP-II	119	-	thiophene, phenyl, C≡C	600	[73]
JNU-200	466.5	-	phenyl, Co^{2+}, Co^{3+}	256	[74]
CPP-Pyr	9.246	0.116	phosphazene, pyrrole	625	[75]

Table S5.5. Optimized parameters of FL-PFO kinetic model.

Kinetic model	Adsorbent	Phase	q_e ($g\ g^{-1}$)	k (hr^{-1})	α	R^2
Fractal-like pseudo-first-order (FL-PFO) $q_t = q_e(1 - \exp(-kt^{\alpha}))$	CTF-DPA	Vapor	5.4157	0.1882	0.5114	0.9999
		Liquid	0.6843	0.0472	0.5971	0.9978
	CTF-TS	Vapor	3.7055	0.1474	0.5908	0.9999
		Liquid	0.5894	0.0463	0.5126	0.9979

Mass transfer into a sphere can be related to the dimensionless time, τ, defined as:

$$\tau = \frac{D_{AB}t}{R^2}$$

where D_{AB} is the diffusivity in the sphere, t is the time, and R is the radius of the sphere. The sphere is fully saturated when the dimensionless time equals or exceeds 1. Hence, we can define an equilibration time as follows:

$$t_{eq} = \frac{R^2}{D_{AB}}$$

In narrow pores, particularly in the gas phase, diffusion is dominated by Knudsen diffusion. The equation for the Knudsen diffusivity is:

$$D_K = \frac{8a}{3}\sqrt{\frac{RT}{2\pi M_A}}$$

where R is the ideal gas constant (8.314 J/mol K), T is the temperature (K), and M_A is the molar mass of the diffusing species (kg/mol). Assuming that the iodine species in gas phase is I_2, the molar mass is 0.2538 kg/mol. If we assume a pore diameter of 1 nm (i.e., a = 5×10^{-10} m), then the Knudsen diffusivity is 5.27×10^{-8} m^2/s. The calculation can easily be scaled to a different pore size: the diffusivity is proportional to the pore size, and the equilibration time is inversely proportional to the pore size.

Substituting into the equilibration time equation leads to times of a few seconds or less for particle diameters up to a millimeter.

However, in practice, most of the iodine in the pore space is in the absorbed state and is less mobile than in the gas phase. If it is assumed that the adsorbed molecules are immobile, then the diffusivity in the equation must be multiplied by the fraction of iodine that is in the gas phase in the pores.

Assuming that the concentration of adsorbed iodine is 1 g/cm^3 and at the vapor pressure (27 Pa at room temperature) in the gas phase, it can be shown that a fraction of 1 in 3.64×10^5 of I_2 is mobile. This value is obtained by calculating the gas-phase I_2 concentration with the ideal gas law, leading to a value of 2.747 $g/m^3 = 2.747\times10^{-6}$ g/cm^3.

Multiplying the Knudsen diffusivity by this fraction, an effective diffusivity of 1.45×10^{-13} m^2/s is obtained.

Based on this value, the equilibration time in a particle with diameter 1 μm ($R = 5\times10^{-7}$ m) is 1.72 s. Because of the square relationship in the equation, the equilibration time is 172 s for a particle diameter of 10 μm, and 17,200 s for a particle diameter of 100 μm. It follows that the dominant mechanism limiting the adsorption (mass transfer or kinetics) depends strongly on the particle diameter.

Aggregates of particles equilibrate faster than single particles with the same size because the dominant mass transfer mechanism between the particles is molecular diffusion, which is about 2 orders of magnitude faster than Knudsen diffusion in this case. Hence, aggregate size is less critical than particle size.

For diffusion of I^- in liquid phase, molecular diffusion is the most likely mass transfer mechanism because diffusivities in liquid phase are on the order of 10^{-9} m^2/s. If it is assumed that the iodide concentration in liquid phase is 1 mg/mL = 1 g/L, then about 1 part in 1000 is mobile in the pore space. This leads to an effective diffusivity of 10^{-12} m^2/s. This leads to an equilibration time of 0.25 s for a particle with diameter of 1 μm, 25 s for a particle with a diameter of 10 μm, and 2500 s for a particle with a diameter of 100 μm. Because the mass transfer is by molecular diffusion, this applies to both particle size and aggregate size. The conclusion is essentially the same as for gas-phase adsorption kinetics.

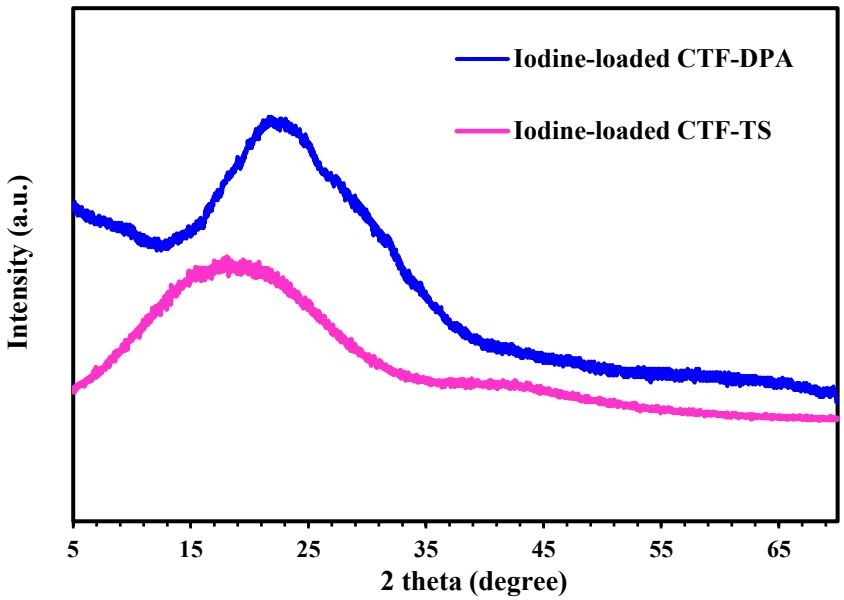

Figure S5.8. XRD patterns of the iodine-loaded CTFs.

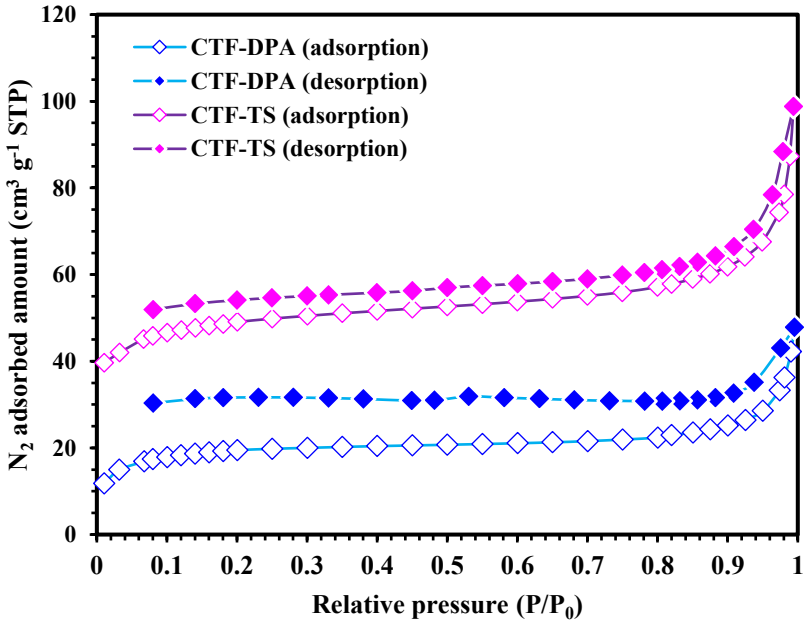

Figure S5.9. N_2 adsorption-desorption isotherms of the iodine-loaded CTFs measured at 77.4 K up to 1 bar.

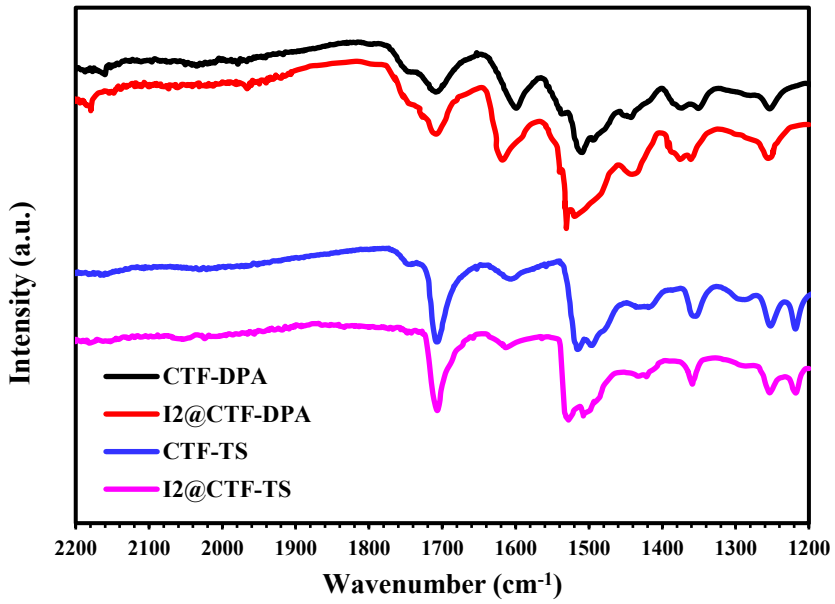

Figure S5.10. FT-IR spectra of the pristine and iodine-loaded CTFs.

Table S5.6. Selected NBO population analysis results for CTF-iodine complexes [a].

Adsorption system	Donor NBO	Acceptor NBO	E(2) (eV)	Adsorption system	Donor NBO	Acceptor NBO	E(2) (eV)
DPA-I	LP (I)	BD* (C-H)	0.073	TS-I	LP (I)	BD* (C-H)	0.042
					LP (I)	BD* (C-H)	0.073
	LP (I)	BD* (C-H)	0.070		LP (I)	BD* (C-H)	0.118
	LP (I)	BD* (C-H)	0.119		LP (I)	BD* (C-H)	0.011
	LP (I)	BD* (C-H)	0.127				
DPA-I_3	BD (I-I)	BD* (C-H)	1.510	TS-I_3	BD (I-I)	LP (I)	0.234
					LP (I)	LP (I)	0.214
	BD (I-I)	LP (I)	0.243		LP (I)	BD* (I-I)	0.379
	LP (I)	LP (I)	0.225				
	LP (I)	BD* (I-I)	0.198		LP (I)	LP (I)	0.336
	LP (I)	BD* (I-I)	3.673		LP (I)	LP (I)	0.191
TPhTAz-I	LP (I)	BD* (C-H)	1.285	TPhTAz-I_3	LP (I)	BD* (C=C)	2.797
	LP (I)	BD* (C=C)	1.362		LP (I)	BD* (C=N)	2.408
	LP (I)	BD* (C=C)	3.582		LP (I)	BD* (C=N)	0.743
					LP (I)	BD* (C-H)	4.719
	LP (I)	BD* (C=C)	1.692		LP (I)	BD* (C-H)	1.595
	LP (I)	BD* (C=C)	2.535				

a. E(2) is the orbital interaction donor-acceptor second-order perturbation energy. Calculated with ωB97XD/6-311+G**/def2-TZVPD. LP, BD, and BD* refer to lone-pair, bonding, and antibonding orbitals, respectively.

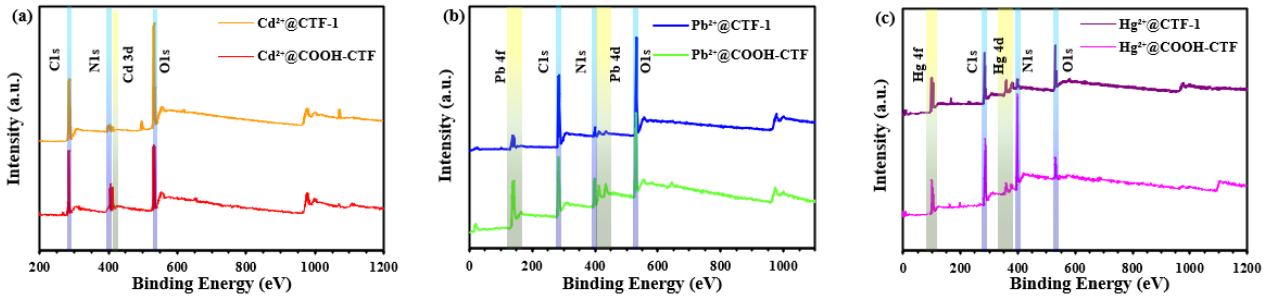

Figure S6.1. XPS spectra of HM cations-loaded CTF adsorbents. (a) Cd^{2+}@adsorbent, (b) Pb^{2+}@adsorbent, and (c) Hg^{2+}@adsorbent.